# SPring-8
# Research Frontiers

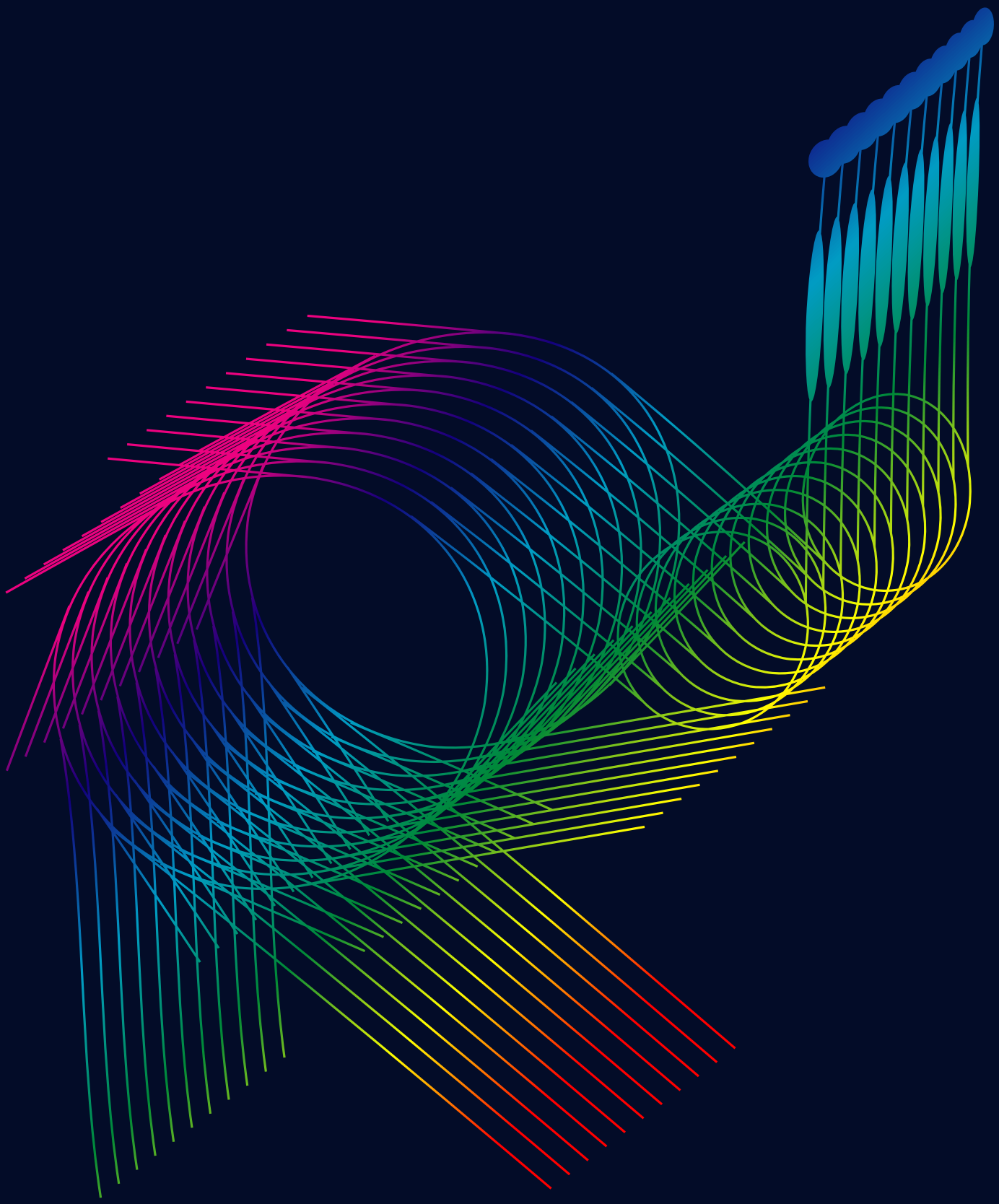

2000／2001

# CONTENTS

# Preface

*Four years have passed since the SPring-8's beam was first made available to the users. This volume of Research Frontiers collects the highlights of the results obtained using SPring-8 during its fourth year, and also describes recent status of the facilities. I hope that this publication would be informative to those currently working on sciences concerned with synchrotron radiation as well as would be instructive to scientists who have not been familiar with synchrotron radiation.*

*Classification in the highlight reports has been changed so that it is friendly to scientists who are interested in but are not an expert in synchrotron radiation. The detailed description of the facilities, which used to be given in our separate publication, the SPring-8 Annual Report, has been moved to this publication as a result of the reorganization of our publications.*

*The users of SPring-8 are classified to three categories: public users, contract beamline owners and facility owners (JAERI and RIKEN). This publication covers the activities of the users in all categories. As for the public use, fifty-five per cent of the total beam time for this period was allocated to this category, and 855 experiments were actually carried out, selected from a total of 1084 proposals.*

*I was appointed the Director General of Synchrotron Radiation Laboratory at SPring-8 in August 2001. I think that SPring-8 is still in a transient from construction to application. Many users have enjoyed the superb quality of the beam of SPring-8. But people concerned with the accelerators and beamlines believe that the machine must be much more potential for new applications than it is utilized now. Those who supported the construction of SPring-8 are now watching how this excellent facility contributes to the society. I would like to invite new challengers to join us to explore latent possibilities of SPring-8.*

A. Kira

*Akira Kira*
Director
SPring-8 / JASRI

**SPring-8 Research Frontiers** describes the outstanding scientific achievements produced at SPring-8 beamlines (BLs): public BLs including R&D BLs, contract BLs, JAERI/RIKEN BLs and an accelerator diagnosis BL. This fourth volume "2000/2001" covers advances made during the two consecutive research terms, the second half of 2000 and the first half of 2001.

In this volume we made some modifications to the editorial framework. The classification of scientific reports was changed from the grouping of the research fields used at the Proposal Review Committee to that of general research disciplines. The article on the facility status in this volume was written in more detail, since the SPring-8 Annual Report, which used to describe the status and activities of the facilities in English is now written in Japanese and we hope that English-speaking user will substitute the SPring-8 Research Frontiers for the SPring-8 Annual Report for their reference.

We invited seven specialists from the Proposal Review Committee to serve as the Editing Coordinators for their respective research fields :

Life Science : *Professor Masaru Tanokura* (The University of Tokyo)
Materials Science : *Professor Satoshi Sasaki* (Tokyo Institute of Technology)
Chemical Science : *Professor Inosuke Koyano* (Himeji Institute of Technology)
Earth & Planetary Science : *Professor Tetsuo Irifune* (Ehime University)
Environmental Science : *Professor Iwao Watanabe* (Osaka Women's University)
Industrial Application : *Professor Tokuhiko Okamoto* (Chubu University)
Instrumentation & Methodology : *Professor Makoto Watanabe* (Tohoku University)

We would like to express our most sincere appreciation to the Editing Coordinators for their efforts in preparing the introductory overviews and providing comments on each research field. We would also like to express our gratitude to users and facility members of SPring-8 for contributing their reports to the SPring-8 Research Frontiers.

**SPring-8 Research Frontiers** will be sent on request. Its full text is also available by accessing the SPring-8 Web site ( http://www.spring8.or.jp/ )

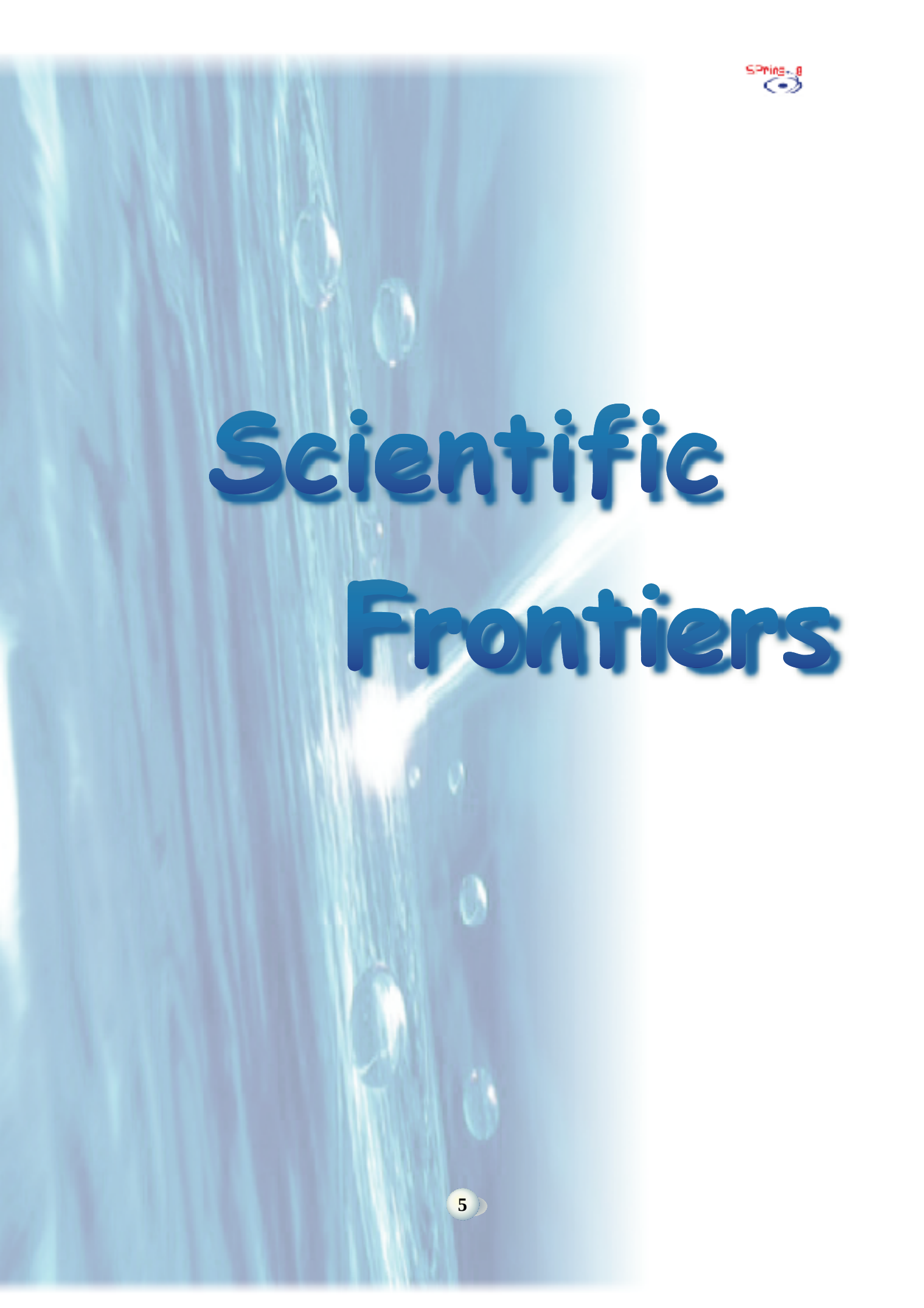
Scientific
Frontiers

# LIFE SCIENCE

SPring-8 operates many beamlines for Life Science experiments. Researchers from universities, private industry and government laboratories around the world use these facilities, and many studies have been reported not only of crystallographic but also of biological significance.

Seven state-of-the-art beamlines are provided for macromolecular crystallography. Many crystals of biological macromolecules have been analyzed, and their structures have been determined. The crystal structure of MinD from *Pyrococcus horikoshii* OT3, a septum site-determining protein, has been determined by the MAD method at BL41XU. This structure reveals the bacterial cell division control. The crystal structure of rat biliverdin reductase has been determined at 1.4 Å resolution at BL44B2. The complexes of biological macromolecules are important to understand the protein-protein or the protein-DNA interactions. The crystal structures of bovine milk xanthine oxidoreductase complexes have been determined both in the dehydorogenase and the oxidase form. The crystal structure of ferredoxin and ferredoxin-$NADP^+$ reductase complex from maize leaves has been determined at 2.6 Å resolution. The crystal structures of human prostaglandin D synthase have been determined, both with and without substrate analogs bound. These complex structures have been determined at BL40B2. The structures of the transcription factor, Runx-1/AML1 (Runt domain) and complexes with DNA reveal the mechanism of regulation of transcription at BL41XU and BL45XU. At BL45XU, designed by “trichromatic concept”, the bacterial flagellar protofilament structure has been determined from 5 μm thick crystals. Recently, a behavior of single molecular units in real time has been observed by a new method, the “diffracted X-ray tracking system.” Using this method, the Brownian motions of biological molecules can be monitored at BL44B2. At BL45XU, motion of activated myosin heads has been detected by fiber X-ray diffraction.

At beamlines for medical research, the high resolution synchrotron radiation X-ray microCT method has been developed, and by this method the three dimensional glomerular micro-structures have been visualized.

*Masaru Tanokura*

# Crystal Structure Analysis of Septum Site-determining Protein MinD from *Pyrococcus horikoshii* OT3

Bacterial cell division requires the formation of a septum at midcell, circumferential invagination of the cytoplasmic membrane, and synthesis of a peptidoglycan layer. The key step in septum formation is the polymerization of essential cell division protein FtsZ at the potential division site. FtsZ recruits several other essential proteins to form mature cell division machinery and the cell division process then progresses. Rod-shaped bacteria such as *Escherichia coli* have three potential division sites in a cell. One of them is at the midcell position, while the others are adjacent to the cell poles. Thus the precise placement of the FtsZ ring at the cell center is a prerequisite for the accurate cell division of bacteria. In *E. coli*, the cell division site is determined by the cooperative activity of *min* operon products MinC, MinD, and MinE. MinC is a nonspecific inhibitor of the septum protein FtsZ, and MinE is the suppressor of MinC. MinD plays a multifunctional role. It is a membrane-associated ATPase and is a septum site-determining factor through the activation and regulation of MinC and MinE (Fig. 1). MinD is also known to undergo a rapid pole-to-pole oscillation movement *in vivo* as observed in fluorescent microscopy [1].

We studied recombinant MinD from *Pyrococcus horikoshii* OT3 (PH0612) expressed in *E. coli*, and determined the three-dimensional structure at 2.3 Å resolution by X-ray crystallography using the Se-Met MAD method at beamline **BL41XU** [2]. The crystal structure consists of a β-sheet with seven parallel and one antiparallel strands and eleven peripheral α-helices (Fig. 2). Although we made no attempt to add ATP or ADP molecules in the purification or crystallization step, the electron density clearly shows that MinD from *P. horikoshii* contains bound ADP and a magnesium ion at the pocket close to the edge of the β-sheet on the surface of the MinD molecule (Fig. 3). It has been shown that the ADP molecule was bound during the growth of the *E. coli* cells, and MinD from *E. coli* has ATPase activity in the presence of $Mg^{2+}$ ion. Therefore, the observed coordination of ADP in the present crystal is considered to be the product of the molecule's ATPase activity.

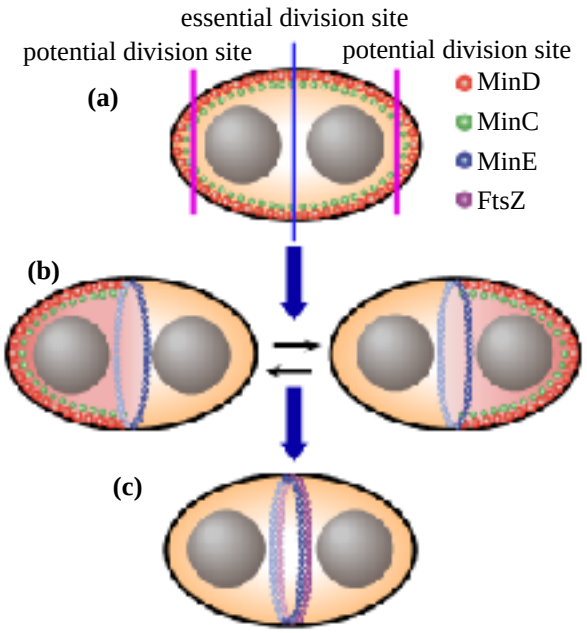


*Fig. 1. The schematic diagram of the bacterial cell division machinery.* ***(a)*** *The rod-shaped bacteria have three potential division sites in the cell. The MinCD complex inhibits division at all potential division sites in the cell.* ***(b)*** *The MinE ring is formed, and the activity of cell division inhibition of MinCD is suppressed by MinE. The MinCD complex undergoes a rapid pole-to-pole oscillation movement.* ***(c)*** *MinE recruits the cell division proteins as FtsZ at midcell division sites. The circumferential invagination with squeeze of FtsZ ring starts.*

Structure analysis shows that MinD is most similar to nitrogenase iron protein which is a member of the family of the P-loop containing the nucleotide triphosphate hydrolase superfamily of proteins. Unlike nitrogenase or other member proteins that normally work as a dimer, MinD was present as a monomer in the crystal. MinD is also known to behave like a motor protein in *E. coli* cells. The present analysis has shown that MinD has a limited structural similarity with family of motor proteins. Although the tertiary structure of ATPase activity site is similar in these proteins, the overall topology is different. Thus, they are distantly related if at all. Both the $^{31}$P NMR and Malachite Green method exhibited relatively low levels of ATPase activity. These facts suggest that there are some additional factor(s) for MinD to exhibit ATPase activity in the cell and MinD may work as a molecular switch in the multiprotein complex in bacterial cell division.

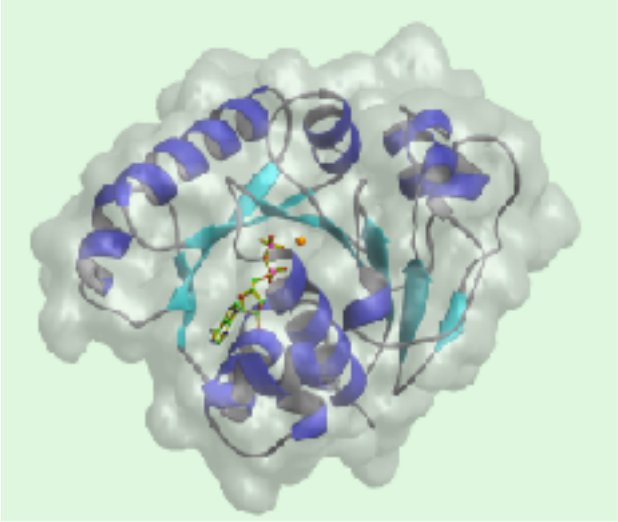

*Fig. 2. The ribbon diagram of the crystal structure of MinD from P. horikoshii with transparent molecular surface. Bound ADP is shown as ball and stick and magnesium ion is shown as an orange ball. The nucleotide binding pocket is close to the edge of the β-sheet. This pocket is exposed to solvent region.*

Naoki Sakai, Min Yao and Isao Tanaka

Hokkaido University

E-mail: yao@castor.sci.hokudai.ac.jp

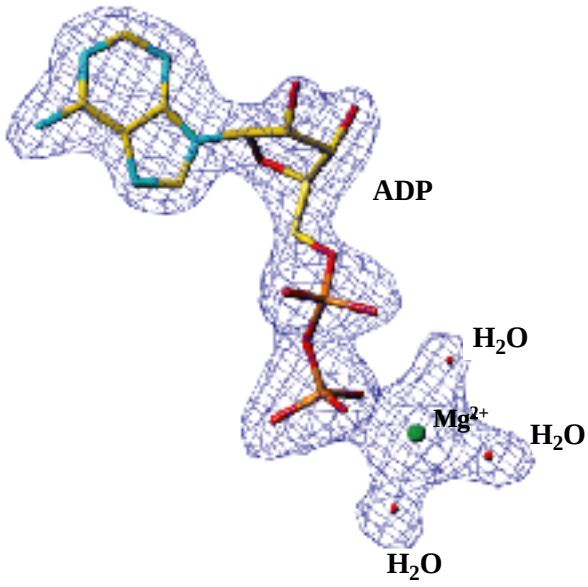


*Fig. 3. Electron density of Mg-ADP region. The sigma-weighted omit map is calculated at 2.3 Å resolution and contoured to 3.0σ.*

**References**

[1] D.M. Raskin and P.A.J. de Boer, Proc. Natl. Acad. Sci. USA **96** (1999) 4971.

[2] Naoki Sakai, Min Yao, Hiroshi Itou, Nobuhisa Watanabe, Fumiaki Yumoto, Masaru Tanokura, and Isao Tanaka, Structure **9** (2001) 817.

# Crystal Structure of Biliverdin Reductase

A heme (Fe-porphyrin complex) is a prosthetic group of hemoproteins such as hemoglobin, myoglobin, cytochromes and so on. In biological systems, the heme is decomposed by two enzymes (hemeoxygenase and biliverdin reductase) and excreted (Fig. 1). Biliverdin reductase (BVR) catalyzes the last step of the heme catabolism, in which the biliverdin is reduced into bilirubin with two electrons from NAD(P)H. Reduction of biliverdin (formation of bilirubin) is important for the disposal of the heme catabolite formed in the fetus since the placenta is permeable to bilirubin but not to biliverdin. Bilirubin is the most abundant biological anti-oxidant in mammalian tissues, and is highly related to neuroprotection, but also to cytotoxicity (kernicterus). Clearly, BVR is a key enzyme and logical pharmacological target for controlling bilirubin level *in situ*.

We have analyzed the crystal structure of rat BVR at 1.4 Å resolution (Fig. 2), whose diffraction data was collected at beamline **BL44B2** [1]. This enzyme consists of two domains that are packed tightly together. The N-terminal domain (123 amino acids) is a characteristic of a dinucleotide binding fold, the so-called Rossmann fold, while the C-terminal domain (169 amino acids) contains six β-strands and eight helices, and is dominated by a large, and predominantly antiparallel six-strande sheet.

*NAD(P)H Binding to BVR:* The Rossmann fold in the N-terminal domain is the most likely NAD(P)H binding site. The 'fingerprint' region (Gly15-Val16-Gly17-Arg18-Ala19-Gly20) and a 'hydrophobic core' (Val11, Val13, Leu24, Leu27, Val42) are found in this region. Glu96 is apparently capable to interact with the nicotinamide ring of NAD(P)H through the hydrogen bond (Fig. 3). Indeed, Glu96Ala mutant of BVR, in which Glu96 was replaced with Ala, did not exhibit the enzymatic activity. A unique property of BVR is its ability to use either NADH or NADPH at different pH optima; NADH is used in the lower pH range of 6.7 - 6.9, whereas NADPH is used at the higher pH of 8.7 [2]. In a model study, in which NADH or NADPH was put on the Rossmann fold of BVR, we found that Arg44-Arg45-Glu46 is located very close to the 2'-position of the adenosine ribose (Fig. 3). In combination with the mutational studies, we proposed that Arg44 and Arg45 play crucial roles in NADPH binding, while Glu46 modulates the NADH binding.

*Biliverdin Binding to BVR:* The putative NAD(P)H binding site is on the lower side of the pocket that is constructed between the N- and C-terminal domains. On the other hand, there are located four basic residues, Arg171, Lys218, Arg224 and Arg226, on the upper side of this pocket (Fig. 3). Since the biliverdin recognition by BVR has been proposed to be achieved through an

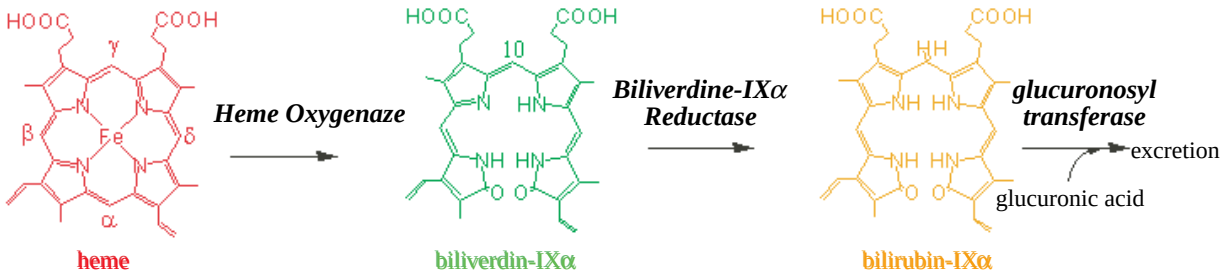


*Fig. 1. Heme degradation pathway in mammals.*

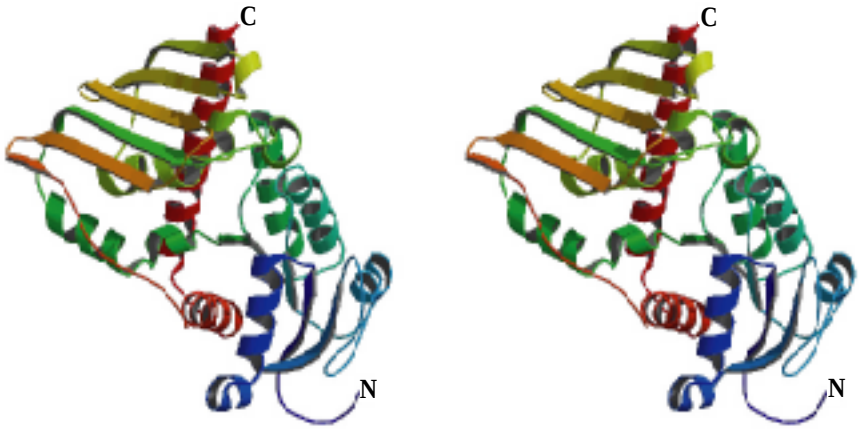


*Fig. 2. Stereo view of the overall structure of rat BVR.*

electrostatic interaction between the negatively charged propionate side chains of biliverdin and positively charged residues of BVR [3], we proposed that cluster of the four basic residues is a possible biliverdin binding site. The pocket is wide enough to accommodate both biliverdin and NAD(P)H. When biliverdin would bind to this site, the distance between the reduction site (C10 *meso* position) of biliverdin and the NAD(P)H nicotinamide is estimated to be ~10 Å. In this model, Tyr97 is located between the nicotinamide and C10 *meso* position, and therefore this residue may mediate a hydride ($H^-$) transfer from NAD(P)H to biliverdin in the enzymatic reaction.

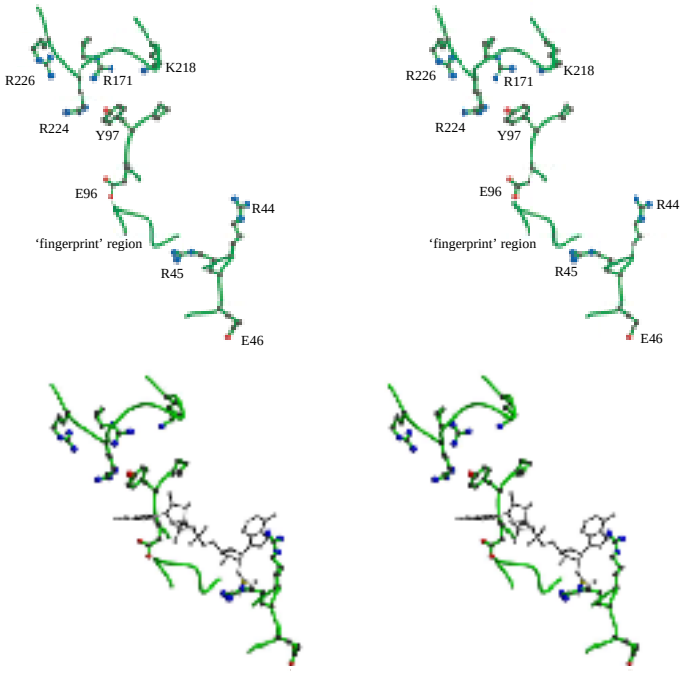


*Fig. 3. The proposed binding sites for NAD(P)H (electron donor) and substrate (biliverdin) in rat BVR.*

Akihiro Kikuchi and Yoshitsugu Shiro

SPring-8 / RIKEN

E-mail: yshiro@postman.riken.go.jp

**References**

[1] A. Kikuchi, S.-Y. Park, H. Miyatake, D. Sun, M. Sato, T. Yoshida and Y. Shiro, Nature Strl. Biol. **8** (2001) 221.

[2] R. K. Kutty and M. D. Maines, J. Biol. Chem. **256** (2981) 3956.

[3] O. Cunningham *et al.*, J. Biol. Chem. **275** (2000) 19009.

# High-Resolution Structure of Bovine Milk Xanthine Oxidoreductase and Inhibitor Complexes

Xanthine oxidoreductase catalyzes the hydroxylation of hypoxanthine and xanthine, the last two steps in the formation of urate in purine catabolism in man. The enzyme is a target of drugs not only against gout [1], but also against oxygen radical-induced tissue damage [2]. Allopurinol has been used as a widely used drug effective against gout and hyperuricemia since it was introduced more than 30 years ago. Bovine milk xanthine oxidase is an archetypal enzyme, which was originally described as aldehyde oxidase in 1902 [3] and has been the benchmark of the metallo-flavoproteins [4,5]. The enzyme from mammalian sources, including man, is synthesized as the dehydrogenase form but it can be readily converted to the oxidase form by oxidation of sulfhydryl residues or by proteolysis. The dehydrogenase shows a preference for $NAD^+$ reduction, while the oxidase fails to react with $NAD^+$ and exclusively uses oxygen molecule as its substrate leading to the formation of superoxide anion and hydrogen peroxide (Fig. 1). The enzyme has been implicated in diseases characterized by oxygen radical-induced tissue damage, such as postischemic reperfusion injury [2]. The crystal structures of xanthine oxidoreductase in the two forms, dehydrogenase and oxidase, have been solved after successful crystallization of both forms of the enzyme, to clarify the structure-based mechanism of conversion [6,7]. The experiment was car out at beamline **BL40B2**.

The active form of the enzyme is a homodimer of molecular mass 290 kDa, with each of the monomers acting independently in catalysis. Each subunit molecule is composed of an N-terminal 20 kDa domain containing two iron sulfur centers, a central 40 kDa FAD domain, and a C-terminal 85 kDa molybdopterin-binding domain with the four redox centers aligned in an almost linear fashion (Fig. 2). The hydroxylation of xanthine takes place at the molybdopterin center (Mo-pt) and the electrons thus introduced are rapidly transferred to the other linearly aligned redox centers as illustrated in Fig. 1. The reaction catalysed by the Mo hydroxylases is distinct from those of other biological hydroxylation systems like P450 in that an oxygen atom is incorporated into the product from water rather than from an $O_2$ molecule [5]. In

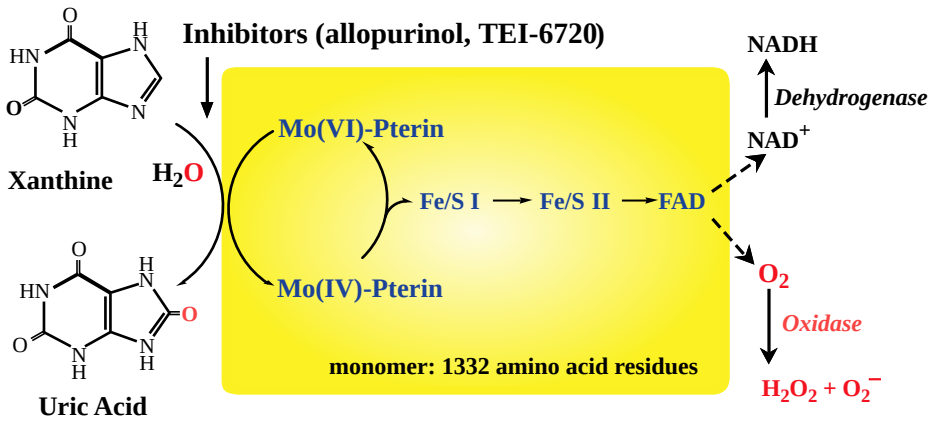


*Fig. 1. Reaction scheme of xanthine dehydrogenase and xanthine oxidase. The enzyme is a dimer (MW 290,000) having two identical subunits of 1332 amino acids.*

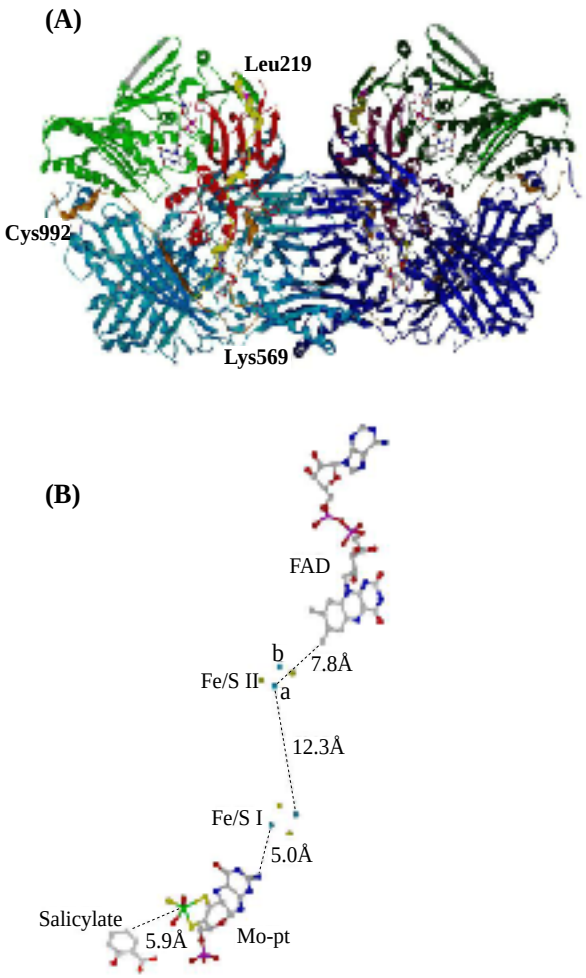


*Fig. 2.* ***(A)*** *Crystal structure of the xanthine dehydrogenase dimer divided into the three major domains. The enzyme contains salicylate, a competitive inhibitor. From N- to C-terminus, the domains are: iron-sulfur-center domain (residues 1- 165; red), FAD domain (residues 226 - 531; green), and Mo-pt domain (residues 590 - 1332; blue). Cofactors are also included.* ***(B)*** *The arrangement of the cofactors and salicylate in one subunit of the enzyme are presented. The Mo ion is in green, the iron ions are in light blue, and the sulfur atoms in yellow.*

the crystal structure of the active enzyme, we assigned a double-bonded sulfur atom, a double-bonded oxygen atom (=O), and an oxygen atom with a single bond (OH) as ligands to the Mo ion. It should be noted that the protein environments of two oxygen ligands are distinct in the high resolution crystal structure and the OH ligand is considered to be labile oxygen based on the structure of the alloxanthine enzyme complex (to be published). In addition to the crystal structure of the complex of the enzyme and alloxanthine, the oxidative product of allopurinol, we solved the crystal structure of the complex of the enzyme and TEI-6720, a strong candidate for a new anti-gout drug. In the crystal structure of the enzyme TEI-6720 complex, numerous hydrogen bonds and hydrophobic interactions were observed between the protein and this extremely potent inhibitor (Fig. 3), and some of them seemed to contribute to strong binding in a similar way to substrate recognition [8].

The FAD active site is the part of the enzyme that shows the largest difference between xanthine dehydrogenase and oxidase [1,2]. Cleavage of a surface-exposed loop of XDH causes major structural rearrangement of a loop close to the flavin ring (Fig. 4). This movement partially blocks NAD substrate access to the FAD cofactor and changes the electrostatic environment of the active site, accounting for the switch of substrate specificity observed for the conversion between the two forms.

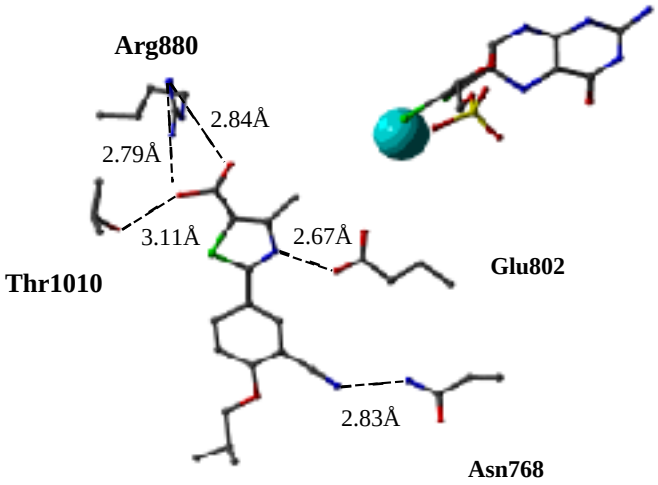


*Fig. 3. Active site structure at the molybdenum center of TEI-6720 inhibitor bound form. The molybdenum atom is shown in cyan.*

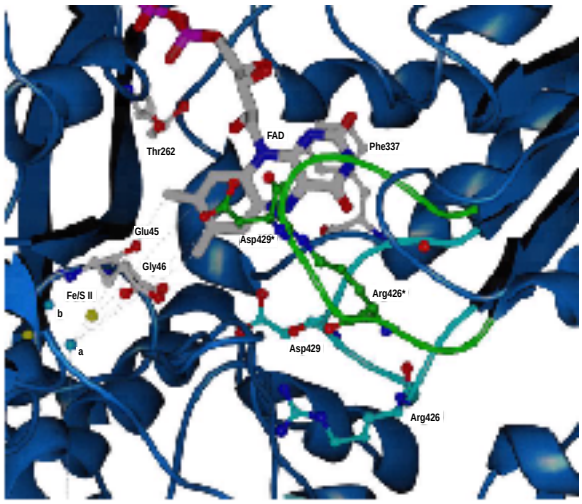


*Fig. 4. Ribbon diagram of the FAD and Fe/S II active sites. The active site loop from Asp 426 to Asp 434 which changes its conformation during the XDH to XO transition is shown in light blue for XDH and in green for XO. The positions of residues Asp 429 and Arg 426 are indicated; their side chains show dramatic shifts in position and are major contributors to the change in electrostatic charge at the flavin site.*

Takeshi Nishino[a], Ken Okamoto[a] and Emil F. Pai[b]

(a) Nippon Medical School
(b) The University of Toronto

E-mail: nishino@nms.ac.jp

**References**

[1] G.B. Elion, Science **244** (1989) 41.
[2] J.M. McCord, N. Engl. J. Med. **312** (1985) 159.
[3] F. Schardinger, Z. Untersuch. Nahrungs Genussmittel **5** (1902) 1113.
[4] T. Nishino, J. Biochem.(Tokyo) **116** (1994) 1.
[5] R. Hille and T. Nishino, FASEB J. **9** (1995) 995.
[6] B.T. Eger *et al.*, Acta Cryst. **D 56** (2000) 1656.
[7] C. Enroth *et al.*, Proc. Natl. Acad. Sci. USA (2000) 10723.
[8] K. Okamoto *et al.*, in preparation.

# Structure of the Electron Transfer Complex Between Ferredoxin and Ferredoxin-NADP$^+$ Reductase

All oxygenic photosynthetically derived reducing equivalents are utilized by combinations of a single multifuctional electron carrier protein, ferredoxin (Fd), and several Fd-dependent oxidoreductases. Plant-type Fd is a small, soluble, acidic protein distributed in plants, algae and cyanobacteria. Each Fd-dependent enzyme is also distributed in the same organism and functions in photosynthetic metabolism, such as Fd-NADP$^+$ reductase (FNR), which is involved in the process of carbon assimilation; nitrite reductase and glutamate synthase, which are involved in nitrogen assimilation; sulfite reductase, which is involved in sulfur assimilation; and ferredoxin-thioredoxin reductase, which is involved in the redox regulation of several enzymes.

About 20 years ago, the first structure of a plant-type Fd was reported [1]. Many biochemists have been studying the interaction sites of Fd based on this 3-D structure. After the crystal structure of FNR as a representative of Fd-dependent enzymes was reported in 1991 [2], further experiments including computer modeling and continuous mutational experiments of this protein-protein interaction have been carried out extensively.

We determined the first crystal structure of the complex of Fd and FNR from maize leaf at 2.59 Å resolution [3] (Fig. 1). The diffraction data was collected at beamline **BL41XU**. The redox partners are in close contact at the prosthetic groups, the 2Fe-2S cluster of Fd and FAD of FNR, the shortest distance being 6.0 Å. Interaction mainly occurs by electrostatic force through salt bridges, and the interface near the prosthetic groups is hydrophobic (Fig. 2). Interestingly, the structures of Fd and FNR in the complex and in the free state alter in a number of ways. Consistent with this, we confirmed FNR recognition sites on the Fd protein by NMR spectroscopy of the complex in solution. Such structural alteration is found at Glu 312 in the active site of FNR (Fig. 3). We propose that this type of molecular communication not only determines optimal orientation of the two proteins for electron

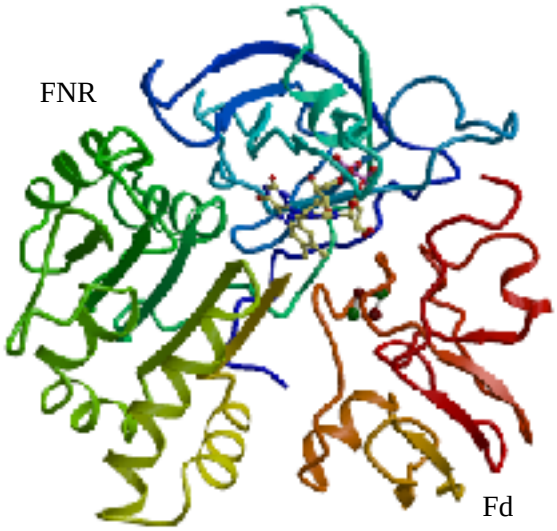


*Fig. 1. Whole structure of the electron transfer complex between Fd (lower right) and FNR (upper left). Two prosthetic groups, FAD and [2Fe-2S] cluster, are located at the interface of two proteins and shown in ball-and-stick models.*

transfer, but also contributes to the modulation of the enzymatic properties of FNR. These structural alterations of two proteins are consistent with previous biochemical and biophysical reports and thought to be important for efficient electron transfer between them. The 3-D structure of the photosynthetic electron transfer complex is important for further understanding of assimilatory reduction and molecular recognition mechanism closely related to the physiological conditions of higher plants.

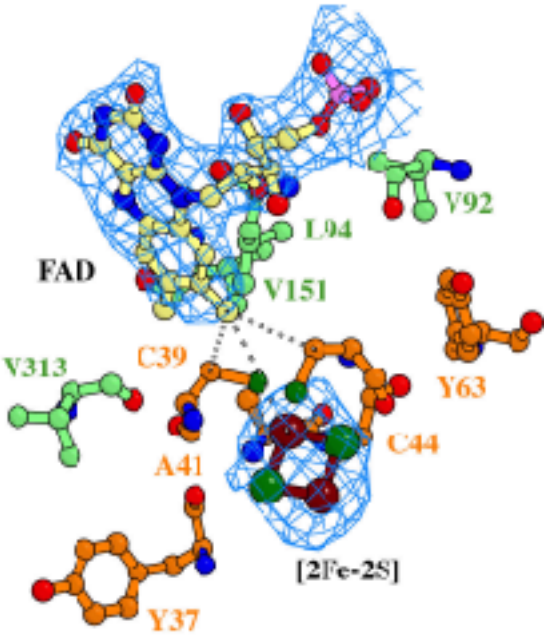


*Fig. 2. Structure of the interface of Fd and FNR. The final 2Fo-Fc map was drawn around the prosthetic groups. The vicinity of the redox active center is hydrophobic and seems to be suitable for the direct electron transfer between two prosthetic groups.*

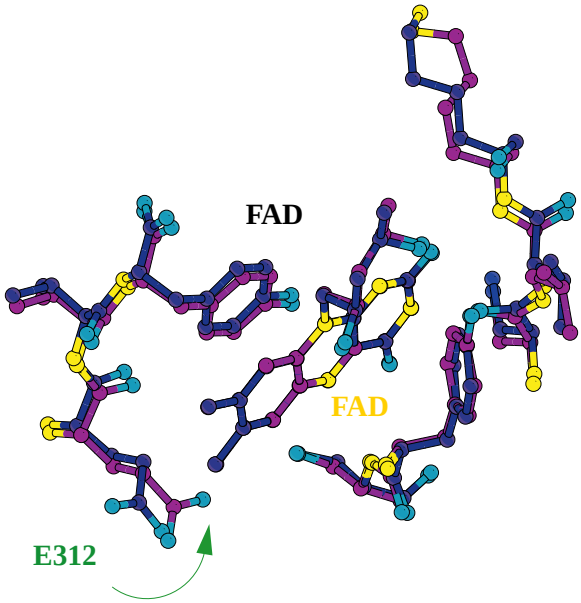


*Fig. 3. Structural alteration of FNR induced by the complex formation with Fd. The structure around the FAD from single FNR is colored in yellow and that of the complex is in green. The side chain of E312 was moved into the active site upon the complex formation with Fd.*

Genji Kurisu and Masami Kusunoki

Osaka University

E-mail: kurisu@protein.osaka-u.ac.jp

**References**

[1] K. Fukuyama *et al.*, Nature **286** (1980) 522.
[2] P.A. Karplus *et al.*, Science **251** (1991) 60.
[3] Genji Kurisu, Masami Kusunoki, Etsuko Katoh, Toshimasa Yamazaki, Keizo Teshima, Yayoi Onda, Yoko Kitama-Ariga and Toshiharu Hase, Nature Struct. Biol. **8** (2001) 117.

# Structure of Prostaglandin D Synthase Complexed with Drug Molecules

Medicines can help people suppress the feelings of headaches or period pains. But at the same time, there are side effects. Sometimes people feel sleepy when they use medicine. Medicine containing aspirin or indometasine inhibits cyclooxygenese (COX) that catalyzes the reaction from arachidonic acid to prostaglandin (PG) $H_2$ in the arachidonic acid cascade (Fig. 1). $PGH_2$ is the starting compound which is utilized to obtain other types of prostaglandin, $PGD_2$, $PGF_{2\alpha}$ and $PGE_2$, and so on. Each PG has a specific function in the tissue concerned. $PGD_2$ in the brain has the function of promoting sleep, however, in other tissues, $PGD_2$ is produced from mast cells as an allergic mediator or inflammatory mediator. $PGF_{2\alpha}$ was the first compound to be discovered which has the role of contracting the oviductal smooth muscle. $PGE_2$ has the role of regulating body temperature and also promotes wakening. The inhibition of the production of $PGH_2$ by medicine causes side effects due to the lack of specific prostanoids in various tissues. Each prostaglandin is formed by a specific enzyme, PGD synthase, PGF synthase and PGE synthase, respectively. As for the design of anti-allergic drugs, the structure of human hematopoietic PGD synthase (H-PGDS) is the most potent target, as demonstrated in an allergic asthma model with prostaglandin D receptor gene-disrupted mice [1], and as also demonstrated by transgenic mice that overproduce $PGD_2$, thus exacerbating asthmatic reactions [2].

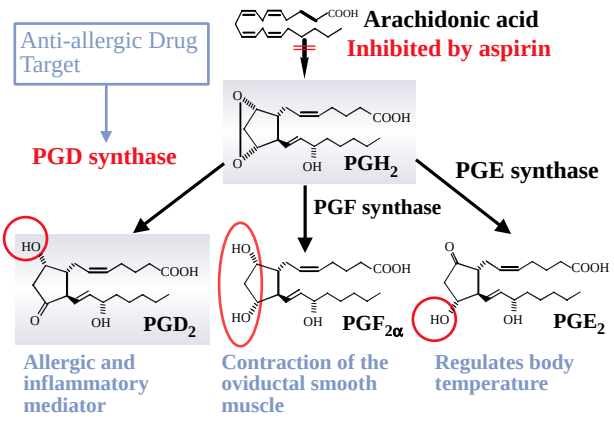


*Fig. 1. Biosynthetic Pathway of Prostaglandins (PGs) with compositional formulas and their roles. The difference of each PG is the stereochemistry of hydroxyl group or functional group.*

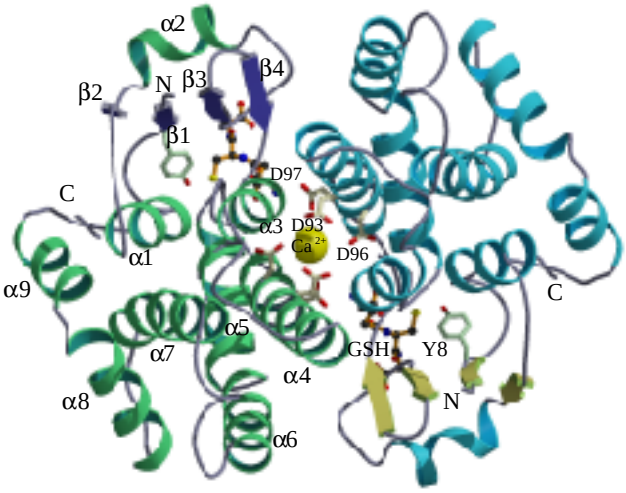


*Fig. 2. The whole structure and the metal binding site of human H-PGDS. The metal binding site was found at the dimer interface where six aspartates exist.*

H-PGDS absolutely requires glutathione (GSH) for stereospecific isomerzation from $PGH_2$ to $PGD_2$. We determined the X-ray structures of the native and substrate analog complexes of human H-PGDS with glutathione (GSH) in the presence of $Ca^{2+}$ or $Mg^{2+}$. The metal binding site was found at the dimer interface where six aspartates, Arg14 and GSH construct a large hydrogen bond network regulated by metal ions (Fig. 2). $Ca^{2+}$ reduces the $K_m$ value for substrate, while, $Mg^{2+}$ reduces the $K_m$ value for GSH as well as the substrate. $Mg^{2+}$ shows a remarkable change in the hydrogen bond

network, promoting a free rotation of Arg14, which results in a low $K_m$ value for GSH. The $Ca^{2+}$- and $Mg^{2+}$-bound complex structures with two kinds of substrate analogs provide snapshots of successive binding of the substrate analogs to the enzyme, indicating a possible novel reaction mechanism, regulated by the metal ion, for the isomerization from the 9,11-endperoxide group of $PGH_2$ to $PGD_2$ with the 9-hydroxy-11-keto group.

Tsuyoshi Inoue[a,b]

(a) Osaka University
(b) Japan Science and Technology Corp., PRESTO

E-mail: inouet@chem.eng.osaka-u.ac.jp

## References

[1] T. Matsuoka *et al.*, Science **287** (2000) 2013.
[2] Y. Fujitani *et al.*, J. Immunol. **168** (2002) 443.
[3] T. Inoue, N. Okazaki, H. Shishitani, S. Kinugasa, Y. Okano, H. Matsumura, Y. Kai, M. Yamamoto, T. Kumasaka, D. Irikura, N. Uodome, O. Hayaishi, and Y. Urade, in preparations.

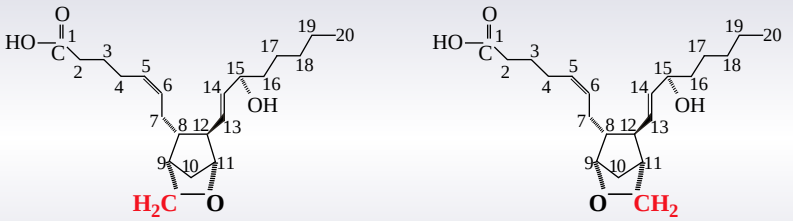


*Fig. 3. Two kinds of substrate analogs used for the complex structure analysis. The difference is in only the location of the oxygen atom in the cyclopentane ring.*

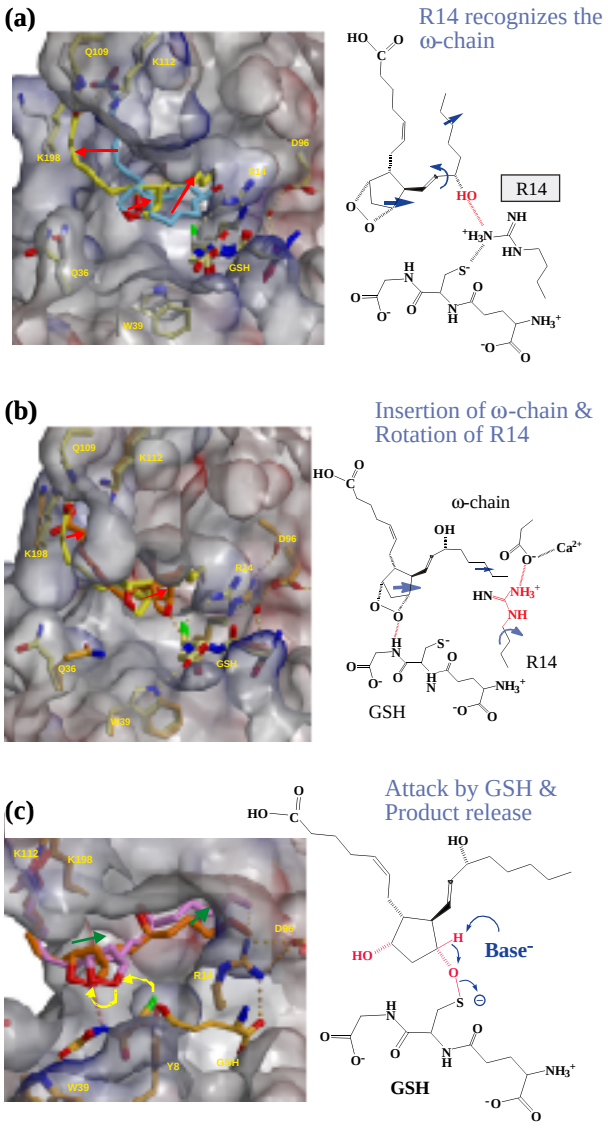


*Fig. 4. We obtained three different binding motifs of the substrate analogs in the presence of $Ca^{2+}$ or $Mg^{2+}$, providing X-ray snapshots of the successive binding of the substrate analogs to the enzyme. We are now proposing the novel reaction mechanism on the right side of each figure.*

# Crystallographic Analyses of the Runx-1/AML1 (Runt domain) - DNA Interaction and Its Allosteric Control by CBFβ

The promoter regions of most genes contain binding sites for multiple transcription factors whose interactions are essential for the correct regulation of transcription. Such interactions include those between different transcription factors as well as those between subunits of the same factor. In the case of some heterodimeric factors (*e.g.*, Jun/Fos and Myc/Max) both subunits bind to specific DNA sequences, and recent X-ray studies of this type of protein have clarified the molecular mechanisms of their DNA binding (*e.g.*, the "scissors grip" by the Fos-Jun heterodimer). On the other hand, some transcription factors consist of one subunit that binds to DNA and one that does not. In most cases of this type of protein, it remains unknown how a non DNA-binding subunit contributes to DNA binding and whether the mechanism by which a non-DNA-binding subunit stimulates DNA binding is shared with different transcription factors. In this type, very little structural information is available to date, *e.g.* the GABPα-GABPβ-DNA complex *(GABP: GA-binding protein). One well-studied* example of this type of transcription factor is the core binding factor (CBF), which functions as a heterodimer consisting of a DNA-binding α subunit and a non-binding β subunit.

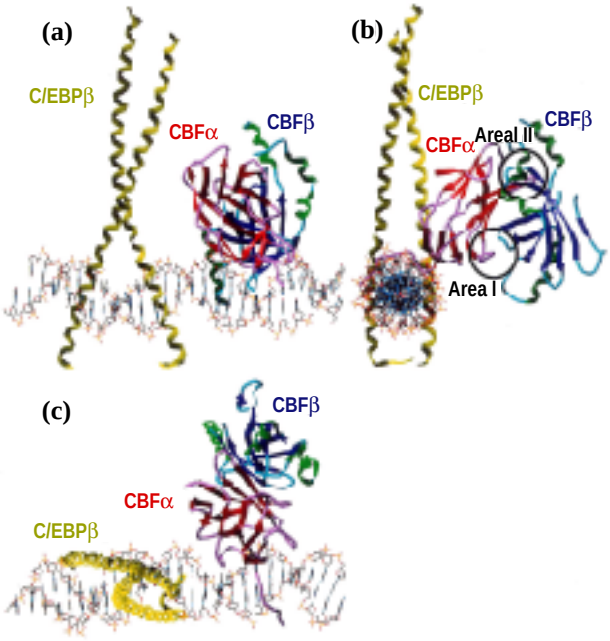


*Fig. 1. Overviews of the CBFα-β-C/EBPβ-DNA quaternary complex from three perspectives [1]. Views (**a**) from the front, (**b**) from the side and (**c**) from the top. Within CBFα, β strands and loops are depicted as red arrows and pink tubes, respectively; within CBFβ, α helices, β strands and loops are depicted as green ribbons, blue arrows and cyan tubes, respectively. The C-terminal region of the C/EBPβ homodimer containing the bZip domain is shown as yellow ribbons. Areas I and II are marked with circles.*

The CBF heterodimeric transcription factors comprised of AML/CBFA/PEBP2α/Runx and CBFβ/PEBP2β subunits are essential for differentiation of hematopoietic and bone cells, and their mutation is intimately related to the development of acute leukemia and cleidocranial dysplasia; (AML: acute myelogenous leukemia, CBFA: core-binding factor A and PEBP: polyomavirus enhancer-binding protein). Here we present the crystal structures of the AML1/Runx-1/CBFα(Runt domain)-CBFβ(core domain)-C/EBPβ(bZip)-DNA, AML1/Runx-1/CBFα(Runt domain)-C/EBPβ(bZip)-DNA, and AML1/Runx-1/CBFα(Runt domain)-DNA complexes, which are abbreviated to CBFα-β-C/EBPβ-DNA, CBFα-C/EBPβ-DNA and CBFα-DNA respectively, obtained from the diffraction experiments at beamlines **BL41XU** and **BL45XU** [1]. Our focus is on the recognition of specific DNA sequences by CBFα and on the mechanism by which CBFβ facilitates DNA binding.

The structure of a complex comprising the CBFα Runt domain and the CBFβ core domain bound to a 26-bp DNA fragment from the CSF-1R promoter, together with the C/EBPβ basic leucine zipper region homodimer, is shown in Fig. 1(a-c). Note that the structures of DNA-bound CBFα are

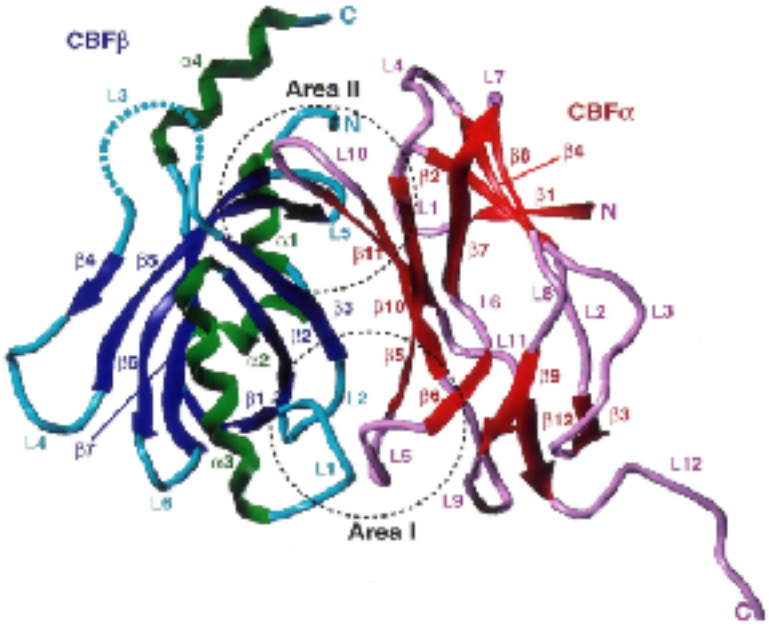


*Fig. 2. CBFα-CBFβ heterodimer structure in complex with the DNA [1]. Two predominantly hydrophilic interaction areas between CBFα and CBFβ (Areas I and II) are marked with dotted circles.*

very similar, with or without CBFβ: the r.m.s. deviation of the α carbon atoms was only about 0.28 Å. Both the CBFα Runt domain and the CBFβ core domain fold principally as β barrel architectures, with the structure of the former being classified as an s-type immunoglobulin fold. The Runt domain recognizes specific bases (TGTGGTT) in both the major and minor grooves of the DNA, mainly using loops. The CBFβ core domain interacts with the CBFα Runt domain at a site distant from the protein-DNA interface. The CBFα-CBFβ interface extends linearly from the DNA and can be divided into two predominantly hydrophilic interaction areas – one proximal to DNA (Area I) and one distal (Area II) – with an intervening hydrophobic area (Figs. 2 and 1b). Contrary to earlier protein-protein and protein-DNA binding assays [2,3], analyses of crystals of the CBFα-β-C/ EBPβ-DNA and CBFα-C/EBPβ-DNA complexes revealed no direct interaction between the C/EBPβ basic leucine zipper domain and the CBFα Runt domain or the CBFβ core domain.

CBFα-DNA binding is enhanced several folds in the presence of CBFβ. To examine the regulation of CBFα-DNA binding by CBFβ, we compared the structure of the CBFα-β-C/EBPβ-DNA complex with those of the CBFα-C/EBPβ-DNA and CBFα-DNA complexes, which lack the CBFβ subunit. Somewhat surprisingly, CBFβ binding causes no dramatic structural changes in the CBFα Runt domain, which implies that CBFβ does not alter the

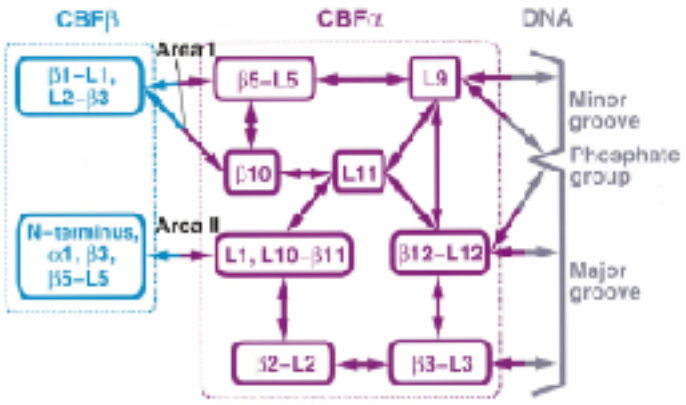


*Fig. 3. Schematic representation of the stabilization network between CBFβ (cyan), CBFα (pink) and DNA (gray) [1].*

overall conformation of the CBFα Runt domain, but only stabilizes it in a conformation suitable for DNA binding. As described above, CBFβ interacts with CBFα via two predominantly hydrophilic regions– Areas I and II, and their stabilization affects the conformations of the flexible loops in contact with the DNA to grip the DNA molecule at both the major and minor grooves (Fig. 3).

Acute leukemia and related diseases associated with biallelic and heterozygous point mutations of AML1/Runx-1 have been reported. In the case of biallelic mutations, no functional AML1/Runx-1 allele remains; in the case of heterozygotes, the DNA binding activity of AML1/Runx-1 from one allele is impaired, with AML1/Runx-1-CBFβ heterodimerization activity retained. Based on the three-dimensional structure of the CBFα-CBFβ heterodimer bound to the DNA, point mutation sites in the heterozygous cases are mapped exclusively to regions of the CBFα-DNA interface (Fig. 4). It is readily apparent that these mutations impair the capacity of CBFα to bind to DNA without affecting the overall folding architecture of CBFα or CBFα-CBFβ heterodimerization, which could explain their dominant negative behavior.

**Acute Myelogenous Leukemia and related diseases**

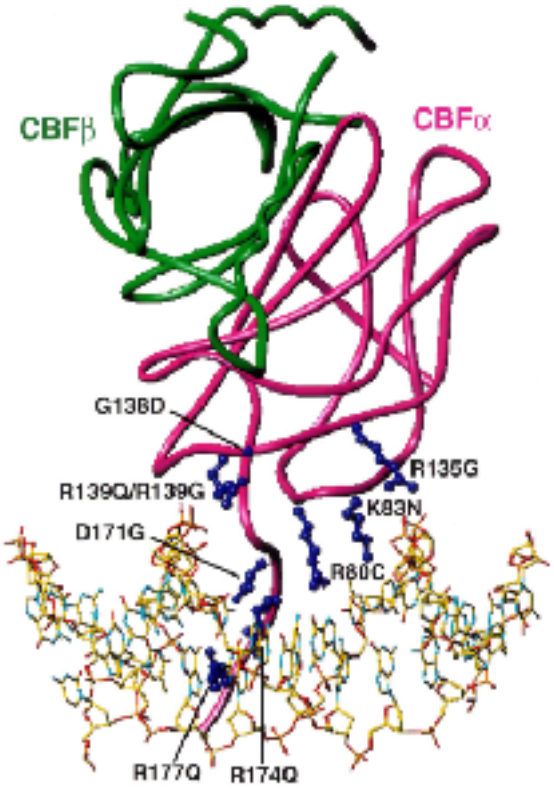


*Fig. 4. Structural maps of CBFα point mutations occurring in acute myelogenous leukemia and related diseases [1]. The mutated residues are shown in green ball and stick presentations. The peptide backbones of CBFα and CBFβ are depicted as pink and cyan tubes, respectively.*

Tahir H. Tahirov[a,b], Taiko Inoue-Bungo[a] and Kazuhiro Ogata[a,b,c]

(a) Kanagawa Academy of Science and Technology (KAST)
(b) SPring-8 / RIKEN
(c) Yokohama City University School of Medicine

E-mail: ogata@med.yokohama-cu.ac.jp

**References**

[1] T.H. Tahirov, T. Inoue, M. Sasaki, K. Kimura, H. Morii, A. Fujikawa, M. Shiina, K. Sato, T. Kumasaka, M. Yamamoto, S. Ishii, K. Ogata, Cell **104** (2001) 755.

[2] D.E. Zhang *et al.*, Mol. Cell. Biol. **16** (1996) 1231.

[3] M.S. Petrovick *et al.*, Mol. Cell. Biol. **18** (1998) 3915.

# A Mechanical Switch Found in the Bacterial Flagellar Protofilament Structure

The bacterial flagellum consists of a rotary motor and a helical propeller by means of which bacteria swim. The flagellar motor is at the base of the flagellum and drives its rotation at around 300 Hz. The long helical propeller is called the flagellar filament, and it grows up to around 15 μm by polymerization of a single kind of protein, flagellin. The filament is not simply a rigid helical propeller but switches its helical form from a left-handed to right-handed ones upon quick reversal of the motor rotation, by which a bundle of several filaments formed during a straight run falls apart quickly, and this makes the bacterial cell tumble and change its swimming direction for chemotaxis or thermotaxis.

It is not a simple question to answer how chemically identical molecules can build curve and twisted tubular structures. It was proposed by Asakura [1] that various helical forms of the flagellar filament are produced by two types of protofilaments with distinct repeat distances and lateral packing modes in each of the 11 protofilaments that form the tubular structure. Electron cryomicroscopic structure analysis of two types of straight flagellar filaments, the L- and R-type, each made of either L- or R-type protofilaments, showed that the overall structure of the flagellin subunit does not change much in the two packing modes [2]. X-ray fiber diffraction revealed that the L- and R-type protofilaments have a subunit repeat distance of 52.7 Å and 51.9 Å, respectively [3]. By simple mechanical simulation to build a tube with a mixture of two types of protofilaments, this difference of 0.8 Å and a small change in the lateral packing explained the curvature and twist of various helical forms of the filament observed by dark-field optical microscopy, demonstrating that this subtle difference is physically meaningful [3].

We then carried out X-ray crystallographic structure analysis of monomeric flagellin to find out what structural changes would be responsible.

Crystallization of flagellin, however, was impossible because flagellin has a strong tendency to polymerize into filaments. We therefore cleaved off 52 $NH_2$- and 44 COOH-terminal residues from 494 amino acid residues of *Salmonella* flagellin to suppress the strong polymerization ability. This 41 kDa fragment named F41 formed crystals but they were only about 5 μm thick. It would have been impossible to collect diffraction data from such a thin crystal without a highly brilliant X-ray beam

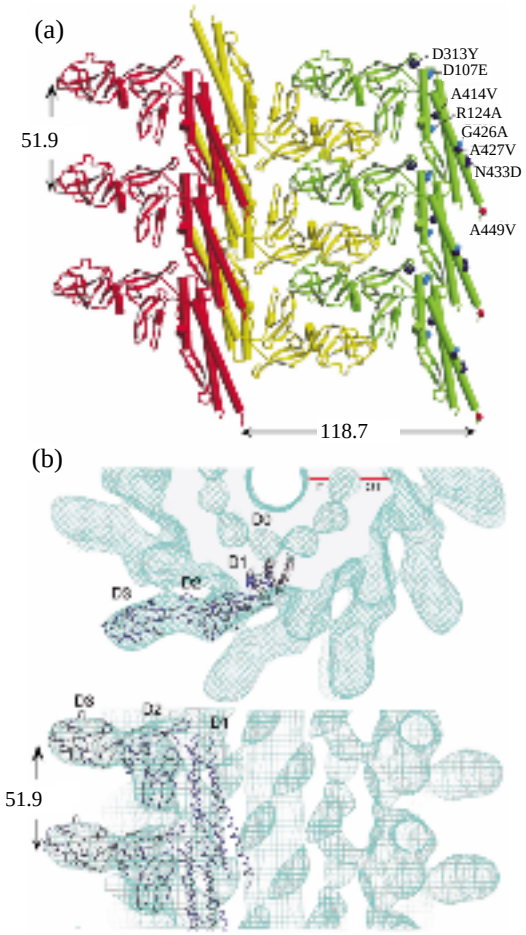


*Fig. 1. Crystal structure of the flagellin fragment F41* ***(a)*** *and docking of the protofilament model into an EM density map* ***(b)****.*

from SPring-8 beamlines. Annealing of frozen crystals was also essential for collecting high-resolution data. We collected a set of multiple anomalous diffraction data to 2.0 Å resolution at one of the RIKEN beamline **BL45XU**, which was designed based on the trichromatic concept [4].

The structure of F41 had three domains. The one with an elongated shape and made of three α-helices and a β-hairpin formed an axial array with very intimate interactions in the crystal packing. The repeat distance was 51.9 Å, exactly the same value as that of the R-type protofilament (Fig. 1a). The atomic model of this array of F41 fitted very well when docked into a density map of the R-type filament deduced by electron cryomicroscopy (Fig. 1b), indicating that this is the atomic model of the protofilament [4].

Because the flagellar protofilament is a kind of mechanical switch that switches between the two states with distinct repeat distances, we carried out a computational simulation of extending the protofilament model to identify the switch region within the molecular structure. We treated three axially aligned subunits as a protofilament model, and while fixing Cα atoms of the top subunit, we translated the bottom subunit by 0.1 Å in the direction extending the protofilament model and did energy minimization of the whole model with Cα atoms of the top and bottom subunits all fixed. We repeated this procedure up to an extension of 6 Å. Up to an extension of 4.5 Å, the middle subunit showed only gradual elongation in every portion of domain D1, but from 4.5 to 4.7 Å, the β-hairpin in domain D1 showed an abrupt jump in its conformation (Fig. 2). We thus identified that this β-hairpin structure, which pairs with three long α-helices to form domain D1, is the mechanical switch in flagellin to produce the two distinct protofilament states with slightly different repeat distances [4].

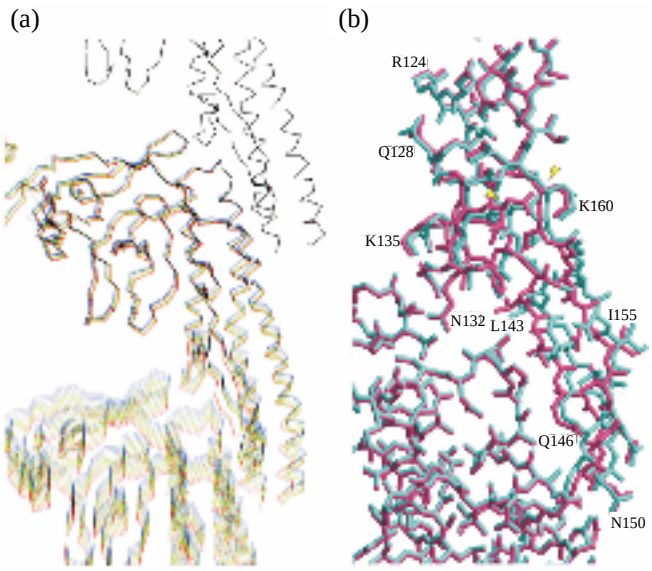


*Fig. 2. Simulated extension of the protofilament model.* ***(a)*** *Superposition of different stages at every 0.5 Å extension.* ***(b)*** *Magnified image of the β-hairpin portion of domain D1. Colors represent 4.5 Å (cyan) and 4.7 Å (pink) extension.*

Fadel A. Samatey[a], Katsumi Imada[a,b] and Keiichi Namba[a,b]

(a) Protonic NanoMachine Project, ERATO, JST
(b) Osaka University

E-mail: keiichi@fbs.osaka-u.ac.jp

**References**

[1] S. Asakura, Adv. Biophs. **1** (1970) 99.
[2] Y. Mimori-Kiyosue *et al.*, Proc. Nat. Acad. Sci. USA **93** (1996) 15108.
[3] I. Yamashita *et al.*, Nature Struct. Biol. **5** (1998) 125.
[4] F.A. Samatey, K. Imada, S. Nagashima, F. Vonderviszt, T. Kumasaka, M. Yamamoto and K. Namba, Nature **410** (2001) 331.

# Dynamical Observations of Individual Protein Molecules with X-rays

In order to understand how protein molecules operate in bio-systems such as membrane or cells, some X-ray techniques were developed to give the time-and-space averaged structural information about protein molecules. Recently, the dynamic behavior of single bio-molecules were directly visualized in real time under an optical microscope [1,2]. These single-molecule techniques have been providing positional information at an accuracy of about $\lambda/100$, far below the optical diffraction limit ($\sim\lambda/2$). In this work, we demonstrated the direct observations of the rotating motion of an individual single nanocrystal, which is bound to individual bio-molecules, using time-resolved Laue diffraction. We achieved time-resolved X-ray ($\lambda_{X\text{-}ray}$ ~0.1 nm) observations of picometer-scale ($\lambda_{X\text{-}ray}/100$) slow Brownian motion in individual bio-molecules in various aqueous solutions.

Most X-ray experiments are based on the average of several observations of many molecules and the behavior of each molecule cannot be determined. In this report, we proposed a new X-ray methodology for direct observations of the behavior of single molecular units in real time and in real space. The new system (Fig. 1), which we call Diffracted X-ray Tracking (DXT), monitors the Brownian motions of a single molecular unit by observations of X-ray diffracted spots from a nanocrystal, tightly bound to an individual single molecular unit in bio-systems [3,4]. DXT does not determine any translational movements, but only orientational movement. Here, in order to detect intra-molecular Brownian motions in individual single biological molecules on a picometer scale, we utilized individual diffraction spots from a nanocrystal, which was tightly bound to the DNA molecules under observation (Fig. 2).

We used the white X-ray mode (Laue mode) of the RIKEN Structural Biology II beamline **BL44B2** to record Laue diffraction spots from Au nanocrystals. The photon flux at the sample position was estimated to be about $10^{15}$ photon/sec/mm$^2$ in the energy range of 7 - 30 kV. The X-ray beam's focal size was 0.2 mm (horizontal) $\times$ 0.2 mm (vertical). A diffraction spot was monitored with an X-ray image intensifier (Hamamatsu Photonics, V5445P) and a CCD camera (Hamamatsu Photonics, C4880-82) with 656 $\times$ 494 pixels. The average exposure time

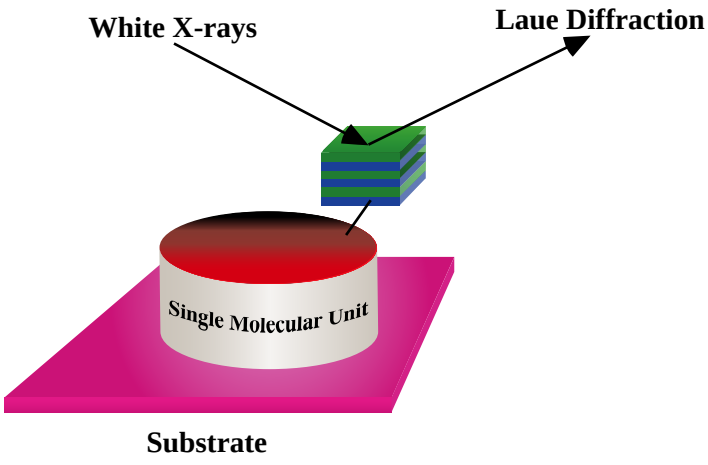


*Fig. 1. Schematic drawing of the detection system for single molecular tracking with X-rays (not to scale). Diffracted X-ray Tracking (DXT) monitors the motion of a single nanocrystal with the guidance of a diffraction spot from the individual nanocrystal itself, which is labeled with the individual single molecular unit.*

was 1 msec.

Figure 3 shows movements of diffraction angles θ from a single nanocrystal coupled to a single DNA molecule (18-mer) at 4 ℃. The observed spots randomly move along the direction of θ. From analyzed data, the observed displacement of θ is assigned as directed Brownian motion [5].

In the future, the biggest challenge will be to observe individual and rare biological processes in living cells. DXT can be used to monitor not translational motions but orientational ones on pico-meter scales. DXT can be expected to observe the structural changes accompanying the activation of ion channels in living cells. Such changes are known as tilting or small orientational motions of the helix in channel pores. DXT can also be expected to monitor the dynamics of ion channels through ionic flux measurements by the patch-clamp technique.

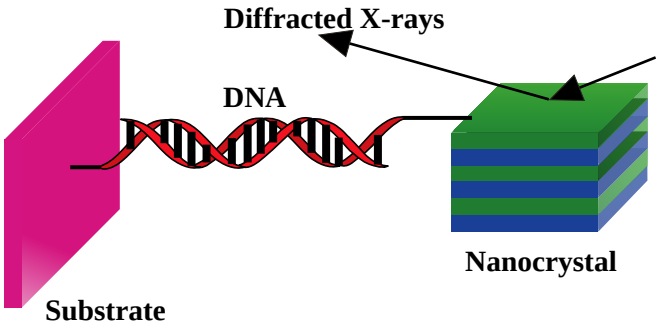


*Fig. 2. Schematic drawing of the X-ray single-molecular detection system for individual DNA molecules in aqueous solutions (not to scale). The diameter of the nanocrystal and the DNA molecule are about 15 nm and 2.5 - 3 nm, respectively.*

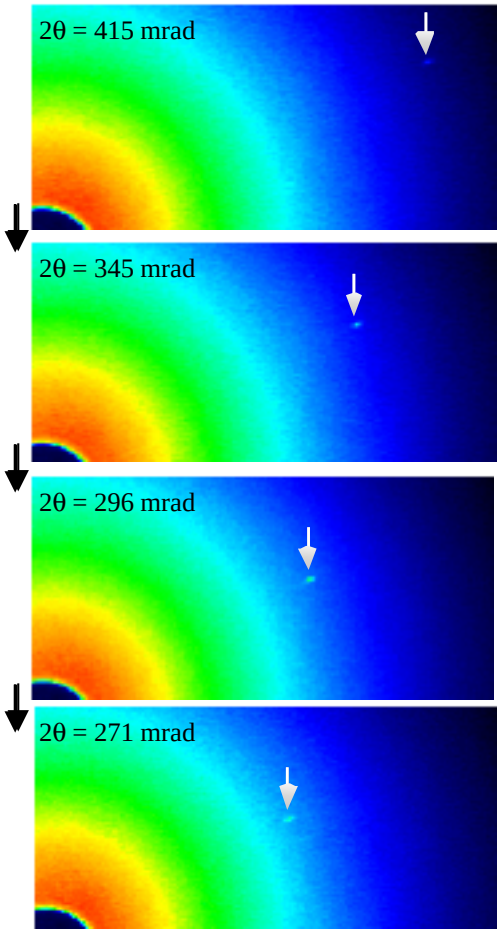


*Fig. 3. Examples of the diffracted spots from the single nanocrystal in aqueous solutions appeared as brightly shining dots (white-blue). Frames are spaced at 180-ms intervals. The exposure time was 1 s.*

Yuji C. Sasaki[a, b, c]

(a) SPring-8 / JASRI
(b) Osaka University
(c) Japan Science and Technology Corpotation, CREST

E-mail: ycsasaki@spring8.or.jp

**References**

[1] Th. Basche *et al.*, Single Molecule Optical Detection, Imaging, and Spectroscopy (Wiley-VCH, Munich, 1997).
[2] S. Weiss, Science **283** (1999) 1676.
[3] Y. C. Sasaki *et al.*, Phys. Rev. **E 62** (2000) 3843.
[4] Y. C. Sasaki, Y. Okumura, S. Adachi, Y. Suzuki, N. Yagi, Nucl. Instrum. Meth. **A 467-468** (2001) 1049.
[5] Y. C. Sasaki, Y. Okumura, S. Adachi, N. Yagi, Phys. Rev. Lett. **87** (2001) 248102.

# Motion of Activated Myosin Heads as Detected by Fiber X-ray Diffraction

Muscle contraction is caused by the interaction between the two contractile proteins, actin and myosin. Each of the proteins polymerizes to form filaments, and the contractile force is generated as the myosin head, which sticks out of the myosin filament backbone, exerts a pull on the actin filament (Fig. 1a, 1b). The myosin head contains all the components needed to exert force, including the actin-binding site and the ATP-binding pocket, while the rest of the myosin molecule (myosin tails) forms the backbone of the filament (Fig. 1c). The recent crystallographic results [1] showed that the head is further divided into two parts, *i.e.*, the motor and the lever arm domains (Fig. 1d). The conventional theory for force generation mechanism assumes that the motor domain grabs the actin filament firmly (by making stereospecific interactions at the actin-myosin interface) and the lever arm makes a swing on it (Fig. 1e).

In the conventional theory, therefore, the stereospecific interactions play a crucial role in force generation. The question is how such interactions can be detected. A potent method to achieve this is to record X-ray diffraction patterns from a muscle or muscle fibers under various conditions. A regular array of molecules, such as that in a protein crystal, gives rise to a number of bright spots or lines at specific positions in the diffraction pattern. They are called reflections, and their positions and intensities carry information about the structure of the molecular array. In the case of muscle, the molecules of myosin and actin are arranged periodically in helices. This arrangement gives rise to a number of line-shaped reflections (layer lines) across the long axis of the muscle fibers, as in the patterns recorded at beamline **BL45XU** [2] (Fig. 2). Figure 2a shows the diffraction pattern recorded from stretched muscle fibers, in which the myosin and actin filaments do not overlap and therefore the myosin heads cannot interact with actin. A few, weak layer line reflections are seen, and they are based on actin repeat. The

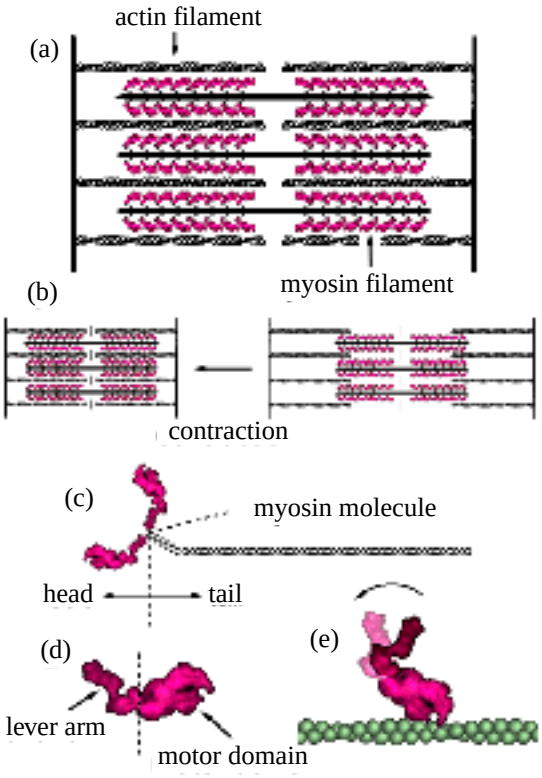


*Fig. 1. Structure of the contractile machinery of muscle.*
*(**a**) Structure of a sarcomere consisting of two sets of filaments (myosin and actin).*
*(**b**) Mechanism of contraction, which is caused by the sliding of the filaments relative to each other.*
*(**c**) Structure of a single myosin molecule.*
*(**d**) Structure of a myosin head, consisting of motor and lever arm domains.*
*(**e**) Conventional explanation of the mechanism of contractile force production, caused by the swing of the lever arm domain on the motor domain bound to an actin filament in a stereospecific manner.*

pattern in Fig. 2b was taken after myosin heads (prepared by severing the whole molecule with protease) were diffused into the stretched muscle fibers as in Fig. 2a in the absence of ATP. This is the condition equivalent to rigor mortem, in which mitochondria no longer produce ATP, and strong stereospecific interactions are known to be formed between actin and myosin (this makes the muscle very stiff). In the diffraction pattern, the actin-based layer lines, notably the one at 5.9 nm (arrow), are strongly enhanced. The enhancement is caused by the myosin heads, which are bound to the actin filament and now follow the actin repeat. It is also noticed that the peak of the reflection at 5.9 nm has shifted inwards.

Addition of ATP to the muscle fibers creates a condition equivalent to contraction. The heads had been cross-linked to actin so that they would not dissociate. In such muscle fibers the heads hydrolyze ATP at a very high rate, because the two contractile proteins are held in close proximity. It is expected from the conventional theory that in such highly activated muscle fibers, stereospecific interactions are formed substantially and therefore the diffraction pattern would be more or less like that in Fig. 2b. However, the recorded pattern (Fig. 2c) was very similar to that in Fig. 2a, *i.e.*, the pattern from naked actin filaments [3]. The results are explained only if the myosin head is swinging as a whole in this highly activated actin-myosin complex, and little stereospecific interactions are formed. It is probable that the motor domain of myosin plays a more dynamic role than simply providing a scaffold for the lever arm swing.

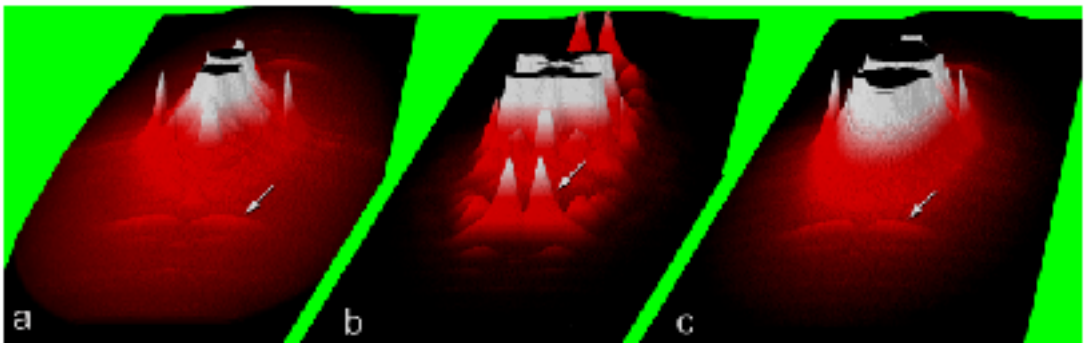


*Fig. 2. Bird's-eye views of the diffraction patterns recorded from an array of overstretched single rabbit skeletal muscle fibers. (**a**) Pattern recorded in the absence of exogenously introduced myosin head. Layer lines typical of bare actin filaments are observed. (**b**) Pattern recorded after myosin heads had been exogenously introduced in the absence of ATP. The actin-based layer lines are strongly enhanced because of the stereospecific labeling of the actin filaments by the myosin heads. (**c**) Pattern recorded in the presence of ATP after exogenously introduced myosin heads had been cross-linked. The actin-based layer lines are as weak as those of bare actin filaments and there is little sign of stereospecific binding. The arrow indicates the layer line indexed to the 5.9 nm repeat of actin monomers.*

Hiroyuki Iwamoto[a], Kazuhiro Oiwa[b] and Tetsuro Fujisawa[c]

(a) SPring-8 / JASRI
(b) Communications Research Lab.
(c) SPring-8 / RIKEN

E-mail: iwamoto@spring8.or.jp

**References**

[1] I. Rayment *et al.*, Science **261** (1993) 50.
[2] T. Fujisawa *et al.*, J. Appl. Cryst. **33** (2000) 797.
[3] H. Iwamoto, K. Oiwa, T. Suzuki and T. Fujisawa, J. Mol. Biol. **305** (2001) 863.

# Global Heterogeneity of Glomerular Volume-distribution Evaluated by Three-dimensional Analysis using Synchrotron Radiation X-ray MicroCT

An estimated glomerular volume within the restricted histological sections has been a conventional index for renal dysfunction. Subtle aspects of glomerular remodeling are, however, difficulties with the conventional approach that compresses three dimensions into two. Therefore, we aimed at visualizing thee dimensional (3-D) glomerular micro-structures using an X-ray microCT (μCT) at beamline **BL20B2**, to accurately measure glomerular volumes throughout a cortex and quantitatively evaluate global heterogeneity of the volume-distribution in a rat with spontaneous diabetes mellitus (DM).

Using the Otsuka Long Evans Tokushima Fatty (OLETF) rats as rats of early stage DM (28 weeks) and control rats (Long Evans Tokushima Fatty; LETO, of the same age, the vessels of the left kidney was filled up with contrast media ($BaSO_4$ + India ink + 8% gelatin). A sampled renal column ($\phi$ 3 - 4 mm) was observed using two μCT systems; BL20B2 μCT for the highest image quality (3 - 6 μm in resolution) and commercially available μCT (10 μm in resolution) (Fig. 1) for data accumulation. The glomerular volumes more than 400 per sample were computed and normalized to body weight. Heterogeneity in glomerular volume-distribution was evaluated by coefficient variation (CV).

By stereomicroscopic observation, we confirmed complete-filling of the vessels with the contrast media. The glomeruli in OLETF were characterized by irregular stereostructures, whereas those in LETO were characterized by regular glomerular

**(a)** CT-imaging of renal cortex

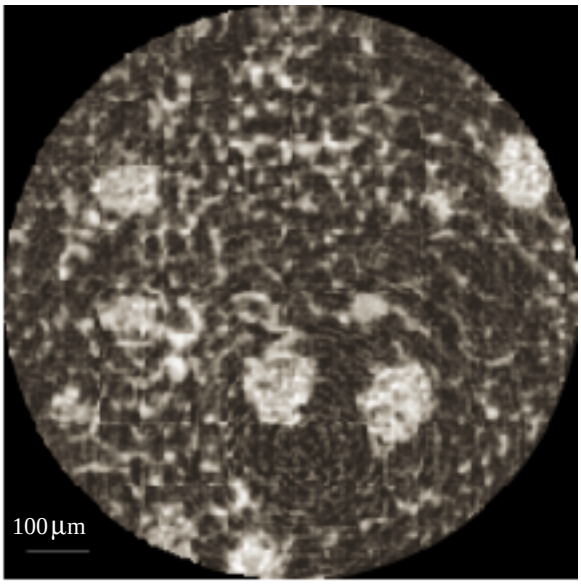


**(b)** 3D-volume rendering image of the glomerulus

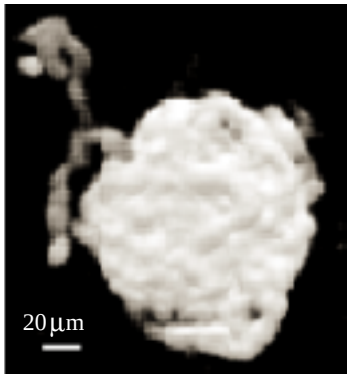


*Fig. 1. Visualization of renal cortex by high resolution (3 μm) microCT.*

structure. The CV of glomerular volume was significantly larger in OLETF than LETO (2.0 *vs.* 0.15, $p < 0.01$). In addition, absolute glomerular volume was larger in OLETF than LETO ($2.3 \pm 0.2 \times 10^6$ *vs.* $1.6 \pm 0.2 \times 10^6$ μm$^3$, $p < 0.01$). The normalized glomerular volume was, however, comparable (NS), indicating glomerular enlargement in early DM may associate with increase in body mass. Both μCT provided similar results.

Highly heterogeneous glomerular volume-distribution in DM rat was quantitatively demonstrated using our developed 3-D glomerular micro-structural visualizing method. This technique provides a new aspect for the evaluation of global heterogeneity in glomerular remodeling under the chronic renal dysfunction, which may provide more sensitive insight into early complications of diabetic nephropathy.

On the glomerular volume evaluation, the SPring-8 μCT and the conventional μCT showed the similar results. However, the SPring-8 μCT system with the high resolution is required for evaluation of the more detailed microvasculature.

Yasuo Ogasawara

Kawasaki Medical School

E-mail: ogasawara@me.kawasaki-m.ac.jp

**References**

[1] Yasuo Ogasawara, Eiji Toyota, Tatsuya Kajita, Fumiyuki Shigeto, Takeshi Matsumoto, Takahisa Asano and Fumihiko Kajiya, Jpn. J. Med. Electro. & Biol. Eng. **39** (suppl.) (2001) 490.

[2] Yasuo Ogasawara, Eiji Toyota, Fumiyuki Shigeto, Tatsuya Kajita, Takeshi Matsumoto, Hiroyuki Tachibana, Hiroshi Nakamoto, Tokunori Yamamoto and Katsukuni Fujimoto, Jpn. Circulation Journal (2002) - in press.

# Materials Science

In our synchrotron facility, many research programs in natural science and technology are being carried out by using diffraction, scattering and spectroscopic techniques. In materials science, the disciplines range from the fundamental research in physics to the application to industry. Many users in various fields of materials science have produced a number of high-quality scientific outputs in the X-ray beamlines of the SPring-8. Examples of such experiments are compiled in this volume.

The above experiments can be now performed at sixteen public and the other beamlines, having full of activity in X-ray single-crystal or powder diffraction on time-dependent crystallography and electron-density distribution (BL02B1, BL02B2), X-ray diffraction at high temperature and pressure or low temperature (BL04B1, BL10XU), local atomic structure of amorphous solid, liquids and melts (BL04B2), Compton and inelastic scattering (BL08W, BL35XU), nuclear resonant scattering (BL09XU), Mössbauer spectroscopy (BL11XU), surface and interface structure (BL13XU, BL14B1), X-ray imaging (BL20B2), white X-ray topography (BL28B2), magnetic scattering (BL39XU) and R&D study (BL46XU, BL47XU). Each of the beamlines provides the requisite number of photons, sufficient energy and spatial resolutions and polarization for the experiments being performed.

*Satoshi Sasaki*

# Bonding Nature in a Novel Superconductor, $MgB_2$

In the beginning of the 21st century, a novel superconductor, $MgB_2$, was discovered by Akimitsu [1]. Because of its comparatively high Tc, 39 K, an anomalous number of experimental and theoretical studies were performed in order to gain an understanding of the mechanism of superconductivity. Since 1954 [2], it has been known that the crystal structure of this material is hexagonal ($AlB_2$ type, space group *P6/mmm*). The characteristic boron honeycomb sheets are sandwiched between the Mg triangular sheets like an intercalated graphite as shown in Fig. 1. The band structure calculations [3] predict the existence of a charge donation of two electrons from the ionized Mg to the boron conduction band while a strong B-B covalent bonding is retained. The superconductivity in $MgB_2$, which appears essentially to come about due to the metallic nature of the Boron 2-D sheets, has been interpreted as a phonon-mediated BCS-type mechanism. Such a two dimensional structure is a common feature in oxide superconductors as well as in intercalated graphite. The doping on the Mg site or Boron 2-D sheets was carried out to reveal the effect of the electron concentration on the superconducting temperature. Several reports of the loss of superconductivity have been presented for $Mg_{1-x}Al_xB_2$, $MgB_{1-x}C_x$, $Mg_{1-x}Li_xB_2$ and $Mg_{1-x}Mn_xB_2$.

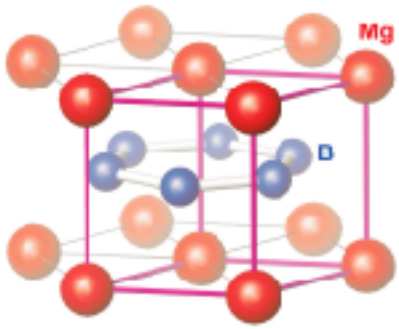


*Fig. 1. Crystal structure of $MgB_2$.*

The pressure evolution of the superconducting transition temperature was also reported and discussed for its relationship with the B-B and Mg-B bonding distances. However, the structural information used in the discussions was limited to the atomic level, *i.e.* lattice constants, bonding distance, etc. An experimental charge density would give a better understanding of how superconductivity links to the electronic and crystal structure of $MgB_2$.

In 2001, we reported on the precise charge densities of $MgB_2$ at R.T. and 15 K using synchrotron radiation powder data and presented experimental evidence for strong B-B covalent bonding, full ionization of Mg atoms at both temperatures as well as charge concentration on boron 2-D sheet at 15 K, which most probably relates to the superconducting mechanism [4].

The $MgB_2$ sample used in this work was prepared by Prof. J. Akimitsu. A pressed pellet of stoichiometric amounts of Mg and amorphous B was heated for 10 hours at 700 ℃ under an argon pressure of 196 MPa. The sample was found to be superconducting with $T_c$ = 39 K. The granularity of the powder was reduced to a diameter even less than 3 microns by the precipitation method in order to obtain homogeneous intensity distribution in the Debye-Scherrer powder ring. The obtained powder sample was sealed in a silica glass capillary (0.3 mm int. diam.). The synchrotron radiation X-ray powder experiment with imaging plates (IP) as detectors was carried out by the Large Debye-Scherrer Camera at beamline **BL02B2** [5]. The He gas circulation type cryostat was used for the measurement at low temperature (Fig. 2). The X-ray powder patterns were measured at room temperature (R.T.) and 15 K(<<Tc). Both data were obtained under the same experimental conditions except for the temperature. The exposure time was 1 hour. The wavelength of incident X-rays was 0.6 Å. The X-ray powder pattern of $MgB_2$ was obtained with a 0.02° step from 9.0° to 65.0° in 2θ, which corresponds to 0.57 Å resolution in *d*-spacing.

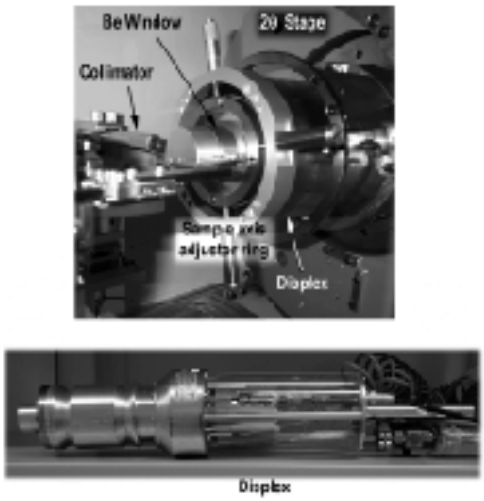


*Fig. 2. The photograph of the displex installed in the Large Debye-Scherrer Camera.*

The charge density distributions at both temperatures were visualized by the MEM/Rietveld method, which is a combination of the MEM and the Rietveld refinement [6]. This method has been successfully applied to the charge density studies of fullerene compounds, intermetallic compounds, α-boron, manganite, etc. For instance, the MEM/Rietveld method using synchrotron radiation powder data has revealed Mn $3d_{x^2-y^2}$ orbital order as a Mn-O bonding electron distribution associated with Mn(3*d*)-O(2*pσ*) hybridization at antiferromagnetic state in manganite, $NdSr_2Mn_2O_7$ [7]. In the present powder data, several weak impurity peaks were found and identified as MgO. The impurity MgO phase was also taken into account in the Rietveld pre-analysis. The space group was assigned to *P6/mmm* for both data at R.T. and 15 K. This implies that there is no structural phase transition from R.T. to 15 K. The results of the Rietveld refinement are shown for R.T. and 15 K in Fig. 3(a) and 3(b), respectively. The refined lattice parameters are listed in Table I. The weighted profile reliability factors of the Rietveld refinement as a pre-analysis for the MEM, $R_{WP}$, were 4.7% and 2.6% for R.T. and 15 K, respectively. And the reliability factors based on the integrated intensities, $R_I$, were 3.1% and 3.4% for R.T. and 15 K, respectively. In the analysis, the structure factors of the 55 reflections were derived from the observed integrated intensities. They were then used for further MEM analysis. Following the Rietveld pre-analysis, the MEM analysis was carried out by the computer program, ENIGMA [8], using 64×64×72 pixels. The reliable factors of the final MEM charge density were 1.7% and 1.5% for R.T. and 15 K, respectively.

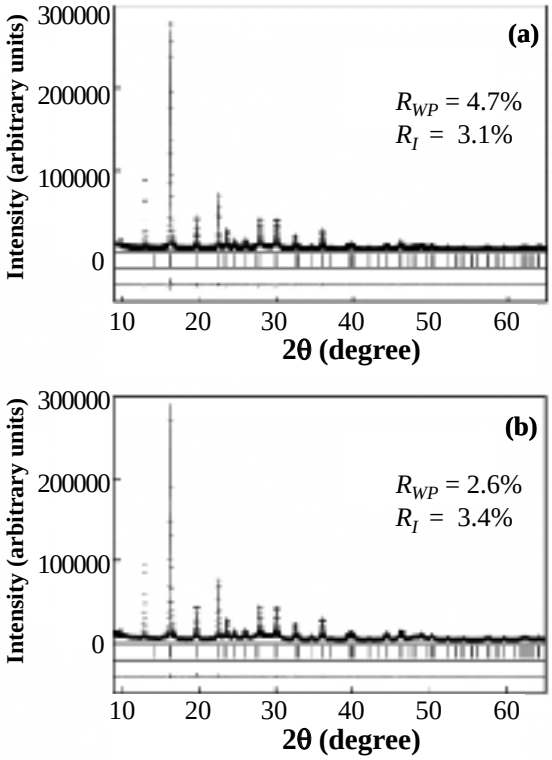


*Fig. 3. Fitting results of Rietveld analysis of $MgB_2$ at **(a)** R.T. and **(b)** 15 K.*

**Table I.** The lattice parameters and B-B, Mg-B atomic distances determined by the Rietveld analysis for $MgB_2$ at R.T. and 15 K.

| | R.T. | 15 K |
|---|---|---|
| Latice Parameter (Å) | a = 3.08831(3)<br>c = 3.52415(8) | a = 3.08365(2)<br>c = 3.51504(4) |
| B-B distance (Å) | 1.78304(8) | 1.78035(1) |
| Mg-B distance (Å) | 2.50682(1) | 2.50170(1) |

A three-dimensional representation of the final MEM charge density at R.T. is shown in Fig. 4 as an equi-charge density surface. The equi-density level is 0.75 e/Å$^3$. The obtained MEM charge density clearly exhibits a strong covalent bonding network of boron 2-D sheet forming the six-membered rings, which are colored in blue. On the other hand, there is no localized electron density between Mg and boron atoms. In the interatomic region, electrons are distributed rather evenly similar to metal bonding. These characteristic density features are preserved in the charge density obtained at R.T. and consistent with the calculated band structures indicating the two band model [3]. Based on this model, several theoretical mechanisms of superconductivity have been proposed [9].

In Fig. 5, the MEM charge densities of the (110) sections containing Mg and boron atoms are shown for R.T. and 15 K with a structure model. The contour lines are drawn only for the lower density region. It is confirmed that there is no significant overlapping of the charge density around the Mg atomic sites. This is a high contrast to that of the boron-boron network. The MEM charge densities clearly reveal the boron-boron covalent bonding features. Although the change in the boron-boron interatomic distance is extremely small between R.T. and 15K as shown in Table I, the charge density values at the bond midpoints show the distinct different values, which are 0.9 and 1.0 eÅ$^{-3}$ at R.T. and 15 K, respectively.

These values are in the range between those of Si (0.7eÅ$^{-3}$) [6] and Diamond (1.4 eÅ$^{-3}$) [6] and very close to the value of hexagonal-BN (1.0 eÅ$^{-3}$) [10].

The valence of the atom was examined by accumulating the number of electrons around a certain atom in the MEM density. So far, the valence of metal atoms encapsulated in metallofullerene has been determined experimentally from the MEM charge densities [6]. The number of electrons around an Mg atom was estimated as about 10.0(1)$e$ and 10.0(1)$e$, respectively. These values are very close to the number of electrons of $Mg^{2+}$ ion. This means that the Mg atoms are fully ionized in $MgB_2$ crystal at both R.T. and 15 K. On the other hand, the number of electrons belonging to the boron 2-D sheets show significant difference, they are 9.9(1)$e$ and 10.9(1)$e$ at R.T. and 15 K, respectively. This can be interpreted as the valence of the whole boron 2-D sheet changing from neutral to monovalent,

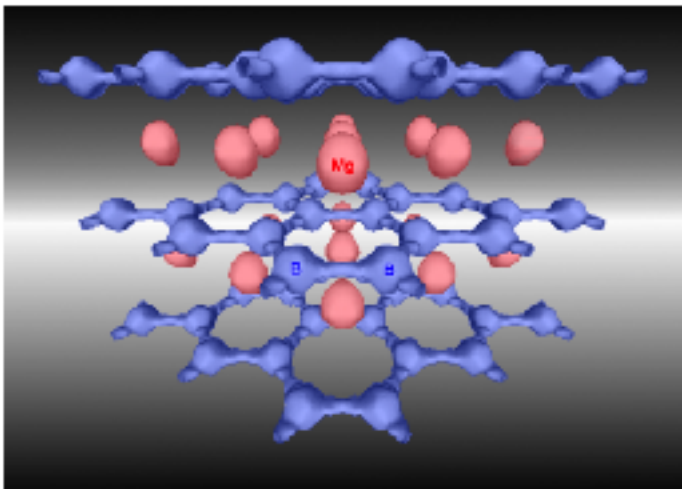


*Fig. 4. The equi-contour (0.75 e/Å$^3$) surface of MEM charge density of $MgB_2$ at R.T.*

*i.e.*, $(B\text{-}B)^{-}$ at 15 K, which gives evidence of the increase of charge at the B-B bond midpoint at 15 K. Though the full charge transfer from Mg to boron 2-D sheets was expected to occur and form an isoelectronic sheet with graphite, no simple direct full charge transfer from $Mg^{2+}$ to boron 2-D sheet was observed. The present results support the following scenario, that is, that the valence electrons are delocalized in the inter-atomic region at R.T., and half of them localized on the boron 2-D sheets at low temperature. This scenario implies the presence of electron transfer from the π bonds consisting of $p_z$ orbitals to in-plain σ bonds consisting of $p_{xy}$ orbitals in the two band model of $MgB_2$ at 15 K. Consequently, a subtle but important charge concentration on boron 2-D sheet at 15 K was found, which most probably relates to the superconductivity of this compound.

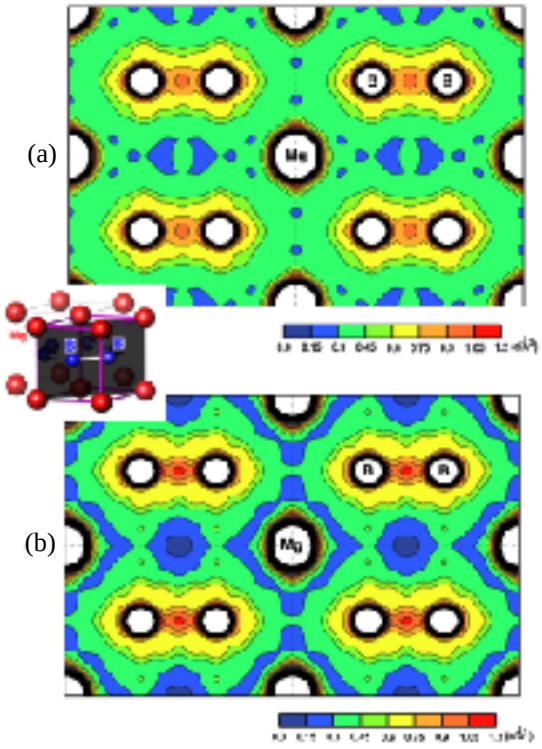


*Fig. 5. The (110) sections of the MEM Charge Density of $MgB_2$ at **(a)** R.T. and **(b)** 15 K with the schematic representation of the crystal structure. The contour lines are drawn from 0.0 to 3.9 at 0.15(e/Å$^3$) intervals for four unit cells.*

Eiji Nishibori, Masaki Takata and Makoto Sakata

Nagoya University

E-mail: a41024a@nucc.cc.nagoya-u.ac.jp

**References**

[1] J. Nagamatsu *et al.*, Nature **410** (2001) 63.
[2] M.E. Jones and R.E. Marsh, J. Am. Chem. Soc. **76** (1954) 1434.
[3] J. Kortus *et al.*, Phys. Rev. Lett. **86** (2001) 4656; preprint cond-mat/0101446.
[4] E. Nishibori *et al.*, J. Phys. Soc. Jpn. **70** (2001) 2252.
[5] E.Nishibori *et al.*, Nucl. Instrum. Meth. in Phys. Res. **A 467-468** (2001) 1045.
[6] M. Takata, B. Umeda, E. Nishibori, M. Sakata, M. Ohno and H. Shinohara, Nature **377** (1995) 46; M. Takata, E. Nishibori and M. Sakata, Z. Kristallogr. **216** (2001) 71.
[7] M. Takata *et al.*, J. Phys. Soc. Jpn. **68** (1999) 2190.
[8] H. Tanaka, *et al.*, J. Appl. Cryst. (2002) - in press.
[9] M. Imada, J. Phys. Soc. Jpn. **70** (2001) 1218; K. Yamaji, J. Phys. Soc. Jpn. **70** (2001) 1476.
[10] S. Yamamura *et al.*, J. Phys. Chem. Solids **58** (1997) 177.

# Novel Structures of $C_{60}$ and $C_{70}$ -Encapsulating Carbon Nanotubes

One of the interesting features of the single-wall carbon nanotube (SWNT) is its nanometer size inner hollow cavity [1,2]. This encourages researchers to study its use in industrial applications such as gas storage cylinders and one-dimensional nanometer molds. Recently, it was shown that bulk quantities of fullerene molecules can be encapsulated in SWNTs [3, 4]. This class of material is called “peapod”. The reason for this can be clearly seen in Fig. 1.

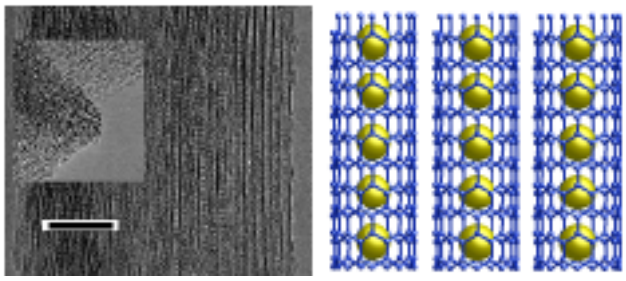

*Fig. 1. The TEM image of $C_{70}$-peapods (left) and a schematic view of peapods (right). The scale is 10 nm. The inset shows a cross section of a bundle.*

A theoretical calculation for $C_{60}$-peapods predicts new features in the band structure around the Fermi level [5], suggesting a possibility of high-temperature superconductivity without any doping. However, it must compete with instabilities such as the charge density wave (CDW) and the spin density wave (SDW), because the fullerene molecules form an one-dimensional crystal inside the tube. The $C_{60}$ or $C_{70}$ molecular orientation is another important freedom. In the case of solid $C_{60}$, it is known that the $C_{60}$ exhibits quasi-free rotation at each lattice site; thus the solid $C_{60}$ is a plastic crystal at room temperature ($T$). When $T$ is lowered, an orientational ordering phase transition is shown at 261 K. On the other hand, the molecular rotation in solid $C_{70}$ is very anisotropic, and the phase transition related to the molecular rotation occurs successively at 280 K and 340 K. The difference between the two molecules in the phase transition is ascribed to the molecular shape: the $C_{60}$ is approximated to a sphere with a mean diameter of 0.71 nm while the $C_{70}$ can be likened to a rugby ball with a short axis of 0.712 nm and a long axis of 0.796 nm.

In the present studies [6], we performed powder X-ray diffraction (XRD) measurements of the $C_{60}$- and $C_{70}$-peapods in a temperature range between 300 K and 1000 K to clarify the structural aspects. The XRD experiments were performed at **BL02B2** of SPring-8 and BL1B of PF. Figure 2 shows examples of the observed XRD patterns taken at room temperature (RT). Although the peaks are assigned to a two-dimensional triangular lattice in the bundles of SWNTs, each Bragg peak is significantly broadened due to the small coherent length, ~20 nm. For this reason, the XRD peak profiles are strongly modulated by the form factors of the tubes and fullerene molecules. We notice a large depression of 1 0 peak intensity around Q~6 (1/nm) on the encapsulation. This is a common feature associated with gas adsorption inside SWNTs [7].

The other important feature is the appearance of new peaks indicated by arrows in Fig. 2 in the encapsulation. These peaks are assigned to the one-dimensional crystals of fullerene molecules inside the tubes. The $C_{60}$ intermolecular distance is estimated to be 0.97 nm. In the case of $C_{70}$, interestingly, there are two different intermolecular distances, 1.0 nm and 1.1 nm, which correspond to two molecular configurations of standing and lying alignments inside the tubes, respectively (Fig. 2).

Figure 3 shows the thermal expansion of intermolecular distances. Although the $C_{60}$-peapods showed complicated behavior depending on the sample treatment, careful measurements strongly suggested that the intrinsic thermal expansion is substantially smaller than those for the

solid $C_{60}$ and for the $C_{70}$-peapods. Along with the rather short $C_{60}$-intermolecular distance of 0.97 nm, the inside of the tubes is found to be some novel environment for the $C_{60}$ molecules. On the other hand, the $C_{70}$-peapods with the standing alignment show a large thermal expansion coefficient of the intermolecular distance, indicating that thermally activated $C_{70}$-stumbling occurs inside the tubes above 300 K. The absence of a clear phase transition in solid $C_{70}$ is probably due to the one-dimensionality of the $C_{70}$-crystal.

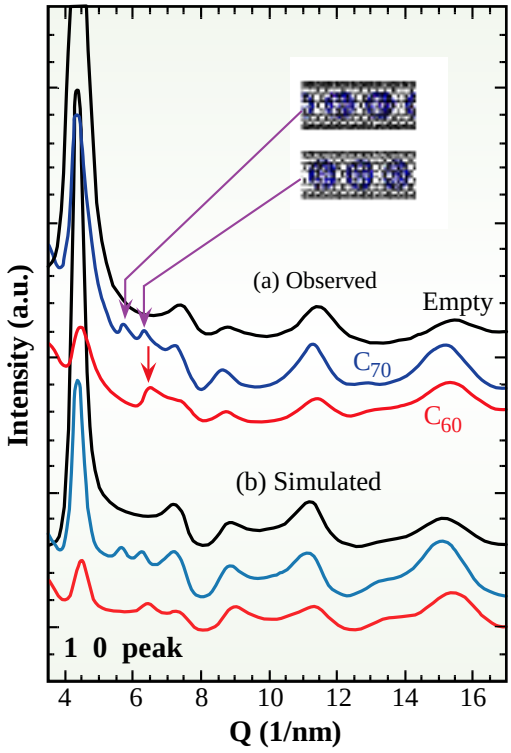


*Fig. 2. The observed and simulated XRD patterns for empty SWNTs, $C_{60}$- and $C_{70}$-peapods.*

Yutaka Maniwa[a], Hiromichi Kataura[a] and Akihiko Fujiwara[b]

(a) Tokyo Metropolitan University
(b) Japan Advanced Institute of Science and Technology

E-mail: maniwa@phys.metro-u.ac.jp

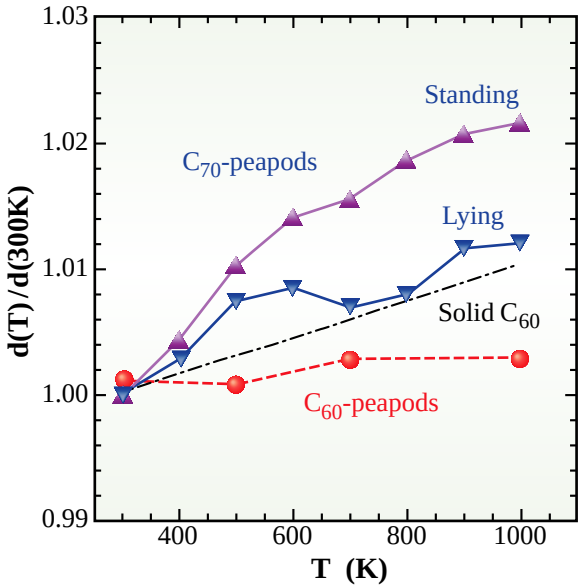


*Fig. 3. Intermolecular distance of $C_{60}$- and $C_{70}$-peapods, normalized at 300 K, as a function of temperature.*

**References**

[1] S. Iijima and T. Ichihashi, Nature (London) **363** (1993) 603.
[2] D.S. Bethune *et al.*, Nature **363** (1993) 605.
[3] B.W. Smith *et al.*, Nature **396** (1998) 323.
[4] H. Kataura *et al.*, Synthetic Metals **121** (2001) 1195.
[5] S. Okada *et al.*, Phys. Rev. Lett. **86** (2001) 3835.
[6] H. Kataura, Y. Maniwa, M. Abe, A. Fujiwara, T. Kodama, K. Kikuchi, H. Imahori, Y. Misaki, S. Suzuki and Y. Achiba, Appl. Phys. **A 74** (2002) 349; Y. Maniwa, H. Kataura, M. Abe, A. Fujiwara, R. Fujiwara, H. Kira, S. Suzuki, Y. Achiba, E. Nishibori, M. Takata, M. Sakata and H. Suematsu, submitted in Science.
[7] Y. Maniwa *et al.*, Jpn. J. Appl. Phys. **38** (1999) L668; A. Fujiwara *et al.*, Chem. Phys. Lett. **336** (2001) 205; Y. Maniwa *et al.*, Phys. Rev. **B 64** (2001) 241402(R).

# Evidence for the Diffusion of Au Atoms into the Te UPD Layer Formed on an Au(111) Substrate

A single atomic layer can be formed by electrochemical processes using underpotential deposition (UPD), which is a surface-limited reaction to a sub-monolayer or monolayer (ML) coverage. In UPD, the electrochemical deposition of foreign metal atoms onto substrate is performed at a positive potential relative to the reversible Nernst potential for bulk deposition (Fig. 1(a)). By alternating the UPD of two different elements we can obtain a binary compound with a layer-by-layer grown structure, that is the electrochemical atomic layer epitaxy (ECALE) (Fig. 1(b)) [1]. Epitaxial growth CdTe layers on an Au single crystal substrate are very important and interesting from the viewpoint of their applications to solar cells.

Since it is considered that the deposition of Cd on an Au substrate easily produces intermetallic compounds, the first step to the formation of CdTe films by ECALE is the UPD of the Te. The structure of Te UPD layer has been studied using a scanning tunneling microscopy (STM) [2,3] and an atomic force microscopy (AFM) [4]. However, structural analysis using STM and AFM is still limited to two-dimensional surface structure. In the present study, the structure which is normal to the surface of the Te UPD layer was revealed by *in situ* specular X-ray reflectivity measurements [5].

The *in situ* specular X-ray reflectivity measurements were carried out using a κ-type multi-axis diffractometer installed at beamline **BL14B1**. The wavelength utilized was λ = 0.110 nm. The Te UPD layer is formed on a pre-treated Au(111) disk electrode in an electrolytic solution contained 0.1 mM $TeO_2$ and 10 mM $H_2SO_4$ as the supporting electrolyte. The potential for the Te UPD is applied to the Au(111) electrode during reflectivity measurements. The theoretical specular reflectivity for the electrode surface is given by the kinematical approximation. In the quantitative determination of the near-surface structure of Te- and Au-layers, the parameters representing the electron density profiles of each layer are optimized so as to adequately describe the observed reflectivity.

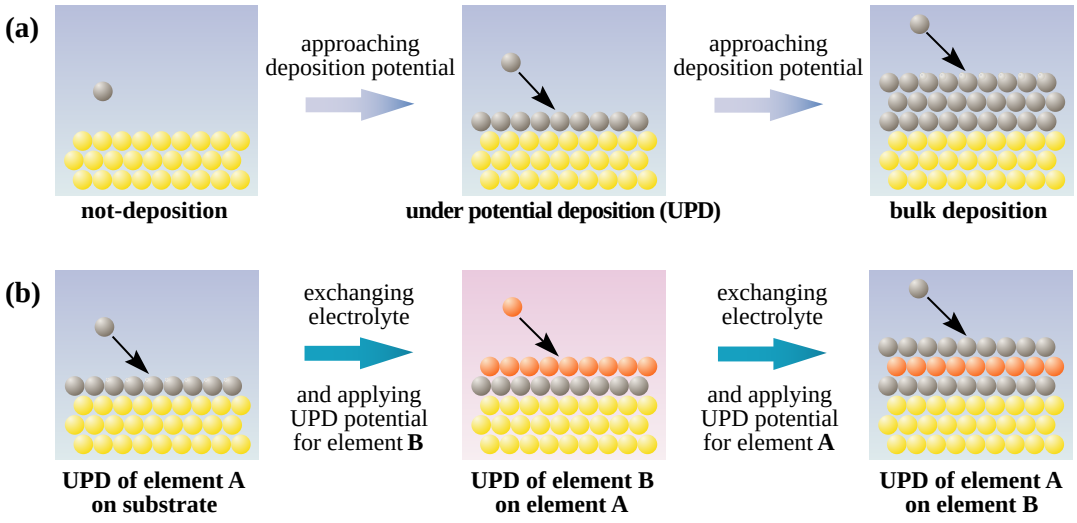


*Fig. 1. Schematic illustrations of* ***(a)*** *underpotential deposition (UPD) and* ***(b)*** *electrochemical atomic layer epitaxy (ECALE).*

The measurements were carried out for the samples which were kept at the UPD potential for 4 to 59 hours. The specular reflectivity for the Te UPD layer formed on an Au(111) substrate is shown as solid circles in Fig. 2. The data collection was performed between 39 to 59 hours after the UPD potential was applied. The dashed red line is calculated profile based on a model that the Te UPD layer is formed just on the Au(111) substrate; we assume the electron density profile in Fig. 3(a), and the Te-coverage of 0.33 ML which is determined from the electrochemical measurement. However, the calculated profile does not fit the observed reflectivity. Therefore, we assume another electron density profile shown in Fig. 3(b); here, the first layer consists of 0.33 ML Te and 0.08 ML Au, while the second layer consists of 0.92 ML Au. The calculated reflectivity (solid blue line in Fig. 2) reproduces the experimental results very well. From the X-ray reflectivity measurements we can conclude that a portion of Au atoms migrates from the top layer of the Au(111) substrate into the top-most Te layer. In consequence, an ideal pure atomic layer formed by the UPD process is not always stable for a long period of time, but atomic interdiffusion may occur within the near-surface layers.

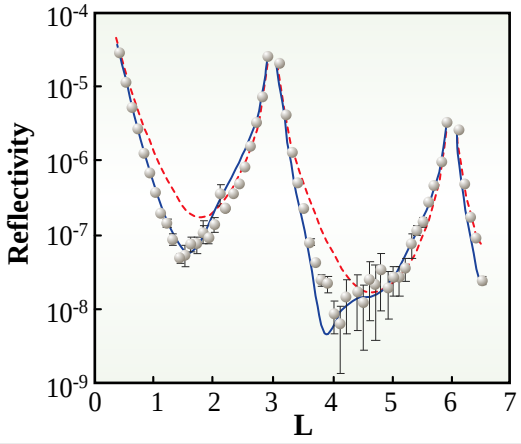


*Fig. 2. Specular X-ray reflectivity from the Te UPD layer on the Au(111) substrate. The data collection was performed between 39 to 59 hours after the UPD potential had been applied. The dashed red line shows the reflectivity expected for a Te layer immediately above the Au(111) substrate. The solid blue line shows the reflectivity expected for the top layer consisting of the UPD Te atoms and Au atoms which diffuse from the Au(111) substrate.*

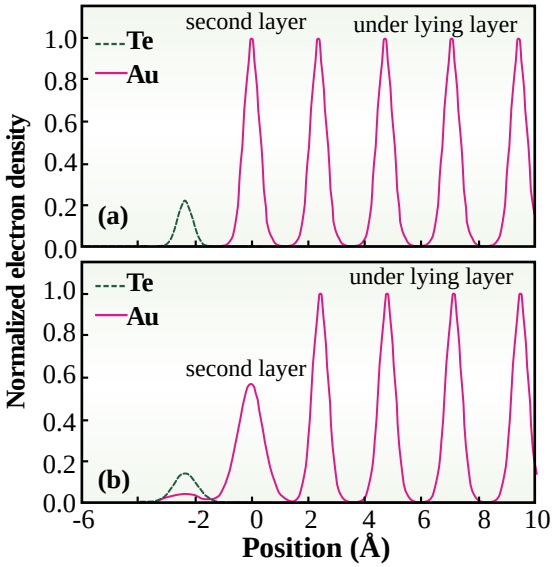


*Fig. 3. Normalized electron density profile normal to the surface for fit to the observed specular X-ray reflectivity. A negative value of position means that a layer is out of the ideally terminated Au surface. **(a)** Model for the top layer consisting of 0.33 ML Te. **(b)** Model for the top layer consisting of 0.33 ML Te and 0.08 ML Au, and the second layer consisting of 0.92 ML Au.*

## References

[1] J.L. Stickney, 'Electrochemical Atomic Layer Epitaxy', in Electroanalytical Chem., A.J. Bard and I. Reubenstein, Editors, Marcel Dekker, New York **21** (1999) 75.

[2] B.E. Hayden and I.S. Nandhakumar, J. Phys. Chem. **101** (1997) 7751.

[3] T.A. Sorenson *et al.*, Surf. Sci. **470** (2001) 197.

[4] N. Ikemiya *et al.*, Surf. Sci. **369** (1996) 199.

[5] H. Kawamura, M. Takahasi, N. Hojo, M. Miyake, K. Murase, K. Tamura, K. Uosaki, Y. Awakura, J. Mizuki and E. Matsubara, J. Electrochem. Soc. **149** (2002) C83.

Hiroyuki Kawamura, Masamitu Takahasi and Jun'ichiro Mizuki

SPring-8 / JAERI

E-mail: kawamura@spring8.or.jp

# Orbital State Study of Mn in Colossal Magnetoresistance Material $La_{2-2x}Sr_{1+2x}Mn_2O_7$ by Magnetic Compton Profile Measurement

Perovskite Mn oxides have been studied in relation to the colossal magnetoresistance (CMR) which is a huge decrease in electric resistance under a magnetic field. Recently, the double-layered manganite $La_{2-2x}Sr_{1+2x}Mn_2O_7$ has become of special interest, because it shows much larger CMR than the base compound $La_{1-x}Sr_xMnO_3$. As shown in Fig. 1, the crystal structure has a common feature in perovskite manganites that the Mn ion is octahedrally surrounded by O ions. In this crystal field, the energy levels of Mn 3*d* orbitals (which is 5-hold degenerated in a free atomic state) split into a triply degenerate $t_{2g}$ and a doubly degenerate $e_g$ states. When a hole is doped in this system, which is introduced by $Sr^{2+}$ ion doping, it goes into the $e_g$ orbital. That makes $e_g$ electrons hop around the Mn sites. The hopping also causes ferromagnetic alignment of the Mn spins through the strong Hund's coupling with localized $t_{2g}$ spins. This is what we call the double exchange (DE) mechanism. It can explain both the coexistence of metallic conduction and ferromagnetism in manganites [1]. However, recent experimental results have revealed that the magnitude of CMR and complicated magnetic phase diagrams cannot be explained only by the simple DE mechanism [2-4]. The importance of the orbital degree of freedom is pointed out as well as the charge and spin ones. This means that the populations of $x^2-y^2$ and $3z^2-r^2$ orbitals in the $e_g$ state play a key role in understanding the transport and magnetic properties of this system.

We have investigated the orbital state in $La_{2-2x}Sr_{1+2x}Mn_2O_7$ by magnetic Compton profile (MCP) measurement [5]. The MCP measurement has been used as a unique method to determine the electron-spin momentum density in ferromagnetic materials. In addition, it has the following advantages to define the orbital occupation; that is, MCP changes its shape depending on the orbital state occupied by magnetic electrons, and it also depends on the direction of the scattering vector of X-rays with respect to the crystalline axis. These features enable us to differentiate the electron population in $x^2-y^2$ and $3z^2-r^2$ orbitals together with $t_{2g}$ state through the measurement of MCP by using a single crystalline sample. Experiments have been made at beamline **BL08W** using circularly polarized X-rays of 270 keV. The MCP's were measured along [100], [110] and [001] directions for $La_{2-2x}Sr_{1+2x}Mn_2O_7$ with x = 0.35 and 0.42.

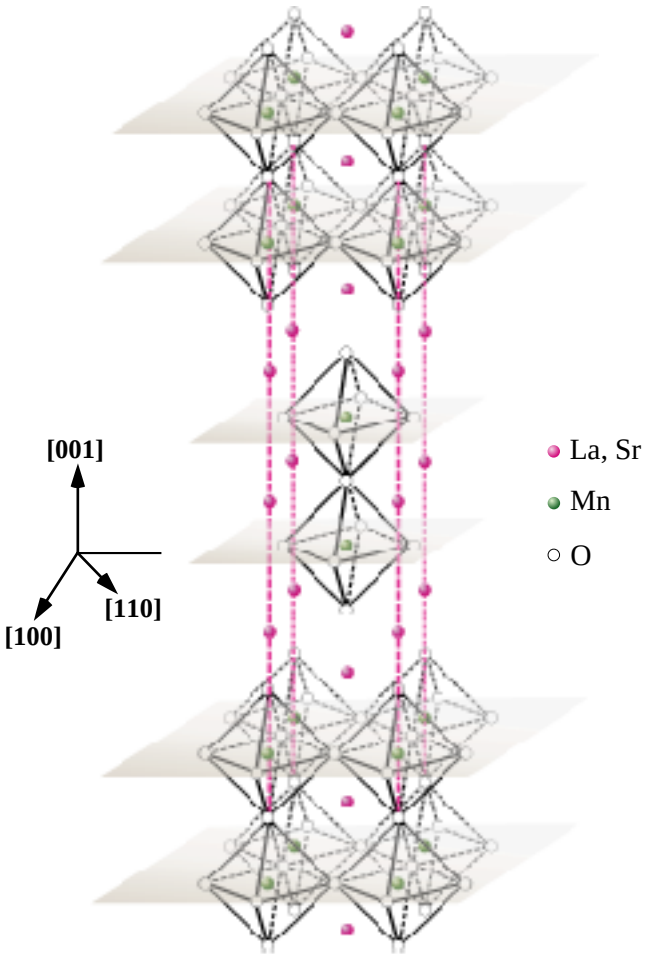


*Fig. 1. The crystal structure of $La_{2-2x}Sr_{1+2x}Mn_2O_7$.*

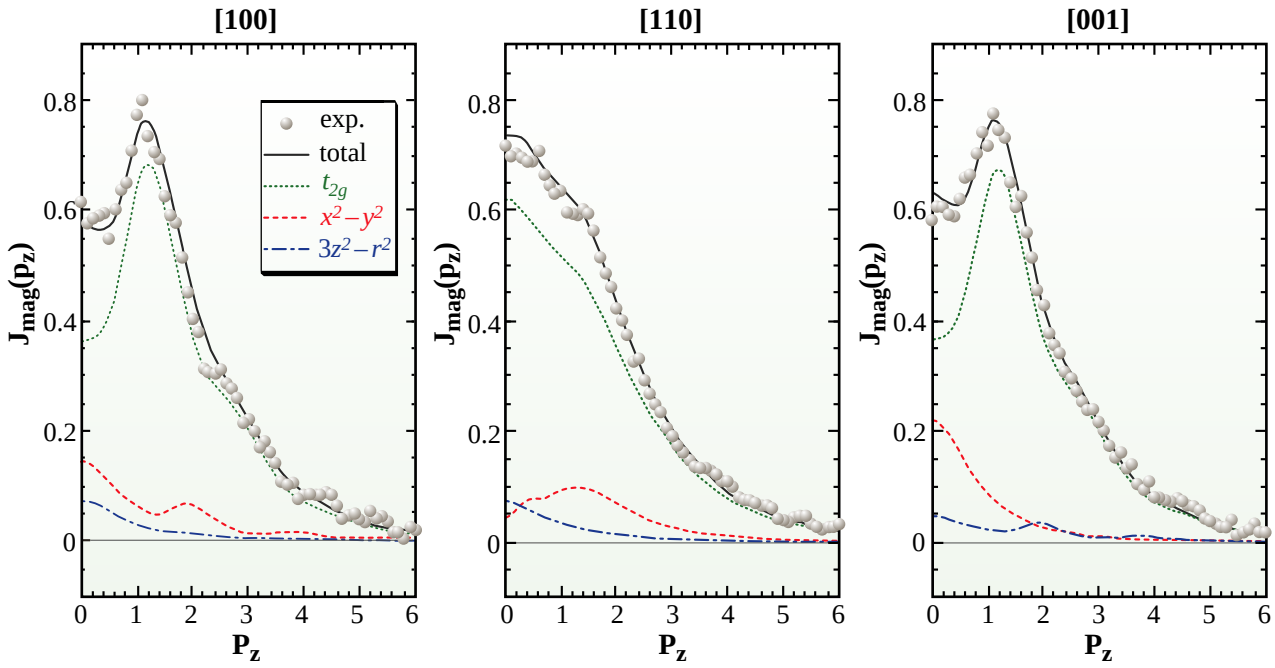


*Fig. 2. The magnetic Compton profiles along the [100], [110] and [001] directions in $La_{2-2x}Sr_{1+2x}Mn_2O_7$ with x = 0.35. Experimental data (solid circles) are shown with fit (solid gray line) using the $MnO_6$ cluster orbitals. Also shown are the $t_{2g}$ orbital (dotted green line), $x^2-y^2$ orbital (dashed red line) and $3z^2-r^2$ orbital (dash-dotted blue line) contributions.*

Figures 2 and 3 show respectively the MCP's of x = 0.35 and 0.42 samples obtained at 10 K. The clear anisotropy of MCP reflects the orbital state of magnetic electrons on Mn site. These MCP's were explained by theoretical Compton profiles obtained from an *ab initio* molecular orbital calculation for the $(MnO_6)^{8-}$ cluster which takes the hybridization effect between Mn 3*d* and O 2*p* orbitals into account. The theoretical analysis of the orbital state was made using these following conditions: Each MCP is normalized by the magnetic electron numbers per site estimated from the hole concentration *x*. The $t_{2g}$ occupation number is fixed to three per site because it is fully occupied. The remainder is fitted by the profiles of $x^2-y^2$ and $3z^2-r^2$ orbitals so that the area of fitted profile coincides with that of experimental one. The results are also shown in Fig. 2 and Fig. 3 with the dashed red line and dash-dotted blue line. Since the area of a profile is proportional to the number of electron spins in a state, the occupation numbers of $x^2-y^2$ and $3z^2-r^2$ orbitals can be thus obtained as 0.47 and 0.18 for x = 0.35 respectively, while they are 0.46 and 0.12 for x = 0.42. These results show that the $e_g$ orbital state is dominated by the $x^2-y^2$ -type orbital with almost constant occupation, while the occupation in $3z^2-r^2$ -type orbital decreases with the increase in the hole concentration *x*. This conclusion would explain the continuous change of magnetic structure from ferromagnetism via canted antiferromagnetism to A-type antiferromagnetism with an increase of *x*. The decrease of population in $3z^2-r^2$ orbital weakens the ferromagnetic coupling between $MnO_2$ layers through $e_g$ electron hopping. The superexchange coupling between $t_{2g}$ spins gradually overcomes the ferromagnetic coupling resulting in the antiferromagnetic structure at high *x* values.

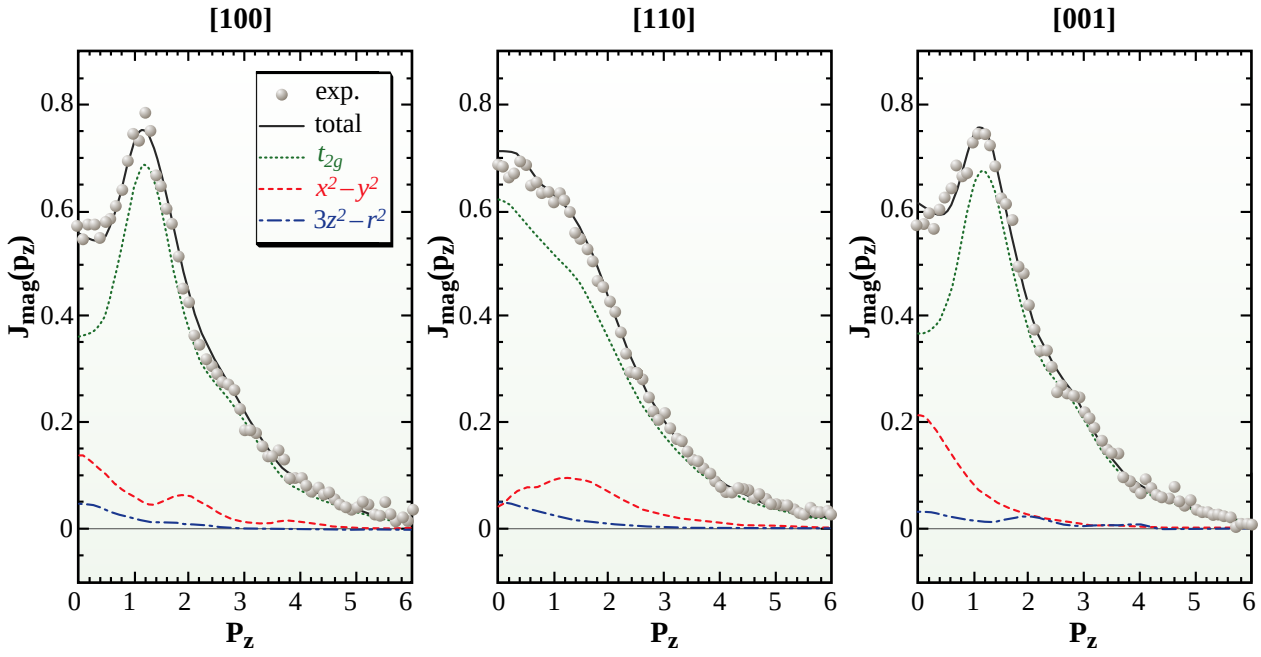


*Fig. 3. Same as Fig. 2 but for x = 0.42.*

Akihisa Koizumi

Himeji Institute of Technology

E-mail: akihisa@sci.himeji-tech.ac.jp

**References**

[1] C. Zener, Phys. Rev. **82** (1951) 403.

[2] Y. Moritomo *et al.*, Nature (London) **380** (1996) 141.

[3] K. Hirota *et al.*, J. Phys. Soc. Jpn. **67** (1998) 3380.

[4] M. Kubota *et al.*, J. Phys. Soc. Jpn. **69** (2000) 1606.

[5] A. Koizumi, S. Miyaki, Y. Kakutani, H. Koizumi, N. Hiraoka, K. Makoshi, N. Sakai, K. Hirota and Y. Murakami, Phys. Rev. Lett. **86** (2001) 5589.

# X-ray Powder Diffraction from Solid Deuterium

Recent optical studies have demonstrated that solid hydrogen exhibits three crystalline phases mainly based on the difference in the orientation of molecules (Fig. 1) [1]. In the diagram, only the crystalline structure of phase I has been determined.

Structural studies of solid hydrogen by X-ray diffraction technique are severely restricted because of the low scattering efficiency of hydrogen and the small size of the sample at high pressure. Because the intensity from a single crystal reflection is higher than that for a polycrystalline sample, the X-ray diffraction experiment with solid hydrogen was first carried out by the use of single-crystal technique at 5.4 GPa, and the crystal structure of phase I was determined to be hcp [2]. Measurements at higher pressures were impeded by the drastic reduction in diffracted intensity due to a significant reduction in the volume of the sample chamber and/or the fragmentation of a crystal under pressure. Louberyre *et al.* have overcome the difficulty with the excellent technique of growing a single crystal in helium and the application of high brilliance third generation synchrotron X-ray sources. By these means, the pressure-volume relation of solid hydrogen and deuterium have been determined to 120 GPa at room temperature [3].

In spite of the low intensity from a polycrystalline sample, the powder diffraction technique is still important because it is simple and convenient, and moreover, single crystals frequently fragment at structural transition accompanying a discontinuous change in volume.

In this work, our interest is focussed on whether or not the powder technique can be used for structural studies of solid hydrogen at high pressures and to determine the crystalline structure of phase II. The transition boundary between phase I and phase II exhibits a strong isotope effect and this shifts to a higher temperature and a lower pressure for deuterium (dotted curve in Fig. 1) [1,4,5]. The powder X-ray diffraction experiments of solid deuterium were carried out in this way.

A diamond anvil cell (DAC), with a tungsten carbide hemispheric seating and a cone-shaped aperture to detect diffracted X-rays, was used for high pressure generation. The top surface of the anvil was 0.3 mm. An Re gasket was pre-indented to 50 μm and a hole of 110 μm diameter was made as a sample chamber. The high-pressure experiments were carried out at beamline **BL10XU**. The wavelength was tuned with an Si (111) double-crystal monochromator to 0.6196 Å. An X-ray refractive lens made of molded PMMA (polymethyl methacrylate, density 1.19 g/cc) was inserted in the X-ray path to enhance the density of the incident beam. The sample was exposed to an X-ray beam through a pinhole collimator of 26 μm diameter. The cell was oscillated within ±5 deg. The typical exposure time was 30 min. The powder patterns were obtained by an angle-dispersive method with an image plate detector.

Figure 2 shows two-dimensional diffraction images from solid deuterium at 62.3 GPa and 300 K. In the figure, two different areas around the Debye-Scherrer rings are selected because the

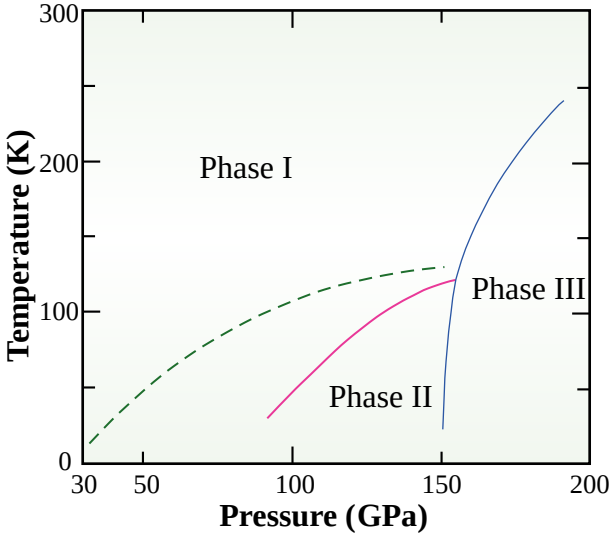


*Fig. 1. Schematic phase diagram of solid hydrogen. The dashed line represents the boundary between phase I and phase II for solid deuterium.*

diffraction around the ring was not uniform. Three diffraction rings from solid deuterium can be observed. These are assigned to the 100, 002 and 101 diffraction rings from an hcp lattice. There were strong arcs from the rhenium gasket. Figure 3 depicts the one-dimensional diffraction pattern integrated around the whole ring. The signal-to-noise ratio of the 101 diffraction line of solid deuterium was about 11. The lattice constants at 62.3 GPa and 300 K were a = 2.015 and c = 3.237 Å. The derived cell volume and the c / a ratio were consistent with single-crystal data [3].

The pressure cell was cooled to 83 K. During the course of cooling, pressure increased greatly to 94 GPa due to the thermal shrinkage of the body of the pressure cell. The pressure was estimated from the pressure-volume relation of the rhenium gasket because the ruby signal was lost in measurement. The pressure was slightly overestimated because of the large compressibility of deuterium, the diffraction profile, however, should be obtained from phase II. Three diffraction arcs from the sample can be observed (Fig. 4), which are also assigned to the 100, 002 and 101 diffraction lines of the hcp lattice. The lattice constants are a = 1.964 and c = 3.145 Å (c/a = 1.601). The center of each molecule is still on the hcp lattice point in phase II.

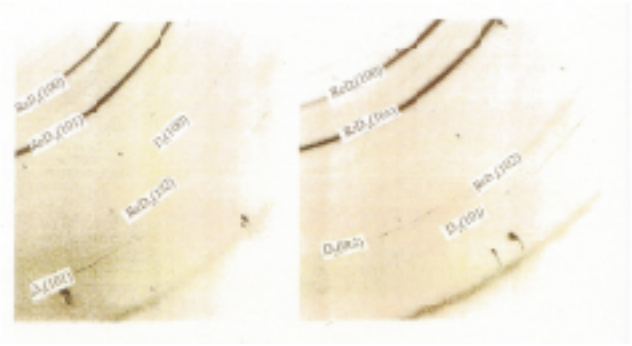

*Fig. 2. Two-dimensional diffraction images from solid deuterium at 62.3 GPa and 300 K. Two different areas around the Debye-Scherrer rings are selected because the diffraction intensity was not uniform around the ring.*

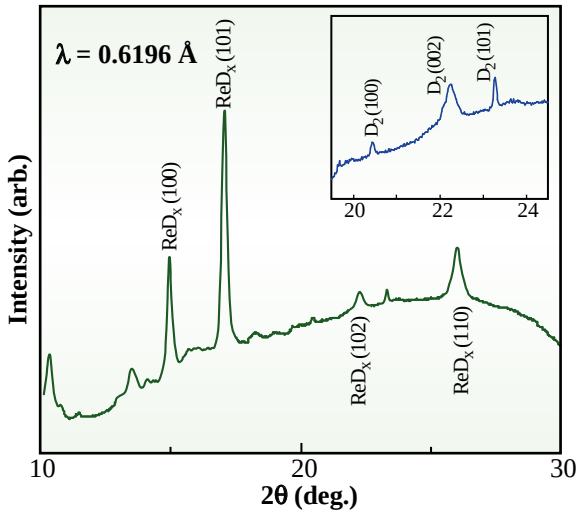


*Fig. 3. Integrated one-dimensional diffraction pattern obtained at 62.3 GPa and 300 K. The inset shows an expanded scale of intensity between 2θ = 19 and 25 deg.*

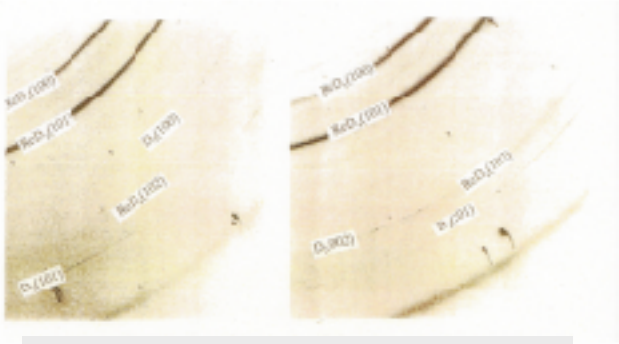

*Fig. 4. Two-dimensional diffraction images from solid deuterium at 94 GPa and 83 K.*

Haruki Kawamura and Yuichi Akahama

Himeji Institute of Technology

E-mail: kawamura@sci.himeji-tech.ac.jp

**References**

[1] H. K. Mao and R. J. Hemley, Rev. Mod. Phys. **66** (1994) 671.

[2] R. M. Hazen *et al.*, Phys. Rev. **B 36** (1987) 3844.

[3] P. Loubeyre *et al.*, H. K. Mao, L. W. Finger, Nature **383** (1996) 702.

[4] A.F. Goncharov *et al.* , Phys. Rev. **B 54** (1996) R15590.

[5] I.I. Mazin *et al.*, Phys. Rev. Lett. **78** (1997) 1066.

## XMCD Measurements of $Fe_4N$ under High-pressure

In $Fe_4N$ perovskite, hybridization between the electron wave-functions and the ligand field presents an important viewpoint for understanding magnetic properties. The insertion of a nitrogen atom into the center of fcc cell of Fe expands the cell volume, and the expanded $Fe_4N$ changes to show a ferromagnetic state with a Curie temperature of 761 K from antiferromagnetic γ-Fe. The small overlap of Fe 3*d* electrons originating from the lattice expansion is what is probably responsible for the transition. If so, then how does the magnetic property of $Fe_4N$ behave under compression?

In order to understand that, use can be made of high-pressure which is an effective external field to modify the lattice constant. The pressure variation of the hybridization and the charge transfer between the iron and the nitrogen provides information which is useful to understand the influences of these substances on the magnetic property of $Fe_4N$.

Spectroscopic analysis such as Mössbauer spectroscopy [1] and X-ray emission spectroscopy [2] have been applied to study magnetism under high-pressure. In recent years, X-ray magnetic circular dichroism (XMCD) has also been applied to probe magnetically polarized electron states. However, XMCD under high-pressure using the diamond-anvil cell has been limited to a range of photon energy above 10 keV, where the X-ray absorption by the diamond crystals is almost negligible. There have been only a few reports on Pt $L_3$-edge shows (11.564 keV) in $Fe_{72}Pt_{28}$ by Odin *et al*. [3] so far. To overcome this limitation, a pair of thinner diamond anvil and intense X-rays with a high degree of circular polarization were utilized; consequently XMCD was successfully measured under high-pressure up to 26 GPa at Fe *K*-edge (7.111 keV) in $Fe_4N$ [4].

The helicity-reversal method using a quarter-wave plate diamond (111) slab was applied to record the high-pressure XMCD spectrum at beamline **BL39XU**. The circularly polarized X-ray passed through a pair of thinner diamond anvils of 2.0 mm in total thickness. A sufficient intensity of the transmitted beam enabled us to measure the XMCD spectrum accurately by data accumulation for over a period of four to five hours. Figure 1 shows the pressure variation of the XMCD spectra

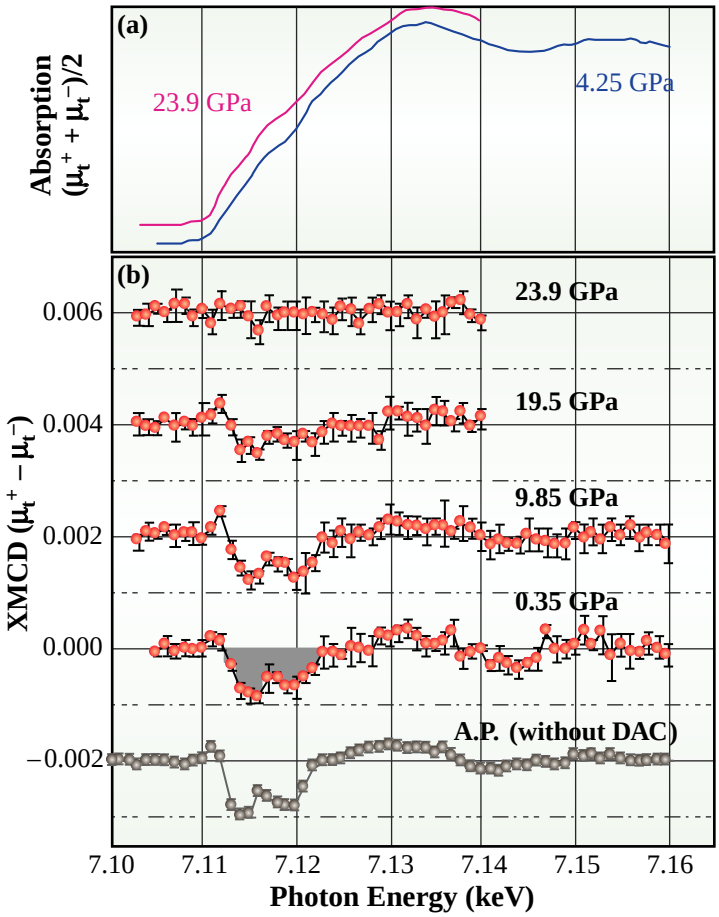


*Fig. 1.* ***(a)*** *X-ray absorption spectra of $Fe_4N$.* ***(b)*** *Pressure variation of XMCD spectra in $Fe_4N$. Each spectrum is shifted 0.002 steps in the y-direction. The error bars correspond to the standard deviation of runs of XMCD measurement.*

under a magnetic field of 0.6 T at room temperature. The XMCD spectrum is characterized by a positive peak at 7.111 keV, which first increases in intensity as the pressure increases and then reduces under further high-pressures. On the other hand, two negative peaks show a monotonous decrease in intensity. The unit-cell of $Fe_4N$ consists of two Fe sites; one is Fe(I) at the corner position and the other is Fe(II) at the face-centered position. Mössbauer spectroscopy shows that these two Fe sites give rise to different pressure dependences of hyper-fine field and isomer shift [1]. Therefore, the pressure variation in the XMCD profile may be ascribed to the different responses of these Fe sites.

The pressure dependence of XMCD is demonstrated by the plot of integrated XMCD shown in Fig. 2. The integrated XMCD corresponds to the area of the two negative peaks represented by the region colored in gray in Fig. 1. The reproducibility of the data was confirmed with two serial measurements. At first, as the pressure increases, the intensity gradually reduces, then decreases above 15 GPa to eventually vanish at around 24 GPa. This behavior is evidence for the pressure-induced transition from a ferromagnetic state to a paramagnetic one, a second-order transition without pressure hysteresis. According to an X-ray diffraction experiment which was carried out separately, this transition is not accompanied by structural transformation.

XMCD at the *K*-edge in pure 3*d* transition metals is strongly affected by small 3*d* orbital moments on the neighboring site [5]. Since spin-orbital interaction induces a 3*d* orbital moment, the XMCD spectrum reflects bulk magnetization in addition to its electronic state. It should be noted that high-pressure XMCD measurement can develop the basic studies of magnetism in 3*d* transition metals and/or 4*f* rare-earth metals.

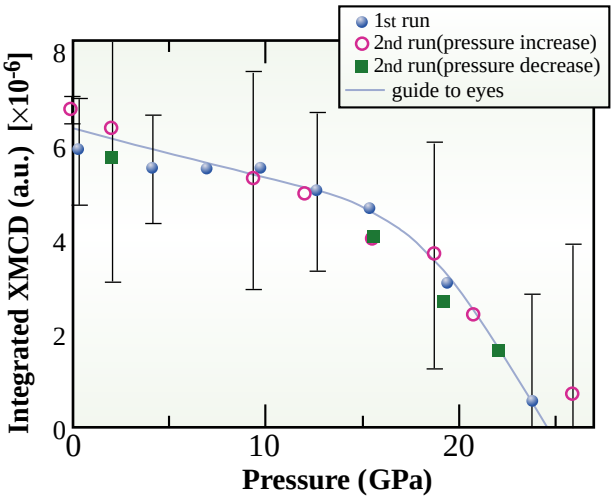


*Fig. 2. Pressure dependences of integrated XMCD. The solid circles, open circles and solid squares correspond to the first run in pressure increase, the second run in pressure increase and the second run in pressure decrease, respectively. The solid line is guide for the eyes.*

Naoki Ishimatsu

Hiroshima University

E-mail: naoki@sci.hiroshima-u.ac.jp

**References**

[1] C. L. Yang *et al.*, J. Mag. Mag. Mat. **151** (1995) L19.

[2] J.-P. Rueff *et al.*, Phys. Rev. Lett. **82** (1999) 3284.

[3] S. Odin *et al.*, J. Appl. Phys. **83** (1998) 7291.

[4] N. Ishimatsu, Y. Ohishi, M. Suzuki, N. Kawamura, M. Ito, H. Maruyama and O. Shimomura, in preparation; Nucl. Instrum. Meth. **A 467-A468** (2001) 1061.

[5] J. Igarashi and K. Hirai, Phys. Rev. **B 24** (1994) 17820.

# Chemical Science

The highly brilliant light from SPring-8, covering the whole range of the wavelength from hard X-rays to far infrared, is very useful not only in the physical sciences but also in the chemical sciences. Soft X-ray undulator beamlines (BL23SU, BL25SU, BL27SU) are particularly useful in chemical studies, because the inner-shell excitation/ionization energies of elements of chemical interest lie in the soft X-ray region. Taking advantage of the very high resolution of these beamlines, an increasing number of high quality studies in spectroscopy and dynamics, both in the gas phase and on the surfaces, has been performed over the years since the commissioning of each beamline. Another important field of chemistry is catalysis, in which the characterization of catalysts containing heavy elements constitutes an essential part of the study. For such characterization, high-energy XAFS beamlines have been successfully used. These include BL01B1 which provides hard X-rays of energies of over 70 keV. Metal clusters in the gas phase, which have attracted a great deal of attention in recent years, have also been uniquely studied using an XAFS technique on another hard X-ray beamline BL10XU, where undulator radiation is available. Infrared beamline BL43IR has also started to yield new results of chemical interest.

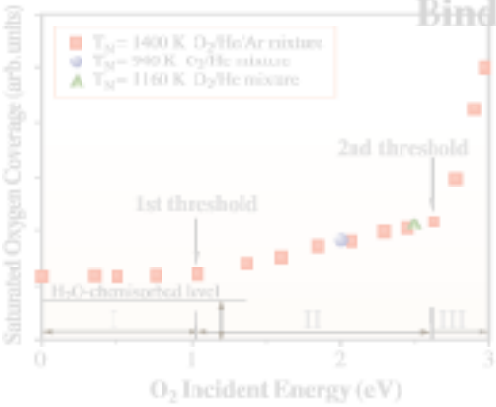


*Inosuke Koyano*

# Nuclear Motion of Polyatomic Molecules Probed by High-resolution Resonant Auger Spectroscopy

When an inner-shell electron of an atom composing a molecule is promoted to an unoccupied molecular orbital, a resonant Auger decay takes place on a femtosecond time scale. Within this short time scale, however, nuclear motion can proceed in the core-excited state. Nuclear motion in a polyatomic molecule is of particular interest because multi-dimensional nuclear motion may be mediated by core excitation. The nuclear motion caused in the core-excited state then mediates nuclear motion in the Auger final states and thus may govern dissociation pathways.

The nuclear motion in the core-excited state proceeds in competition with the resonant Auger decay and thus should be reflected in the resonant Auger spectrum. To probe the nuclear motion in the core-excited state as well as in the Auger final state in the resonant Auger spectra, we installed a high-resolution electron spectroscopy apparatus on beamline **BL27SU** [1]. The apparatus consists of a state-of-the-art SES2002 electron energy analyzer (Gammadata-Scienta), a gas cell, and a differentially pumped experimental chamber, and allows us to observe the resonant Auger spectra of gaseous molecules with an unprecedented resolution when they are combined with a high-resolution soft X-ray monochromator at BL27SU [2].

We present here two typical showcases of our observations; the resonant Auger spectra of the boron trifluoride molecule $BF_3$ [3] and those of the water molecule $H_2O$ [4].

The $BF_3$ molecule in the ground state has a planar structure of $D_{3h}$ symmetry, whereas it has trigonal pyramidal structure of $C_{3v}$ symmetry in the core-excited state in which a B 1*s* electron is promoted to the lowest unoccupied molecular orbital $2a_2$". We probed out-of-plane nuclear motion for the deformation from $D_{3h}$ to $C_{3v}$ following the core excitation, by means of resonant Auger spectroscopy.

The spectrum (b) in Fig. 1 represents the direct photoemission from the six valence orbitals in $BF_3$, whereas the spectrum (a) is recorded at the B $1s \rightarrow 2a_2$" resonance. The electron emission for the C, D, and E bands is strongly enhanced by the B $1s \rightarrow 2a_2$" excitation, suggesting that the participator Auger decay takes place. In the resonantly enhanced spectrum, one can see long progressions of out-of-plane vibrations in the Auger final states. The highly excited out-of-plane vibrations are a direct reflection of the out-of-plane nuclear motion in the core-excited state.

The $H_2O$ molecule has a bent structure of $C_{2v}$ symmetry. The two lowest unoccupied molecular orbitals $4a_1$ and $2b_2$ are the antibonding counterparts of the two OH bonding orbitals $3a_1$ and $1b_2$. The O $1s^{-1}$ $4a_1$ core-excited state is known to be dissociative, whereas the O $1s^{-1}$ $2b_2$ core-excited state has a shallow potential minimum so that the vibrational structure can be seen in the O $1s \rightarrow 2b_2$ resonance [5]. We demonstrated that one can control the two-dimensional nuclear motion of the Auger final state by changing the nuclear

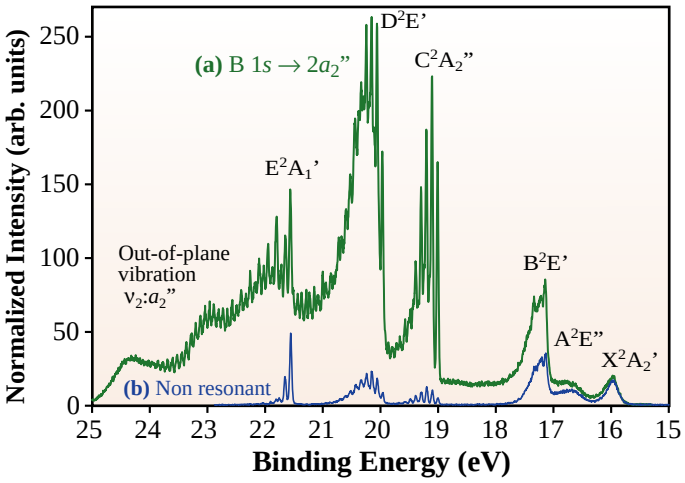


*Fig 1. Valence-electron spectra of $BF_3$ **(a)** after excitation of the B $1s^{-1}2a_2$" state and **(b)** direct photoemission.*

motion in the O $1s^{-1}$ $2b_2$ core-excited state.

The electron spectra recorded at four photon energies across the O $1s \rightarrow 2b_2$ resonance are presented in Fig. 2. Here the largest contribution to the spectral width comes from the Doppler width due to the thermal motion of the sample molecules. The spectra cover the binding energy region 17.0 - 20.0 eV, where the electron emission from the $1b_2$ orbital is present. The bottom spectrum (a) represents the direct photoemission spectrum, whereas the other three spectra (b), (c), and (d) are recorded approximately at the energies of the ($\nu_1$, $\nu_2$) = (0,0), (1,0) and (2, 0) vibrational components, respectively, of the O $1s \rightarrow 2b_2$ band. When the Auger final state is populated via the O $1s \rightarrow 2b_2$ (0,0) excitation (spectrum (b)), the vibrational structure of the $\nu_2$ mode with spacing of ~ 200 meV is partially resolved. The vibrational structure, however, becomes less resolved at the O $1s \rightarrow 2b_2$ (1,0) and (2,0) excitations (spectra (c) and (d)). To discover the reason for this, we carried out *ab initio* calculations. The results show reasonable agreement with the experimental spectra as can be seen in Fig. 2. It is clear from the *ab initio* spectra that more and more vibrational components with a mixture of the $\nu_1$ and $\nu_2$ modes are populated with the increase in the excitation energy. In this way we confirm that it is possible to control the two-dimensional nuclear motion in the $1b_2^{-1}$ Auger final state by tuning the incident energy to different portions of the O $1s^{-1}$ $2b_2$ core-excited state.

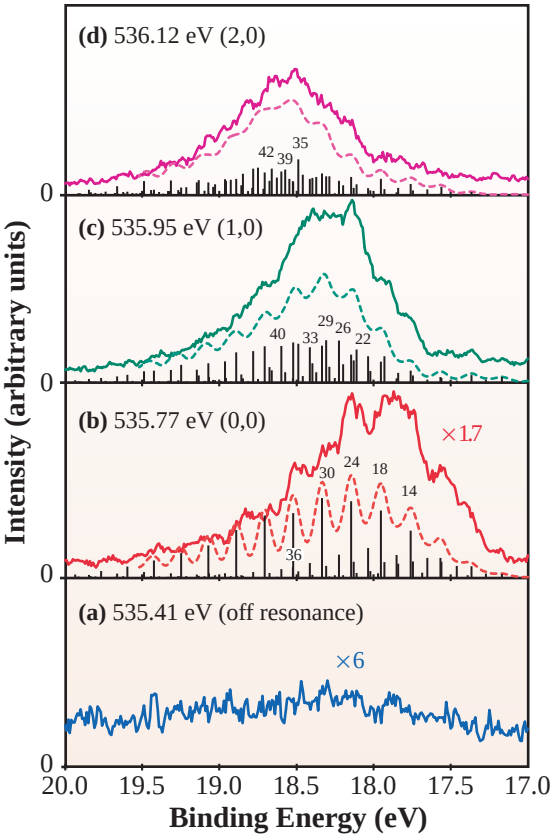


*Fig. 2. Measured and calculated resonant Auger spectra of $H_2O$ decay to the $1b_2^{-1}$ Auger final state at various excitation energies across the O $1s \rightarrow 2b_2$ band, continuous and dashed lines. The calculated vibrational components are represented by vertical bars.*

Kiyoshi Ueda

Tohoku University

E-mail: ueda@tagen.tohoku.ac.jp

**References**

[1] Y. Shimizu *et al.*, J. Electr. Spectrosc. Relat. Phenom. **114-116** (2001) 63.

[2] H. Ohashi *et al.*, Nucl. Instrum. Meth. **A 467-468** (2001) 533.

[3] K. Ueda, to be published in Surface Rev. Lett.; K. Ueda, A. De Fanis, K. Okada *et al.*, to be published in Chem. Phys.

[4] A. De Fanis *et al.*, J. Phys. **B 33** (2002) L23.

# Photoemission Study on the Surface Reaction Dynamics of Si(001) Oxidation by Supersonic $O_2$ Molecular Beams

In the surface reaction dynamics study, the roles of translational kinetic energy ($E_t$) of incident molecules are an area of current interest. For instance, the dissociative chemisorption of $O_2$ molecules takes place on Si(001) surfaces at room temperature (passive oxidation). In order to understand the roles of the incident energy in $O_2$ molecules, $E_t$ dependencies of passive oxidation, induced by supersonic $O_2$ molecular beams (SSMBs), have been investigated by photoemission spectroscopy using high-energy-resolution synchrotron radiation (SR).

All experiments were performed at the experimental station for surface chemistry: SUREAC2000 [1,2] at **BL23SU**. The base pressure is less than $5\times10^{-9}$ Pa when liquid $N_2$ is filled in the shroud and the manipulator. Monochromated SR beams of about 400 eV and 830 eV were used for Si-2*p* and O-1*s* photoemission measurements with a surface sensitive condition (escape depth: 0.3 nm). The $O_2$ SSMBs are generated by the adiabatic expansion of a mixture of $O_2$, He and Ar using a high temperature nozzle. The maximum $O_2$ incident energy was calculated to be 3 eV. The typical SSMB flux density and the photon flux were estimated to be $2\times10^{14}$ molecules$\cdot$cm$^{-2}\cdot$s$^{-1}$ and $2\times10^{10}$ photons$\cdot$s$^{-1}$, respectively.

First, an $H_2O$-chemisorbed Si(001) surface was formed before $O_2$ exposure. Dangling bonds of the topmost Si dimers were terminated by H and OH in the $H_2O$-chemisorbed Si(001) surface. It was exposed to $O_2$ gas up to saturation. The oxidized surface was irradiated again by the $O_2$ SSMBs with respect to surface normal until the saturation coverage was achieved. The $E_t$ dependence of the saturation coverage is shown in Fig. 1 [3]. Referring to the first-principles molecular dynamics calculation [4], the lower break was assigned to a potential energy barrier for the backbond oxidation of the topmost Si atoms, and the higher one was assigned to a potential energy barrier for the backbond oxidation of the second layer (subsurface) Si atoms.

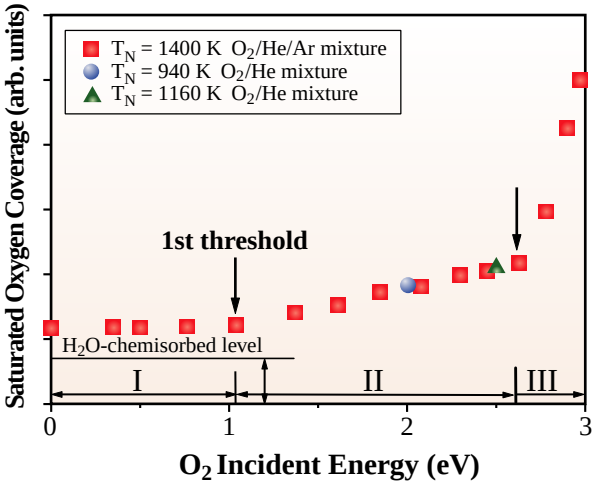


*Fig. 1. The saturated oxygen coverage on the partially-oxidized ($H_2O$-chemisorbed) Si(001) surface as a function of translational kinetic energy of incident $O_2$ molecules. The symbol ■ represents the results obtained by varying mixing ratio of $O_2$/He/Ar keeping a nozzle temperature ($T_N$) of 1400 K. The symbol ● and ▲ represent the results obtained by different gas mixing ratios and nozzle temperatures of 940 K and 1160 K, respectively.*

Different oxidation states are expected to appear in Si-2*p* photoemission spectra in each incident energy region. Representative Si-2*p* photoemission spectra are shown in Fig. 2 [5]. They were de-convoluted into bulk Si (Si-$2p_{1/2}$ and $2p_{3/2}$), interface Si, H-terminated Si and oxidized Si: $Si^{n+}$ (n = 1 - 4). The photoemission peak intensity ratio for the $2p_{1/2}$ and $2p_{3/2}$ components was measured to be 1:2 under a bulk sensitive condition so that the ratio was used for the de-convolution. The LS-coupling scheme may be no longer good due to crystal field effects even for the $Si^{2+}$ component [6]. Therefore, the spin-orbit splitting was taken into account for bulk Si, distorted interface Si, H-terminated Si, and $Si^{1+}$ components except $Si^{2+}$, $Si^{3+}$ and $Si^{4+}$ components. The Si-2*p* spectrum of the Si(001) surface before $O_2$ exposure consists of bulk Si, Si-H and Si-OH ($Si^{1+}$) components as shown in Fig. 2(a). The spectral profile obtained after $O_2$ exposure with $E_t$ = 0.04 eV, representative in the region I, is very close to that before $O_2$ exposure. This fact implies that the Si-OH and Si-H bonds prohibit further oxidation by $O_2$ molecules. On the other hand, the spectral profile changed dramatically when the $O_2$ SSMBs with incident energy larger than the first threshold, 1.0 eV, were irradiated to the surface. An Si-2*p* spectrum for $E_t$ = 2.0 eV is shown in Fig. 2(c) as a representative in region II, indicating the $Si^{4+}$ formation. The direct oxidation of Si dimer backbonds due to energetic $O_2$ collisions can take place in this incident energy region so that the topmost Si atoms can be surrounded

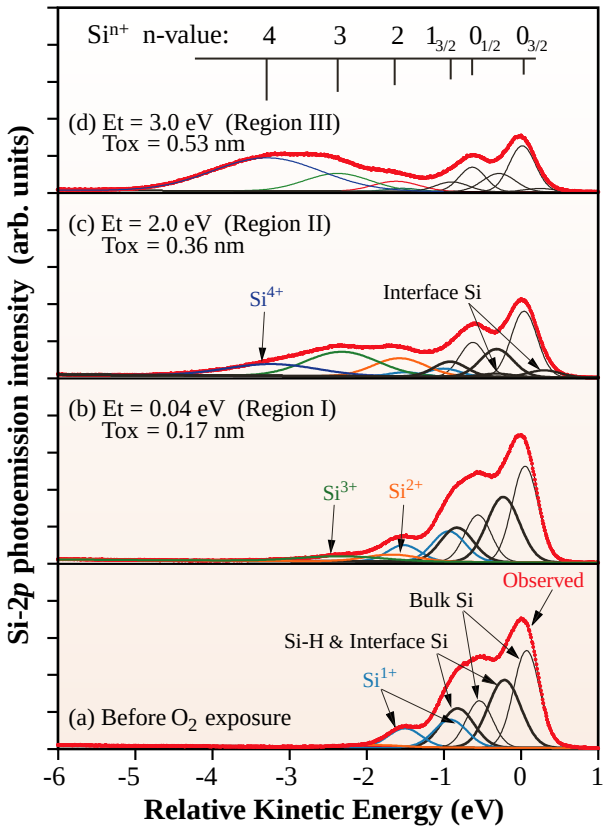


*Fig. 2. Si-2p photoemission spectra for Si(001) surfaces oxidized up to saturation coverage at room temperature by $O_2$ molecules with various incident energies ($E_t$) : **(a)** for the initial (partially-oxidized) Si(001) surface, **(b)** for $E_t$ = 0.04 eV, **(c)** for $E_t$ = 2.0 eV and **(d)** for $E_t$ = 3.0 eV, respectively. $T_{ox}$ represents the oxide layer thickness.*

by up to four oxygen atoms. The Si-2*p* spectrum for $E_t$ = 3.0 eV shows that $Si^{3+}$ and $Si^{4+}$ contributions share a large part of the satellite peaks, as shown in Fig. 2(d). Such a large contribution is interpreted as the incident-energy-induced dissociative chemisorption of $O_2$ molecules at the subsurface backbonds in the energy region III as well as the topmost Si dimers bridge sites and their backbond sites. The oxide layer thickness was estimated approximately to be 0.53 nm. Consequently, the thickness of ultra-thin oxide layer, less than 1 nm, can be controlled at room temperature by controlling the translational kinetic energy of incident $O_2$ molecules in a hyperthermal energy region. Reaction models are also presented in Fig. 3.

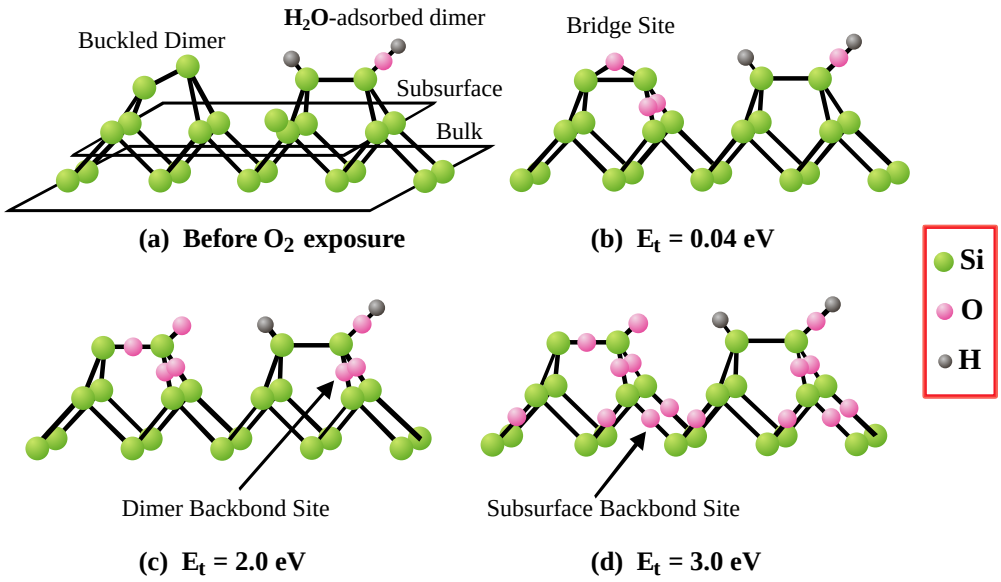


*Fig. 3. Reaction models of incident-energy-induced oxidation processes:* ***(a)*** *for the partially-$H_2O$-chemisorbed Si(001) surface,* ***(b)*** *for the residual Si dimer oxidation by $O_2$ exposure,* ***(c)*** *for the Si dimer backbond oxidation by $O_2$ incident energy larger than the first threshold (1.0 eV),* ***(d)*** *for the subsurface backbond oxidation by $O_2$ incident energy larger than the second threshold (2.6 eV), respectively.*

Yuden Teraoka and Akitaka Yoshigoe

SPring-8/JAERI

E-mail: yteraoka@spring8.or.jp

**References**

[1] Y. Teraoka and A. Yoshigoe, Jpn. J. Appl. Phys. **38**, Suppl. **38-1** (1999) 642.

[2] Y. Teraoka and A. Yoshigoe, Appl. Surf. Sci. **169-170** (2001) 738.

[3] A. Yoshigoe, M. Sano and Y. Teraoka, Jpn. J. Appl. Phys. **39** (2000) 7026.

[4] K. Kato and T. Uda, Phys. Rev. **B 62** (2000) 15978.

[5] Y. Teraoka and A. Yoshigoe, Appl. Surf. Sci. **190** (2002) 75.

[6] Y. Miyamoto and A. Oshiyama, Phys. Rev. **B 44** (1991) 5931.

# X-ray Absorption Fine Structure of Free Selenium Clusters

Although clusters have attracted great interest as intermediate states between atomic and condensed states of matter [1], general methods for the size-selective structural analysis of neutral clusters have not been established so far. Recently we measured the Photoelectron Photoion Coincidence (PEPICO) spectra for selenium dimer $Se_2$ and larger species such as $Se_5$ [2,3]. The PEPICO spectra reveal that the multiply charged ions are produced as a result of de-excitation processes following the *K*-shell excitation and fragmented to atomic ions with z charges, $Se^{z+}$, owing to the Coulomb explosion (see Fig. 1). The branching ratios from the parent cluster to the daughter ions exhibit clear dependence on the size *N* of the parent clusters. In particular, the branching ratios in the non-resonant absorption region are well reproduced considering that the charges were randomly distributed within the clusters before the Coulomb explosion. Based upon these findings, we proposed a new method for the size-selective EXAFS of neutral free clusters by utilizing the PEPICO measurements [3].

The basic relations we have suggested are the simultaneous equations of the X-ray absorption coefficients per atom, $\alpha$ (hν), parameterized by z, as follows:

$$I(h\nu, z) = \sum N A_N B_N(z) \alpha (h\nu) \qquad (1),$$

where I(hν, z) is the integrated PEPICO intensity for the z charged ion, $A_N$ is the abundance of parent clusters consisting of N atoms and $B_N(z)$ is the branching ratio. Since $A_N$ and $B_N(z)$ can be estimated either from experiments or calculations, $\alpha$ (hν) was deduced by solving eq. (1) from the PEPICO measurements.

In order to verify eq. (1) experimentally, we have carried out synchronous XAFS-PEPICO measurements for an Se cluster beam at the X-ray undulator beamline **BL10XU**. The neutral cluster beams were produced by a supersonic jet expansion method, intersected with the X-rays at right angles in the horizontal plane. The photoions produced by absorbing an X-ray photon were extracted upward by a constant electric field to a detector, while the photoelectrons were extracted downward. The procedures of the synchronous measurements are summarized in a flow chart (see Fig. 2). The XAFS spectrum was measured by the host computer that also controls the multi-channel-

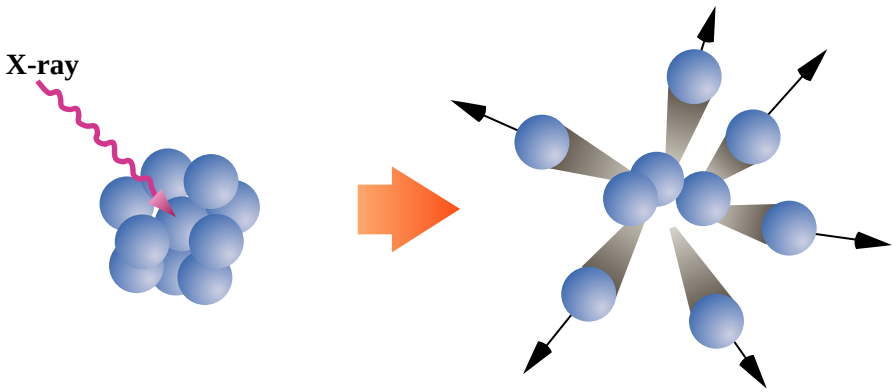


**(a) X-ray absorption** **(b) Coulomb explosion**

*Fig. 1. Schematic illustration of the X-ray absorption **(a)** and the Coulomb explosion **(b)** taking place in a cluster.*

analyzer, by which PEPICO spectra are taken, as well as the angle of the X-ray monochromators and the gap of the undulator.

In our experiment, $Se_2$, $Se_5$, $Se_6$ and $Se_7$ were produced and their relative abundances were 66:16:11:7, respectively. In Fig. 3 EXAFS spectrum $\chi(k)$ for "$Se_5$" deduced from eq. (1) is shown by circles. Here "$Se_5$" includes $Se_5$, $Se_6$ and $Se_7$, as in previous studies [2-5]. Although the number density of Se atoms in the cluster beam is smaller than that in the bulk Se samples by more than ten orders of magnitude, the EXAFS oscillation is clearly seen. The line denotes the smoothed variation $\chi(k)$ for $Se_2$ in the cluster beam, which is in good agreement with $\chi(k)$ for $Se_2$ in the vapor phase [6] except for the scaling factor. The spacing of the EXAFS oscillation clearly demonstrates that the bond length of "$Se_5$" is longer than that of $Se_2$. More precisely, the former proves to be 2.35 Å and the latter 2.16 Å [7], which is fully consistent with a pile of EXAFS data for various forms of Se [8]. Therefore, we conclude that the proposed size-selective XAFS is a reliable and realistic method.

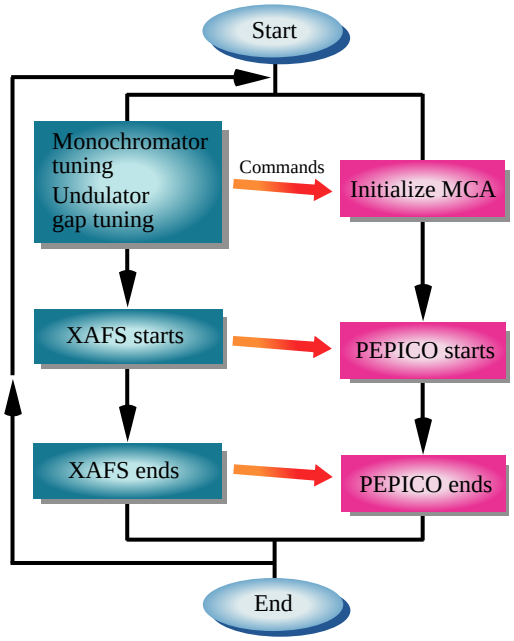


*Fig. 2. A flow chart of the XAFS-PEPICO synchronous measurements. Procedures by the host computer are shown on the left and those by the multi-channel-analyzer on the right.*

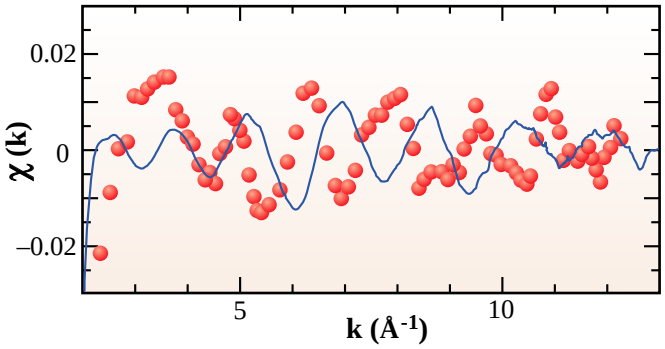


*Fig. 3. EXAFS spectra $\chi(k)$ for $Se_2$ (line) and "$Se_5$" (circles).*

Makoto Yao and Kiyonobu Nagaya

Kyoto University

E-mail: yao@scphys.kyoto-u.ac.jp

**References**

[1] Clusters of Atoms and Molecules, ed. H. Haberland (Springer, 1994).

[2] T. Hayakawa *et al.*, J. Phys. Soc. Jpn. **69** (2000) 2039.

[3] T. Hayakawa *et al.*, J. Phys. Soc. Jpn. **69** (2000) 2850.

[4] M. Yao, T. Hayakawa, K. Nagaya, K. Hamada, Y. Ohmasa, M. Nomura, J. Synchrotron Rad. **8** (2001) 542.

[5] M. Yao *et al.*, Jpn. J. Appl. Phys. suppl. **38-1** (1999) 564.

[6] S. Hosokawa *et al.*, J. Chem. Phys. **97** (1992) 786.

[7] K. Nagaya, M. Yao, T. Hayakawa, Y. Ohmasa, Y. Kajihara, M. Ishii, Y. Katayama, submitted in Phys. Rev. Lett.

[8] M. Inui *et al.*, J. Phys. Soc. Jpn. **57** (1988) 553.

# Investigation of Local Structure of Re Active Site in Re/γ-$Fe_2O_3$ Catalysts by Re-*K* Edge EXAFS

Re/γ-$Fe_2O_3$ catalysts possess a characteristic activity on methanol partial oxidation reaction to produce methylal ($CH_2(CH_3O)_2$) selectively [1]. The reaction proceeds under a mild condition and the selectivity is more than 90%. In addition, the lifetime of the Re/γ-$Fe_2O_3$ is quite long. In many cases, rhenium forms sublimable oxides such as $Re_2O_7$ under the oxidative conditions and cannot be used as oxidation catalysts. Thus, $ReO_x$/γ-$Fe_2O_3$, an active and long living rhenium catalyst under oxidative conditions, is quite unusual. This may be due to an unusual local structure of the rhenium species.

To elucidate the structure of the rhenium species, we measured the Re *K*-edge EXAFS of Re/γ-$Fe_2O_3$ and Re/$Al_2O_3$ at SPring-8. As $Fe_2O_3$ support absorbs X-rays at the energy range of Re $L_{III}$-edge (10 - 11 keV), Re $L_{III}$-edge EXAFS is difficult to measure because of its large background. On the other hand, as $Fe_2O_3$ support does not absorb X-rays in the energy range of Re *K*-edge (71 - 72 keV), Re *K*-edge EXAFS can be measured with small background. Thus Re *K*-edge EXAFS is a useful technique to elucidate the local structure around Re species in Re/γ-$Fe_2O_3$ catalysts.

Catalyst preparation has been described elsewhere[1]. Re *K*-edge EXAFS spectra of $ReO_x$/γ-$Fe_2O_3$ and $ReO_x$/$Al_2O_3$ catalysts with various Re loadings were measured at beamline **BL01B1** with the transmission mode at ca. 10 K. The spectra were analyzed by use of the UWXAFS package [2]. After background subtraction, $k^3$ weighted EXAFS functions were Fourier transformed (FT) to the R-space and fitted in this space. The FT *k* range and fitting R-ranges were 40 – 140 $nm^{-1}$ and 0.1 – 0.4 nm, respectively. Backscattering amplitudes and phase shifts were calculated by the FEFF8 code [3]. The line broadening due to the resolution of monochromator and core-hole lifetime was estimated to be 15 eV and was taken into account to calculate the phase and amplitude.

Figure 1 shows an X-ray absorption spectrum of Re(9.2 wt%)/γ-$Fe_2O_3$. EXAFS oscillations were observed in a wide energy range even though the near edge structure was smeared by broadening. Figures 2 show Fourier transformed EXAFS functions of Re/γ-$Fe_2O_3$ and Re/$Al_2O_3$ catalysts together with the result of curve fitting analysis. Phase shift was not corrected in these figures. Table I shows structural parameters obtained by curve fitting analysis for Re/γ-$Fe_2O_3$ and Re/$Al_2O_3$ catalysts. In the EXAFS functions of Re/γ-$Fe_2O_3$, a strong peak of Re-O was observed at 0.175 nm in all Re loadings. In addition, a peak for Re-Fe was observed at 0.382 nm in EXAFS of Re(9.2 wt%)/γ-$Fe_2O_3$. On the contrary, Re-O contribution in the EXAFS of Re/$Al_2O_3$ was a convolution of two Re-O bondings, at 0.175 nm and 0.2 nm. In addition,

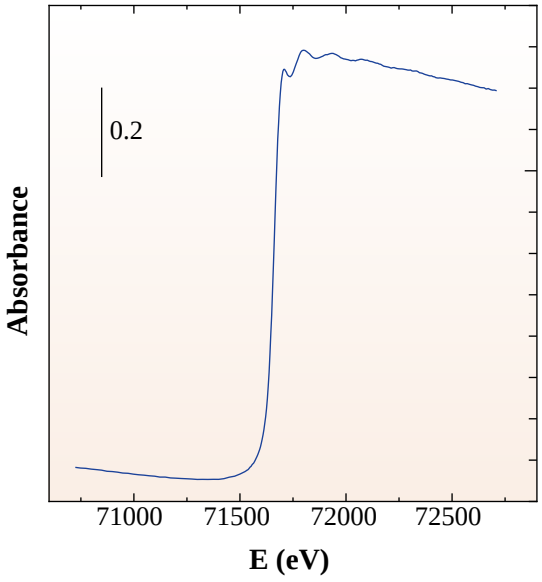


*Fig. 1. Re K-edge X-ray absorption spectrum of Re (9.2 wt%)/γ-$Fe_2O_3$.*

several peaks corresponding to $ReO_2$ were observed in EXAFS of Re(9.2 wt%)/$Al_2O_3$. A Re *K*-edge EXAFS analysis revealed that tetrahedral $ReO_4$ structure was stabilized by forming Re-Fe binary oxide on $\gamma$-$Fe_2O_3$ support. The $ReO_4$ structure is unstable on the $Al_2O_3$ surface and converts to $ReO_2$. Figure 3 shows the proposed structure of an Re-Fe binary oxide formed on Re/$\gamma$-$Fe_2O_3$ catalyst. The $ReO_4$ structure bound to Fe ion and the formation of sublimable $Re_2O_7$ was prohibited. A Re *K*-edge EXAFS study revealed that active $ReO_4$ species were stabilized by forming Re-Fe binary oxide on the $\gamma$-$Fe_2O_3$ surface.

**Table I.** Structural parameters of supported Re catalysts delivered by curve fitting analysis of Re *K*-edge EXAFS.

| Sample ($\Delta E_0$/eV, $R_f$(%)) | shell | CN [(a)] | R [(b)]/0.1 nm | $\sigma^2$ [(c)]/$10^{-5}$ nm$^2$ |
|---|---|---|---|---|
| Re (1.7wt%)/$\gamma$-$Fe_2O_3$ (0, 1.0) | Re-O | 4 | 1.75 | 3 |
| Re (9.2wt%)/$\gamma$-$Fe_2O_3$ (-5, 0.9) | Re-O<br>Re-Fe | 4<br>1 | 1.75<br>3.82 | 3<br>20 |
| Re (2.0wt%)/$Al_2O_3$ (0, 0.8) | Re-O<br>Re-O | 4<br>1 | 1.75<br>1.95 | 3<br>1 |
| Re (9.2wt%)/$Al_2O_3$ (7, 2.7) | Re-O<br>Re-O | 1<br>3 | 1.76<br>2.00 | 1<br>4 |

(a) coordination number
(b) interatomic distance
(c) Debye-Waller factor

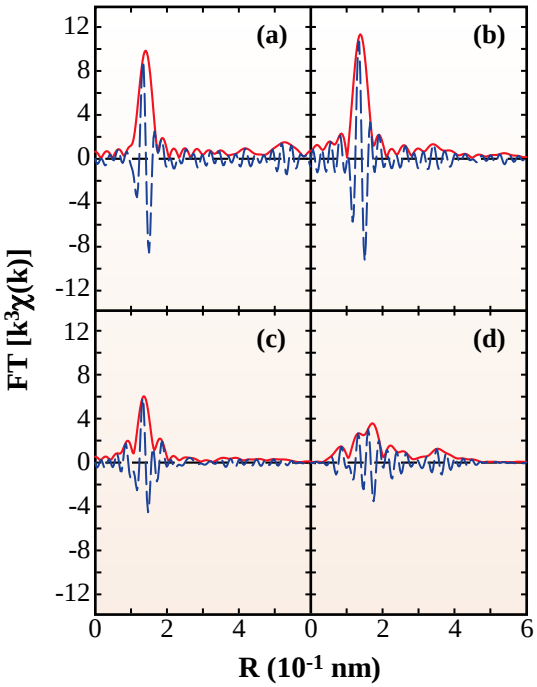


*Fig. 2. Fourier transformed Re K-edge EXAFS functions ($k^3$ $\chi$ (k)) of Re(1.7wt%)/$\gamma$-$Fe_2O_3$ **(a)**, Re(9.2wt%)/$\gamma$-$Fe_2O_3$ **(b)**, Re(2.0wt%)/$Al_2O_3$ **(c)**, and Re(9.2wt%)/$Al_2O_3$ **(d)**. Red and blue lines represent observed and calculated EXAFS functions, respectively.*

T. Shido, F. Nakagawa and Y. Iwasawa

The University of Tokyo

E-mail: shido@chem.s.u-tokyo.ac.jp

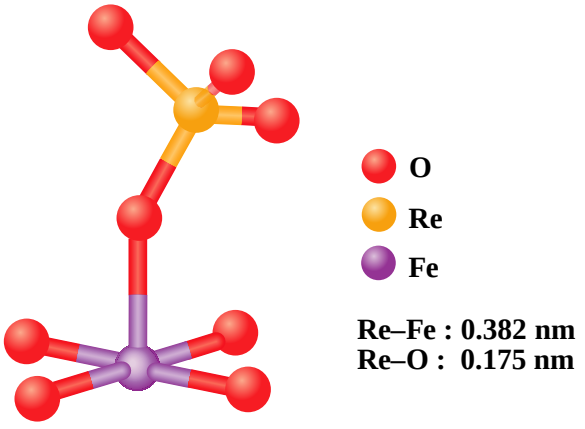


*Fig. 3. Proposed structure of Re active site on Re/$\gamma$-$Fe_2O_3$ catalysts.*

**References**

[1] Y.-Z. Yuan *et al.*, J. Chem. Soc. Chem. Commun. (2000) 1421.
[2] E.A. Stern *et al.*, Physica **B 208** (1995) 117.
[3] A.L. Ankudinov *et al.*, Phys. Rev. **B58** (1998) 7565.
[4] T. Shido, F. Nakagawa and Y. Iwasawa, in preparation.

# Earth & Planetary Science

A number of studies related to Earth and Planetary Science have been successfully conducted at different beamlines at SPring-8, using various techniques combined with the brilliant photon sources. These include high pressure mineral physics using both large-volume multianvil devices and diamond anvil cells (DAC), crystal structure analyses of minute synthetic and natural minerals, X-ray spectroscopic chemical analyses, etc. Here, two studies on phase transitions under very high pressures using DAC are reported using different light sources in the IR and undulator beamlines. The former (Shinoda *et al.*) study found a new phase transition in $Mg(OH)_2$ accompanied by a change in the proton state in its crystal structure, while the latter (Ono *et al.*) first demonstrated the tetragonal-orthorhombic phase transition in $SiO_2$ at high pressure and high temperature. These successful results are indeed due to highly brilliant and small beams available at SPring-8, as the sample volume in DAC is extremely limited. Another interesting result is reported by Tsuchiyama *et al.*, who applied an X-ray CT technique to tiny chondrules (spherical inclusions present in some meteorites) and first revealed their three dimensional shapes without destroying the surrounding host material. They discuss the dynamic aspects of the chondrules when they were crystallized from liquid droplets and also speculate on the environments where they originated, on the basis of analyses of the observed shapes. Thus the various techniques combined with the third-generation photon source expand the frontiers of new research in Earth and Planetary Science at SPring-8.

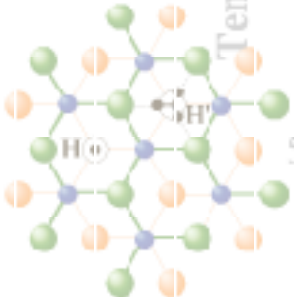

*Tetsuo Irifune*

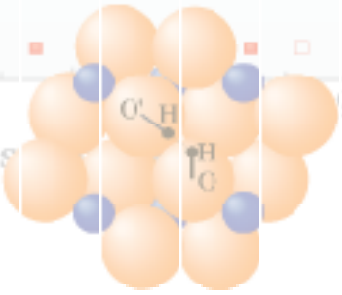

# High Pressure Phase Transition and Behavior of Proton in Brucite $Mg(OH)_2$

Various kinds of OH-related chemical species are included even in nominally anhydrous minerals. Even if there is a small amount of hydrous component in minerals, OH affects the physicochemical properties of minerals during geological reactions. Investigation of OH in minerals is an important theme for earth science.

The major geological reactions occur under conditions of high temperature and high pressure deep under the surface of the Earth, such as at the lower crust and mantle. From the interests of the behavior of OH or protons in minerals under conditions of high temperature and high pressure, infrared (IR) microspectroscopy with a high temperature diamond anvil cell (HTDAC) is a useful method to investigate a small quantity of hydrous components and the behavior of protons in minerals.

The crust and mantle of the Earth consist of rocks of which the chemical components are chiefly Si, Mg and O. Magnesium hydroxide $Mg(OH)_2$ (mineral name: brucite) is a prototype of hydrous magnesium silicates because of its simple chemical composition and crystal structure. The behavior of brucite under high temperature and high pressure has been widely studied by X-ray and neutron diffraction and Raman and IR spectroscopy. In this article, we report on the IR absorption spectra of brucite under conditions of high temperature and high pressure, measured with an HTDAC and an IR microscope at beamline **BL43IR** [1].

A lever-type and externally heating HTDAC was settled on a pulse stage of 1 μm steps under the IR microscope of BL43IR. The ruby fluorescence technique was used for measuring pressure at an elevated temperature. A thermo-couple located very closely to a diamond was used for measuring temperature. Fluorocarbon fluid (Fluorinert) was used as a pressure transmitting medium. A rhenium gasket of 250 μm thickness was preindented and drilled with a YAG laser (1064 nm ). The IR spectra were measured with an $LN_2$ cooled InSb detector and a Bruker FTIR IFS 120 HR under the conditions of 4 $cm^{-1}$ resolution and 512 scans. A natural clear single crystal of brucite from Zimbabwe was prepared. Two series of experiments using (001) platelet sample were carried out. The sample was pressurized at 25 ℃, and no further pressure was applied during the heating of the sample. Because of thermal expansion of HTDAC including pressure transmitting medium, the internal pressure was increased by heating with a fixed load.

The crystal structure of brucite is a $CdI_2$ type structure with $MgO_6$ octahedral layers (brucite layer) stacked along the c-axis and the OH dipole oriented normal to the brucite layers (Fig.1).

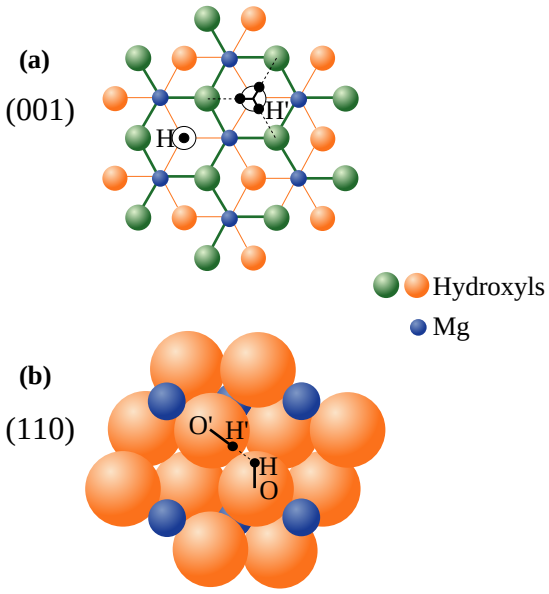


*Fig. 1. Schematic crystal structure of brucite.* ***(a)*** *shows (001) view of brucite layer where an upper and lower hydroxyls are thick and thin lines.* ***(b)*** *shows a (110) horizontal view of layers. The original OH dipole is vertical to a brucite, and represented as an O-H dipole. The O'-H' dipole indicates a pressure induced OH dipole in brucite.*

Although X-ray studies showed no phase transition involving Mg-O substructure under high pressure up to 30 GPa, a pressure induced IR absorption peak at 3650 $cm^{-1}$ was observed at 10 GPa in a DAC study [2]. Shinoda & Aikawa [3] also observed the pressure induced absorption peak by DAC and polarized IR spectroscopy, and assigned it to a new OH dipole under pressure, suggesting that a phase transition of brucite involved only protons.

Figure 1 shows a schematic drawing of a new proton site of brucite under pressure. Figure 2(a) shows the IR absorption spectra of a (001) platelet single crystal of brucite from 0.1 MPa, 25℃ to 8.2 GPa, 220 °C. An absorption peak of the original OH dipole is observed at 3700 $cm^{-1}$ under 0.1 MPa, 25 °C. A pressure induced absorption peak appeared at 3650 $cm^{-1}$ over 3 GPa at 25 ℃. The sample was pressurized up to 3.6 GPa and heated. Absorbance of the pressure induced peak increased on compression and decreased on heating. The position of the pressure induced peak shifted to a lower wavenumber on compression, suggesting enhanced hydrogen bonding between an OH dipole and the neighboring O. In heating, the pressure induced peak continued to be observed at 7.7 GPa, 160 ∝℃ and disappeared at 8.2 GPa, 200 ℃. After cooling, the internal pressure remained at 7.9 GPa and the intense pressure induced peak appeared again.

Figure 2(b) shows IR absorption spectra up to 16.5 GPa, 360 ℃. In the higher pressure region, the pressure induced peak was observed at the higher temperature. The pressure induced peak can be observed under 320 ℃ 16.3 GPa, it then disappeared at 340 ℃ 16.0 GPa. The tiny peaks at 16.5 GPa 360 °C are interference fringes between culet faces of diamonds. After cooling, pressure remained at 17.6 GPa and the intense pressure induced peak appeared again (17.6 GPa, 23 °C). After depressing, the pressure induced peak disappeared and the original peak still remained.

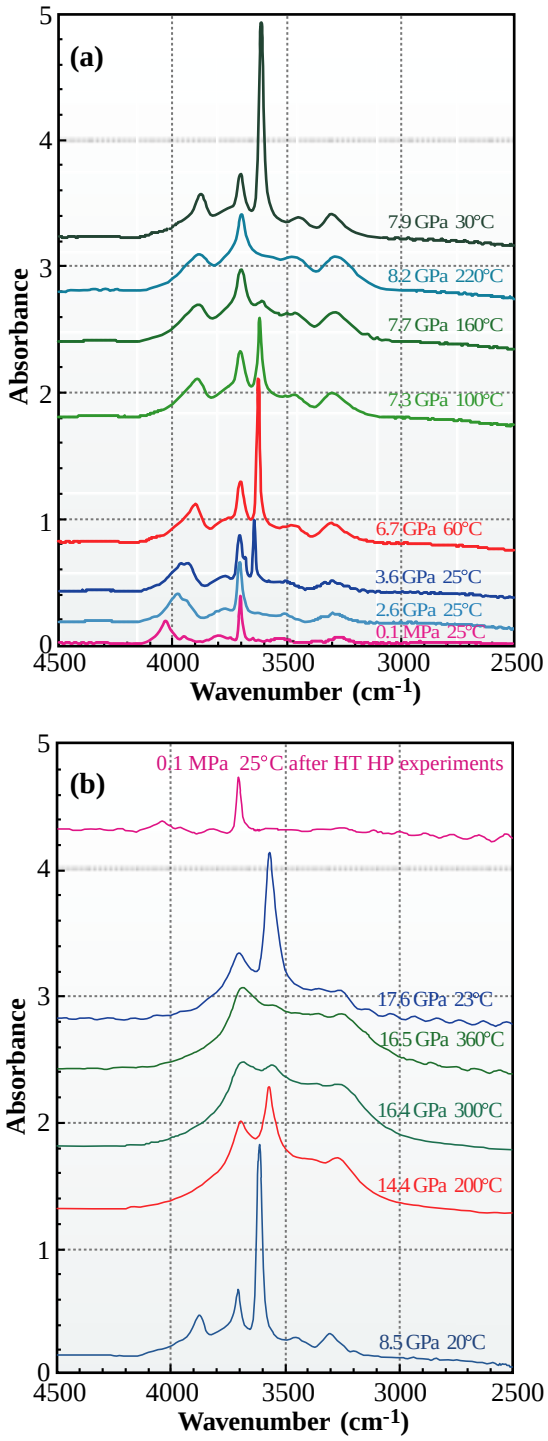


*Fig. 2. IR absorption spectra of (001) platelet single crystal of natural brucite from Zimbabwe up to 8.2 GPa 220 ℃ **(a)**, and 16.5 GPa 360 ℃ **(b)**. An absorption peak at 3700 $cm^{-1}$ is due to the original OH stretching motion and the pressure induced peak appears in the lower wavenumber side of the original.*

As shown by the *in-situ* observations, the onset of the pressure induced peak is a reversible and unquenchable phenomenon and indicates a high pressure phase transition involving a new proton site. The formation process of the new OH dipole can be proton transfer between brucite layers. At ambient pressure, there is no interaction between the OH in a brucite layer and the O' of the next layer. By compression, the O···O' distance is shortened, and the energy levels of two neighboring OH groups overlap.

The activation energy of proton transfer to adjacent oxygen is lowered by shortening the O···O' distance proton transfer is enhanced, and the resultant O'H' dipole is formed by proton transfer between donor OH and the nearest neighboring acceptors O' (Fig. 1).

In Fig. 3, solid circles and squares show the presence of the pressure induced peak, and the open ones do not show the presence of the pressure induced peak. Therefore, a boundary between the open and solid marks in Fig. 3 must be a phase boundary of brucite. The two proton state is stable in the high pressure region [4].

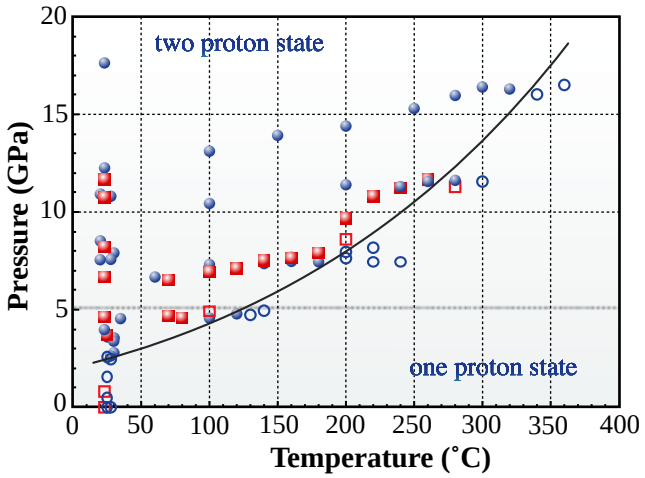


*Fig. 3. The circles and squares represent two series of HT and HP experiments with (001) platelet single crystals of brucite. The points where the pressure induced peak was observed are represented by solid marks and the open ones show points where there was no pressure induced peak. A thick line indicates a phase boundary of brucite between the two proton and one proton states.*

Keiji Shinoda

Osaka City University

E-mail: shinoda@sci.osaka-cu.ac.jp

**References**

[1] S. Kimura *et al.*, Nucl. Instrum. Meth. **A** (2001) 893.

[2] M.B. Kruger *et al.*, J. Chem. Phys. **91** (1989) 5910.

[3] K. Shinoda and N. Aikawa, Phys. Chem. Minerals **25** (1998) 197.

[4] K. Shinoda, M. Yamakata, T. Nanba, H. Kimura, T. Moriwaki, Y. Kondo, T. Kawamoto, N. Niimi, N. Miyoshi, N. Aikawa, Phys. Chem. Minerals (2002) - in press.

# Phase Boundary of Silicon Dioxide $SiO_2$ under High-pressure and -temperature Determined by *In Situ* DAC Laser Heating Technique

The physical properties and structural evolution of silicon dioxide ($SiO_2$) at high pressure and high temperature have attracted attention in geophysical science because silicon dioxide is a primary component of minerals in the interior of the Earth. The mantle of the Earth consists of mostly $SiO_2$, MgO, FeO, $Al_2O_3$, and CaO components. Therefore, there is a possibility that $SiO_2$ plays key role in the structure and dynamics of the Earth's mantle. The possibility of a pressure-induced tetragonal-orthorhombic (*$P4_2/mnm$-Pnnm*) phase transition in $SiO_2$ was suggested by crystal chemical arguments [1]. The transition occurs in the vicinity of 50 GPa at room temperature and has now been investigated from both experimental [2,3] and theoretical perspectives [4,5]. Although detailed knowledge has been accumulated on the high-pressure behavior of $SiO_2$, most studies have been limited to room temperature. The second-order tetragonal-to-orthorhombic transition at high pressure and high temperature has been studied in $GeO_2$ [6], which is regarded as an analogue of $SiO_2$. *In situ* observation at high pressure and high temperature is required to determine the phase boundary of the high-pressure phases, because the orthorhombic phase in $SiO_2$ is unquenchable, converting to the tetragonal phase on decrease of temperature and release of pressure.

An *in-situ* X-ray diffraction measurement system under high pressure and temperature with use of a diamond anvil cell (DAC) apparatus has been set up at beamline **BL10XU** [7]. The samples were heated with a multimode continuous wave Nd:YAG laser using double-sided laser heating techniques, which minimized the temperature gradients of the heated area. The sample temperature was measured from one side of the sample using the spectroradiometric method. The heated samples were probed by angle-dispersive X-ray diffraction technique. The incident X-ray beam was

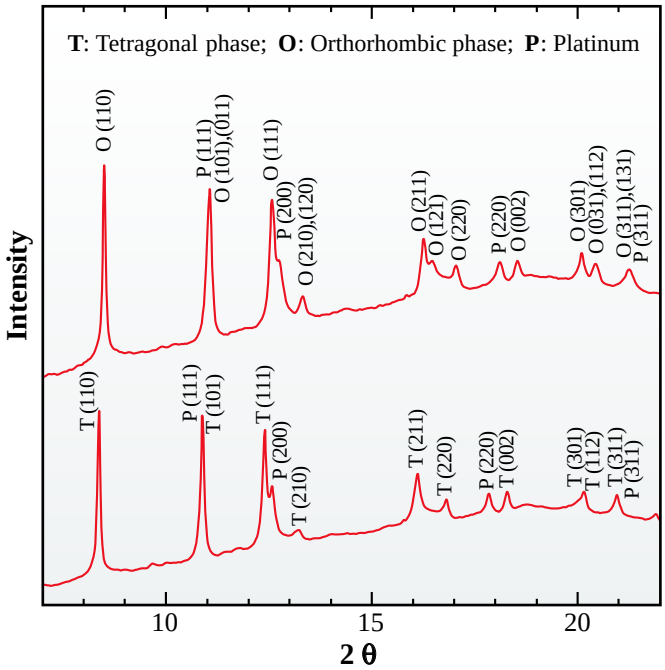


*Fig. 1. X-ray diffraction patterns for silicon dioxide phases using angle-dispersive technique with DAC experiments.*

monochromatized to wavelength of 0.4127 Å. The X-ray beam size was collimated to 16 - 20 μm diameter. Pressure was determined from the measured unit cell volume of platinum using the equation of state for platinum mixed with the sample.

We conducted two runs at pressures between 45 to 92 GPa and at temperatures between 300 K to 2200 K. The typical diffraction patterns of the tetragonal ($P4_2/mnm$) and the orthorhombic ($Pnnm$) phases are reproduced in Fig. 1. The changes from double peaks in the orthorhombic phase (*211-121* and *301-031*) to single peaks in the tetragonal phase indicated that the orthorhombic phase transformed to the tetragonal phase. Our determinations of the tetragonal and orthorhombic stability fields are summarized in Fig. 2. Zhang *et al.* [8] reported that an equilibrium phase boundary between coesite (monoclinic) and stishovite (tetragonal) of $SiO_2$ at about 10 GPa could not be determined below 1273 K because of the kinetics of the phase transition. However, the second-order phase transition between the tetragonal and orthorhombic phases in $GeO_2$ occurs without pressure and temperature hysteresis [6]. Therefore, it was possible to determine the phase boundary between the tetragonal and orthorhombic phase of $SiO_2$ at low temperature in this study.

Shigeaki Ono

Japan Marine Science & Technology Center

E-mail: sono@jamstec.go.jp

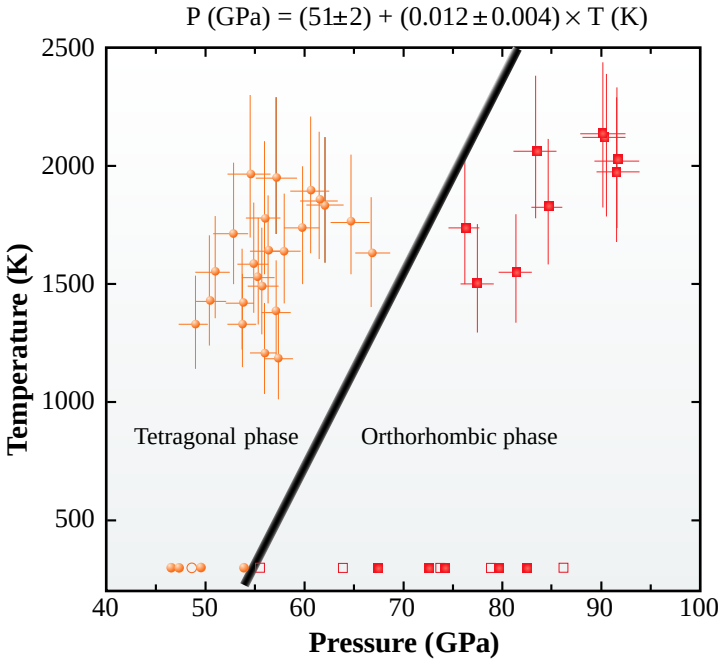


*Fig. 2. The experimental results and a phase boundary determined by in situ observation. The solid circles and squares represent conditions where the tetragonal and orthorhombic phases were stable [9]. The open symbols represent data from Andrault et al. [3]. The solid line is the inferred phase boundary between the tetragonal and orthorhombic phases in silicon dioxide.*

**References**

[1] L. Nagel and M. O'Keeffe, Mateer. Res. Bull. **6** (1971) 1317.
[2] K. J. Kingma *et al.*, Nature **374** (1995) 243.
[3] D. Andrault *et al.*, Science **282** (1998) 720.
[4] C. Lee and X. Gonze, J. Phys. Condens. Matter **7** (1995) 3693.
[5] D. M. Teter and R. J. Hemley, Phys. Rev. Lett. **80** (1998) 2145.
[6] S. Ono, K. Hirose, N. Nishiyama and M. Isshiki, Am. Mineral. **87** (2002) 99.
[7] T. Watanuki *et al.*, Rev. Sci. Instrum. **72** (2001) 1289.
[8] J. Zhang *et al.*, Phys. Chem. Mineral. **23** (1996) 1.
[9] S. Ono, K. Hirose, M. Murakami and M. Isshiki, Earth Planet. Sci. Lett. **197** (2002) 187.

# Three-dimensional Structures of Chondrules: their Motions in the Primordial Solar Nebula

Chondrules are characteristic constituents in primitive meteorites, or chondrites. These tiny spherical objects (0.1 to a few mm in diameter) are mainly composed of silicates with minor amounts of metallic iron and/or iron sulfide. Chondrules were formed in the primordial solar nebula about 4.5 billion years ago prior to the formation of the Earth. They were once molten due to the instantaneous heating of solid precursors and cooled rapidly. In order to elucidate their origin and obtain information on the solar nebula, many researchers have examined chondrules extensively using different methods. However, their three-dimensional structures have not been thoroughly investigated so far. X-ray computed tomography (CT) can give information about the internal structure without damaging the samples and provide 3-D structures by stacking successive sliced images. In SPring-8, a micro X-ray CT system has been developed (Fig. 1) [1-2]. The major advantages of an X-ray CT system using SR are (i) high resolution 3-D images due to the well-collimated beam and (ii) elimination of CT image artifacts (beam hardening) and qualitative correlation of CT image brightness (CT-value) with linear attenuation coefficient by using a monochromatic beam. We applied this system to the chondrules.

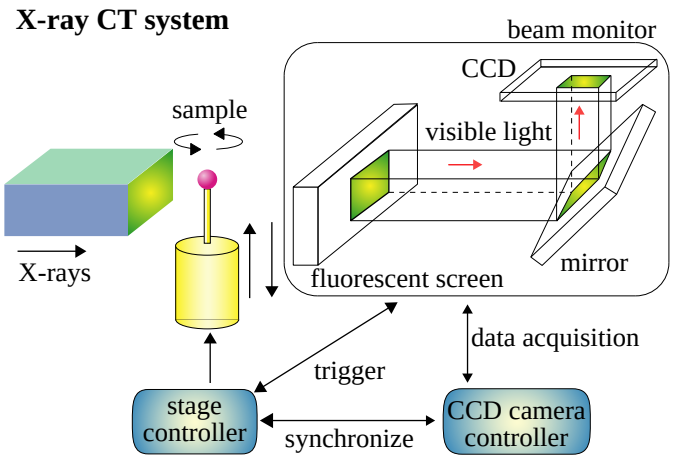


*Fig. 1. A schematic illustration of micro X-ray CT system at BL20B2.*

Chondrules of about 1-2 mm in diameter taken from the Allende meteorite (CV3 chondrite) were imaged at beamline **BL20B2** with monochromatic beams at 17.5 - 25 keV [3]. The cross sectional images (CT images) were reconstructed from 360 projections taken by sample rotation. The 3-D structures were obtained from 150-300 images. The voxel size of 5.83 μm × 5.83 μm × 5.83 μm ("voxel" is an element of 3-D images whereas the term "pixel" is used in 2-D images) gave a spatial resolution of about 13 μm [1]. Figure 2 shows examples of 3-D CT images of the chondrules. We examined both the external shapes and internal structures of the chondrules three-dimensionally using image analysis techniques.

It is known that the chondrules are not perfect spheres. This was discovered by the two-dimensional observation of thin sections. However, their external 3-D shapes have not been described qualitatively. We approximated the shapes of the chondrules as ellipsoids with three different axial radii (a, b and c) [4]. We found that the shapes of the chondrules are diverse from oblate shapes ($a < b \sim c$), general ellipsoids ($a < b < c$) to prolate shapes ($a \sim b < c$) with the aspect ratio of 0.73 - 0.97 (Fig. 3).

Chondrules contain voids as well as metal and sulfide grains. It is hard to recognize voids in thin sections by conventional means because some parts of the samples might be removed when making thin sections. The CT study showed that most of the chondrules have voids (<0.001 - 0.9 vol.%). This shows that voids are an important constituent. Voids in the chondrules may be formed by

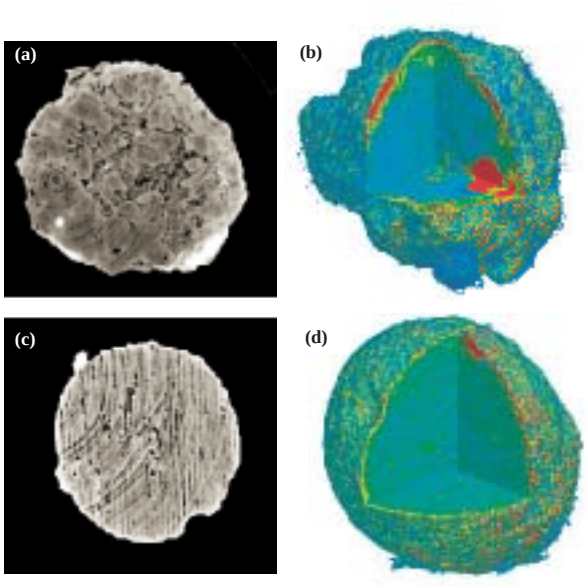


*Fig. 2. Examples of CT images of chondrules and their 3-D structures. **(a)** A CT image of porphyritic chondrule. **(b)** Its 3-D structure. **(c)** A CT image of barred olivine chondrule. **(d)** Its 3-D structure. 3-D images are rendered in pseudo color.*

(i) bubbling of volatile components, (ii) trapping of nebula gas during chondrule formation by instantaneous heating of dust balls or (iii) shrinking of chondrules by solidification. We found that the voids are concentrated along the minor axis of an oblate chondrule [5]. This strongly suggests that the chondrule was spinning during their formation in a molten state and the voids were moved towards the minor axis by centrifugal force. The 3-D distribution of metal and sulfide grains also shows spinning along the minor axes of the oblate chondrules or along the major axes of the prolate ones [4].

Chondrules have different textures, such as porphyritic and barred olivine (BO). In BO chondrules, parallel sets of bar-shaped crystals of olivine ($(Mg,Fe)_2SiO_4$) were observed in thin sections. The CT study showed that BO chondrules consist of parallel sets of thin olivine plates [3]. Interestingly, these BO chondrules are oblate and the normal directions of the olivine plates are almost the same as the minor axes of the oblate chondrules (Fig. 4). If we assume that all BO chondrules are oblate or prolate, we can estimate their 3-D structures from the thin sections two-dimensionally. Statistical observation of BO chondrules in thin sections suggested that the normal directions are nearly parallel to the minor axes of many oblate chondrules or to the major axes of some prolate chondrules. These features may be also explained by the spinning of the chondrules probably because centrifugal force affects the nucleation and crystallization of olivine although no definitive mechanism is known at present.

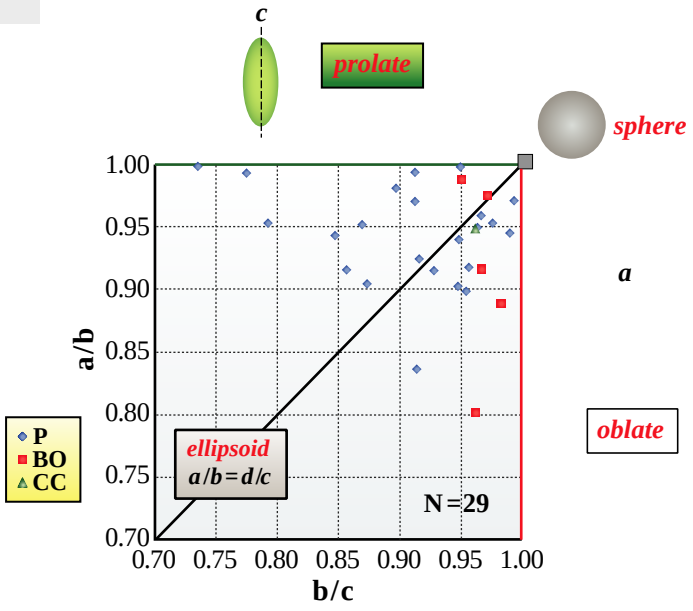


*Fig. 3. Aspect ratios, a/b and b/c, of chondrules. The axial radii, a, b and c, were obtained by ellipsoid fitting for each chondrules. P: porphyritic, BO: barred olivine, CC: crypto crystalline.*

The idea of spinning chondrules leads to important information on chondrule formation and nebula conditions. Prolate chondrules might be formed by aerodynamic drag during molten states. The major axis should correspond to the rotation axis and the parallel axis to the direction of movement, like a volcanic bomb or a flying football. If this is the case, the presence of prolate chondrules shows that some dense gas was present in the nebula where the chondrules were formed, or that the relation between the gas pressure and the relative speed of chondrule motion can be estimated from the aspect ratios of the prolate chondrules. On the other hand, we can estimate the spinning rates of the oblate chondrules by considering the balance between the surface tension of droplet chondrules and centrifugal forces by the spinning. The angular velocity of rotation, the equatorial radius of the drop, its density and the interfacial surface tension determines the shape of such rotating droplet. The spinning rate of the chondrules is estimated to be about 50 - 200 rps. Such a high spinning rate favors a specific chondrule formation process, such as rotation by drag heating of irregular-shaped dust balls by a shock wave or collision of small heavenly bodies.

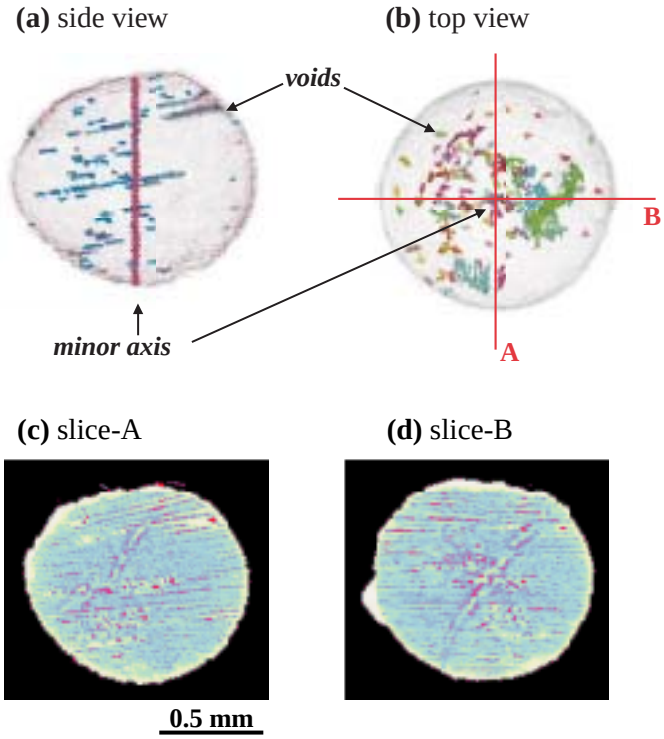


*Fig. 4. 3-D structure of a barred olivine chondrule. Rendered in pseudo color. **(a)** A side view of the oblate chodrule. **(b)** A top view of the oblate chodrule. **(c)** A sliced image along A-direction. **(d)** A sliced image along B-direction. Individual voids are shown as different colors in **(a)** and **(b)**. A parallel set of olivine bars (cyan) is seen in **(c)** and **(d)**.*

Akira Tsuchiyama[a], Tsukasa Nakano[b] and Kentaro Uesugi[c]

(a) Osaka University
(b) Geological Survey of Japan, AIST
(c) SPring-8 / JASRI

E-mail: akira@ess.sci.osaka-u.ac.jp

**References**

[1] K. Uesugi *et al.*, Proc. SPIE **3772** (1999) 214.
[2] K. Uesugi *et al.*, Nucl. Instrum. Meth. Phys. Res. **A 467-468** (2001) 853.
[3] A. Tsuchiyama *et al.*, Lunar Planetary Sci. **XXXI** (2000) 1566.
[4] Shigeyoshi *et al.*, Abstr. 2001 Fall Meeting Jpn. Soc. Planet. Sci. (2001) 113 (in Japanese).
[5] A. Tsuchiyama *et al.*, Lunar Planetary Sci. **XXVIII** (1997) 1453.

# Environmental Science

We desperately need good tools to find ways to recover the Earth filled with a polluted atmosphere, water, and soil, and people who have suffered damage by this unhealthy environment. Of course, SPring-8 is open to those who are struggling with an environment which has been destroyed. Some of the important results recently obtained in SPring-8 concerning very practical purposes rather than purely basic science are presented here.

Takaoka, Yamamoto and Tanaka applied the XAFS method to dilute samples. They found that the ash from waste incinerators contains various metallic elements and that some of the chemical forms were of those catalysts active in forming dioxin, one of the most poisonous chemicals ever made by man. Since the compositions and the chemical forms of the waste depend upon the various conditions under which the incinerator is operated, their study is expected to suggest the design and operation of an improved incinerator.

Hayakawa and Tohno installed an X-ray microscope in BL39XU station. The microscope is able to produce element maps on a section of thin (sliced) samples and also an XAFS spectrum for a small area on the sample. They demonstrated that their microscope detected elements of femtogram levels in a very small aerosol. Such information on elemental constituent and the XANES spectrum should be used to identify the origin of the aerosol particle and predict its influence upon the environment.

Takagawa and Hayakawa further extended the use of the microscope to biological samples. One of the biggest tragedies our county ever encountered is that many people lost their lives or became handicapped by what is believed to be intake of cadmium-contaminated rice, a disease known as *itai-itai* (very painful) disease. The microscope was used to visualize the Cd distribution in kidney, the organ most damaged by the disease. The technique is also proved to be useful in the detection of mercury, which is known to be the key element for *Minamata* disease. Thus, this is a powerful weapon to fight against diseases caused by the contamination of environment.

*Iwao Watanabe*

# Direct Speciation of Copper, Lead, Antimony, Zinc and Chromium in Municipal Solid Waste Incinerator Fly Ash by X-ray Absorption Fine Structure Spectroscopy

In Japan, about 50 million tons of municipal solid waste (MSW) are generated every year and more than 75% of MSW is incinerated. MSW incineration is an excellent technology from the viewpoint of the weight and volume reduction of MSW and public sanitation. However, approximately 100 kg of bottom ash and 30 - 50 kg of fly ash are generated when 1 ton of MSW is incinerated. Fly ash contains many toxic substances, various heavy metals and dioxins. It is usually detoxified and disposed in landfills. It is necessary to verify whether the chemical state of heavy metal changes into an insoluble state.

Furthermore, the formation of chlorinated aromatic compounds from an MSW incinerator (MSWI) is known to occur on the surface of fly ash [1]. Some heavy metals act as catalysts. Catalytic activities differ according to the kinds of heavy metal and its species. To evaluate the formation of chlorinated aromatic compounds on fly ash, it is necessary to examine the species of heavy metal in fly ash. Therefore, in this research, direct speciation of copper, lead, antimony and zinc in fly ash taken from the MSWI was conducted using X-ray absorption fine structure spectroscopy (XAFS).

The speciation of fly ash and the content of target elements are presented in Table I. Fly Ash 1 and 3 were sampled from the electrostatic precipitators in different continuous stoker-type MSWIs respectively. Fly Ash 2 was sampled from the bag filter in a continuous stoker-type MSWI. Fly Ash 4 was sampled from the bag filter in an ash melting plant. Fly Ash 2 and 4 contain large quantities of calcium compounds, because calcium hydroxide is injected before the bag filter for acid gas removal. The XAFS measurements were carried out at beamline **BL01B1**. The spectra were collected in fluorescence mode at room temperature with an Si(111) or Si(311) monochromator. The detailed procedure of data reduction has been described elsewhere [2].

Copper is the most active in the formation of dioxin among heavy metal catalysts. Figure 1 shows Cu *K*-edge XANES spectra of four kinds of fly ash and reference materials. According to the position of Cu *K*-edges, Cu(I) the compounds were considered to be contained in MSWI Fly Ash 1 - 3. In the Fly Ash 4 from an ash melting plant, the pre-

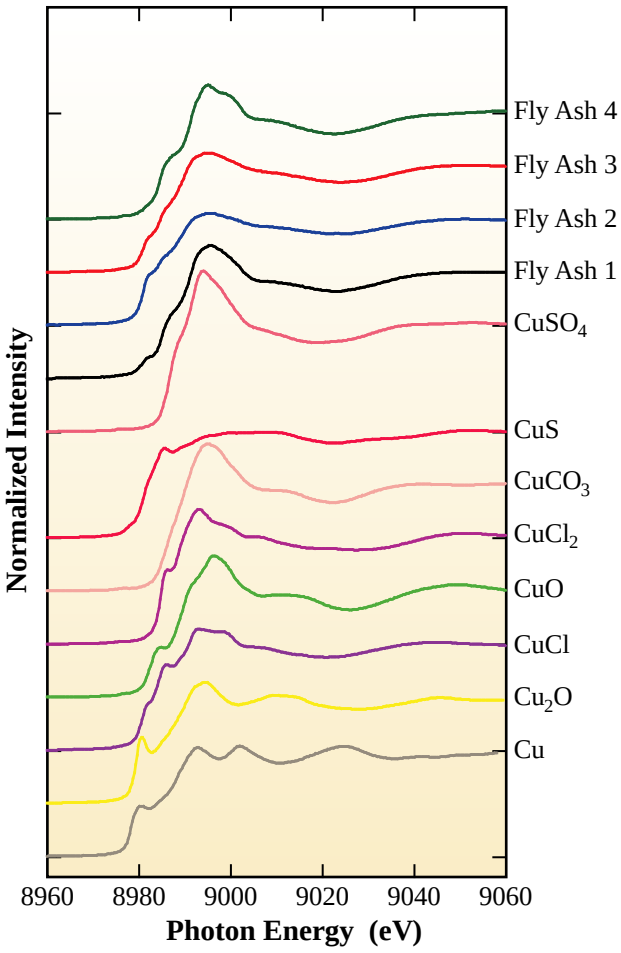


*Fig. 1. Cu K-edge XANES spectra in fly ash and reference materials.*

edge peak from the 1*s* - 3*d* transition appeared at 8976 eV and the chemical state of copper was estimated to be only Cu(II) compounds. The copper in fly ash was mainly estimated to be a mixture of $CuCl_2$, CuO and Cu(I) compounds by the XANES spectra. Figure 2 shows $k^3$-weighted EXAFS spectra for four fly ash and reference materials. According to the EXAFS spectra, the fly ash samples were classified into two patterns. As the wave number increased, the EXAFS spectra became ambiguous in Fly Ash 2 and 3 but clear in Fly Ash 1 and 4. The EXAFS spectra indicated that a Cu-Cl bond existed in Fly Ash 2 and 3 in comparison with those of reference materials. On the other hand, the dioxin concentrations in Fly Ash 1 - 4 are 1.5, 6.7, 6.2 and 3.5 ng-TEQ/g, respectively. Dioxins have 210 isomers. Of the various isomers of dioxins, 17 isomers carrying chlorine atoms at the 2-, 3-, 7-, 8-positions are particularly toxic. Therefore, toxicity equivalency conversion is conducted to obtain a total measure of the toxicity of the mixtures of many isomers. The factor called toxic equivalent factor indicates the relative toxicity referring to 2-, 3-, 7-,8-tetrachlorinated dibenzo–p-dioxin as a standard to yield toxic equivalent (TEQ) value [3]. The difference of the EXAFS spectra was considered to have a relationship with the dioxin concentration. Namely the Cu compounds in Fly Ash 1 and 4 were deactivated to give them a lower activity for the formation of dioxin than those in Fly Ash 2 and 3.

As for other heavy metals, lead was mainly estimated to be $PbCl_2$ in MSWI Fly Ash 1 - 3 and PbO in ash melting plant Fly Ash 4 by Pb $L_{III}$-edge XANES spectra. The same results were also suggested from the EXAFS spectra. According to Zn *K*-edge XANES spectra, the peak shape of Fly Ash 2 was very similar to that of Fly Ash 3. Whereas, that of Fly Ash 4 was different from the others and the peak position shifted to higher photon energy. Zinc was mainly estimated to be $ZnCl_2$ in MSWI Fly Ash 1-3 and the mixture of $ZnCO_3$, ZnO and $ZnCl_2$ in ash melting plant Fly Ash 4. There was no difference in the Sb *K*-edge XANES spectra among the measured fly ash. Antimony in the fly ash was considered to be Sb(V)

**Table I**. The specification of fly ash and concentrations of target elements.

| Sample | Fly Ash 1 | Fly Ash 2 | Fly Ash 3 | Fly Ash 4 |
|---|---|---|---|---|
| Operation | Continuous | Continuous | Continuous | Continuous |
| Furnace type | Stoker | Stoker | Stoker | Coke bed type ash melting furnace |
| Dust collector | ESP | BF | ESP | BF |
| Acid gas removal | | $Ca(OH)_2$ injection | Wet scrubber | $Ca(OH)_2$ injection |
| Cu (mg/kg) | 1900 | 1700 | 3000 | 1500 |
| Pb (mg/kg) | 8200 | 11000 | 13000 | 15000 |
| Zn (mg/kg) | 34000 | 25000 | 29000 | 38000 |
| Sb (mg/kg) | 1800 | 1200 | 1400 | 940 |
| Dioxins (ng-TEQ/g) | 1.5 | 6.7 | 6.2 | 3.5 |

ESP: electrostatic precipitator, BF: bag filter, TEQ: toxic equivalent

compounds. The EXAFS spectra indicated that antimony combined not only with oxygen but also with chlorine.

From this research, we were able to obtain the information about the species of heavy metals and suggest the relationship between dioxin concentrations and chemical states of copper compounds in actual Fly Ash [4].

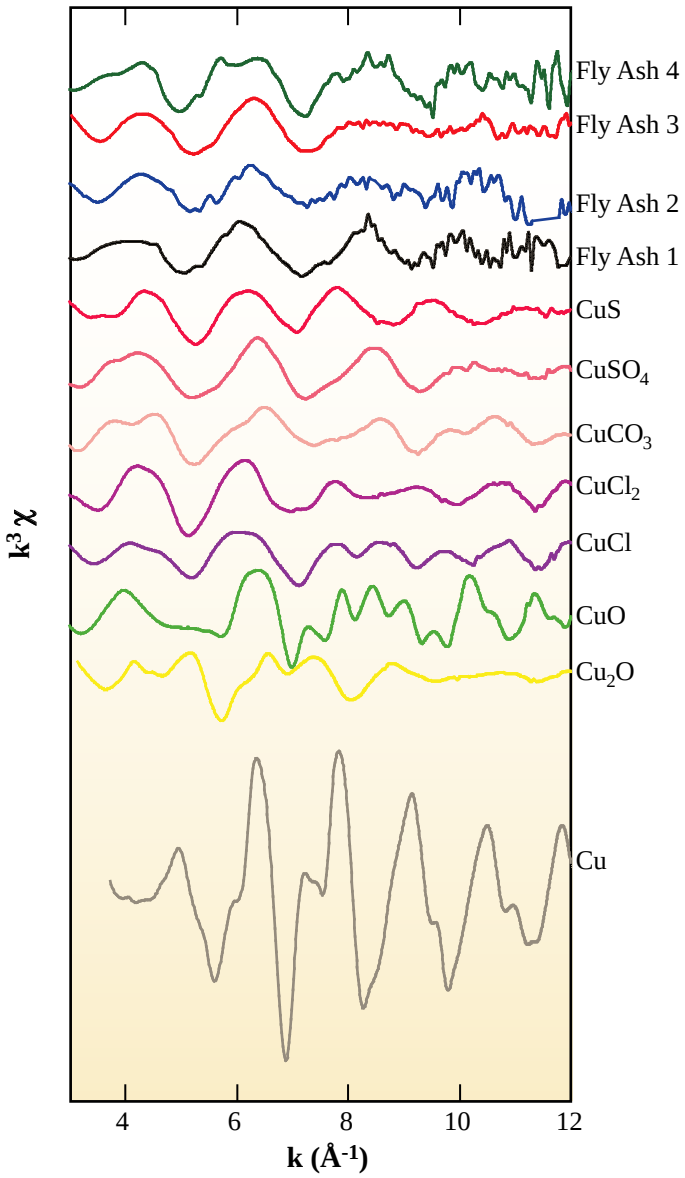


*Fig. 2. EXAFS spectra of Cu in fly ash and reference materials.*

Masaki Takaoka, Takashi Yamamoto and Tsunehiro Tanaka

Kyoto University

E-mail: takaoka@epsehost.env.kyoto-u.ac.jp

**References**

[1] L.Stieglitz *et al.*, ISWA 88 Proc. of 5th Int. Solid Wastes Conf. **1** (1988) 331.

[2] T. Tanaka *et al.*, J. Chem. Soc. Farad. Trans. **84** (1988) 2987.

[3] M. Van den Berg *et al.*, Environmental Health Perspectives **106** (1998) 775.

[4] Masaki Takaoka, Nobuo Takeda, Tsunehiro Tanaka, Takashi Yamamoto, Proc. of the 12th Annual Conference of The Japan Society of Waste Management Experts (2001) 875.

# Trace Characterization of Individual Aerosol Particles using an X-ray Microprobe

The elemental compositions of atmospheric aerosols are related both to their origin (source) and with physical and chemical processes during transportation. Therefore, the analysis of individual aerosol particles has been received great interest in terms of source apportionment and estimation of transformation reactions, etc . An electron probe micro-analyzer (EPMA) has been utilized for this purpose [1]. However, owing to the significant background beneath the signal, the detectable elements are limited to the major components. A combination of a newly installed X-ray microprobe and X-ray fluorescence (XRF) detection has realized trace quantification down to fg (femtogram ) level and chemical state diagnosis using XANES (X-ray absorption near edge structure) spectra has become possible. Some new possibilities for discovering the history of individual aerosol particles are under discussion.

Figure 1 shows the experimental layout around the specimen. A pair of elliptical mirrors (Kirkpatrick and Baez mirror, KB mirror) were installed at beamline **BL39XU**. Its effective aperture is approximately 150 × 150 μm$^2$, and Rh coated mirrors cover X-rays up to 18 keV. The preliminary experimental results show a focal spot down to 2 μm(V) × 4 μm(H) with the photon flux more than 1× 10$^{10}$ photons/s for monochromatized 10 keV X-rays [2]. A sample was mounted on the XY scanning stage, and XRF from the sample was detected with a conventional Si(Li) detector. To avoid an excessive counting rate, a sample-detector distance of 100 mm was used. The minimum detection limit (MDL) of the XRF analysis was evaluated with a series of thin metal films deposited onto the Kapton foils of 10 μm in thickness, and the evaluated MDL was 0.3 fg for Ni using 10 keV X-ray microbeam.

Coarse and fine fractions of aerosols were collected separately in two-stage filterpacks (8 and 0.4 μm Nuclepore filters) with a 50% effective cutoff diameter of 1 μm. Sampling was conducted at the Uji campus of Kyoto University during the Asian dust storm (Kosa) event. A coarse fraction of the

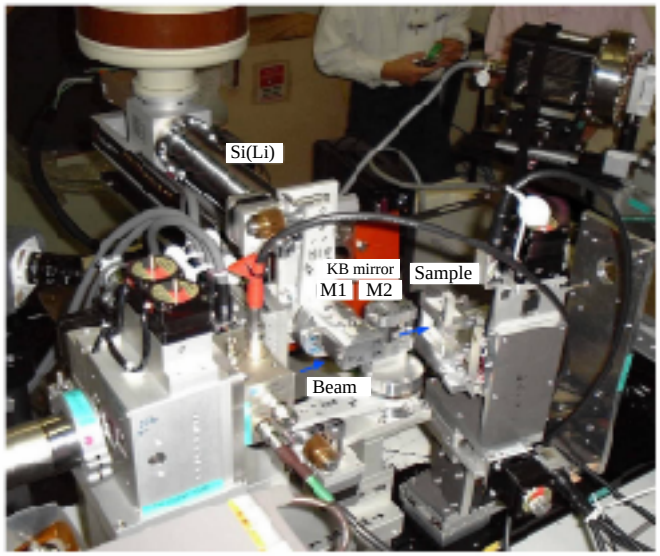


*Fig. 1. Experimental setup for the X-ray microprobe.*

collected aerosol particles was subjected to XRF measurement.

Figure 2 shows an Fe XRF image of the aerosol particles obtained with a 10 keV X-ray microbeam. Black points represent particles which give strong Fe signals. The sizes of the large particles were evaluated from a cross section of the Fe XRF image, and the sizes of the particles less than the beam size were estimated from the Fe signal on the assumption that the portion of the Fe composition was the same among the particles.

Figure 3 shows micro-XANES (X-ray absorption near edge structure) spectra of aerosol particles marked on an Fe image, (a) and (b) in Fig. 2. The XRF yield method was used to obtain these spectra. The XANES spectrum obtained for particle (b) is identical to that of hematite $Fe_2O_3$, and most of the other particles gave similar spectra. Chemical shifts in the absorption edge between the spectra of the aerosol particles and those of a reference, Fe thin film show the difference in valence state of Fe, and the Fe in the aerosol particle (a) might be in a divalent state.

Figure 4 shows XRF spectra measured from an individual aerosol particles. The diameter of the particle (a) is estimated to be 10 μm from the cross section of the Fe XRF image. Considering that the matrix of the particle is quartz, the mass of the particle can be estimated to be 1.2 ng from the density of the quartz (2.2 g/cm$^3$). Owing to the atmospheric environment and the rather poor excitation efficiencies for light elements, no peak was observed for S and Cl. However, Ca, Ti, Cr, Mn, Fe, Ni, Cu and Zn were detected. For small particles attenuation of XRF inside the sample can be neglected, and semi-quantitative information can be obtained from a comparison of the XRF signals between the sample and reference thin films previously measured. The absolute amounts of Ca, Ti, Mn and Ni in the particles were estimated to be 220, 120, 110, 17 fg for the particle (a) and 470, 100, 30, 3 fg for the particle (b), respectively [3]. Similarly, semi-quantitative analyses of the particles were carried out for 16 particles on this sample, and the difference of elemental compositions (elemental profiles) was

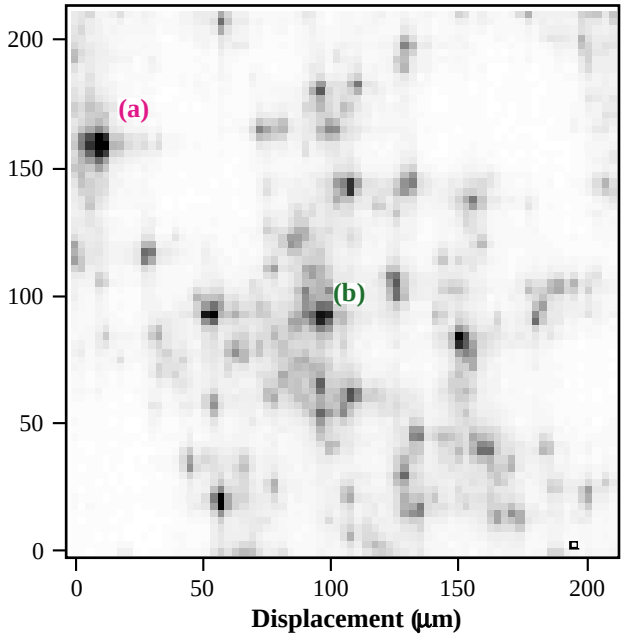


*Fig. 2. Fe XRF image of aerosol particles on a Nuclepore filter. 10 keV X-rays were used for excitation.*

found between the particles. Further interpretations of elemental profiles are being carried out to reveal the origin and the transportation process of individual aerosol particles. Utilizing this unique characteristics of the X-ray microprobe of ultra-high sensitivity, analyses of a single rain drop and a single fog droplet [4] are now in progress.

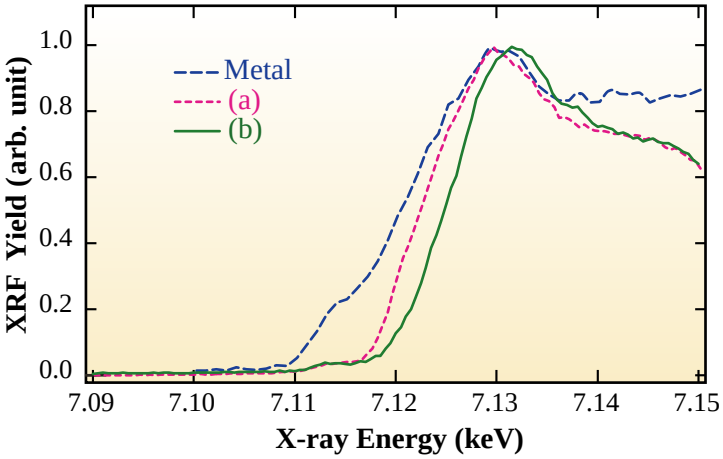


*Fig. 3. Micro XANES spectra from individual aerosol particles marked on the Fe image (see Fig. 2). The reference metal spectrum is imposed in the figure.*

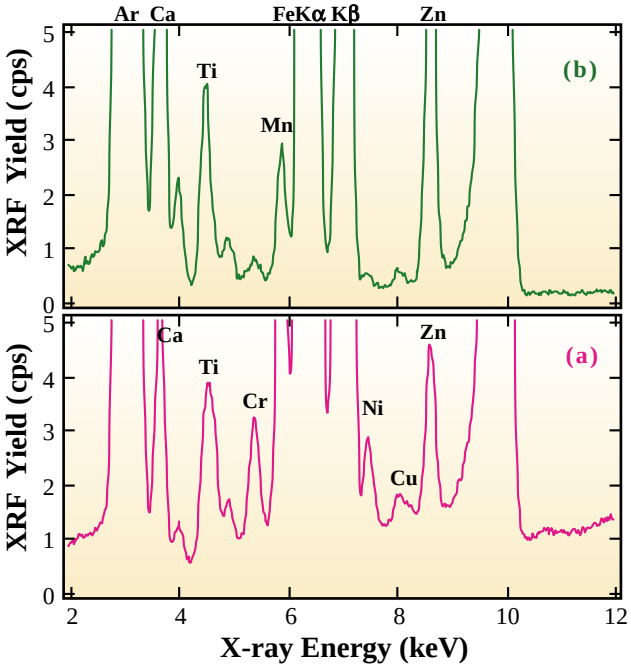


*Fig. 4. XRF spectrum from individual aerosol particles (a) and (b) marked in Fig. 2.*

Shinjiro Hayakawa[a] and Susumu Tohno[b]

(a) Hiroshima University
(b) Kyoto University

E-mail: hayakawa@hiroshima-u.ac.jp

**References**

[1] K. R. Spurny eds., "Analytical Chemistry of Aerosols", Lewis Publishers (1999).

[2] S. Hayakawa *et al.*, J. Synchrotron Rad. **8** (2001) 328.

[3] S. Hayakawa, S. Tohno, K. Takagawa, A. Hamamoto, Y. Nishida, M. Suzuki, Y. Sato and T. Hirokawa, Anal. Sci. 17s (2001) i115.

[4] S. Tohno *et al.*, J. Aerosol Sci. **32** (2001) S873.

# Imaging of Heavy Metal Distribution in Thin Tissue Sections of Itai-itai Disease Kidney and Rat Kidney by X-Ray Fluorescence Analysis

Itai-itai disease is an endemic disease of Toyama prefecture, Japan, and once was a big social problem. It has been claimed that Cd-polluted Jinzu River water caused this disease based on epidemiological studies of patient distribution. However, the pathological contribution of Cd to itai-itai disease is still controversial. The kidney is one of the major organs damaged in itai-itai disease, and it is of great interest to investigate Cd distribution in itai-itai diseased kidneys since it is known that their Cd concentration is lower than that of non-itai-itai-disease kidneys.

On the other hand, the relationship between Hg intoxication and Minamata disease is well established. The proximal urinary tubule of the kidney is one of the target tissues for Hg toxicity, and the precise location in the proximal urinary tubules (segments [1]) sensible for Hg toxicity has

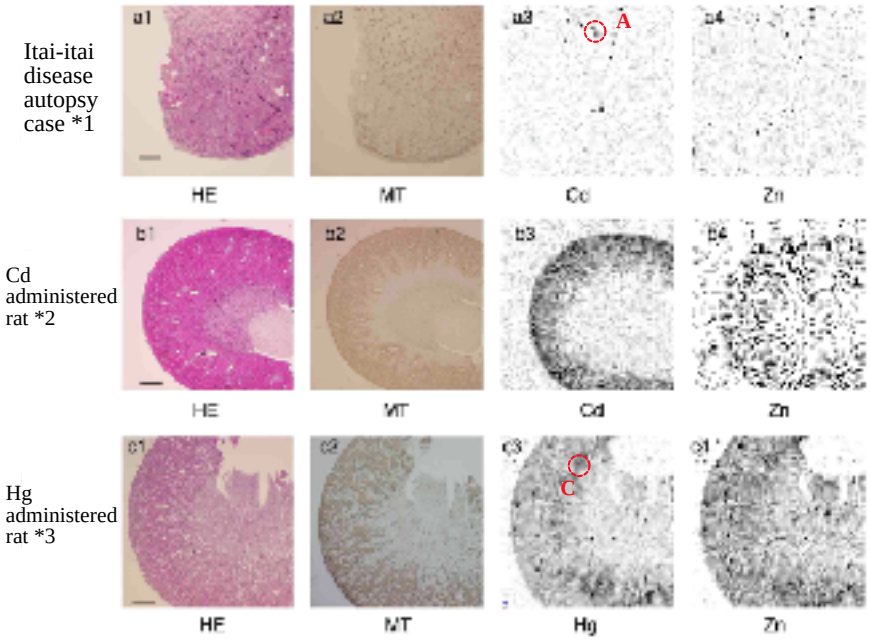


*Fig. 1. Formaline fixed paraffin embedded kidney tissue sections. Section thickness is 3 µm for HE and MT, 6 µm for microbeam X-ray fluorescence (XRF) analysis (Cd, Zn, and Hg). HE=hematoxylin-eosin staining, MT=immunohistochemistry with anti-metallothionein antibody. DAB was used as chromogen (the brown color is the signal). Bar = 1 mm.*
**1 Cd concentration is 16 ppm in the kidney cortex and 13 ppm in the medulla by AAS analysis. XRF: 32 keV X-rays were utilized for excitation. Beam size was approximately 100 µm. The counting time was 2 sec/spot. Spatial resolution is 125 µm/step.*
**2 Young male Wistar rat was used. Cd was administered by intraperitoneal injection of 2 mg Cd/ml $CdCl_2$ solution in distilled water, 2 mg Cd/kg body weight. After eight weeks of breeding with standard laboratory food and water, the animal was sacrificed. Cd concentration is 43 ppm in the cortex, 3 ppm in the medulla by AAS analysis. XRF condition was same as shown in *1 above.*
**3 Young male Wistar rat was used. Hg was administered by intraperitoneal injection of 1 mg/ml $HgCl_2$ solution in distilled water. After the first injection of 1 mg $HgCl_2$/kg body weight, the animal was bred for two weeks, injected with 2 mg $HgCl_2$/kg body weight for the second time, bred for one week, and sacrificed. The Hg concentration is 32 ppm in the cortex, 1.2 ppm in the medulla by AAS analysis. XRF: 13 keV X-rays were utilized for excitation. The beam size was approximately 100 µm. The counting time was 2 sec/spot. Spatial resolution is 125 µm/step.*

been analyzed using dissected nephrons. However, the direct analysis of Hg distribution in Formalin-fixed-paraffin-embedded tissue sections routinely used in histopathological study has not been reported.

So far, it is not possible to visualize Cd distribution in kidney sections by either EPMA or SIMS. Microprobe X-ray fluorescence analysis at beamline **BL39XU** [2] made this possible for the first time [3] (Fig.1 a3). As a positive control, Cd-administered rat kidney was also analyzed (Fig. 1 b3). Pictures of hematoxylin-eosin (HE) stained section and immunohistochemistry with anti-metallothionein (MT) antibody are also shown since Cd is known to exist bound to MT in the kidney (Fig. 1).

For Cd analysis, 32 keV X-rays were utilized for *K*-excitation. In Cd-administered rat kidney, Cd is distributed widely in the cortex (Fig. 1 b3). The distribution pattern of Cd matches well with that of MT, compatible with the biochemical findings suggesting that Cd exists bound to MT in the kidney. The distribution of MT is limited to the epithelium of the proximal urinary tubules, suggesting that segment S1+2 is the main portion of the Cd storage. In itai-itai diseased kidney, the Cd signal is limited to several spots in the medulla while the Cd signal in the cortex is background level (Fig. 1 a3). These spots seem to be corresponding to collecting urinary ducts, which show a strong signal in anti-MT immunohistochemistry (Fig. 1 a2). However, the precise identification of these spots should be carried out in the future since the outline of the kidney structure is not visible and the distribution of MT is wider than that of the Cd spots. The distribution pattern of Zn partially corresponds to that of Cd, suggesting that some part of Zn also exists bound to MT. The XRF spectra measured in spots A and B (blank) are shown in Fig. 2.

As a comparison, distribution of Hg in Hg-administered rat kidney was also analyzed (Fig. 1 c3). Although it is known that the cause of Minamata disease is organic Hg including methyl-Hg, $HgCl_2$ was administered to the rat as a pilot study. In the case of Hg analysis, 13 keV X-rays were utilized for *L*-excitation. Images of Hg and Zn in paraffin embedded tissue section are shown in Fig.1 c3 and c4. In this experiment, a strong Hg deposition was observed in the area between the cortex and the outer medulla, suggesting that segment S3 of the proximal urinary tubule is the main portion of Hg deposition. The distribution pattern of Hg does not correspond to that of MT

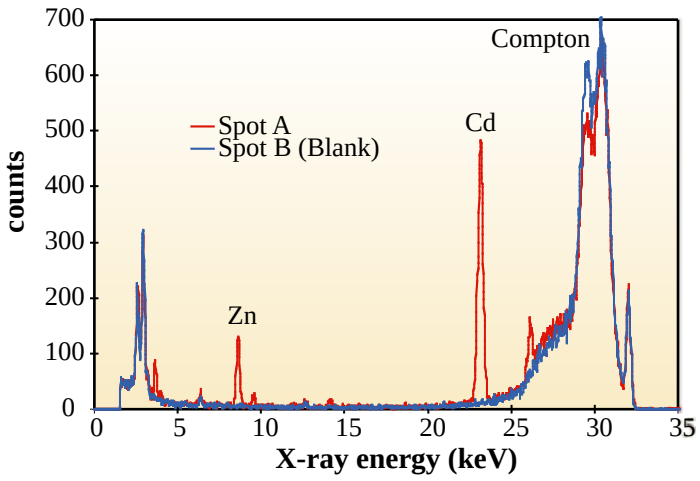


*Fig. 2. XRF spectra measured in spots A and B (blank) in Fig. 1 a3.*

very well, which suggests the existence of other binding proteins for Hg. The XRF spectra measured in spots C and D (blank) are shown in Fig. 3. With this X-ray energy an X-ray microbeam produced with the newly installed Kirkpatrick-Baez mirror system [4,5] was also available. The beam size was 4 μm × 4 μm in this measurement, and Fig. 4 shows the resultant image of a small area around spot C in Fig. 1 c3.

Microbeam X-ray fluorescence analysis is found to be a useful method to analyze heavy metal distribution in thin tissue sections. Distributions of Cd and Hg in paraffin embedded human and rat kidneys were demonstrated for the first time. This method will be an important tool to analyze heavy metal toxicosis, including itai-itai disease and Minamata disease.

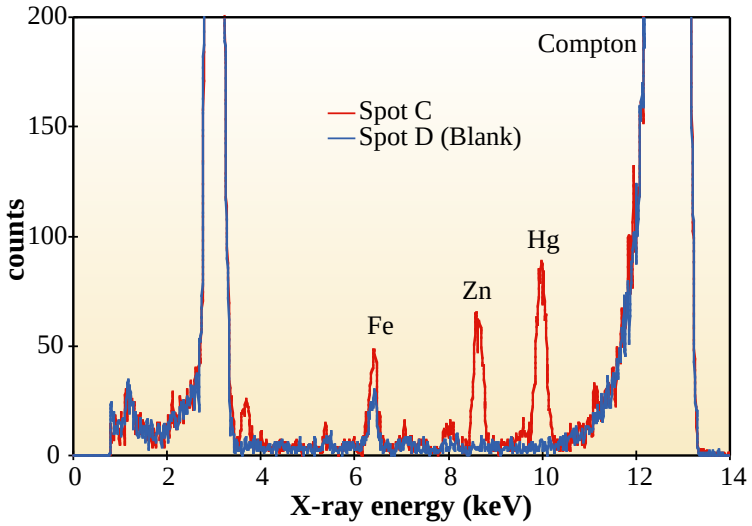


*Fig. 3. XRF spectra measured in spots C and D (blank) in Fig. 1 c3.*

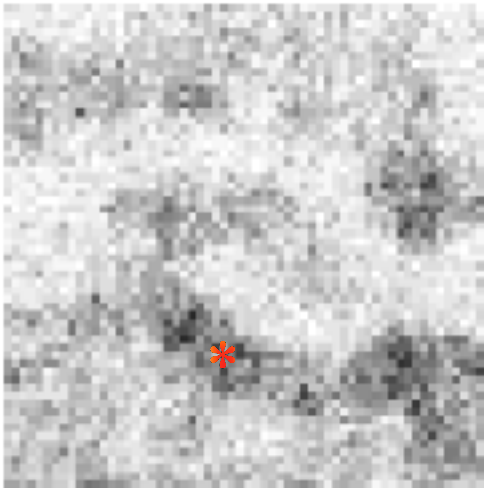

*Fig. 4. Hg imaging of a small area around spot C in Fig. 1 c3. XRF: The energy of X-ray for excitation was 13 keV. The beam size was approximately 4 μm × 4 μm. The counting time was 2 sec/spot. Spatial resolution is 5 μm/step. The signal seems to be located in the epithelium of the urinary tubules since the width of band-like Hg positive area (*) is approximately the same as the diameter of the urinary tubules.*

Kiyoshi Takagawa[a] and Shinjiro Hayakawa[b]

(a) Toyama Medical and Pharmaceutical University
(b) Hiroshima University

E-mail: takagawa@ms.toyama-mpu.ac.jp

**References**

[1] W. Kriz and L. Bankir, Kidney Int. **33** (1988) 1.
[2] S. Hayakawa *et al.*, J. Synchrotron Rad. **5** (1998) 1114.
[3] J. Kawai *et al.*, J. Trace Microprobe Tech. **19-4** (2001) 541.
[4] S. Hayakawa, N. Ikuta, M. Suzuki M. Wakatsuki and T. Hirokawa, J. Synchrotron Rad. **8** (2001) 328.
[5] S. Hayakawa, S. Tohno, K. Takagawa, A. Hamamoto, Y. Nishida, M. Suzuki, Y. Sato and T. Hirokawa, Anal. Sci. - in press.

# INDUSTRIAL APPLICATION

This section consists of four very interesting projects which achieved industrial application at different beamlines in 2000B and 2001A. It is said that the speed of the development of products is increasing every year from the point of view of environmental purification and oil saving. Though many efforts have been made to maintain an atmosphere of a keen competition among industries, it is very difficult to secure an international race. Collaboration between a company and another company, or a company and a university or public institution is the royal road, which offers indispensable information to search out the nature of materials and to rapidly supply interesting products.

Material researchers require a wealth of knowledge and experience to complete work on the products. And they need the power to discover the relations of the character of the materials and the analyzed results.

Now, we have acquired synchrotron radiation facilities which enable us to estimate a sample in a moment, and the results obtained in a experiment will make their way to industrial technology. It is expected that use of these facilities will throw light on unknown regions.

*Tokuhiko Okamoto*

# Structural Study on a Layered Thermoelectric Material: $InGaZnO_4$

Thermoelectric energy conversion is attracting much interest as a possible application for "environmentally friendly" electric-power generators and highly reliable, accurate temperature-controllable refrigerators used as electronic devices. The performance of a thermoelectric device is defined by its material properties through the figure of merit, $ZT = S^2T/\rho(\kappa_e+\kappa_l)$, where $S$ is Seebeck coefficient, $T$ is operating temperature, $\rho$ is resistivity, and $\kappa_e$ and $\kappa_l$ are carrier and lattice thermal conductivities, respectively. Although a thermoelectric material, such as $Bi_2Te_3$, which has a $ZT$ of about 1, is used in particular fields, its performance is still insufficient for wider commercial use. Thus, the development of new materials with large $ZT$ is the one of the main issues in thermoelectric research.

Electronically and structurally two-dimensional (2-D) materials can be good thermoelectrics, because $S$ increases in a 2-D electronic state [1] and $\kappa_l$ is reduced in the 2-D crystal structure. A $YFe_2O_4$-type layered compound, $InGaZnO_4$, is a candidate for 2-D material. It has a 2-D crystal structure, as shown in Fig. 1, with $InO_2$ layers and double $GaZnO_2$ layers. Moreover, calculation of the electronic structure by means of a cluster model predicted that only the $InO_2$ layers provide 2-D electrical conduction, if the z coordinates of Ga and Zn sites are significantly different [2]. However, no experimental results on the local structure around Ga and Zn sites have been reported, though such a structural feature plays a key role in understanding the electrical structure of $InGaZnO_4$. We have, thus, studied the crystal structure of $InGaZnO_4$ to discuss the 2-D electronic and structural properties by using synchrotron radiation X-rays.

A powder sample of $InGaZnO_4$ was prepared by solid-state reaction. X-ray powder diffraction data were collected with a Debye-Scherrer-type diffractometer at beamline **BL02B2**. The crystal structure was refined by the Rietveld method using the program RIETAN.

Figure 2 shows the X-ray diffraction pattern and its Rietveld refinement profile. The crystal structure of $InGaZnO_4$ is rhombohedral space group $R\bar{3}m$, and Ga and Zn atoms are distributed randomly at 6c crystallographic positions between $InO_2$ layers.

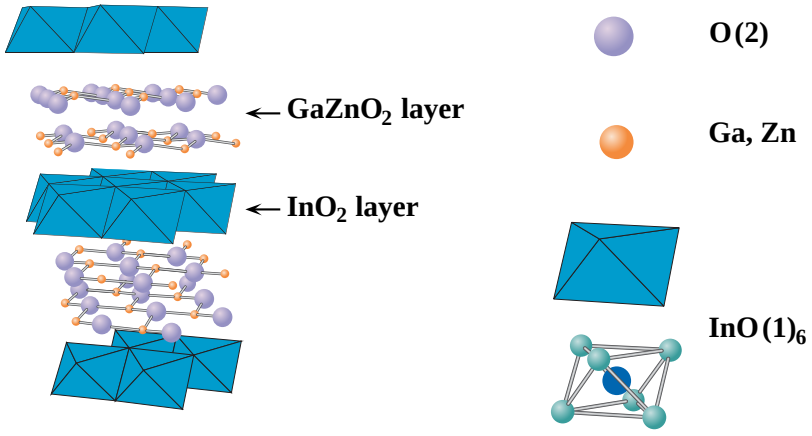


*Fig. 1. Crystal structure of $InGaZnO_4$.*

However, since the valence state and ionic radii of Ga and Zn are different, the positions of these atoms are also different. The structure refinement based on a model with different z coordinates for Ga and Zn gives a fairly good fit to the observed diffraction pattern.

The results of Rietveld refinement show that the z coordinates of the Ga and Zn sites differ by 3 to 4%. The difference in local structures around the Ga and Zn atoms is shown in Fig. 3. The random displacement of Ga and Zn atoms causes small overlapping of the 4*s* orbital of Ga and/or Zn as predicted by the cluster-model calculation, leading to the insulating nature of the $GaZnO_2$ layer. The In-In atomic distance in the $InO_2$ layer, on the other hand, is smaller than that in the Sn-doped $In_2O_3$ (ITO: a transparent conducting oxide with high carrier mobility). This suggests that the direct overlapping of In 5*s* orbitals causes the high electrical conductivity in the layer. These structural features revealed by our analysis are consistent with the 2-D model in the cluster calculation. However, a preliminary result of the band-structure calculation indicates nearly 3-D electrical conduction due to the orbital overlap between In 5*s* and Ga 4*s*, in spite of the difference in the z coordinates of Ga and Zn [3]. A precise electronic-band-structure calculation using the refined structural parameters is now in progress.

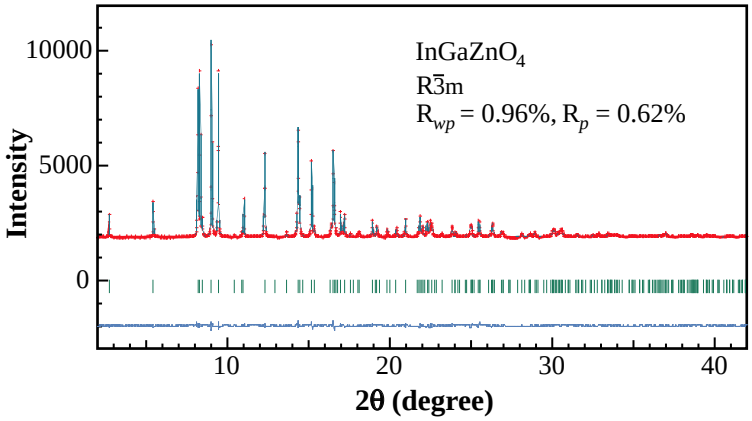


*Fig. 2. High-resolution X-ray diffraction pattern of $InGaZnO_4$ and its Rietveld profile.*

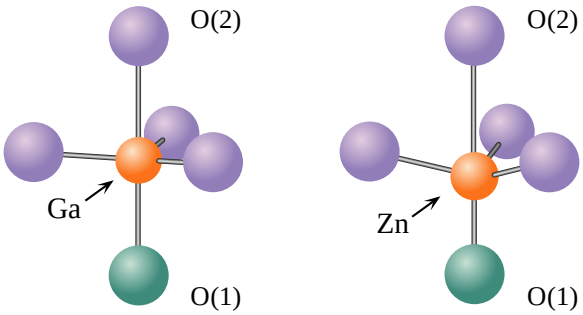


*Fig. 3. Schematic of refined local structures around Ga and Zn atoms.*

Hideto Imai, Yuichi Shimakawa and Yoshimi Kubo

Fundamental Research Lab., NEC Corporation

E-mail: h-imai@ce.jp.nec.com

**References**

[1] L. D. Hicks and M. S. Dresselhaus, Phys. Rev. **B 47** (1993) 12727.

[2] M. Orita *et al.*, Phys. Rev. **B 61** (2000) 1811.

[3] H. Imai, Y. Shimakawa, H. Kimura and Y. Kubo, in preparation.

# Local Structure around In Atoms in InGaN Single-quantum-well by XAFS

$In_xGa_{1-x}N$ is a key material in high-brightness blue/green light-emitting diodes (Fig. 1) and purplish-blue laser diodes [1]. Although such devices have very high densities of threading dislocations, they show a high quantum efficiency in contrast to conventional III-V and II-VI semiconductor-based devices [2]. In mole fluctuation in InGaN active layers is proposed as its origin [3]. In the model, injected carriers are localized into fluctuation-induced potential minima and can efficiently contribute to radiative recombination before captured by dislocation-activated non-radiative recombination centers, which is considered to lead to the high quantum efficiency. Therefore, in order to make the emission mechanism clear in InGaN-based light-emitting devices, it is important to clarify local structures around In atoms in InGaN.

Extended X-ray Absorption Fine Structure (EXAFS) is a powerful tool to investigate local structures in thin layers composed of two or more elements. There are some reports on local structures around In atoms in InGaN by EXAFS [4-6]. The value, however, varies widely even for atomic distances mainly due to the quality of samples. In this work, EXAFS measurements around an In *K*-edge were carried out for a high quality InGaN single-quantum-well (SQW) green light emitting diode.

The sample is an $In_{0.45}Ga_{0.55}N$ SQW of 3 nm thickness, which was grown by metallorganic chemical vapor deposition (MOCVD) on a sapphire (0 0 0 1) substrate. It consists of a sapphire substrate, GaN buffer layer, n-GaN:Si barrier layer (4000 nm), $In_{0.45}Ga_{0.55}N$ SQW (3 nm), p-$Al_{0.2}Ga_{0.8}N$:Mg barrier layer (100 nm), and p-GaN layer (500 nm) (Fig. 2). The XAFS measurements were made at beamline **BL01B1** and the XAFS data were collected with a double-crystal monochromator using Si (111) crystals [7]. The beam was focused on the sample surface. In $K\alpha$-fluorescence emission was measured using a 19 elements Ge detector. The angle between the incident X-ray beam and the sample plane was 2 degrees. The sample was rotated in-plane to remove the Bragg diffraction.

In order to analyze the experimental EXAFS data, XANADU and FEFF6.0 code were used.

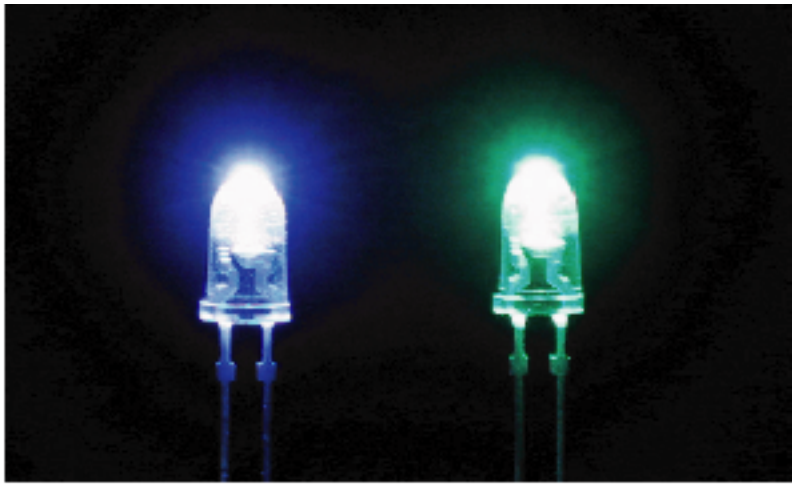

*Fig. 1. High-brightness InGaN blue and green LED.*

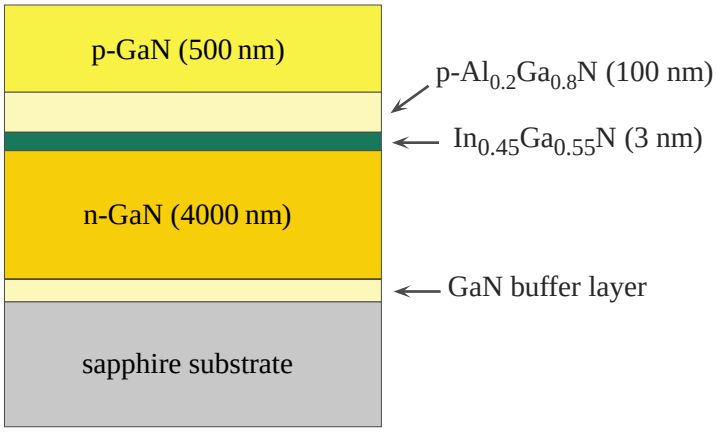


*Fig. 2. A schematic view of the structure of the green LED.*

What caused the greatest difficulty in the measurement in this system was a quite small photon-counting rate in the detector because the cap on the InGaN SQW (about 600 nm thick, Fig. 2) reduces the incoming photon of In-$K\alpha$. The Fourier transforms (FT) of the present EXAFS are shown in Fig. 3. Since the structure of InGaN is a wurtzite type, the first nearest peak includes the contribution of In-N bond and the second nearest peak includes that of In-Ga and In-In for $In_{0.45}Ga_{0.55}N$. To optimize the values of the structure parameters, these two peaks are individually fitted by the non-linear least square method (curve-fitting) for the *k*-range of 5.0 ~ 12.5 $Å^{-1}$ after the energy shift, the phases and amplitudes are corrected. First, we analyzed the InN powder as a standard sample and obtained reasonably good results ($r_{In\text{-}N}$ = 2.15 Å, $r_{In\text{-}In}$ = 3.53 Å). Then, we applied the empirical parameters from the standard sample to $In_{0.45}Ga_{0.55}N$ SQW. The results for the interatomic distances are as follows: $r_{In\text{-}N}$ is 2.11 Å, $r_{In\text{-}Ga}$ is 3.25 Å, and $r_{In\text{-}In}$ is 3.31 Å. We had good agreement between the theoretical FT by curve-fitting and the experimental one for $In_{0.45}Ga_{0.55}N$ (Fig. 3). The interatomic distances in the $In_{0.45}Ga_{0.55}N$ SQW are shorter in comparison with those in InN. Especially the reduction of In-In distance is prominent. The present EXAFS gives structural information about the horizontal direction of the SQW surface, because the electric vector of the incident X-ray is polarized in the plane of the sample surface. It is possible that $r_{In\text{-}In}$ has been greatly shortened in the horizontal direction affected by the atomic spacing of upper and lower GaN in the $In_{0.45}Ga_{0.55}N$ SQW. Comparison between the measurements of the horizontal and vertical directions to the SQW will be important in the next research project. As for the coordination number ($N$), $N_{In\text{-}N}$ is 3.2 for the first peak, and $N_{In\text{-}Ga}$ and $N_{In\text{-}In}$ are 11.3 and 1.9 respectively, for the second peak. The EXAFS results suggest that In atoms are homogeneously distributed and may make an ordered phase in the $In_{0.45}Ga_{0.55}N$ SQW [7]. However, there remains a possibility that the actual average concentration of In atom for the present sample is lower ($x \sim 0.2$) than $x = 0.45$ and a more accurate determination of the local structure is in progress.

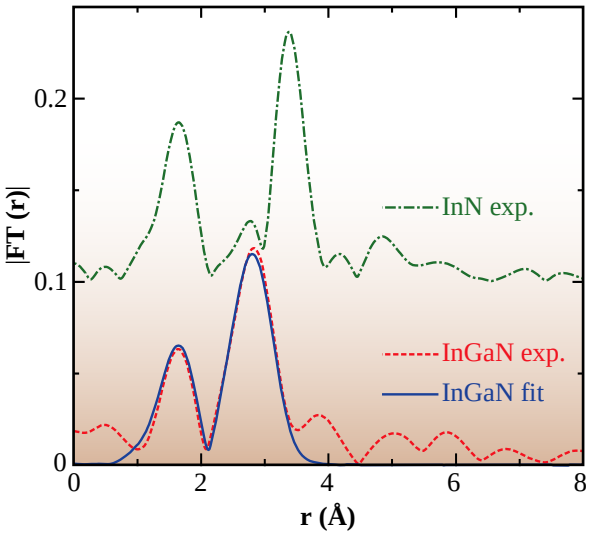


*Fig. 3. Fourier transforms of In K-edge EXAFS kχ(k) for InGaN SQW (dashed red line, fluorescence) and InN powder (dash-dotted green line, transmission). Solid blue line is FEFF fit result for InGaN SQW. The energy shift, phases and amplitudes are not corrected in these Fourier transforms.*

Takafumi Miyanaga[a], Takashi Azuhata[a] and Takashi Mukai[b]

(a) Hirosaki University
(b) Nitride Semiconductor Res. Laboratory, Nichia Corporation

E-mail: takaf@cc.hirosaki-u.ac.jp

**References**

[1] S. Nakamura *et al.*, The Blue Laser Diode, 2nd ed. (Springer, Berlin, 2000).

[2] S.F. Chichibu *et al.*, In Introduction to Nitride Semiconductor Blue Lasers and Light Emitting Diodes, eds. S. Nakamura and S.F. Chichibu (Taylor & Francis, London (2000) 153.

[3] S. Chichibu *et al.*, Appl. Phys. Lett. **69** (1996) 4188.

[4] N.J. Jeffs *et al.*, Mat. Res. Soc. Symp. Proc. **512** (1998) 519.

[5] S.C. Bayliss *et al.*, Materials Science and Engineering **B 59** (1999) 292.

[6] T. Miyajima *et al.*, Phys. Stat. Sol. (b) **228** (2001) 45.

[7] S. Matsuda, T. Miyanaga, T. Azuhata, T. Homma, R. Maruko, S. Chichibu, T. Sota, T. Mukai, T. Uruga, H. Tanida, Abstracts of 4th XAFS Meeting in Japan (2001).

# Fluorescence XAFS Analysis of Some Industrial Materials

BL16B2 and BL16XU, named "SUNBEAM", are contract beamlines constructed by an Industrial Consortium of 13 companies in cooperation with JASRI in 1999 [1]. We, representing seven interested companies [2] in the consortium, have frequently made the opportunity to measure various industrial materials in cooperation by offering our skills to each other.

During the first semester of 2001, we performed a fluorescence XAFS analysis of certain industrial materials, such as semiconductor devices, catalysts, fluorescent substances, and fuel cells using a Lytle detector [3] at **BL16B2**. Here, we report the results of the analysis of SiGe thin films for a narrow band gap semiconductor device, Lanthanum Manganese oxides for a solid oxide fuel cell.

SiGe film, which is a narrow band gap thin film semiconductor material, is being researched for use in high electron mobility semiconductor materials and infrared sensors. This material can be amorphous, microcrystalline or a mixture of these states, according to fabrication conditions. We attempted local structure analyses by XAFS, because the electronic and optical properties of SiGe films are significantly affected by their structural conditions. An amorphous Ge (a-Ge) film and three microcrystalline SiGe (μc-SiGe) films, which have different Si/Ge compositions, were examined. The Ge concentration was determined by X-ray photoelectron spectroscopy (XPS). Each film (about 0.5 μm in thickness) was fabricated on a glass substrate.

Figure 1 shows a schematic drawing of a microcrystalline material that consists of an amorphous region and microcrystalline regions. The μc-SiGe films which we measured have similar structures to those in Fig. 1, and the grain size was within the range of 10 to 20 nm.

The XAFS measurements were performed using a Lytle detector, since the counting rate of solid state detectors (SSD) is insufficient for these samples. A Ga filter was set in front of the ionization chamber of the Lytle detector to reduce the scattering X-rays. Kr was used as an ionization gas.

Figure 2 shows the Fourier transforms (RDF) of the EXAFS spectra for each sample. The difference between the distance to the first neighbor atom of crystalline Si and that of crystalline Ge is 0.1 Å, and those of SiGe are thought to be within this range.

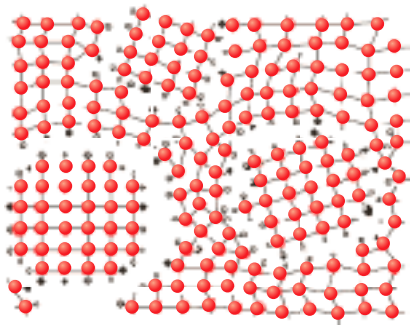

*Fig. 1. Schematic drawing of microcrystalline material (provided by National Institute of Advanced Industrial Science and Technology).*

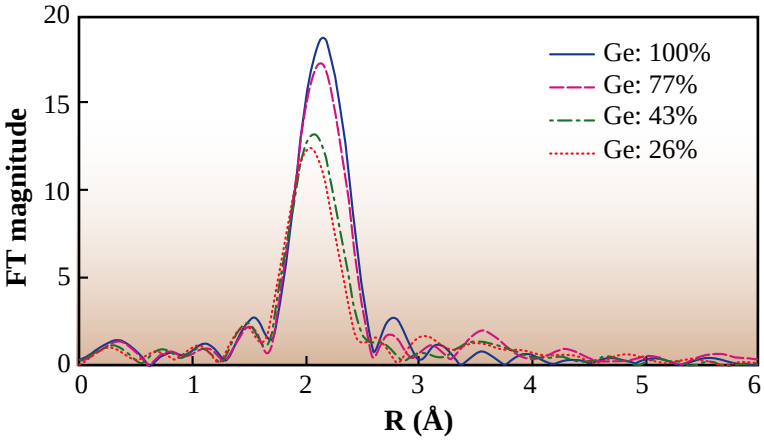


*Fig. 2. Fourier transforms of $k^3$-weighted Ge K-edge EXAFS spectra of SiGe films.*

The figure reveals that the distance is longer as the Ge concentration increases within less than 0.1 Å. This method provides excellent radial resolution for these kinds of thin film materials.

In Fig. 3, the distance values to the first neighbor atom derived from a curve-fitting analysis of XAFS spectra were plotted against Ge concentration. The distance values derived from powder X-ray diffraction (XRD) data for crystalline Si and Ge were also plotted. There is a tendency for the distance derived from XAFS to be longer than the average distance between crystalline Si and Ge.

XAFS observes both microcrystalline and amorphous regions, and the distance values by XAFS reveal the average values of both regions. Generally, the bond length of amorphous material is longer than that of crystalline material. Therefore, our XAFS results suggest that the SiGe materials contain both amorphous regions and crystalline regions. On the other hand, crystallographic analyses observe only crystalline regions. We believe a combination of Lytle detector based XAFS and crystallographic analyses can determine the structure of microcrystalline thin film materials.

The perovskite-manganites are technologically important materials as electro-catalysts and electrode materials for high temperature fuel cell applications. Their electronic, catalytic and magnetic

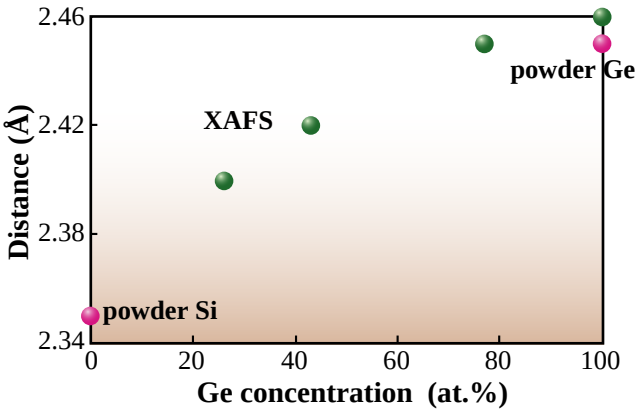


*Fig. 3. Distance to the nearest atom taken by XAFS and powder diffraction.*

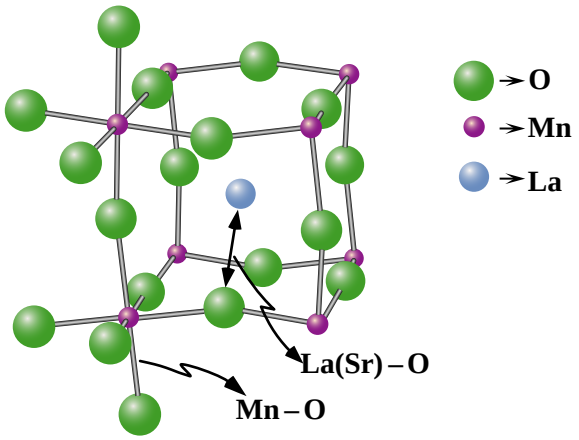


*Fig. 4. Schematic drawing of crystal structure of perovskite-type Lanthanum Manganese oxide.*

properties are of intrinsic interest, since the crystal and electron structure are changed by the constituted elements. The Lanthanum Manganese oxide, $LaMnO_3$, is semiconductor and has orthorhombic lattice (Pbnm), whereas Sr-doped solid-solutions $La_{1-x}Sr_xMnO_3$ have rhombohedral lattice (R-3c) and their electrical properties around room temperature varies from semiconducting to metallic behavior in the composition range between x = 0.3 and 0.4. A schematic drawing of $LaMnO_3$ is shown in Fig. 4. Recently, we characterized the temperature dependence of the electrical properties of $La_{1-x}Sr_xMnO_3$ and their crystal structure by X-ray Rietveld analysis. However, the role of Sr in La-site, which occupies the crystallographically equivalent site, is not yet clear. In this study, XAFS spectra near the Mn, Sr and La-*K* edge of the $LaMnO_3$ and $La_{1-x}Sr_xMnO_3$ solid-solutions were measured by the fluorescent X-ray method using a Lytle-detector.

The $LaMnO_3$ and $(La_{1-x}Sr_x)MnO_3$ ($0.1 \leq x \leq 0.4$) solid solutions respectively have an orthorhombic $GaFeO_3$-type (Pnma) and a rhombohedral $LaAlO_3$-type (R-3c) structure. Although a slight change of threshold energy in the Mn-*K* edge was observed, the obvious difference was not seen to the XANES spectrum of La(*K*), Sr (*K*) and Mn(*K*)-edge in these

solid solutions. Figure 5 shows the Fourier transforms (RDF) of $La_{0.7}Sr_{0.3}MnO_3$ compound at Mn-*K* edge. The RDF derived from the fluorescent X-ray method agrees with that of the transmitted X-ray method.

Figure 6 shows the composition dependence of La-O, Sr-O and Mn-O distances obtained by XAFS analysis, together with La(Sr)-O and Mn-O obtained by X-ray Rietveld analysis (XRD) in $La_{1-x}Sr_xMnO_3$ solid solutions. The Mn-O and La-O distances of $LaMnO_3$(x = 0.0) are respectively 1.98 Å and 2.77 Å, which shows good agreement with those derived from ionic radius. The first neighbor Mn-O distance obtained by XAFS continuously decreases from 1.98 Å at x = 0.0 to 1.94 Å at x = 0.4, which is in good accordance with that obtained by XRD. The La(Sr)-O distance obtained by the XRD also decreases from 2.77 Å to 2.74 Å in all the compositional range. However the La-O obtained by the XAFS drastically decreases and becomes 2.67 Å in the compositional range of $0.3 \leq x < 0.4$. This distance is shorter than that obtained by XRD and derived from ionic radius. The Sr-O remained around 2.78 Å in all the compositional range. These facts indicate that the valence state of Mn and the local structure around substituted Sr in La-site was different from those in $LaMnO_3$.

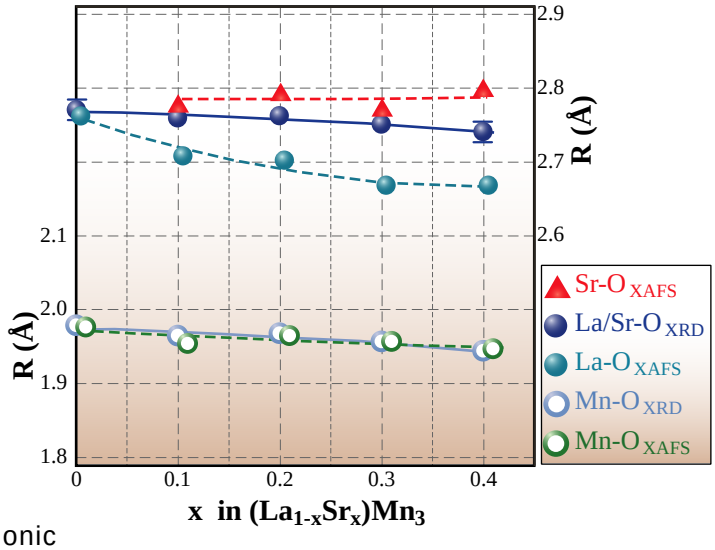


*Fig. 6. Compositional dependence of La-O, Sr-O and Mn-O distances in $La_{1-x}Sr_xMnO_3$ solid solutions.*

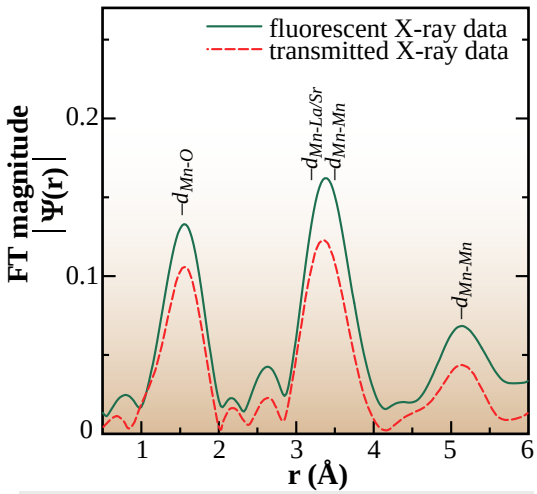


*Fig. 5. Fourier transforms of $k^3$-weighted Mn K-edge XAFS spectra of $La_{0.7}Sr_{0.3}MnO_3$.*

Hiroshi Deguchi[a], Akira Mikami[b] and Tohru Yamamoto[c]

(a) Kansai Electric Power Co., INC.
(b) SANYO Electric Co., LTD.
(c) Central Research Institute of Electric Power Industry

E-mail: K422950@kepco.co.jp

**References**

[1] Y. Hirai, SPring-8 Annual Report 1999 (1999) 100.
[2] Matsushita Technoresearch, INC., Sumitomo Electric Industries, LTD., Toyota Central Research & Develop. Labs., INC., SANYO Electric Co., LTD., Central Research Institute of Electric Power Industry, Kansai Electric Power Co., INC. & Osaka University.
[3] F.W. Lytle *et al.*, Nucl. Instrum. Meth. **226** (1984) 542.

# XAFS Analysis of the Structural Change in Si-Zr-C-O Fiber Accompanied by Thermal Decomposition

As the operating gas temperature of gas turbine engines increases year by year in response to issues related to energy and the environment, the materials temperature of such high-temperature parts as the turbine blades, stator, and combustor liner are nearing the limit for adiabatic metallic materials even when cooling is applied. For this reason, there is much interest in studies on the application of ceramic materials in gas turbine engines, and continuous fiber-reinforced ceramic matrix composite (CFCMC) materials, which are expected to exhibit high damage tolerance, are highly promising (Fig. 1) [1]. An experiment has been carried out at beamline **BL01B1** [2].

Figure 2(a) is a schematic illustration of the CFCMC structure. We are now working on process development, parts fabrication technology development, and materials evaluation technology development centered around SiC-based composite materials (Si-Zr-C-O/SiC) that use Si-Zr-C-O amorphous fiber as the reinforcing fiber [3-7].

The decline in strength of Si-Zr-C-O/SiC materials in a high-temperature environment, as is shown in Fig. 2(b), is attributed mainly to the decline in fiber strength due to the thermal decomposition and crystallization of the Si-Zr-C-O fiber, which is mainly responsible for the strength of the Si-Zr-C-O/SiC composite. Also, in ambient air, embrittlement caused by fiber/matrix boundary oxidation may have an effect [4].

Figure 3 is an outline of the Si-Zr-C-O/SiC fabrication process developed by Kawasaki Heavy Industries, Ltd. The Si-Zr-C-O fiber is prepared as a woven pre-form. A thin gradient layer of C/SiC is deposited on the surface of each filament in the pre-form by the CVD method. After the pre-form is impregnated with polycarbosilane xylene solution, it is pyrolized to form the SiC matrix [3,4]. As shown in Fig. 3, the Si-Zr-C-O fiber is exposed to a high temperature under reduced pressure and inert gas pressure in the fabrication process. Moreover, the operating environment of gas turbines is high-pressure ambient air. For these reasons, understanding the structural changes in the Si-Zr-C-O fiber in these differing environments should provide a guideline for optimizing the process conditions so as to control the degradation of materials in the fabrication stage or for improving the materials configuration so as to increase durability.

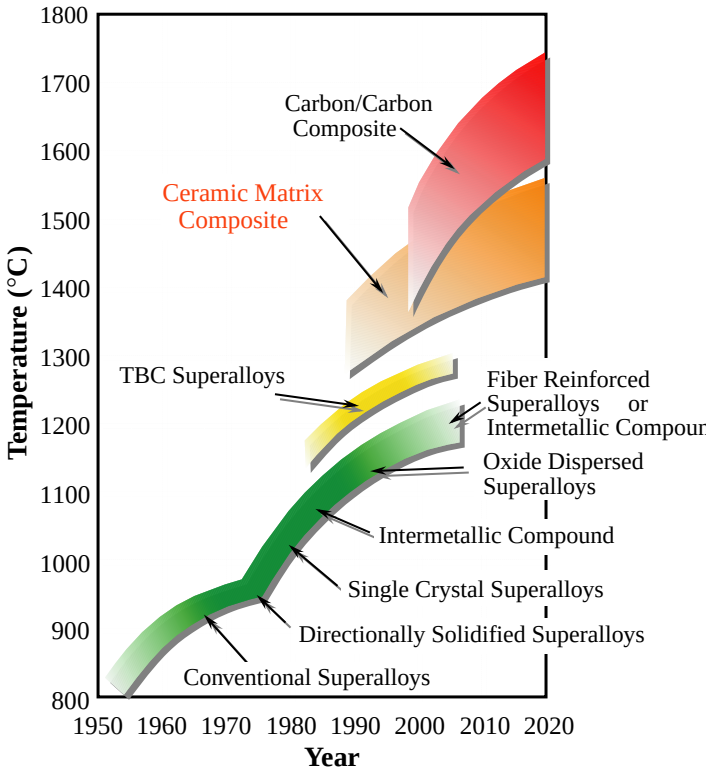


*Fig. 1. Development status of heat resistant materials [1].*

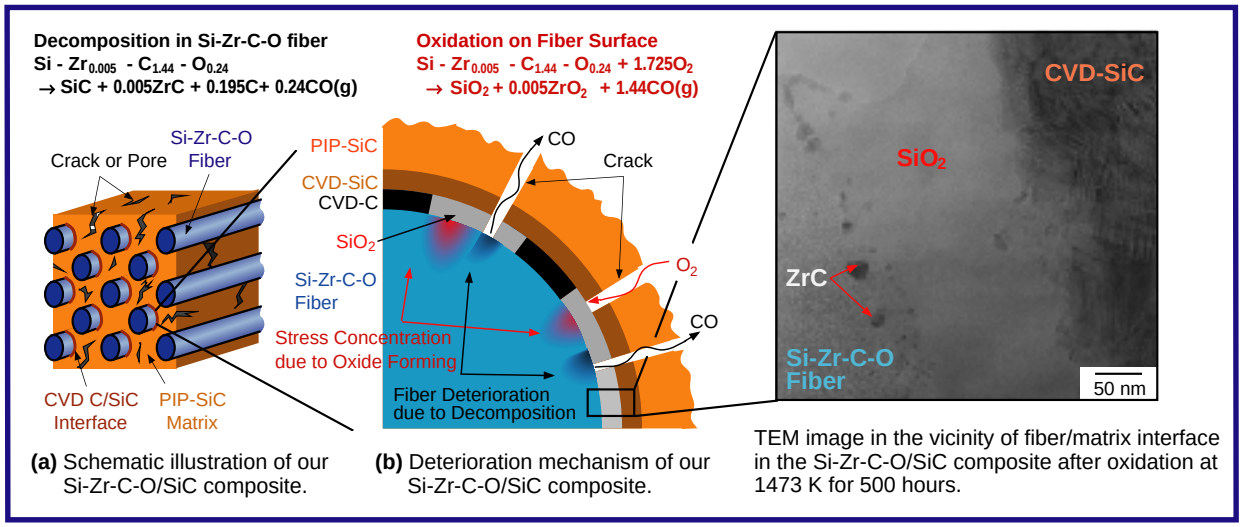


*Fig. 2. Schematic illustrations of our Si-Zr-C-O/SiC composite and its deterioration mechanism in ambient atmosphere.*

Figure 4 shows the XANES spectra at Zr *K*-edge of the Si-Zr-C-O fiber after heat treatment at 1673 K, and the zirconium foil. In the Si-Zr-C-O fiber heat-treated in ambient air and argon, the spectra were not much different from that of the as-fabricated fiber. However, in the Si-Zr-C-O fiber heat-treated in a vacuum, the spectra differed from that of the as-fabricated fiber after just four hours, and underwent an even more pronounced change when treated for 16 hours. This indicates that some kind of the change in the electronic structure of Zr occurred for the fiber heat-treated in vacuum

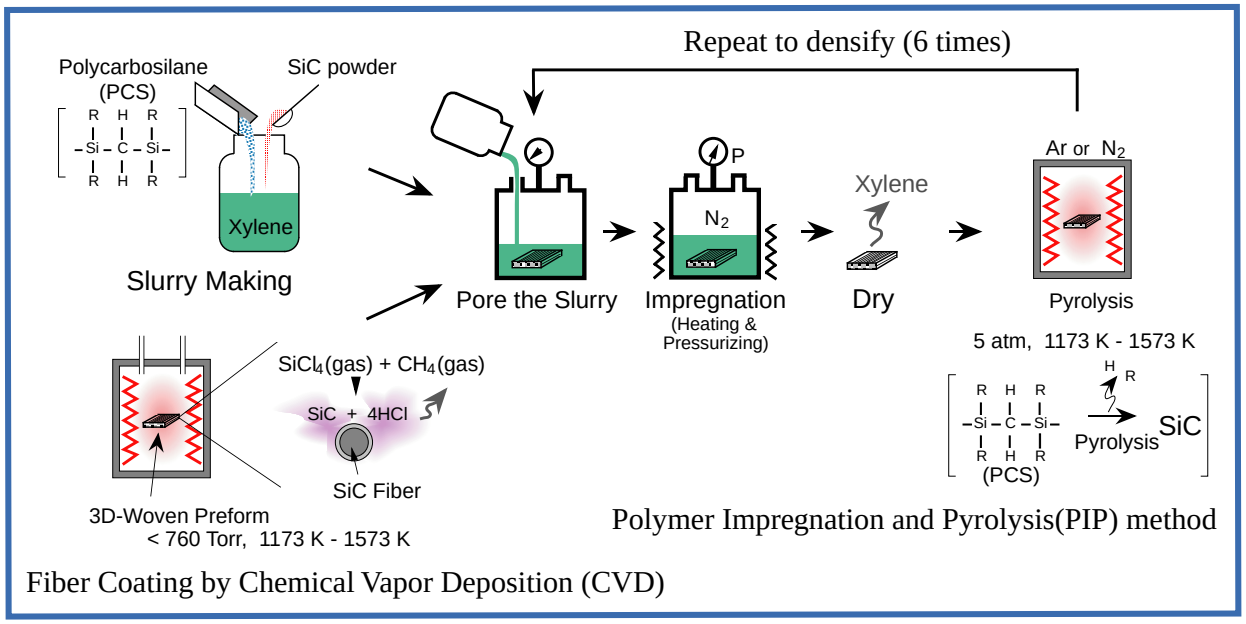


*Fig. 3. Schematic illustrations of the fabricating procedure for our Si-Zr-C-O/SiC composite.*

in a short time.

Figure 5 shows the Fourier transformation of XAFS spectra at Zr *K*-edge. A significant difference exists between the spectrum of the Si-Zr-C-O fiber heat-treated in ambient air and argon and that heat-treated in a vacuum. The peak near 3 Å , which is characteristic of the fiber after vacuum treatment, is believed to be zirconium because it can also be seen in metallic zirconium foil.

The peak near 4.2 Å in the sample after vacuum treatment is fairly strong despite the great distance, and it is believed to be zirconium with a higher atomic weight. These results reveal that the behavior of zirconium in the crystallization stage varies according to the heat-treatment atmosphere. Because the thermal decomposition of Si-Zr-C-O fiber is accompanied by the formation of carbon monoxide gas as shown by the equation in Fig. 2(b), the reaction can be expected to progress faster in a vacuum than in an argon atmosphere. Comparing the lower three spectrum in detail, the spectrum of the Si-Zr-C-O fiber heat-treated in ambient air and that of as-fabricated fiber are quite similar, but that heat-treated in argon is slightly different from the former two.

It has been reported that when Si-Ti-C-O fiber is heat-treated in ambient air, an oxide film formed on the fiber surface inhibits CO gas emission accompanied with the thermal decomposition of Si-Ti-C-O fiber, and consequently the thermal decomposition is controlled [8]. The same oxide film up to 0.5 μm thick on its surface was found on Si-Zr-C-O fiber heat-treated in ambient air. Therefore it can be supposed that the difference between the spectrum of the Si-Zr-C-O fiber heat-treated in ambient air and that of argon is related to the rate of the thermal decomposition, although further study will be required to conclude this.

Figure 6 shows a comparison of the Fourier transformation of XAFS spectra at the Zr *K*-edge of Si-Zr-C-O/SiC composites, containing Si-Zr-C-O fiber at about 40 vol.%, before and after high-temperature exposure under various conditions. The spectra for those composites, even when exposed to such a high temperature as 1773 K for as long as 400 hours, exhibited no major differences, and were close to that of the Si-Zr-C-O fiber heat-treated in an argon atmosphere in Fig. 5 rather than that in ambient air. These results suggest that the CVD process, which is conducted in a reduced pressure atmosphere, or pyrolysis step in inert gas, are effective for certain structural changes of the Si-Zr-C-O fiber.

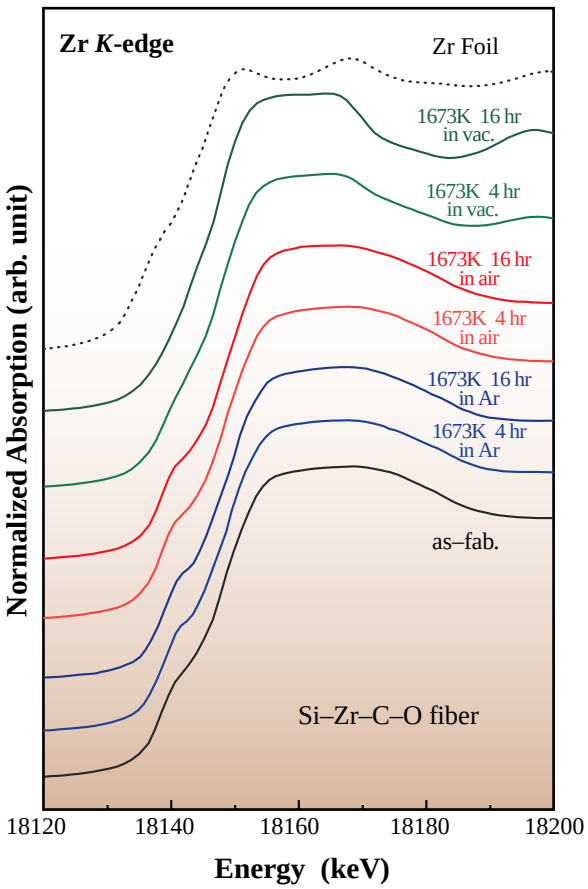


*Fig. 4. XANES spectra of Si-Zr-C-O fibers after heat treatment, compared with as-fabricated fiber and Zr foil.*

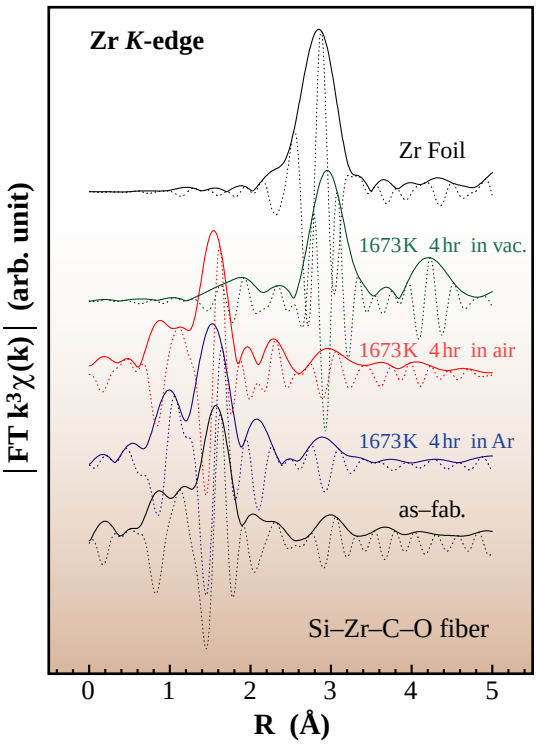


*Fig. 5. Fourier transformation of XAFS spectra for Si-Zr-C-O fibers after heat treatment, compared with as-fabricated fiber and Zr foil.*

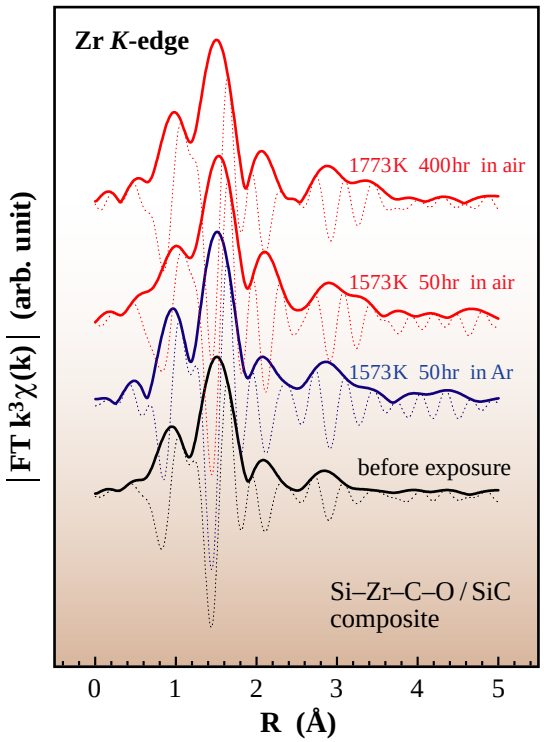


*Fig. 6. Fourier transformation of XAFS spectra for Si-Zr-C-O/SiC composites before and after heat treatment.*

Kenichiroh Igashira[a], Kozi Nishio[b] and Etsuya Yanase[b]

(a) Kawasaki Heavy Industries, Ltd.
(b) The New Industry Research Organization

E-mail: igashira@ati.khi.co.jp

**References**

[1] D. W. Petrasek *et al.*, Metal Progress 2, **130** (1986) 27.
[2] K. Igashira, K. Nishio and E. Yanase, to be submitted in J. of the Ceramic Soc. of Japan.
[3] K. Igashira *et al.*, J. Jpn. Inst. Metals, No. 8, **62** (1998) 766.
[4] K. Igashira *et al.*, J. Jpn. Inst. Metals, No. 12, **60** (1996) 1229.
[5] K. Igashira *et al.*, ECCM-8, ed. By V. Crivelli, Woodhead Publishing **4** (1998) 39.
[6] K. Nishio *et al.*, J. Gas Turbine Soc. of Japan, No. 98, **25** (1997) 94.
[7] K. Nishio *et al.*, Transactions of the ASME **121** (1999) 12.
[8] K. Kakimoto *et al.*, J. Jpn. Inst. Metals, No. 8, **57** (1993) 957.

# INSTRUMENTATION & METHODOLOGY

The technological developments to fully utilize high brightness has successively brought about new researches in SPring-8. In this issue, five reports have been selected among the fields of Instrumentation and Methodology. The first describes the synchronization between the laser and the SR pulses, which opens the way to pump-probe X-ray diffraction experiments. The second and third reports concern interferometry. The second reports on the effect of intensity interference which was observed to be much larger than had previously been reported. The experiment used a monochromator with a very narrow bandwidth and the 27-m undulator. The third report shows that the intensity correlation technique provides the visibility of the interference in the X-ray interferometer with separate components. The fourth reports on nuclear resonant scattering from $^{161}$Dy which has come into practical use in addition to that from $^{57}$Fe. The fifth addresses the X-ray fluorescence analysis of very small amounts of trace elements, obtaining a good signal to background ratio as well as overcoming low detection efficiency by employing a down-sized wavelength-dispersive spectrometer.

*Makoto Watanabe*

## Laser-SR Synchronization

A synchronization system between an intense pulsed laser and synchrotron radiation (SR) pulses has been developed at beamline **BL29XUL** for laser + SR pump-probe experiments such as time-resolved X-ray diffraction and absorption measurements, and for studies on the mixing of X-ray and optical photons. Since the SPring-8 SR has a pulse duration of typically 40 ps (FWHM), the synchronization technique of laser pulses with a precision of less than a few tens picoseconds is required to achieve a perfect overlap of both pulses.

The synchronization scheme is shown in Fig. 1. The output timing of a mode-locked Ti:sapphire laser (oscillator) is synchronized with the radio frequency (RF) provided by the master oscillator which controls the RF cavity for acceleration of the electron bunches in the storage ring. The repetition rate of the laser pulse is determined by its cavity length, which is controlled by a piezo-electric translator with a feedback circuit. The intense picosecond laser pulses with a pulse energy of about 1 mJ were obtained by amplification of the pulses picked up from a mode-locked Ti:sapphire laser. The repetition rate of amplified laser pulses was controlled to be 1/*n* of the RF, where *n* is a multiple of the number of RF buckets in the ring, so that the laser pulses meet the SR pulses originated from a particular electron bunch in partial filling patterns [1].

A monitoring system of the timing for both beams on a picosecond time scale should also be developed, since conventional methods, such as optical cross correlation technique, are still not available for the hard X-ray SR + laser combination. We used a picosecond X-ray streak camera as a timing monitor [2]. Both pulses simultaneously irradiated a photocathode on the streak camera. This method ensures a precise measurement of the interval between both beams without being affected by the drift of the streak trigger timing. The laser and the X-ray SR beams were introduced to the photocathode through a dichroic mirror made of a surface-polished Be plate installed in a vacuum chamber. Figure 2 shows the streak profiles obtained at a fine adjustment of the interval between the laser and SR pulses. Synchronization between the laser and the SR pulses was achieved with a precision of ±2 ps.

Application of this synchronization system to an investigation of electron bunch dynamics is also described here. Since the laser pulses are precisely locked to the phase of the RF in the

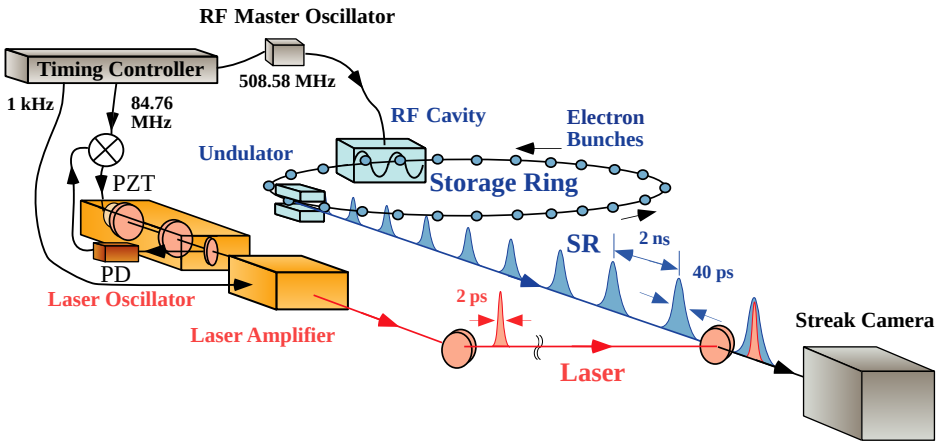


*Fig. 1. Laser-SR synchronization system.*

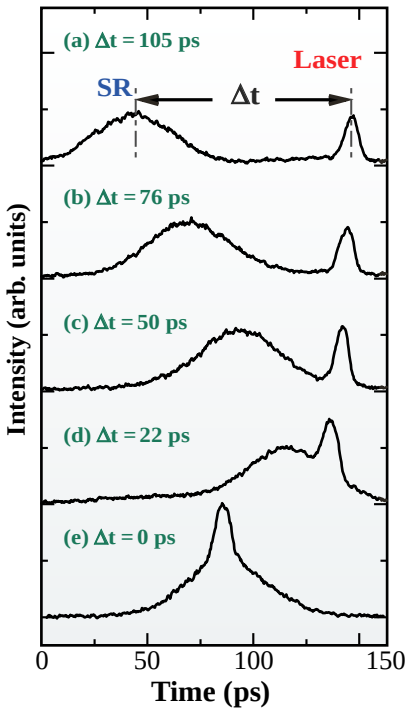


*Fig. 2. Overlap of laser pulses with SR pulses.*

storage ring, we used this system to show that closing undulator gaps shifts the arrival time of the SR pulses, which is due to the electron energy loss produced by the undulator radiation. The graphs in Fig. 3 are obtained under the conditions that the gaps of 14 undulators are fully opened (a) and closed (b) while the BL29ID gap is fixed to monitor the timing. The shift of the SR pulses between (a) and (b) has a good agreement with the expectations for the increased power loss [3].

Some picosecond time-resolved X-ray diffraction experiments were performed using the laser-SR synchronization system. Figure 4(a) shows the time-resolved rocking curves of a GaAs crystal, obtained by varying the delay between the pump laser and the probe X-ray pulses. The Bragg peak is shifted by the lattice expansion with a response time of a few hundred picoseconds. The diffracted

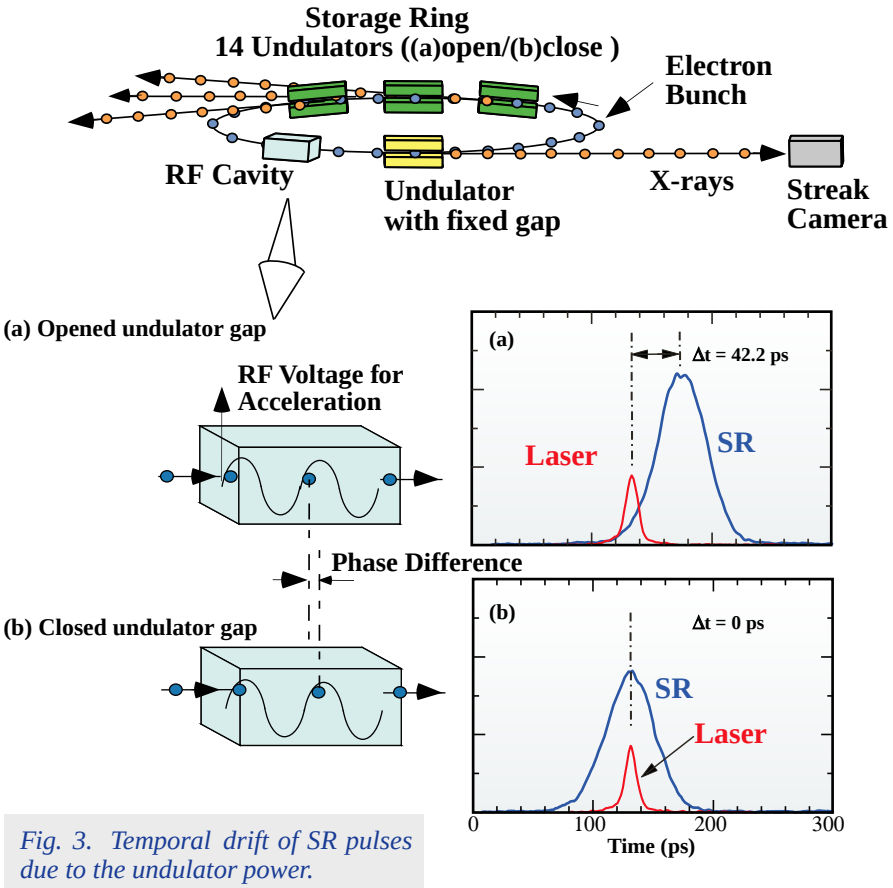


*Fig. 3. Temporal drift of SR pulses due to the undulator power.*

X-ray intensity at a certain offset angle is drastically changed according to the Bragg peak shift as shown in Fig. 4(b). It is to be noted that the lattice recovered from the expansion within 1 ms corresponding to a laser pulse repetition rate of 1kHz. We also investigated the optical switching method of the X-rays using the lattice expansion, as shown in Fig. 5. A single pulse was extracted from the synchrotron radiation pulse train using a double crystal arrangement of GaAs, in which the two crystals were irradiated by way of two successive laser pulses with an appropriate time delay [4]. This technique may enable individual beamline-users to employ SR pulsation with a pattern required for their experiments, which is usually supplied with a filling pattern of electron bunches in the storage ring. Further development of a faster X-ray switch will allow for an ultrashort X-ray pulse to be shaped from a single SR pulse.

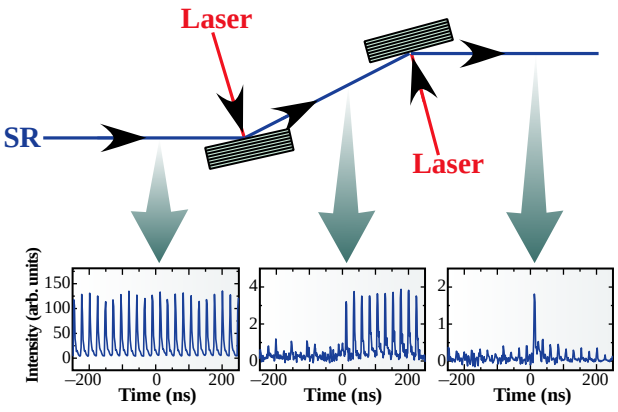


*Fig. 5. Extraction of a single X-ray pulse from the SR pulse train by optical-switching using laser-induced lattice expansion.*

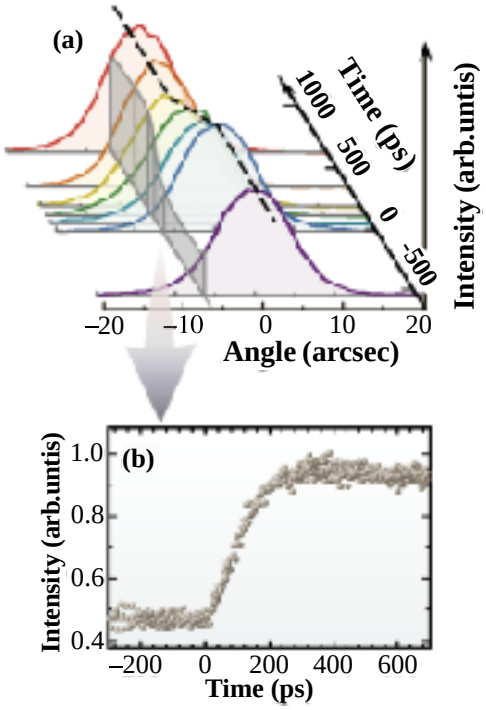


*Fig. 4. **(a)** Time-resolved rocking curves and **(b)** change in diffracted X-ray intensity at an offset angle of –7 arcsec.*

Yoshihito Tanaka

SPring-8/RIKEN

E-mail: yotanaka@postman.riken.go.jp

**References**

[1] Y. Tanaka *et al.*, Nucl. Instrum. Meth. **A 467-468** (2001) 1451.

[2] T. Hara *et al.*, Rev. Sci. Instrum. **71** (2000) 3624; Nucl. Instrum. Meth. **A 467-468** (2001) 1125.

[3] Y. Tanaka *et al.* , Rev. Sci. Instrum. **71** (2000) 1268.

[4] Y. Tanaka, T. Hara, H. Yamazaki, H. Kitamura, T. Ishikawa, to be published in J. Synchrotron Rad. (2002).

# X-ray Intensity Interferometry using ΔE = 120 μeV Monochromatized Beam

Intensity interferometry developed by Hanbury-Brown and Twiss [1] is a powerful method to investigate the statistical properties of light (higher-order coherence). In particular, when it is applied to chaotic light, the spatial and temporal coherence (first-order coherence) can be determined with very fast time resolution, less than ns. These advantages have promoted interesting applications in various fields including astronomy, quantum optics, laser physics, and nuclear physics. Nowadays, application of the method to the X-ray region is of great importance both for diagnosing modern synchrotron light sources and for utilizing coherent X-rays. We report on our recent development of X-ray intensity interferometry and its application to characterizing the spatial coherence of synchrotron radiation [2].

We briefly present the principle. If one took a beam image *instantaneously* for chaotic light, one would observe a number of bright and dark spots in a *speckle* pattern. Such intensity distribution results from the interference of light, and the spatial coherence length can be determined simply by measuring the spot profiles. Because the actual profile varies quite rapidly (with a time scale of the temporal coherence time), the coincidence technique is useful for fast detection. Here the interference is simply observed as an enhancement of the coincidence rate. When the technique is applied to pulsed light such as synchrotron radiation, one can greatly improve the detecting time resolution as short as the incoming pulse width, which is 10 to 100 ps in our case [3].

Nevertheless, the extension of intensity interferometry to the X-ray region [4] has been difficult. The primary reason is that the temporal coherence time, which is inversely proportional to the energy bandwidth $\Delta E$, is much shorter than the incident pulse width. This has obstructed the clear detection of the enhancement of the coincidence.

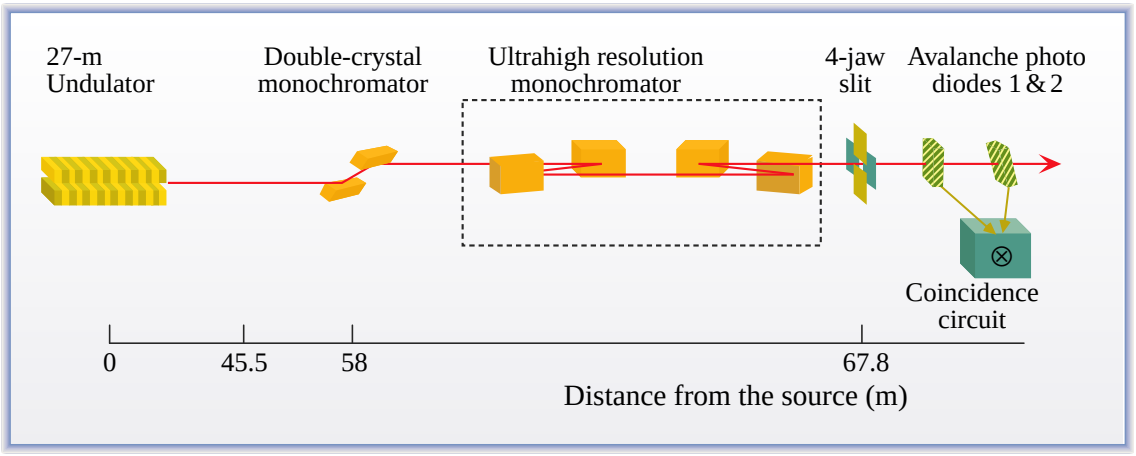


*Fig. 1. Schematic view of the experimental setup. Undulator radiation was pre-monochromatized with the Si 111 double-crystal monochromator. The ultrahigh resolution monochromator was installed in the experimental hutch 1. The coincidence signals between outputs of two detectors were counted with changing aperture of the 4-jaw slit.*

In addition, the brightness of the X-ray source was too low to obtain a good signal to noise ratio within a reasonable measurement time.

Recently, we achieved a significant improvement of energy resolution by developing an ultrahigh resolution monochromator: at 14.41 keV, 120-μeV bandwidth was realized using four-bounced asymmetric reflections [5]. The temporal coherence time is expected to reach ~ 40 % of the incident pulse width. With the monochromator the experiment was performed at beamline **BL19LXU** for the 27-m undulator [6], which is the brightest X-ray source. The setup is schematically shown in Fig. 1. The coincidence counts between two detectors were measured as a function of vertical slit width, as plotted in Fig. 2. The spatial coherence length was consequently determined to be 72.6 μm. A vertical source size of 12.8 μm was obtained from the value with van Cittert-Zernike's theorem. The source size almost agreed with that independently measured by the accelerator group. Furthermore, we characterized the coherence degradation in the transmitted beam through a filter and in the diffracted beam with diamond crystals [2].

To summarize, the combination of the narrowest bandwidth monochromator with the brightest X-ray source proved that X-ray intensity interferometry can be applied to the task of determining X-ray spatial coherence properties. This opens up new and broad opportunities to characterize beam qualities not only of the third-generation synchrotron sources but of the next generation ones.

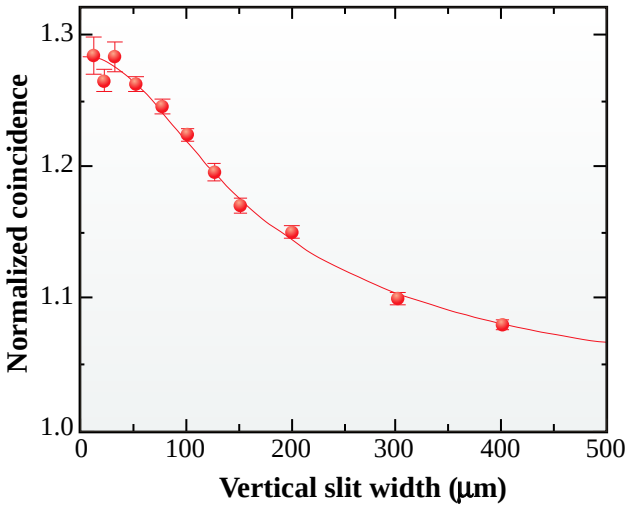


*Fig. 2. Normalized coincidence as a function of the vertical slit width. The line shows a fit based on a Gaussian source profile.*

Makina Yabashi

SPring-8 / JASRI

E-mail: yabashi@spring8.or.jp

**References**

[1] R. Hanbury-Brown and R. Q. Twiss, Nature (London) **177** (1956) 27.

[2] M. Yabashi, K. Tamasaku and T. Ishikawa, Phys. Rev. Lett. **87** (2001) 140801.

[3] E. Ikonen, Phys. Rev. Lett. **68** (1992) 2759.

[4] Y. Kunimune *et al.*, J. Synchrotron Rad. **4** (1997) 199; E. Gluskin *et al.*, *ibid.* **6** (1999) 1065.

[5] M. Yabashi, K. Tamasaku, S. Kikuta and T. Ishikawa, Rev. Sci. Instrum. **72** (2001) 4080.

[6] H. Kitamura *et al.* , Nucl. Instrum. Meth. Phys. Res. Sect. **A 467-468** (2001) 110; M. Yabashi *et al* , *ibid.* **467-468** (2001) 678; T. Hara *et al.* , Rev. Sci. Instrum. **73** (2002) 1125.

# X-ray Interferometer of Separate Components

In the hard X-ray region most optical elements, such as monochromators, polarizers, collimators and beam expanders, are designed based on dynamical diffraction with perfect crystals. Interferometers, one of the most important optical elements, are also made of perfect crystals. For example, a skew-symmetric triple-Laue interferometer, which is an X-ray analogue of the Mach-Zehnder interferometer, has four thin blades making Laue case diffractions (Fig. 1(a)). First one acts as a beam splitter dividing the incident beam into two coherent beams. Two mirrors change the propagating directions of the two beams, and they meet on the last blade. The last blade is a recombinator, usually termed an analyzer, the periodic electron density of which analyzes a standing wave made by the interference between the two beams and yields Moire fringes. The spacing of the raw interference fringes is too small to be perceived directly due to the angstrom scale of the wavelength. So we can conclude that we need to achieve an angstrom scale stability for the operation of X-ray interferometers, otherwise the interference fringes will be smeared out. This is the reason why most X-ray interferometers are constructed on a single block of perfect crystal.

However we may need a separate component interferometer, which is more flexible and has a greater potential than the monolithic interferometer. For example, we can have a larger separation, say 1000 m, when the skew-symmetric interferometer is made from separate components. (Note that the two coherent beams propagate parallel to each other inside the interferometer.) Using a large skew-symmetric bicrystal interferometer, we are planning to detect the red-shift of X-rays due to the gravitational field of the earth in the 1-km-beamline **BL29XUL** [1]. Up to date, the separate component interferometers have been realized on a conventional static method, where the interference intensity oscillation was measured by scanning a phase plate or the image of interference fringes were taken after the separate components were extremely stabilized as if there were made of a single crystal block.

One big problem on the separate component interferometers is the stringent requirement of stability, which is estimated to be less than $10^{-10}$ m for translation and/or $10^{-10}$ radian for angle. The conventional approach to the separate component interferometers is suitable for a phase sensitive applications, such as phase contrast imaging, because the effect of instability on phase information is relatively smaller. However, the conventional static method cannot be applied to visibility sensitive applications. The visibility is subject to degradation by residual instability of the interferometer, so that the measured value may be lower than the true value. We need to compare the intrinsic values of visibility measured under different conditions of components, *e.g.*, coherence measurements by Young or Michelson interferometers.

Here we consider a new interferometric method to measure visibility [3]. Using this method, we can measure directly the intrinsic value of visibility and do not need to stabilize the interferometer. The principle is easy but somewhat tricky. We suppose the output intensity of the interferometer changes like $I(\phi) = \langle I_0 \rangle (1 + V\cos(\phi))$, where $\langle I_0 \rangle$ is the average intensity, $V$ is the visibility, and $\phi$ is the phase variable which is related to relative translational and/or angular shifts among the components. Since $\phi$ is related to the angstrom scale, it varies rapidly due to mechanical vibration and thermal drift, if special care is not taken to stabilize the interferometer. When intensity correlation is measured, it will be averaged over $\phi$

and become $\langle I^2 \rangle = \langle I_0 \rangle^2 (1+V^2/2)$. Thus the visibility is determined from the intensity correlation.

We have investigated the relation between visibility and the intensity correlation using a skew-symmetric bicrystal interferometer. Figure 1(b) shows a schematic view of the experimental setup at BL29XUL [2]. This bicrystal interferometer consists of two separate Si blocks, one mounted on the splitter and the mirror-1, and the other mounted on the mirror-2 and the analyzer. The separation of the two blocks was 500 mm. We measured the intensity correlation of the output beam with two avalanche photo diodes (APD) using a coincidence technique. To verify interference, we also monitored the beam image by a CCD based beam monitor (not shown in Fig.1(b)).

Figure 2 shows the two dimensional map of normalized coincidence measured in the $\Delta\theta_1$-$\Delta\theta_2$ plane. Here, $\Delta\theta_1$ and $\Delta\theta_2$ represent rotation angles within the scattering planes of each crystal block. The coincidence rate was found to have a narrow peak along $\Delta\theta_1 = \Delta\theta_2$ line. This suggests that only the narrow region where the two blocks are nearly parallel can be used for interferometry. Note that the two crystal blocks are exactly parallel on the $\Delta\theta_1 = \Delta\theta_2$ line, as if the interferometer is made of a single crystal block. The reason why the coincidence was enhanced with the narrow range along $\Delta\theta_1 = \Delta\theta_2$ was discussed in Ref. [4]. The beam images taken along the constant-$\Delta\theta_1$ line ($\Delta\theta_1$=0.5") show clearly that the interference fringes were observed within the same region where the

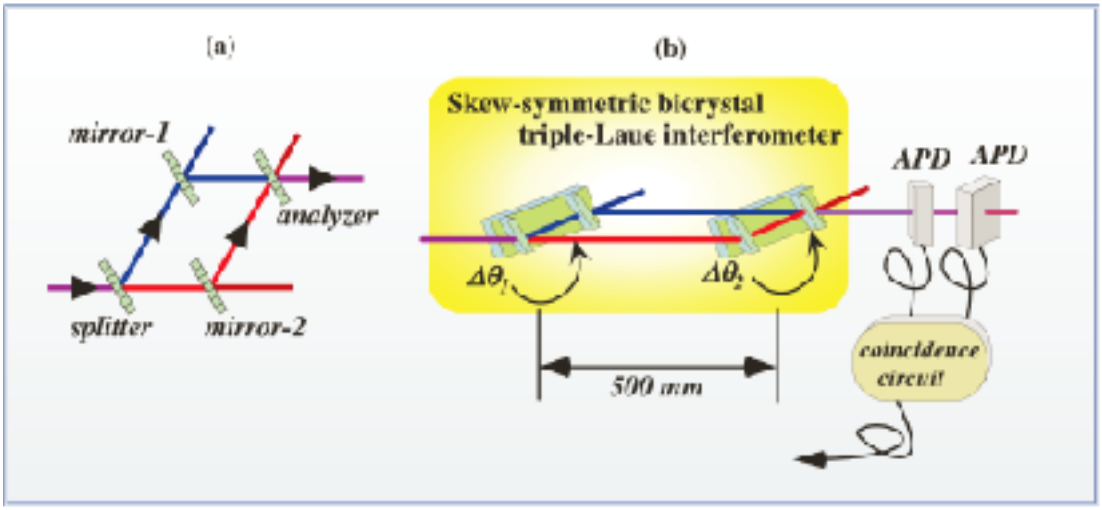


*Fig. 1.* ***(a)*** *Schematic view of a skew-symmetric triple Laue interferometer, which is an optical X-ray of Mach-Zehnder interferometer. Laue case diffractions take place at the four thin blades, splitter, two mirrors, and analyzer (recombinator).* ***(b)*** *Schematic side view of the experimental setup. The interferometer consists of two Si crystals separated by 500 mm. The output intensity was monitored by two APD detectors in transmission geometry, which were connected to the coincidence circuit to measure the intensity correlation.*

coincidence had a peak (Fig. 2(b)). Thus the theoretical relation, $\langle I^2 \rangle \sim 1+V^2/2$, was confirmed semiquantitatively.

We overviewed briefly the interferometry with separate components and intensity correlation, using the skew-symmetric interferometer. The intensity correlation technique was found to be a good measure of visibility and may be useful in visibility sensitive applications by separate component interferometers, such as Young or Michelson interferometers.

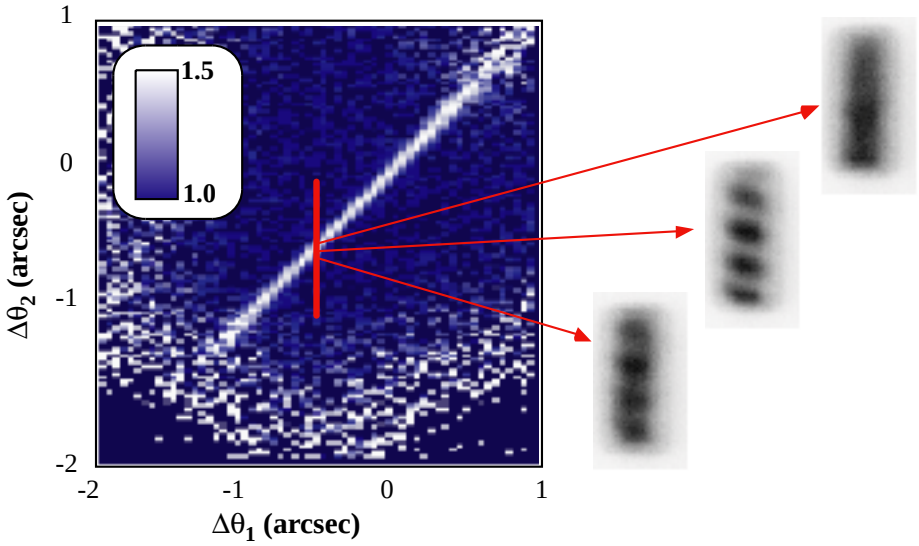


*Fig. 2. Two-dimensional map of the normalized coincidence, and the beam images taken along the constant-$\Delta\theta_1$ line (red line). The normalized coincidence had a sharp peak along $\Delta\theta_1 = \Delta\theta_2$ line, where the interference fringes were observed clearly in the beam images.*

Kenji Tamasaku

RIKEN / SPring-8

E-mail: tamasaku@postman.riken.go.jp

**References**

[1] T. Ishikawa *et al.*, Proc. SPIE **4145** (2000) 1.

[2] K. Tamasaku, Y. Tanaka, M. Yabashi, H. Yamazaki, N. Kawamura, M. Suzuki and T. Ishikawa, Nucl. Instrum. Meth. **A 467-468** (2001) 686.

[3] M. Yabashi *et al.*, Jpn. J. Appl. Phys. **40** (2001) L646.

[4] K. Tamasaku, M. Yabashi and T. Ishikawa, Phys. Rev. Lett. **88** (2002) 044801.

# Nuclear Resonant Scattering from $^{161}$Dy at 25.65 keV

Nuclear resonant scattering (NRS) of synchrotron radiation [1] provides several methods for investigating materials. On one hand, time differential measurements allow access to nearly all of the hyperfine and materials science information of conventional Mössbauer experiments, with added structural information possible due to the use of a scattering geometry and the extremely brilliant X-ray beam. On the other, nuclear inelastic scattering (NIS) uses the narrow nuclear resonance as a probe of the nuclear motions within a material, allowing access to phonon spectra on meV energy scales. Most NRS experiments provide information specifically about the excited resonant nuclei (*i.e.*, hyperfine fields at the resonant nucleus, phonons that include the resonant nucleus, structural and motional correlations among the resonant nuclei). This specificity allows one to obtain very precise information. It also provides clear impetus for extending the number of available transitions beyond the few that are now commonly used.

NRS experiments with new resonant transitions are largely limited by instrumentation. While stronger synchrotron sources always present new opportunities, in fact present sources are strong enough (at least for low to mid-range X-ray energies) to provide rather high flux in the resonant bandwidth of many transitions. Using that flux, without large losses either in optics or detection, however, is a significant challenge. Here we describe a new setup, commissioned at **BL35XU**, for nuclear scattering with the 25.65 keV resonance of $^{161}$Dy. In principle, this resonance is convenient for synchrotron based studies, having a relatively long (42 ns) lifetime and a large cross-section (low internal conversion). In addition, the difficulties in obtaining narrow lines in conventional (radioactive source) Mössbauer measurements make the synchrotron based work especially appealing. However, practically, significant instrumentation work is required to make experiments feasible. We have developed a new monochromator and a new detector optimized for this resonance [2].

Our monochromator uses a thin coupling crystal placed inside of a high order channel cut crystal operating near backscattering (see Fig. 1). By using the coupling crystal both in reflection and transmission, this design allows one to get extremely close to backscattering (Bragg angles near 90 degrees) without the very big crystals that would be needed for previous designs [3]. Thus,

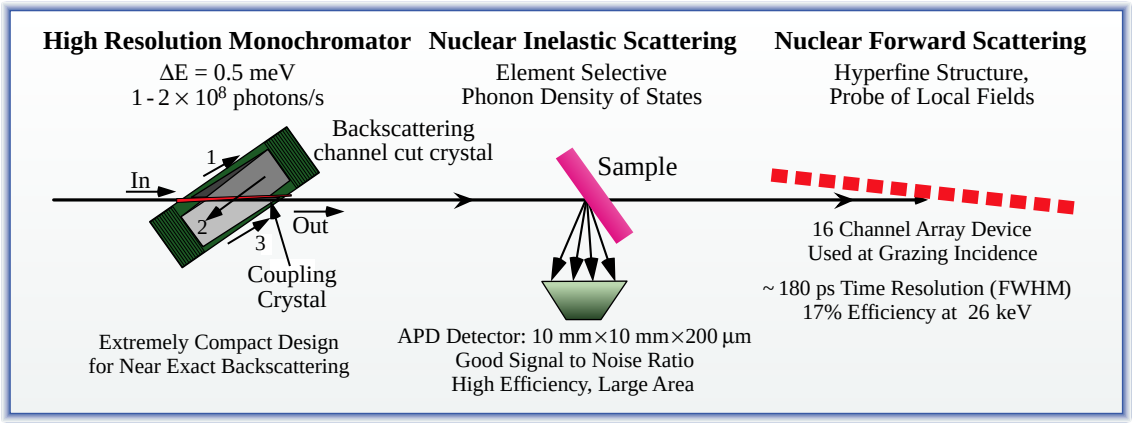


*Fig. 1. Schematic of the setup for nuclear resonant scattering with $^{161}$Dy summarizing properties of important components.*

one can take full advantage of the large angular acceptances available near backscattering, while retaining a compact, in-line, geometry. In particular, working at 25.65 keV (using the (6 2 0) and (18 12 6) reflections – Bragg angles of 16.3 and 87.4 degrees, respectively) we have obtained a 0.52 meV bandwidth ($\Delta E/E = 2\times10^{-8}$) and a peak throughput of about $2\times10^{8}$ photons/s, both in good agreement with theory (additional discussion can be found in [4]). The monochromator was used to measure nuclear inelastic scattering from several samples, and results from a $DyB_2C_2$ sample (natural abundance, 19% $^{161}$Dy) are shown in Fig. 2. In particular, the relatively simple phonon density of states makes it easy to identify the various multi-phonon contributions appearing at high temperature, while the inset shows the derived density of states, with some softening evidence at room temperature.

In general, this monochromator design should be easy to use in the 20 - 30 keV range and work on a monochromator for the Sn resonance at 24 keV is in progress [5]. At lower energies, absorption in the silicon coupling crystal becomes a problem, but this might be avoided by using a less absorbing material (*e.g.* diamond or beryllium). Extension to higher energy in silicon is also possible, but, the backscattering reflectivity of the silicon falls off quickly, so other materials (*e.g.* sapphire) with a higher Debye temperature might be advantageous, if a suitable quality crystals can be found. At exact backscattering, this design becomes reminiscent of an X-ray Fabry-Perot interferometer, suggesting a way of controlling the coupling into/out of such an interferometer that is independent of the backscattering mirrors.

Development of a proper detector for nuclear forward scattering (NFS) from $^{161}$Dy is challenging. This is because one needs both high efficiency (as the resonance is narrow and count rates are small) and extremely good time resolution (as the hyperfine splitting of the $^{161}$Dy resonance can lead to beat frequencies of ~10 GHz). These two conditions are usually mutually exclusive in silicon avalanche photodiodes (APDs) since making them thicker to improve the efficiency degrades the time resolution:

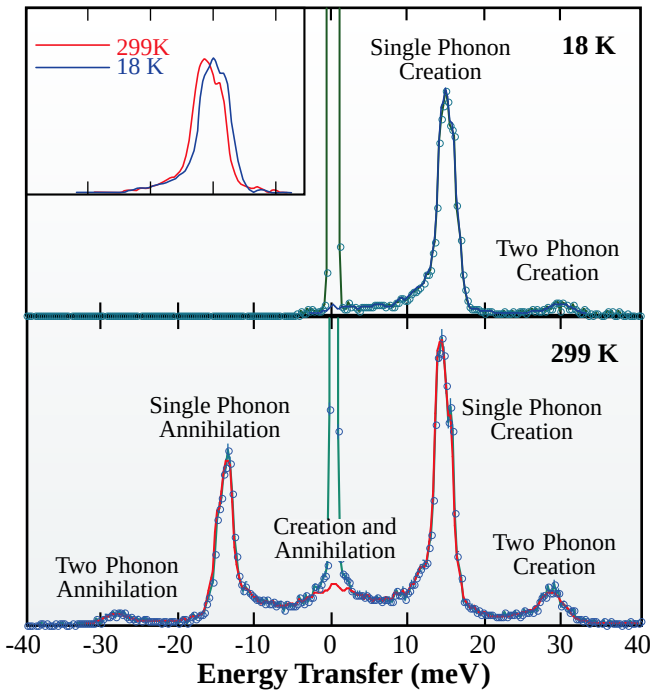


*Fig. 2. Nuclear inelastic scattering from $DyB_2C_2$ at low temperature and room temperature. The solid lines in the figure are calculations based on the derived partial density of states DOS (shown in the inset – 22.5 meV full scale). See text for discussion.*

the ratio of the active thickness to the time resolution for an APDs is approximately constant, and equal to the saturation drift velocity of the electrons in the APD (~100 μm/ns for silicon). However, this trade-off may be circumvented using an array of thin devices at grazing incidence, allowing a long path length through the silicon, without making the electron transit time spread longer. An array of 16 elements (each $1 \times 2.5$ mm$^2$ on a 1.1 mm pitch) allowed us to achieve 180 ps resolution with about a 0.5 mm path length in the silicon, corresponding to ~17% efficiency at 25.65 keV. While the 180 ps resolution is not quite sufficient to resolve the fastest beats from $^{161}$Dy it is sufficient so that there are no isolated lines in the response – beats will appear from all excited levels. The time response measured from a Dy foil at low temperature is shown in Fig. 3, the excellent time resolution is clearly evident, and the general quality of the data is confirmed by the good agreement with theory.

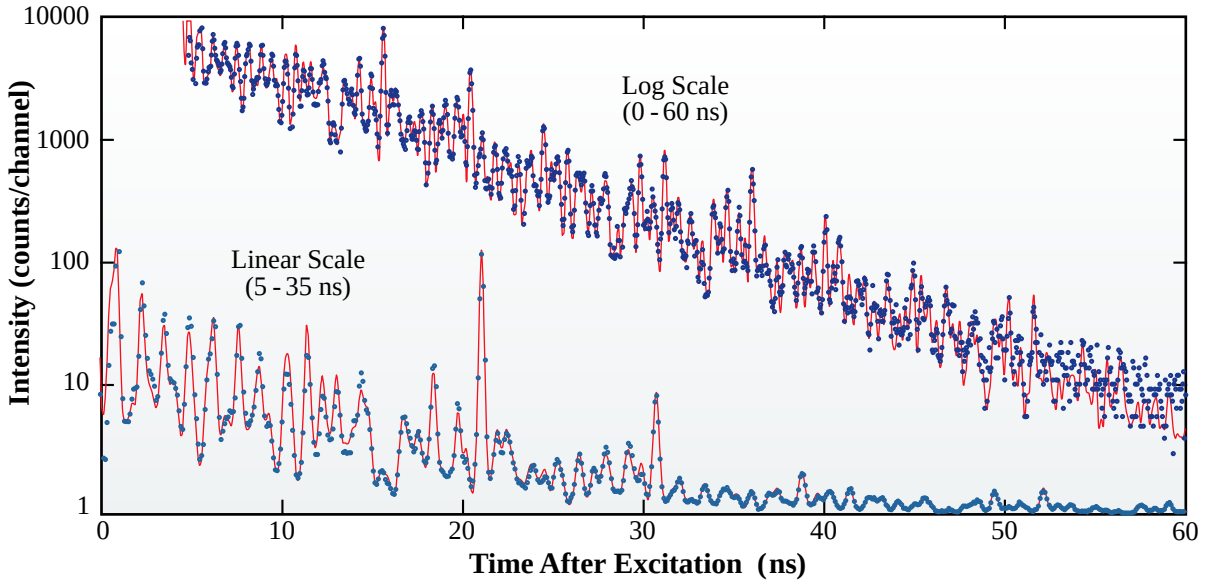


*Fig. 3. Nuclear forward scattering from a (non-enriched) $^{161}$Dy foil at low temperature. The agreement between the fit (solid line) and the data serve to highlight the good performance of the detector. Note both log and linear plots are shown and that the axis labels are for the log plot.*

Alfred Q. R. Baron[a], Yoshikazu Tanaka[b] and Tetsuya Ishikawa[a,b]

(a) SPring-8 / JASRI
(b) SPring-8 / RIKEN

E-mail: baron@spring8.or.jp

**References**

[1] E. Gerdau and H. de Waard, *Hyperfine Interactions* **123-125** (2000) and references therein.

[2] A.Q.R. Baron, Y. Tanaka, D. Ishikawa, D. Miwa, and T. Ishikawa, to be published.

[3] T. Ishikawa *et al.*, Rev. Sci. Instrum. **63** (1992) 1015; M. Yabashi and T. Ishikawa, SPring-8 Annual Report **1999** (2000) 151.

[4] A.Q.R. Baron, Y. Tanaka, D. Ishikawa, D. Miwa, M. Yabashi and T. Ishikawa, J. Synchrotron Rad. **8** (2001) 1127.

[5] D. Miwa, D. Ishikawa, A. Baron *et al.*, work in progress.

# Detection of Trace Metals by Means of an Efficient Wavelength-dispersive X-ray Fluorescence Spectrometer

Trace metals sometimes play quite significant roles in spite of the extreme small amounts in which they exist, not only in industrial research but also in environmental and biomedical sciences. The synchrotron X-ray fluorescence technique [1] is a powerful probe for trace metals, and in particular, total-reflection X-ray fluorescence (TXRF) [2] using a mirror-polished substrate as a sample support, can detect trace metals with very high sensitivity. So far, an energy-dispersive spectrometer based on a Si(Li) detector has been employed, because of its high detection efficiency and tolerable energy resolution (130 ~ 170 eV for 5 ~ 10 keV X-rays) for separating X-ray fluorescence from the neighboring elements. However, there exist obvious limits in detection power; the biggest problem is the scattering background, the low-energy-side tail of which severely restricts the detection of weak X-ray fluorescence signals. Therefore, one should note that upgrading the detection power is not always straightforward, even when brilliant sources are available.

A new idea comes with the use of wavelength-dispersive (WD) spectrometers to improve the signal to background ratio by eliminating scattering X-rays with enhanced energy resolution (Fig. 1) [3]. Since there is usually a trade-off between resolution and efficiency, one promising candidate is a spectrometer with downsized Johansson-type focusing optics with moderate energy resolution (~ 10 eV for 5 ~ 10 keV X-rays) [4-7]. Although another way to accomplish this might be to use conventional optics with flat crystals [8,9], the loss of detection efficiency can be a problem for trace analysis. Figure 2 schematically shows a wavelength-dispersive TXRF spectrometer, which is equipped with a Ge(220) analyzing crystal

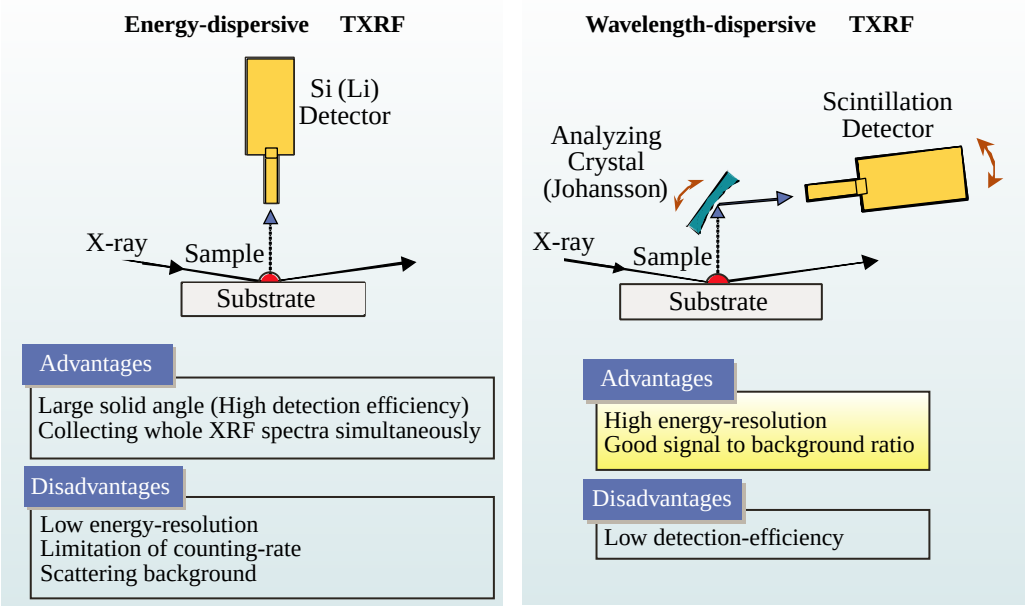


*Fig. 1. Comparison between conventional energy-dispersive and the present wavelength-dispersive TXRF. The main idea of the present research is the employment of the Johansson-type spectrometer instead of a Si(Li) detector in TXRF experiments. The expected problem is low efficiency for ultra trace element analysis, but the present downsized spectrometer can solve it.*

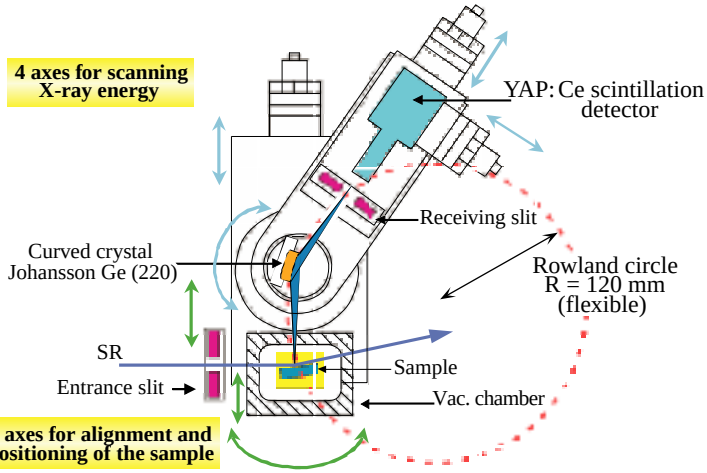


*Fig. 2. Schematic view of the downsized Johansson TXRF spectrometer developed at Nat'l Inst. for Materials Science (NIMS), Tsukuba.*

(Rowland radius 120 mm) and a YAP:Ce detector [10] with a 0.07 mm receiving slit. The most important feature is reasonably high detection efficiency with only a small loss of energy resolution [6].

Experiments have been performed at beamline **BL40XU** with quasi-monochromatic X-rays from a helical undulator source (ID gap 10.8 mm, fundamental peak 10 keV) and focusing optics based on K-B mirrors (Fig. 3). The beam size used is 30 μm × 30 μm. Figure 4 shows typical TXRF spectra for a drop of liquid (0.1 μl) containing 20 ppb Fe, Co and Ni. The scan requires 5 sec/point and the total measuring time is 10 - 15 min. The energy resolution is around 6 ~ 7 eV, around 20 times better than that obtained using a conventional energy-dispersive TXRF spectrometer. This

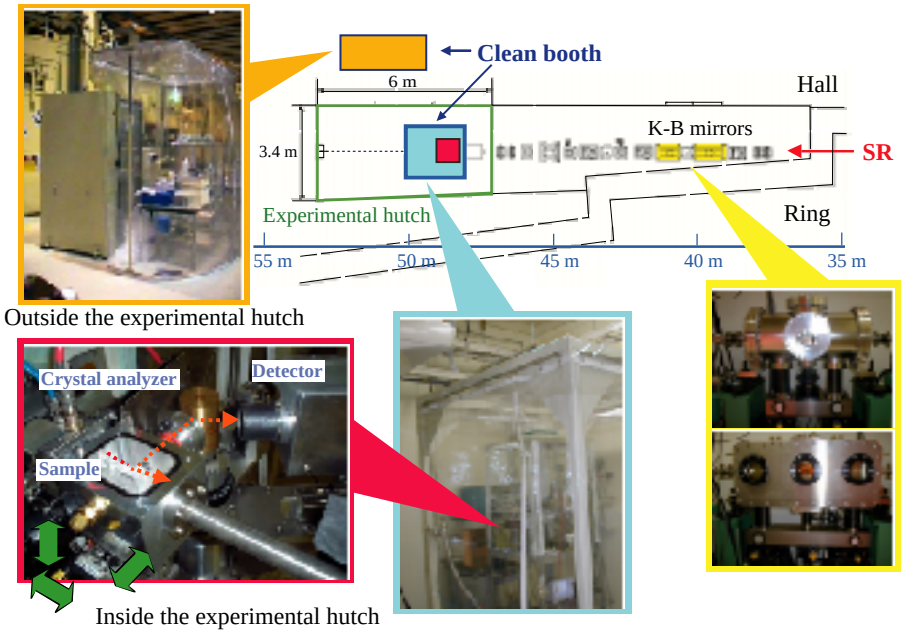


*Fig. 3. Experiments setup at BL40XU. Combination of high-flux undulator beam and efficient XRF spectrometer.*

contributed to reducing the influence of scattering background and X-ray fluorescence from the neighboring elements. Since the energy resolution is enhanced one can see even chemical effects by looking carefully in the area around Kβ spectra [7], which exhibit some satellite lines.

Figure 5 shows another result for Ni in a 0.1 μl drop. The technique shows good linear relation in a wide dynamic range. The absolute detection limit obtained is 0.31 fg for Ni, and the concentration in a 0.1 μl drop is 3.1 ppt, or further lower for a usual 1 ~ 50 μl solution sample. The results are almost 1.5 ~ 2 decades better than the current best record performed with a Si(Li) detector [11]. The present technique is competitive with trace analysis, such as AAS and ICP-MS (Fig. 6). Besides extremely high sensitivity, capability of analyzing very small amount of samples is significant for practical analysis. Another advantage is the non-destructive nature for the measurement. New opportunities for advanced analytical applications could be opened up.

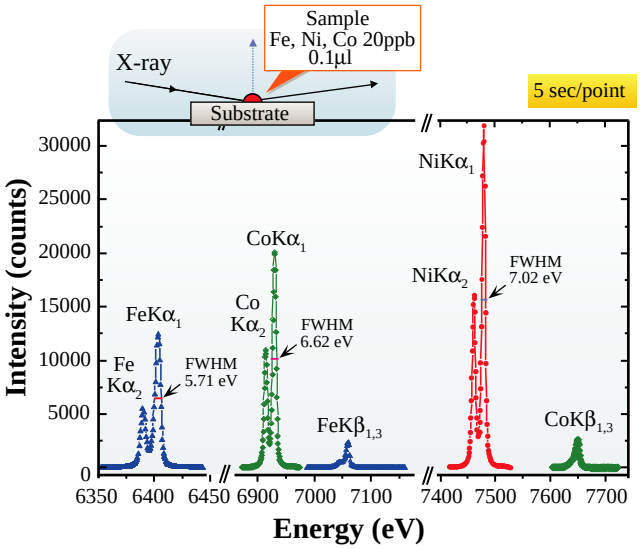


*Fig. 4. Typical TXRF spectra for trace elements (Ni, Co and Fe, 20 ppb each) in a micro drop (0.1 micro litter). Details of the experiment are covered in the main text.*

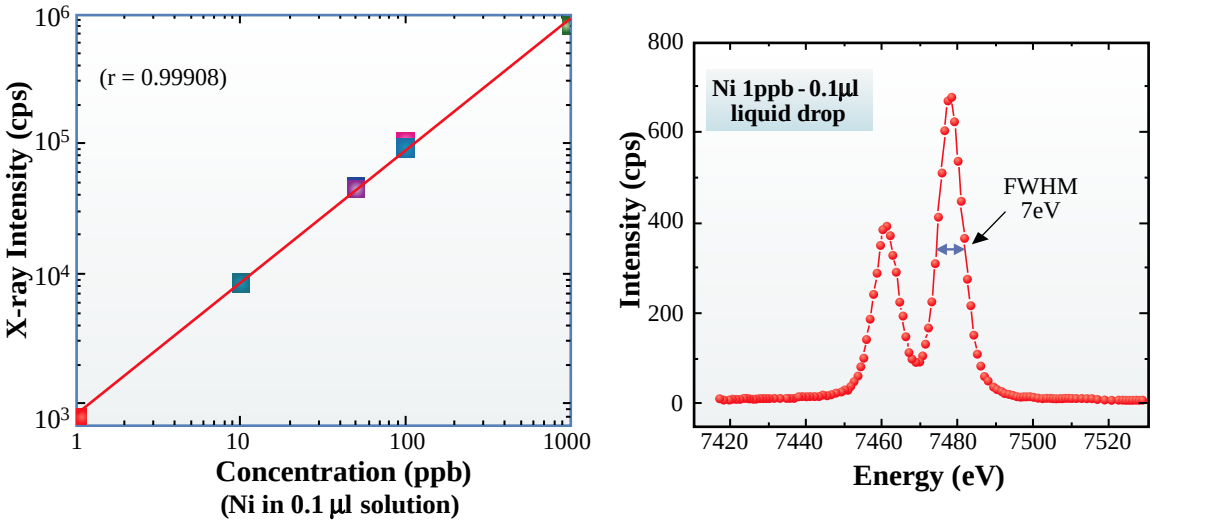


*Fig. 5. Performance of the present wavelength-dispersive TXRF spectrometer, ppt level detection limit with less than ΔE = 10 eV.*

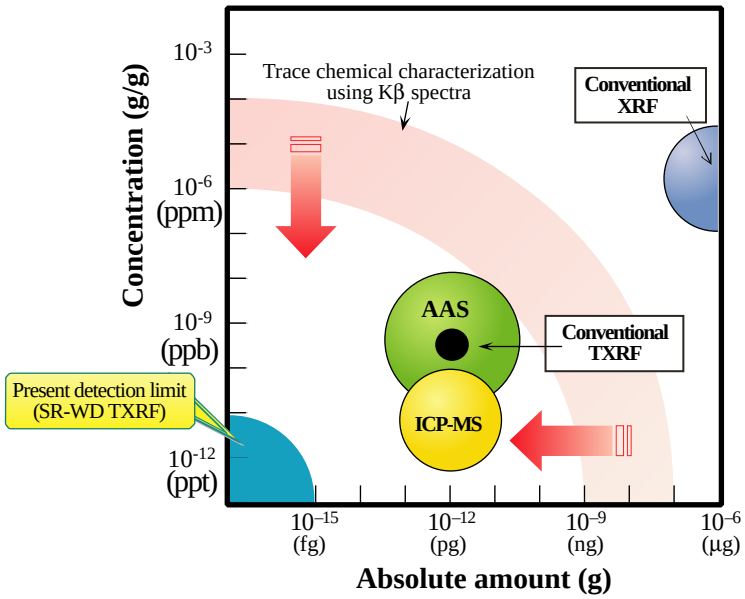


*Fig. 6. Comparison of relative and absolute detection limits. Combination of the undulator source and the present TXRF spectrometer can provide the most powerful tool for trace element analysis. AAS: atomic absorption spectrometry; ICP-MS: inductively coupled plasma-mass spectrometry.*

Kenji Sakurai

National Institute for Materials Science (NIMS)

E-mail: sakurai@yuhgiri.nims.go.jp

**References**

[1] A. Iida and Y. Gohshi, Handbook on Synchrotron Radiation, eds. S. Ebashi, M. Koch and E. Rubenstein, Chap. 9, **4** (1991) 307.

[2] R. Klockenkamper, "Total-Reflection X-ray Fluorescence Analysis", John Wiley & Sons, New York (1997).

[3] K. Sakurai, H. Eba, K. Inoue and N. Yagi, Anal. Chem. (2002) - in press.

[4] K. Sakurai and H. Eba, Jpn. J. Appl. Phys. Suppl. **38-1** (1999) 650.

[5] H. Eba *et al.*, Anal. Chem. **72** (2000) 2613.

[6] K. Sakurai *et al.*, Nucl. Instrum. Meth. **A 467-468** (2001) 1549.

[7] K. Sakurai and H. Eba, Nucl. Instrum. Meth. **B** (2002) - in press.

[8] N. Awaji *et al.*, Jpn. J. Appl. Phys. **39** (2000) L1252.

[9] P. Pianetta *et al.*, Thin Solid Films **373** (2000) 222.

[10] M. Harada *et al.*, Rev. Sci. Instrum. **72** (2001) 4308.

[11] P. Wobrauschek *et al.*, Spectrochim. Acta **B 52** (1997) 901.

# Accelerators & Beamlines Frontiers

# Beam Performance and Upgrades of the Storage Ring

## Orbit Stability

Beam orbit stability is crucial for the generation of brilliant and stable photon beams for synchrotron radiation sources. Its realization is thus very important among various accelerator problems. Recently the beam orbit stability has been markedly improved and consequently orbit jumps by periodic orbit correction are being suppressed to a level where jumps are undetectable to users. This is due to the combination of the following four improvements. First is an improvement in current stabilizing circuits in the quadrupole magnet power supplies, which markedly reduce the current ripples and drifts. Second, with a reduction of horizontal orbit oscillation around 1Hz by the above improvement in current stabilizing circuits and an averaging of the beam position data on VME, the reproducibility of BPMs have been improved from several to about one micron in r.m.s. Therefore, any setting errors of correcting dipole magnets are drastically reduced in each orbit correction procedure. Third, to reduce errors due to the setting resolution of the correcting dipole magnet, air-core-type correcting dipole magnets with both high resolution and low hysteresis were installed. The twelve correcting dipole magnets in each plane are now used in routine user operation. Fourth, the correction algorithm was changed to utilize the good reproducibility of the BPMs, *i.e.*, the real orbit deviation is used as a correction target instead of the re-synthesized one making use of the Fourier harmonics of the orbit deviation. Figure 1 shows the amplitude changes of the betatron tune-harmonics (40th for horizontal and 18th for vertical) of COD for one day after the above improvements. The amplitude changes stay within 1μm and the orbit jump is small before and after the beam refilling. Before these improvements, the amplitude changes were about 5 μm for horizontal and about 3 μm for vertical. To achieve further orbit stability of sub-micron, a task force for orbit stability was organized and has been conducting overall improvement activities from a multilateral point of view.

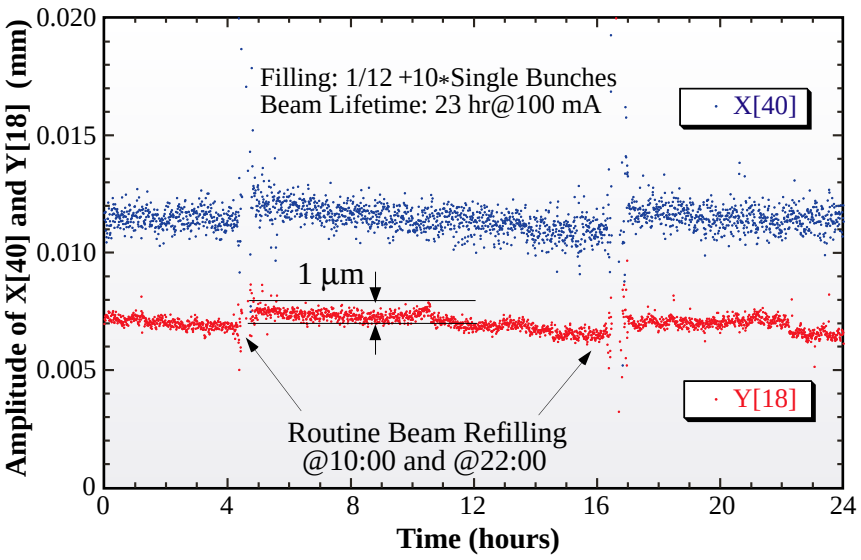


*Fig. 1. Typical one-day orbit stability in a several bunch operation.*

## Electron Beam Emittance at User Operation

The lattice structure of the SPring-8 storage ring is a typical DBA configuration. This kind of configuration has an advantage in reducing electron beam emittance by extra radiation from insertion devices (IDs), because the ID radiation enhances the radiation damping but scarcely excites the betatron oscillation. At present, 22 IDs were installed in SPring-8 and are routinely employed in user operations. Most of them are in-vacuum types, the peak field of which is rather higher than an out-of-vacuum type. The above facts suggest us the possibility that the emittance reduction due to the ID radiation is not negligible. By using the ID parameters, we calculated dependence of the emittance on the extra radiation loss by IDs. We also measured the horizontal beam size variation by a visible light interferometer when ID gaps are closed to the minimum value one by one to estimate the emittance variation. Figure 2 shows the calculated horizontal emittance reduction ratio against the radiation loss increment by IDs together with the measured one. Here the horizontal axis stands for increment of the radiation loss by closing IDs. Both data agree well, as can be seen in Fig. 2. The horizontal emittance reduces as the radiation in the horizontal plane increases and it reaches ~5.3 nm·rad when all ID gaps are minimum. On the other hand, the vertical emittance is generated by six kinds of IDs with a horizontal magnetic field such as an elliptical multi-pole wiggler.

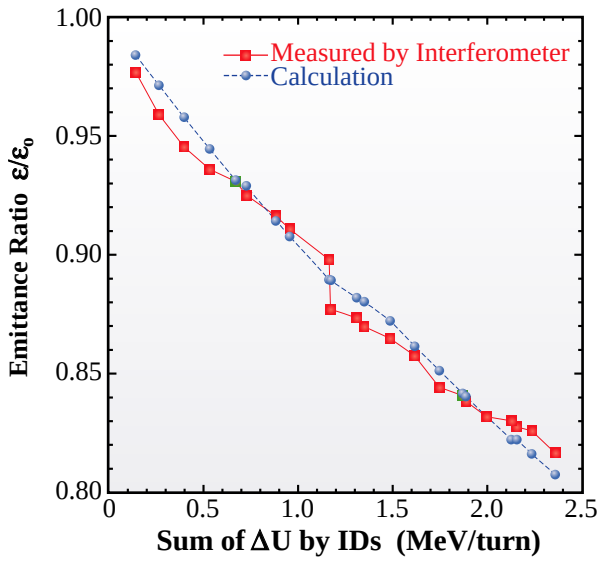


*Fig. 2. Calculated emittance reduction rate against radiation loss by IDs as compared to measured value by interferometer, where $\varepsilon$: with IDs and $\varepsilon_0$: without IDs.*

## Accelerator Diagnostics Beamline

The accelerator diagnostics beamline #1 has a bending magnet light source, and wide band spectral availability including visible/UV light, and soft and hard X-rays is expected. The beamline consists of a front end in the accelerator tunnel, an optics hutch in the experiment hall, a visible light transport line transporting visible/UV light from the optics hutch to a dark room located in the experiment hall, and an X-ray transport line in the optics hutch. The visible light transport line was completed in 2000. Single bunch impurity has been measured by a gated photon counting method, which utilizes fast Pockels cells for switching light pulses, and the bunch length has been measured by a streak camera. The X-ray transport line (Fig. 3) was installed in 2001. It has a double crystal monochromator, which covers the energy range of 4 to 14 keV by Si(111) Bragg reflection. The monochromator crystals and their mechanisms can be moved off the beam axis in the monochromator vacuum chamber when use is made of white X-rays including both soft and hard X-rays. The X-ray

transport line as well as the front end has no Be window, which would obstruct soft X-ray and visible/UV light and potentially distort the wavefront and degrade the quality of beam diagnostics such as the imaging resolution.

The precise measurement of the small vertical size of an electron beam is one of the most challenging subjects of the accelerator beam diagnostics of low emittance synchrotron radiation sources. The resolution of electron beam imaging is significantly improved by utilizing synchrotron radiation in shorter wavelength regions. X-ray imaging observation of the electron beam using a single phase zone plate is in preparation at the X-ray transport line. A monochromatic X-ray is selected by the double crystal monochromator. The magnification factor of the zone plate is about 0.3, and an X-ray zooming tube will be used as a detector to compensate for demagnification.

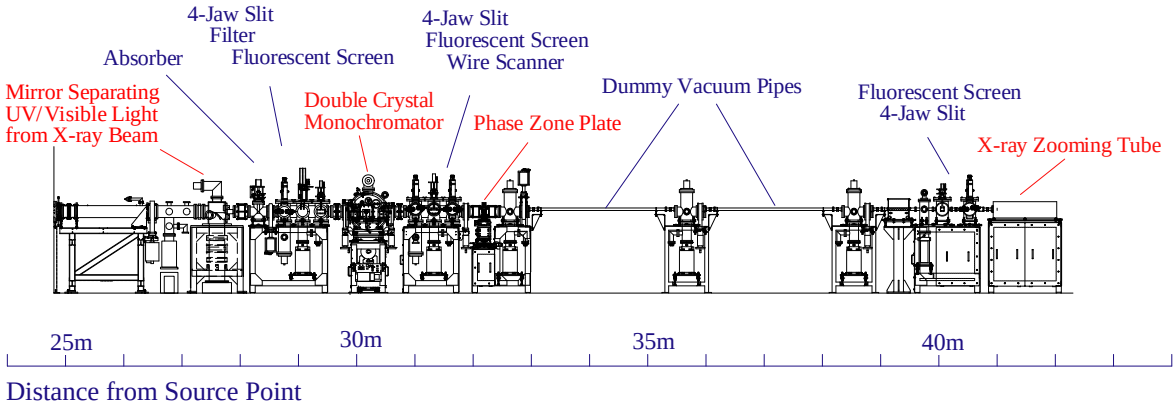


*Fig. 3. X-ray transport line of accelerator beam diagnostics beamline #1.*

The R&D of accelerator components and new types of light sources are other major research subjects. In the X-ray transport line, there are two dummy vacuum pipes of approximately 2 m length, which will be replaced by an apparatus for the specific purposes of R&D. For example, the study of the effects of synchrotron radiation on cooling water in vacuum components such as absorbers is in progress. Production of γ-ray photons with energy of the order of 10 MeV is in preparation, which utilizes the backward Compton scattering of the far infrared laser photons injected to the storage ring.

## Other Research and Developments Activities

The following research and development activities were performed:

- Analysis of beam instability and bunch-by-bunch feedback test.
- Beam loss analysis in the injection process and installation of new injection septum magnets to realize a top-up operation.
- Test of low energy operation at the booster synchrotron and the storage ring.

## Accelerator Stabilization

An energy compression system (ECS), which was completed in 2000, achieved remarkable beam performances improvements as follows:

• The energy spread of the 40 ns beam was compressed from 3.5% to 1.4% at the beam current of 350 mA. Consequently, the injection current into the synchrotron was increased about five times without decrease the injection efficiency.

• The energy fluctuation of the 1 ns beam at a beam charge of 1.9 nC was reduced from 0.06% rms to 0.02% rms as illustrated in Fig. 4.

• The injection rate into the New SUBARU storage ring – 1.5 GeV synchrotron radiation source for VUV region – reached more than 90% and maintained this during one operation cycle of three- or four-weeks.

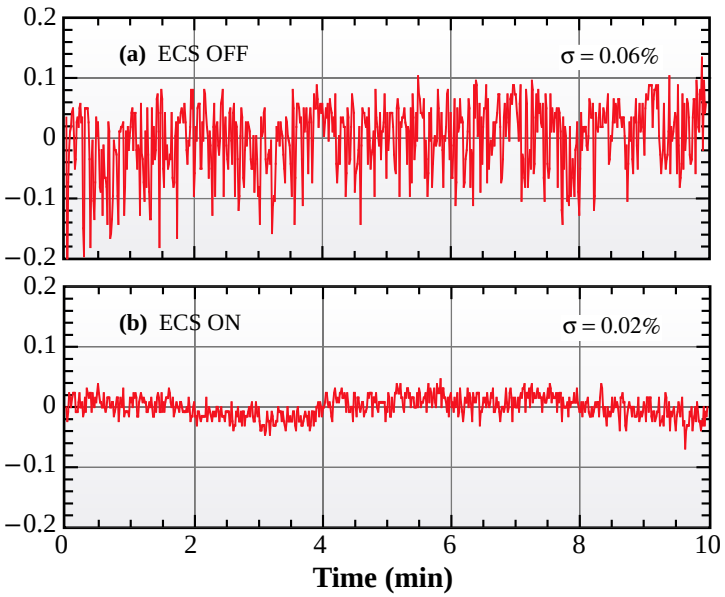


*Fig. 4. ECS reduced the energy fluctuations of 1 ns beams at 1.9 nC.*

## Uniform Bunch Current at Several Bunch Operations

In the several bunch operations of the storage ring, each bunch current is equalized at the injection to the storage ring by adjusting manually the current of the linac gun. The current can be changed by modifying the voltage of the grid pulser, or by inserting an iris in front of the gun. Though a change in the accelerating charge results in a change of the beam loading which leads to a change in the beam energy, an ECS works to stabilize the beam energy extracted from the linac. The stored bunch current of the storage ring is measured by the monitoring signal amplitude from a button pickup using an oscilloscope which monitors the trigger delays. The typical deviation of the bunch current to the mean value is less than 3%.

### Development of RF-gun

We introduced a new 0.3 TW laser system for the RF-gun in order to stabilize the laser power and make the laser pulse width variable. It has a power stability of about 3% and the pulse width can be selected from 1 to 19 ps. The vacuum system was also reinforced, with the result that the dark current from the cathode plane was reduced to 1/10 of its previous value.

A preliminary experiment presented the minimum normalized beam emittance of 6 π mm•mrad at a beam charge of 0.3 nC/bunch. Figure 5 shows a photograph of the RF-gun experimental setup.

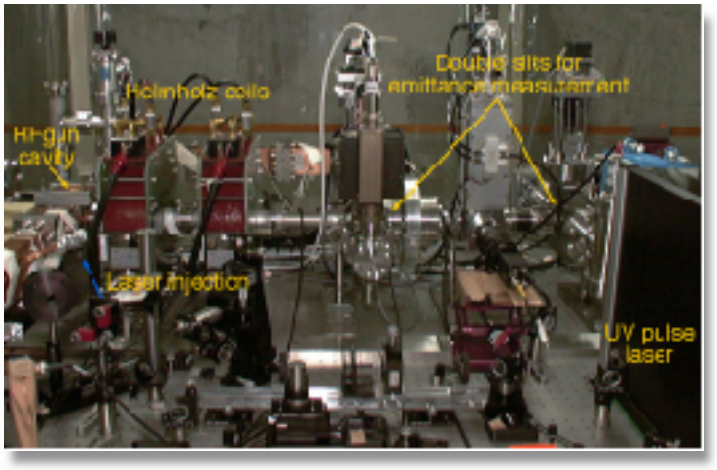


*Fig. 5. RF-gun experimental setup on an optical bench.*

## Upgrades of RF Timing System

### Improvements of the Timing System of the Booster Synchrotron

The timing system of the synchrotron receives a 508.58 MHz RF reference signal and a 1-cycle signal at a rate of 1 Hz from the RF station of the storage ring and regenerates many timing signals such as a gun trigger, pulse magnet triggers and ramping patterns. We improved the timing system of the synchrotron to give it better stability and flexibility. In the SPring-8 RF timing system, a phase-locked-loop (PLL) feedback, using the signal returned in the same optic fiber reflected by the mirror located at the end point was applied for phase stabilization. PLL feedback was already adopted most of the entire signal-transmission line between the RF station of the storage ring and the RF low power system of the synchrotron. A lso, the phase control part in the RF low power system was stabilized by PLLs. In 2001, a PLL feedback was introduced in the remaining part of the signal-transmission line. As a result, the fluctuation in the RF phase between the synchrotron and the storage ring is less than 0.3 degree. The fluctuation in the RF phase between the linac and the synchrotron has been remarkably improved. The measured time jitter of a gun trigger to the RF signal is 18 ps in r.m.s. This improvement results in benefits to other advanced operations of the synchrotron, for example, storing an electron beam for longer than 1 second, changing the injection cycle from 1 Hz to a slower frequency to increase the RF knock-out operation period and ejecting the low energy beam during ramping up.

## Development of the New RF Synchronization System between the Linac and Circular Accelerators

A new synchronization system for two different RFs was introduced. A 508.58 MHz RF is used in both the booster synchrotron and the storage ring, and the linac uses a 2856 MHz independent RF. The phase between the 508.58 and 2856 MHz RFs was not locked. In the new synchronization method, the pre-trigger signal triggers a 2856 MHz RF generator, which consists of an arbitrary waveform generator and a frequency multiplier. The time width generating the 2856 MHz RF is about 290 μs. The RF for a linac is generated by the RF of a circular accelerator. The uniqueness of this method is that an RF for a linac is not continuously generated but pulsing. The RF generator apparatus for a linac is simple and can be applied to any combination of two RFs. With this new method, beam intensity from the linac was kept almost constant even with higher peak current, and the shift of the beam energy center became smaller than that when an independent synthesizer is used. The block diagram is shown in Fig. 6. The energy stability was not only almost constant but also fell to 0.015% and beam quality was remarkably improved.

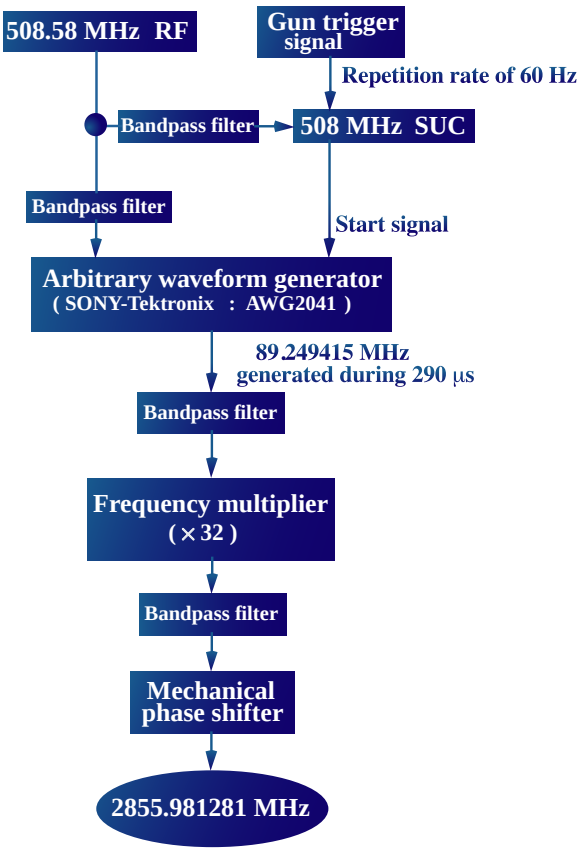


*Fig. 6. Block diagram of the new synchronization method between the 508.58 MHz and 2856 MHz RFs.*

Haruo Ohkuma and Noritaka Kumagai
SPring-8 / JASRI

# Characterization of Total Reflection Mirrors Fabricated with Chemical Vaporization Machining (CVM) and Elastic Emission Machining (EEM) Techniques

One of the most irritating problems in X-ray optics for 3rd generation synchrotron radiation has been spatial fringes observed in the totally reflected beam by mirrors. The relatively high spatial coherence of the X-rays from 3rd generation sources makes interference fringes caused by figure errors in mirrors fabricated with conventional polishing techniques. To fabricate higher-quality mirrors with less figure- and slope-errors is a challenge to realize the coherence preserving optics which are required for both 3rd and the coming 4th generation sources.

A group from the Department of Precision Science and Technology of Osaka University and the SPring-8 Optics Group started collaboration on the fabrication of new-generation mirrors in February 2001. X-ray reflection properties are compared by observing the images of the reflected beam at different mirror-detector distances among mirrors fabricated with (i) a conventional polishing technique, (ii) chemical vaporization machining (CVM) [1], and (iii) elastic emission machining (EEM) [2].

A characterization setup was constructed at the one-kilometer experimental station of BL29XU [3], using a standard diffractometer for precision optics [4] as a mirror orientator, and Hamamatsu Zooming Tube as a high spatial-resolution image detector (Fig. 1). A sample mirror prepared from a (001) Si slab was firstly prepared with a conventional polishing technique, a striped region was refined by a CVM technique, and then a part of the CVM-finished striped region was further refined by an EEM technique (Fig. 2)[5].

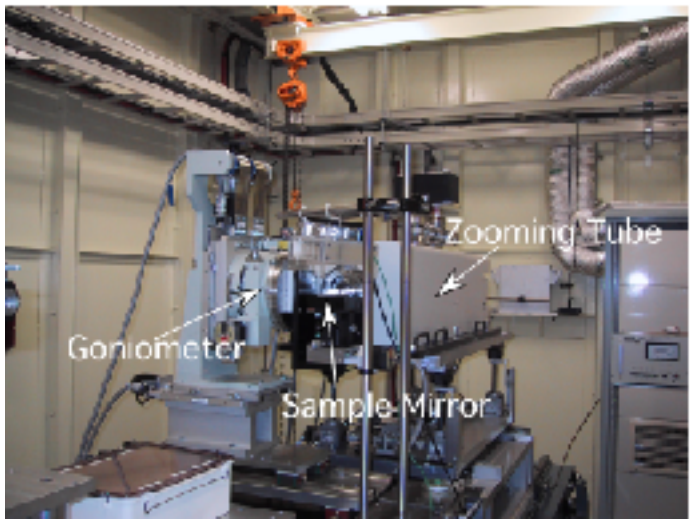


*Fig. 1. A mirror characterization setup constructed at the 1-km endstation of BL29XUL.*

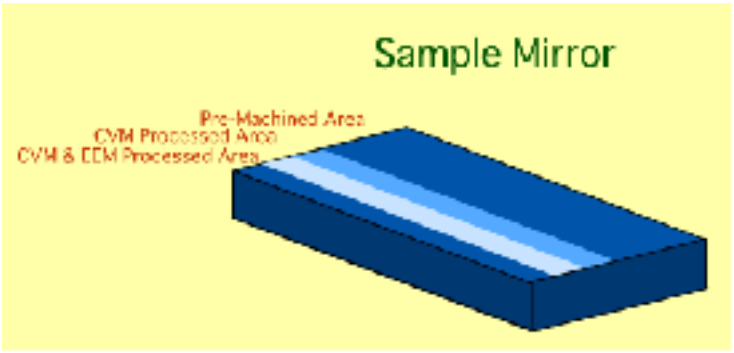


*Fig. 2. Sample mirror. A (001) surface of Si (50 mm × 100 mm) was firstly finished with a conventional polishing technique (Pre-Machined Area). A striped area was refined by a CVM technique, and a part of this was further refined by an EEM technique.*

In Fig. 3 are shown images of reflected beam from a conventionally polished area (designated as Pre-Machined), a CVM finished area and an EEM-CVM finished area taken at three different sample-detector distances (166 mm, 566 mm, and 966 mm). The surface profiles measured with an optical interferometric technique are also shown. A slight curvature of the conventionally polished region gave rise to a focusing effect, changing the size of the reflected beam with the detector position. High-contrast interference fringes can be observed on the pre-machined surface. CVM correction of the surface profile could remove the curvature, and bring the peak-to-valley height error to within several nm. Nevertheless, the fringe contrast in the reflected beam images still remains. Additional EEM correction of the surface profile reduced the peak-to-valley height error to below 2 nm. The fringe contrast in the reflected beam images faded out for the EEM finished surface, except on the edge region where the edge effect is dominant.

For the correction of surface figure with the EEM technique, an advanced metrology with high accuracy is quite important. We found that the widely used surface profile measurement technique, the Long Trace Profiler (LTP) [6] had insufficient spatial resolution for the fabrication of mirrors suppressing interference fringes. Therefore, stitching interferometry combining the ZYGO NEW-VIEW with large area Fizeau interferometer was developed. The surface profile measured with the new stitching technique reproduced the observed beam profiles fairly well by calculating numerically the Fresnel-Kirchhoff integral for the incident full-spatially-coherent X-rays [5]. An algorithm to retrieve the surface figure from beam images at different sample-detector distances was also successfully developed [7].

Since both CVM and EEM are based on chemical processes which occur in removing atoms from the mirror surface, they do not damage the crystal lattice of the works. Therefore, these techniques are easily applicable to Bragg-diffraction optical elements such as monochromator crystals. A good agreement between the observation and Fresnel-Kirchhof simulation has opened up a new possibility to fabricate figured mirrors for focusing optics with CVM and EEM. A preliminary prototype has already been fabricated, giving a 0.1 μm wide line focus for 15 keV X-rays.

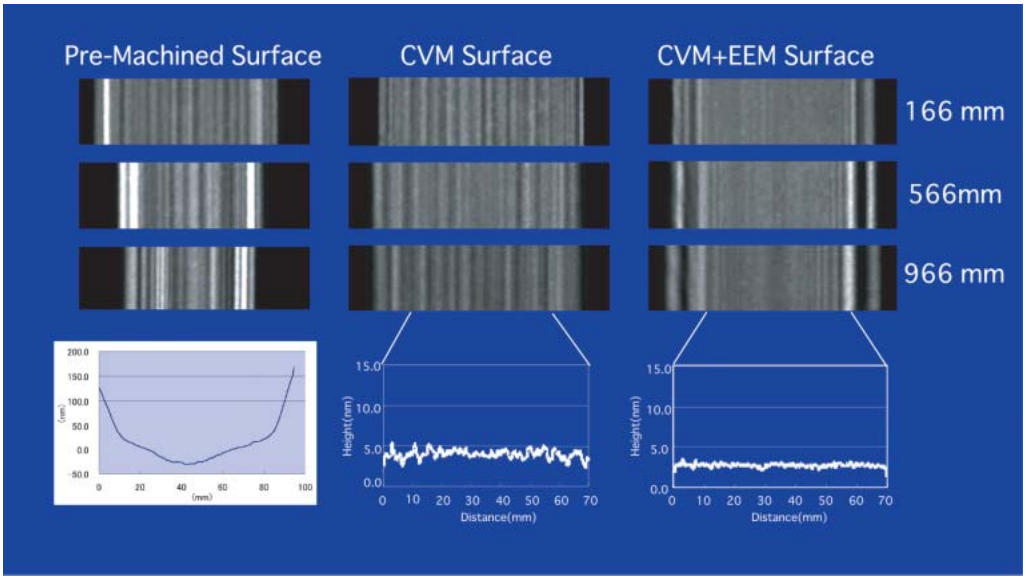


*Fig. 3. Images of reflected beams from conventionally polished (designated as Pre-Machined) area, CVM finished area and a CVM+EEM finished area recorded at 166 mm, 566 mm and 966 mm from the center of mirror. Corresponding surface profiles measured with an optical interferometer are shown. Glancing angle of 1.2 mrad at 15 keV X-rays.*

**References**

[1] Y. Mori *et al.*, Precision Engineering **9** (1987) 123.

[2] Y. Mori *et al.*, Rev. Sci. Instrum. **71** (2000) 4620; Y. Mori *et al.*, Rev. Sci. Instrum. **71** (2000) 4627.

[3] T. Ishikawa, K. Tamasaku, M. Yabashi, S. Goto, Y. Tanaka, H. Yamazaki, K. Takeshita, H. Kimura, H. Ohashi, T. Matsushita and T. Ohata, Proc. SPIE **4145** (2001) 1.

[4] K. Tamasku *et al.*, Nucl. Instrum. Methods **A467-468** (2001) 686.

[5] Y. Mori *et al.*, Proc. SPIE **4501** (2001) 30.

[6] P. Z. Takacs, Proc. SPIE **749** (1987) 59; P. Z. Takacs and S. Qian, US Patent 4884679 (1989).

[7] A. Souvorov, M. Yabashi, K. Tamasaku, T. Ishikawa, Y. Mori, K. Yamauchi, K. Yamamura and A. Saito, J. Synrotron Rad., submitted.

Yuzo Mori[a] and Tetsuya Ishikawa[b]

(a) Osaka University
(b) SPring-8 / JASRI∑RIKEN

# One-dimensional Microstrip Germanium Detector

The momentum resolution of the Cauchois-type spectrometer reaches 0.13 atomic units at the high-energy inelastic scattering beamline (BL08W) [1]. The spectrometer is equipped with a conventional Germanium detector with four slits in front to allow such observations as Fermi surface signatures of $Sr_2RuO_4$. Now the spectrometer is to be equipped with a one-dimensional microstrip Germanium detector so as to establish a higher detection efficiency around the 80 keV X-ray region as well as a high background rejection capability [2].

There are one hundred twenty eight cathode strips that are photo-chemically formed on the Germanium crystal, the width, the interstrip, and the length of which are 300 μm, 50 μm, and 50 mm, respectively. When compared with the original system, the data-taking speed is expected to be 30 times faster in the new detector system. Owing to the high momentum resolution and the high detection efficiency, the spectrometer will yield a few dozen Compton profiles of, for example, heavy element metals or alloys, during a reasonable beamtime with a sufficient accuracy. Reconstructing the three-dimensional momentum densities from the multifold Compton profiles observed should significantly enrich knowledge about their Fermi surfaces.

The one-dimensional microstrip Germanium detector mentioned above was constructed during the second stage of the R&D program on the position-sensitive detector for the beamline. In order to handle the large number of the readout channels, four 32-parallel-input front-end hybrid-boards

*Fig. 1. 128-channel microstrip Germanium detector with four 32-parallel-input front-end hybrid boards mounted.*

(IDEAS, VA32c-TA32cg ) were adopted as charge-sensitive pre-amplifiers and discriminators. These boards are currently controlled by a Windows-based PC data acquisition system (IDEAS, VADAQ ). Because of its A/D conversion time of 30 μsec, however, the data-taking speed achieved with the new detector system is still limited and is only four times faster than the original system. In order to improve the speed, a data acquisition system with flush ADC VME modules and a conversion time of 100 nsec maximum is currently under development.

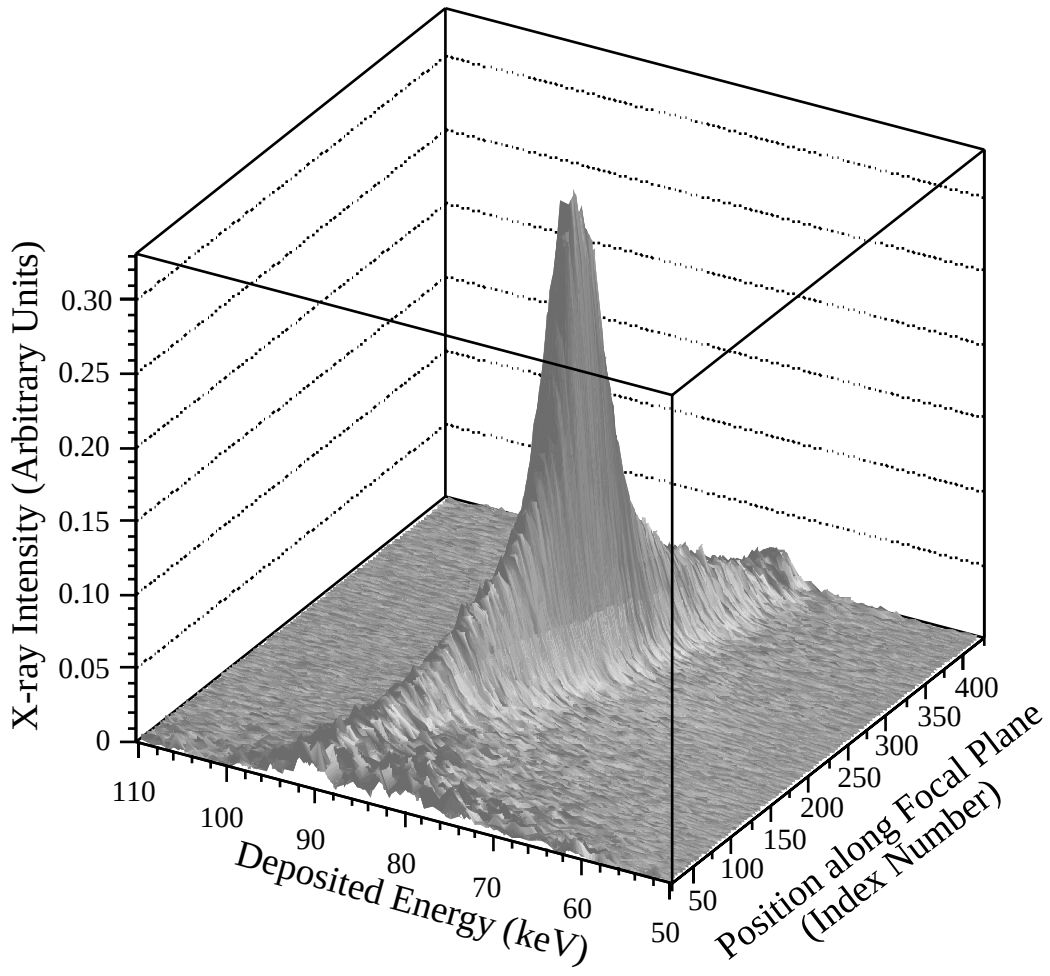


*Fig. 2. X-ray energy spectra observed at focal plane with a sample of Nb in 2-D representation.*

**References**

[1] SPring-8 Research Frontiers 1998/1999, p. 77.
[2] SPring-8 Research Frontiers 1998/1999, p. 98.

Masayo Suzuki and Naoto Yagi
SPring-8 / JASRI

# Facility Status

## SPring-8 Campus

# Machine Operation

The operational statistics since the inauguration are shown in Fig. 1. In 2001, the SPring-8 storage ring was operated in three- or four-week period for one operation cycle. The total operation time of accelerator complex was 5456.1 hours. About 74% of the operation time was available to users. The injection time and the down time due to failure accounted for 1.1% and 1.6% of the operation time, respectively. The remaining 23.4% was dedicated for: (i) the machine and beamline study, (ii) the machine and beamline tuning, (iii) the commissioning of new beamlines.

The operation modes of three different filling patterns were delivered to the user time; 37.8% in the multi-bunch mode, 38.9% in the several bunch mode such as 203-bunch mode (203 equally spaced bunches) and 84 equally spaced 4-bunch trains, and the remaining 23.3% in the hybrid filling mode such as a 1/12-partially filled multi-bunch with 10-isolated bunches. In 2001, several-bunch mode has been on the increase. For the hybrid filling mode, 1 or 1.5 mA is stored in each isolated bunch. A purity of isolated bunch better than $10^{-9}$ is routinely being delivered.

The operation schedule for the accelerator complex is usually fixed semiannually. These semiannual terms are referred to as the research terms for users, the first and second halves of which are denoted as xxxxA and xxxxB, respectively. In the first three years after the inauguration of SPring-8, the research term was defined on the basis of the Japanese fiscal year. From the year of 2000, however, the research term has been defined on a calendar year basis for the smooth scheduling with the Proposal Review Committee members.

In the past four years, the SPring-8 accelerator complex has experienced long-term shutdowns for two months in summer and one month in winter in order to install insertion devices and front-end components for new beamlines.

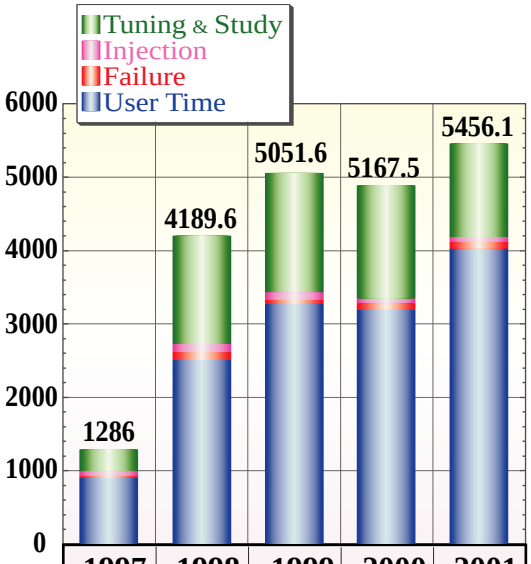


| | 1997 | 1998 | 1999 | 2000 | 2001 |
|---|---|---|---|---|---|
| Tuning & Study (Accel. & BL) | 304 | 1457.6 | 1624.2 | 1815 | 1276.5 |
| Injection | 50 | 110 | 95.2 | 70.4 | 59.3 |
| Failure | 26 | 110 | 57.2 | 88.7 | 87.1 |
| User Time | 906 | 2512 | 3275 | 3193.4 | 4033.2 |

*Fig. 1. Operational statistics since the inauguration.*

# BEAMLINES

The beamlines at the SPring-8 Facility are categorized into four groups as listed below:

(1) Public Beamlines,
(2) Contract Beamlines,
(3) JAERI / RIKEN Beamlines,
(4) Accelerator Beam Diagnosis Beamlines.

The public beamlines are constructed with the support of the national budget, and are entirely open for public use. This category of public beamlines includes the R&D beamlines, which were constructed for the purpose of developing new devices and beamline equipment such as optical elements, detection systems, and so forth. Used mainly by SPring-8 staff, the R&D beamlines are also open to public. Now 24 public beamlines are operational and available for public use. The Trace Element Analysis Beamline, BL37XU, will soon be completed and ready for public use.

The contract beamlines are, on the other hand, facilities that are installed, owned, operated and maintained by universities, companies and other organizations. Beamline contractors can use their beamline almost exclusively. Hyogo Prefecture took the lead in the contract beamline construction and the Industrial Consortium, Institute for Protein Research (Osaka Univ.), the Research Center for Nuclear Physics (Osaka Univ.) and National Institute for Materials Science followed in that order, after which the first foreign contract beamlines (BL12B2 and BL12XU) were constructed by the Asia and Pacific Council for Science and Technology

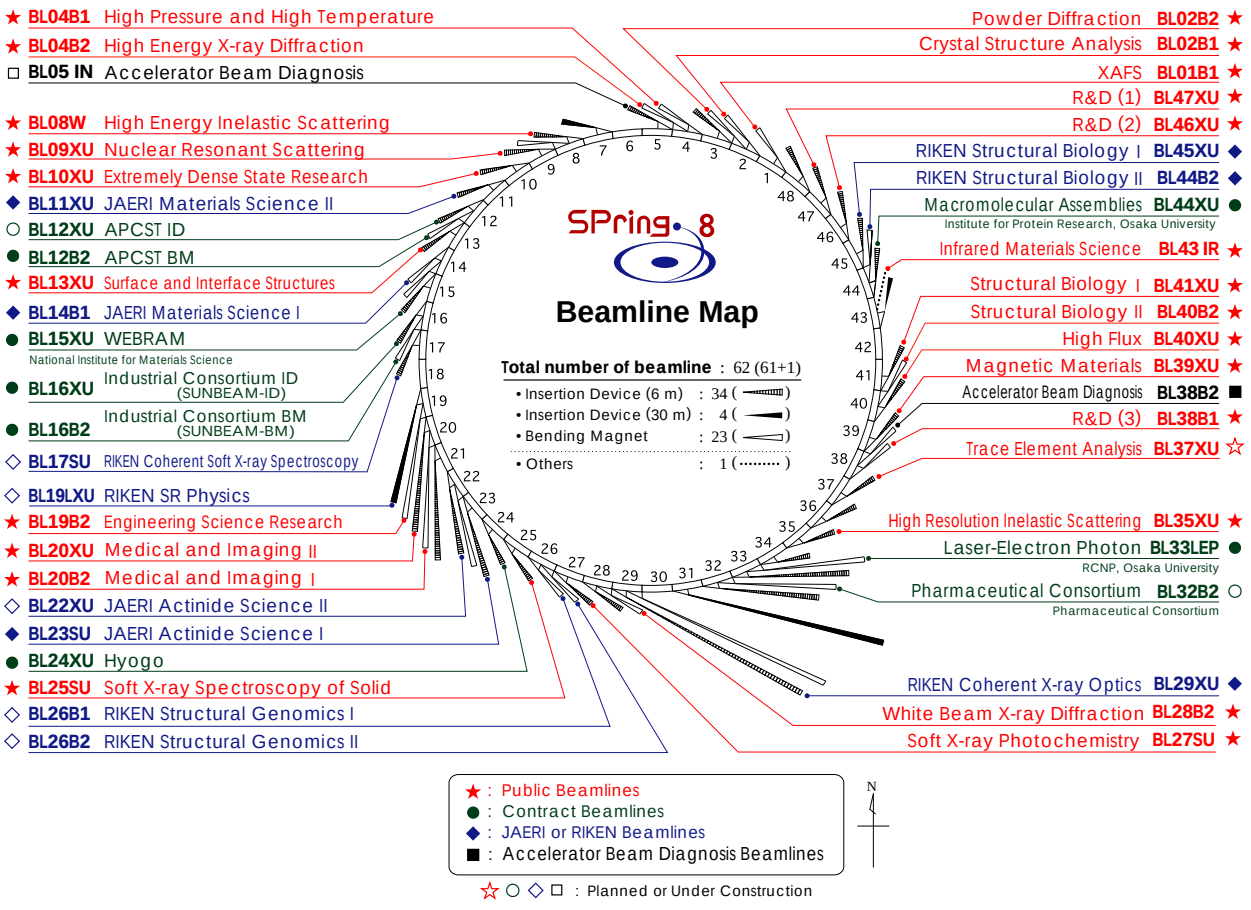


*Fig. 2. Beamline Map.*

in Taiwan. Currently those eight contract beamlines are all in operation. The ninth contract beamline by the Pharmaceutical Consortium for Protein Structure Analysis is now under construction. The JAERI/RIKEN beamlines are those constructed by JAERI and RIKEN to promote their own research activities. 11 beamlines have been constructed or are under construction by JAERI and RIKEN for the exclusive use of JAERI and RIKEN scientists. BL19LXU, one of RIKEN beamlines, is an ID beamline with a long undulator at a 30 m-long straight section and was installed while rearranging the magnets in the storage ring during the summer shutdown of 2000. BL26B1 and BL26B2 are beamlines that will be used for "high throughput" protein crystallography following the human genome project. BL29XU has two experimental stations, one located at the experimental hall, and the other at the end of the 1 km beamline.

Dedicated to studying the characteristics of the electron beam accumulated in the storage ring, the accelerator beam diagnosis beamlines are currently under the exclusive use of the JASRI accelerator group.

As of October 2001, two beamlines are currently in the phase of commissioning (BL12XU, BL19LXU, BL22XU) and six beamlines (BL17SU, BL26B1, BL26B2, BL32B2, BL37XU) are under construction.

All beamlines are shown in the Beamline Map (Fig. 2). Including the two accelerator beam diagnosis beamlines, we have 47 beamlines, *i.e.*, about 75% of 62 beamlines that SPring-8 can accommodate.

# User Operation

Each year SPring-8 holds two calls for proposals to use its public beamlines. Beam time is then allocated to selected applicants for the forthcoming SPring-8 research term. The first such term (1997B) ran from October 1997 (when the facility opened) until the end of Japan's financial year, March 1998. The second research term (1998A) ran from April 1998 until October 1998. After a somewhat longer third research term (1999A) from November 1998 until June 1999, SPring-8 roughly divided the year's user beam time into two terms with the summer shutdown in between. The proposal submission deadlines for the sixth and seventh research terms (2000B and 2001A) were October 21, 2000 and May 26, 2001, respectively. SPring-8 Proposal Review Committee approved 380 out of the 582 proposals submitted for 2000B and 409 out of 502 for 2001A. The numbers of selected proposals for proprietary research were 12 in 2000B, and 8 in 2001A, respectively. And the percentage of selected proposals from overseas was 5% for both terms. SPring-8 operational results for the period from 1997B to 2001A are shown in Table 2. This table shows each user beam time allocated and the number of users and experiments conducted, which are illustrated in Fig. 3. For reference, the relevant data of contract beamlines is also indicated. In 2001A, SPring-8 provided users with 2,381 hours of beam time in five operation cycles. 2,915 individuals used the facility's public beamlines in 473 separate experiments. Between October 1997, opening of SPring-8 for research, and the end of 2001A, a total of 15,951 public and contract beamline users conducted 2,462 experiments.

| Research Term | User Time (hours) | Public BL | | Contract BL | |
|---|---|---|---|---|---|
| | | Experiments | Users | Experiments | Users |
| 1997B: 1997.10 - 1998.03 | 1,286 | 94 | 681 | | |
| 1998A: 1998.04 - 1998.10 | 1,702 | 234 | 1,252 | 7 | |
| 1999A: 1998.11 - 1999.06 | 2,585 | 274 | 1,542 | 33 | 467 |
| 1999B: 1999.09 - 1999.12 | 1,371 | 242 | 1,631 | 65 | 427 |
| 2000A: 2000.01 - 2000.06 | 2,106 | 365 | 2,486 | 102 | 794 |
| 2000B: 2000.10 - 2001.01 | 1,558 | 382 | 2,370 | 88 | 620 |
| 2001A: 2001.02 - 2001.06 | 2,381 | 473 | 2,915 | 103 | 766 |
| TOTAL | 12,989 | 2,064 | 12,877 | 398 | 3,074 |

*Table 2. SPring-8 operational results.*

**Public Beamlines (25)**

| BL # | Source | Beamline Name | Status |
|---|---|---|---|
| BL01B1 | BM | XAFS | in operation |
| BL02B1 | BM | Crystal Structure Analysis | in operation |
| BL02B2 | BM | Powder Diffraction | in operation |
| BL04B1 | BM | High Pressure and High Temperature | in operation |
| BL04B2 | BM | High Energy X-ray Diffraction | in operation |
| BL08W | W | High Energy Inelastic Scattering | in operation |
| BL09XU | U | Nuclear Resonant Scattering | in operation |
| BL10XU | U | Extremely Dense State Research | in operation |
| BL13XU | U | Surface and Interface Structures | in operation |
| BL19B2 | BM | Engineering Science Research | in operation |
| BL20XU | U | Medical and Imaging II | in operation |
| BL20B2 | BM | Medical and Imaging I | in operation |
| BL25SU | U | Soft X-ray Spectroscopy of Solid | in operation |
| BL27SU | U | Soft X-ray Photochemistry | in operation |
| BL28B2 | BM | White Beam X-ray Diffraction | in operation |
| BL35XU | U | High Resolution Inelastic Scattering | in operation |
| BL37XU | U | Trace Element Analysis | under construction |
| BL38B1 | BM | R&D (3) | in operation |
| BL39XU | U | Magnetic Materials | in operation |
| BL40XU | U | High Flux | in operation |
| BL40B2 | BM | Structural Biology II | in operation |
| BL41XU | U | Structural Biology I | in operation |
| BL43IR | BM | Infrared Materials Science | in operation |
| BL46XU | U | R&D (2) | in operation |
| BL47XU | U | R&D (1) | in operation |

**Contract Beamlines (9)**

| BL # | Source | Beamline Name | Status |
|---|---|---|---|
| BL12XU | U | APCST ID (APCST) | in commissioning |
| BL12B2 | BM | APCST BM (APCST) | in operation |
| BL15XU | U | WEBRAM (National Institute for Materials Science) | in operation |
| BL16XU | U | Industrial Consortium ID (Industrial Consortium) | in operation |
| BL16B2 | BM | Industrial Consortium BM (Industrial Consortium) | in operation |
| BL24XU | U | Hyogo (Hyogo Prefecture) | in operation |
| BL32B2 | BM | Pharmaceutical Consortium (Pharmaceutical Consortium) | under construction |
| BL33LEP | BM | Laser-Electron Photon (Osaka University) | in operation |
| BL44XU | U | Macromolecular Assemblies (Osaka University) | in operation |

**JAERI/RIKEN Beamlines (11)**

| BL # | Source | Beamline Name | Status |
|---|---|---|---|
| BL11XU | U | JAERI Materials Science II (JAERI) | in operation |
| BL14B1 | BM | JAERI Materials Science I (JAERI) | in operation |
| BL22XU | U | JAERI Actinide Science II (JAERI) | under construction |
| BL23SU | U | JAERI Actinide Science I (JAERI) | in operation |
| BL17SU | U | RIKEN Coherent Soft X-ray Spectroscopy (RIKEN) | under construction |
| BL19LXU | U | RIKEN SR Physics (RIKEN) | in commissioning |
| BL26B1 | BM | RIKEN Structural Genomics I (RIKEN) | under construction |
| BL26B2 | BM | RIKEN Structural Genomics II (RIKEN) | in commissioning |
| BL29XU | U | RIKEN Coherent X-ray Optics (RIKEN) | in operation |
| BL44B2 | BM | RIKEN Structural Biology II (RIKEN) | in operation |
| BL45XU | U | RIKEN Structural Biology I (RIKEN) | in operation |

**Accelerator Beam Diagnosis Beamline (2)**

| BL # | Source | Beamline Name | Status |
|---|---|---|---|
| BL05IN | U | Accelerator Beam Diagnosis | under construction |
| BL38B2 | BM | Accelerator Beam Diagnosis | in operation |

*Table 1. SPring-8 beamlines.*

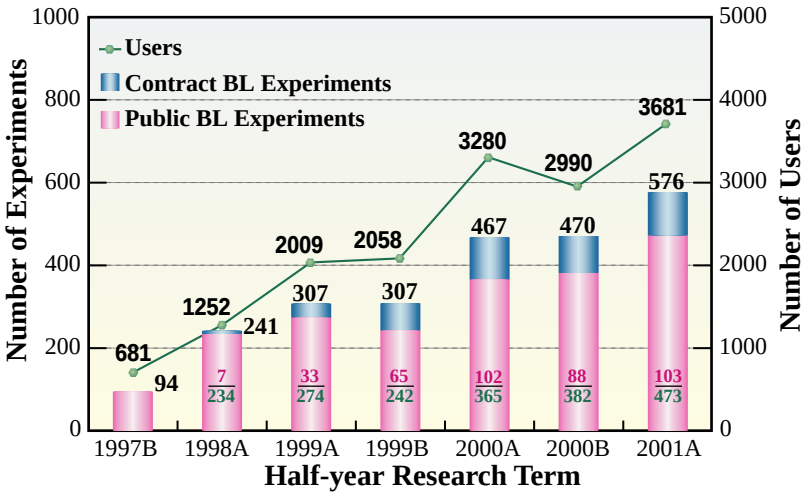


*Fig. 3. Number of users and experiments conducted.*

Figures 4 and 5 indicate the transition of the number of selected proposals by the affiliation of applicants and by the research fields from 1997B to 2001A. As can be seen from the charts, the trend for each year has been almost the same during the period. In other words, as for the classification by the affiliations, universities have accounted for close to 70% and other organizations have made up the rest almost equally. The same trend applies to the classification by the research fields. The ratio of life science, diffraction & scattering and others has been 1:1:1 throughout the same period. The ratio of XAFS, spectroscopy and method & instrumentation, all of which are categorized as "others," has also been 1:1:1. The ratio remained the same except for the first research term (1997B).

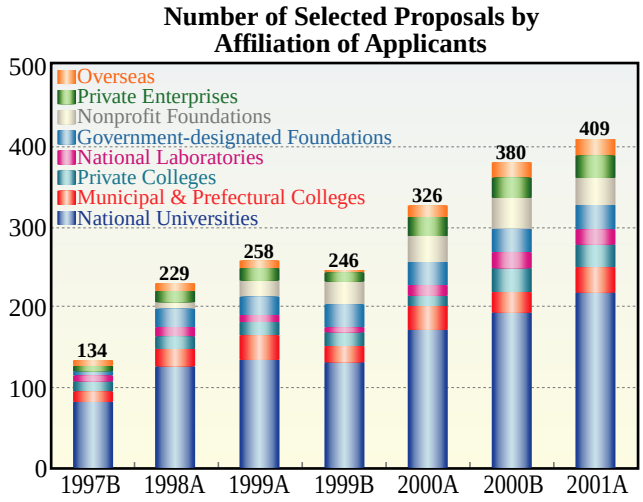


*Figure 4*

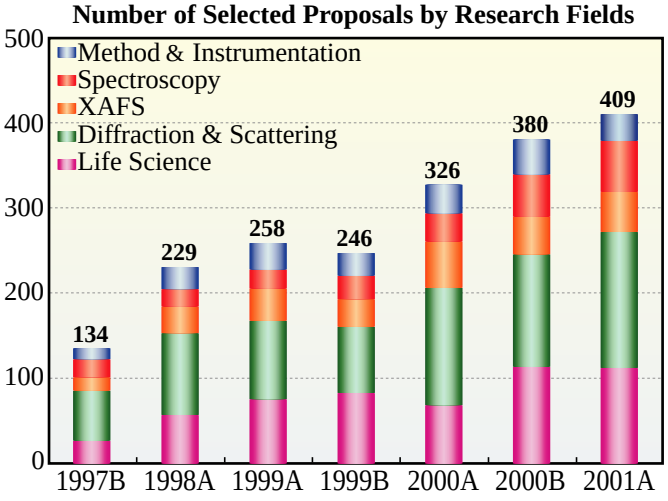


*Figure 5*

## Proprietary Research

For proprietary research, users can keep their results by paying beam time fees. This system is useful when there is some confidential information for commercial purposes in experiments and samples and the users do not want to disclose the results. Since the start of the system in the fourth half-year research term (1999B), 18 experiments have been carried out as proprietary research.

## Long-term Use of Beamlines

Apart from the regular public use, SPring-8 has created a system for the long-term use of beamlines where users can secure beam time for a longer period of time. While the regular beam time is valid for six months, the beam time for this long-term use is valid for up to three years. This system aims to further promote research that will produce outstanding results in the field of science and technology, that will pave the way for new research areas and research methodology and that will help improve the technology for industrial base significantly by getting the most of the characteristics of SPring-8.

## Industrial Research

Together with the promotion of research activities in the field of basic science, contributing to the reinforcement of the technological basis in industry has been one of the major aims of the SPring-8 project. Since its foundation in 1990, JASRI has sought possible ways of industrial applications of SR science.

The framework of the contract beamlines is to facilitate the construction of beamlines by industries at the SPring-8 Facility. Hyogo Prefecture constructed a contact beamline (BL24XU), and has been conducting experiments on protein crystal analysis, surface/interface analysis of inorganic materials, X-ray micro-beam analysis, and X-ray imaging since May 1998. There have been two beamlines (BL16XU and BL16B2) constructed by the industrial consortium that is composed of thirteen companies in the fields of electronics, steel, electric power and automobiles. Since October 1999, the consortium has been carrying out its experiments on X-ray diffraction, X-ray fluorescence analysis, and X-ray micro-beam experiments at the BL16XU, and XAFS and X-ray topography at the BL16B2. Another contract beamline, BL32B2, constructed by the industrial consortium that is made up of 22 pharmaceutical companies is now in commissioning phase and is expected to be ready by the summer of 2002 for experiments and research on protein structure analysis for drug design. In addition, a new beamline for the industrial applications of SR science has been added to the lineup of public beamlines, which is a bending magnet beamline (BL19B2) for experiments on XAFS, multipurpose X-ray diffractometry, and X-ray fluorescence spectroscopy. Its construction will be completed sometime in fall 2001.

## Research Results

When using SPring-8 for non-proprietary research, users are exempted from beam time fees if they submit an Experiment Report within 60 days after their experiment. JASRI expects that users will disclose their research results obtained through non-proprietary research in scientific journals. In cases where the results are disclosed, uses must report to JASRI and have them registered with JASRI.

The number of research results produced by public and contract beamline users and JASRI staff is 1,003 as of August 2001.

# Budget and Manpower

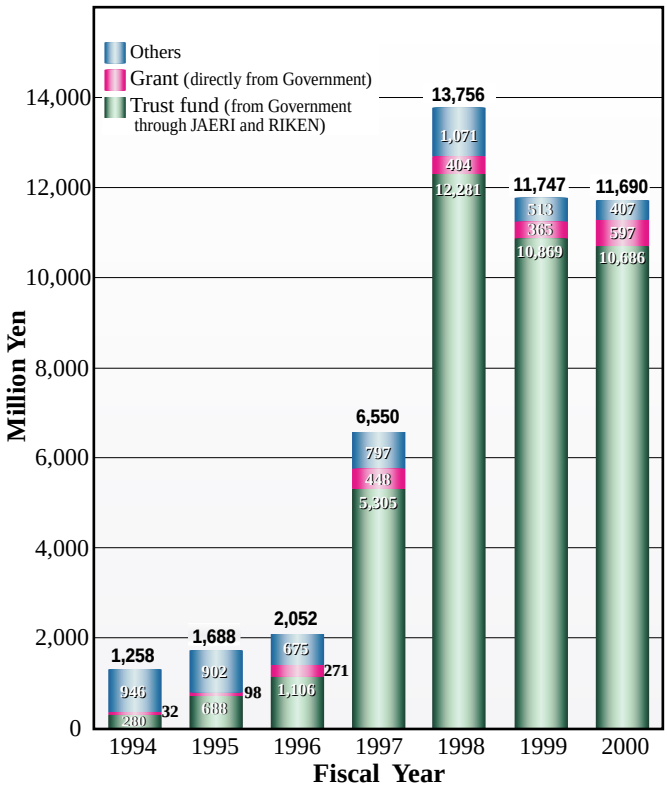


*Fig. 6. Budget.*

The SPring-8 Facility is supported by the Government, in accordance with the guidelines given by the "Council for Aeronautic, Electronics, and other Advanced Technologies." During the course of the facility construction, namely from 1987 to 1997, an overall national budget of 108.9 billion yen was appropriated through JAERI and RIKEN. The breakdown of the budget is as given in Fig 6.

The construction phase was from 1987 to 1997. During this phase, construction of the accelerators was completed. At the end of the phase, the JAERI-RIKEN Project Team was dissolved. JASRI then entrusted with the responsibility for the operation, was maintenance and improvements of SPring-8, technical support for the new beamline construction, and R&D for new SR applications. The total budget for JASRI for fiscal year 2000 was 11,690 million yen. About 90 % of the total budget was allocated for the operation and maintenance of SPring-8, which came from the government through JAERI and RIKEN. The yearly change in the budget for the period from 1994 to 2000 is shown in Fig 6. It is clear that JASRI's budgetary situation has become steady with the transit from the construction phase to the utilization phase in 1998.

When the JAERI-RIKEN SPring-8 Project Team was formed in October 1988, the total number of the staff was 66 and the number increased to 220 by April 1, 1995. At that time, the total number of JASRI staff was only 36. A certain number of the staff started to be transferred from the team to JASRI in preparation for operation and administration of the SPring-8 Facility. When the team was dissolved in 1997, most of the staff had been transferred to JASRI. By the end of July 2000, the total number of full-time staff at JASRI amounted to 338. The number of on-site staff of JAERI Kansai Research Establishment is approximately 60 and RIKEN Harima Institute, approximately 230. The number of staff in the research complex composed of JAERI, RIKEN and JASRI could, therefore, be larger than 600.

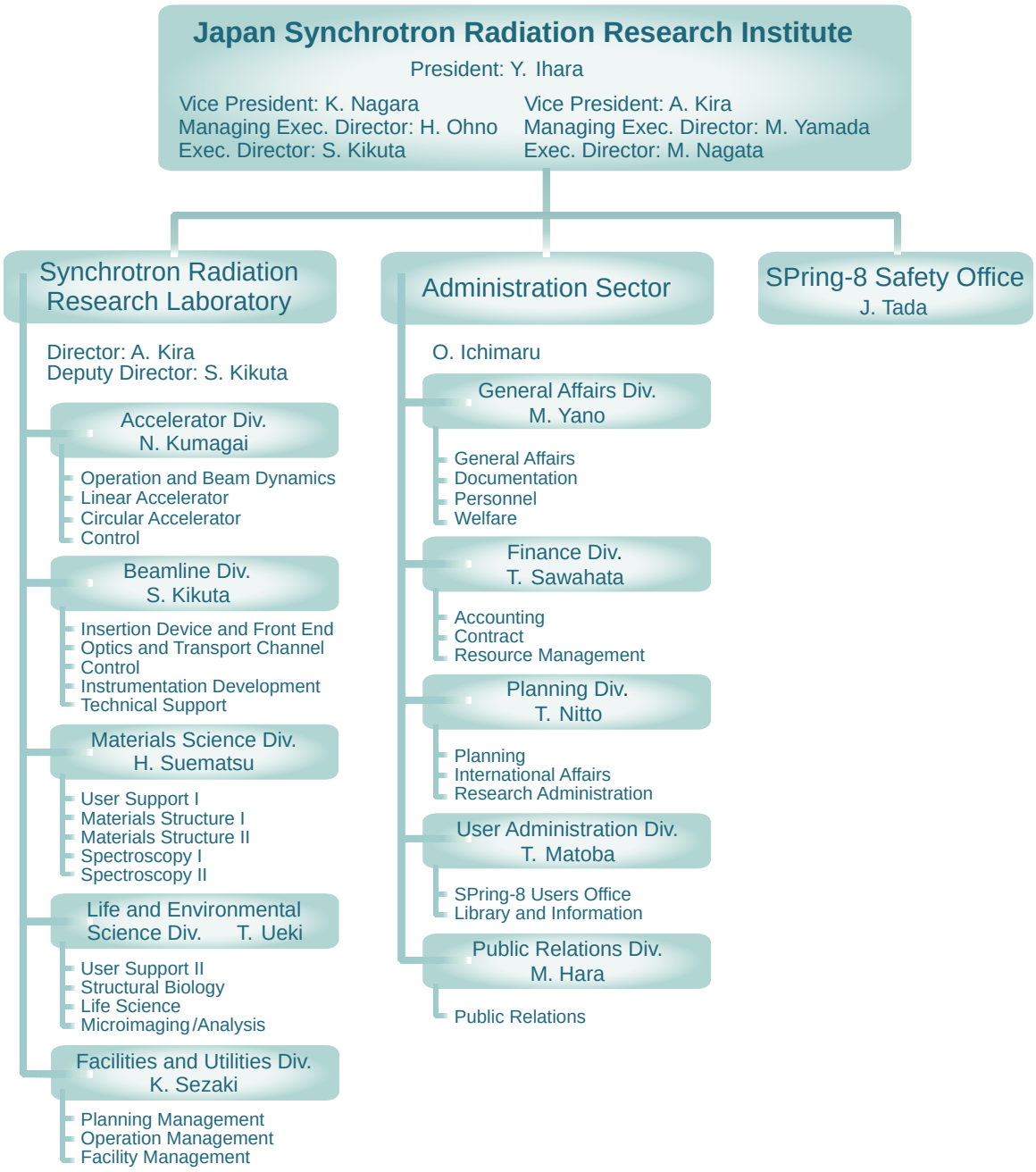


*Fig. 7. SPring-8 Organization.*

# Organization and Committees

The organization that JASRI has formed to accomplish its missions is as shown in Fig. 7. As can be seen in the organization chart, JASRI consists of the Synchrotron Radiation Research Laboratory, the Administration Sector and the SPring-8 Safety Office.

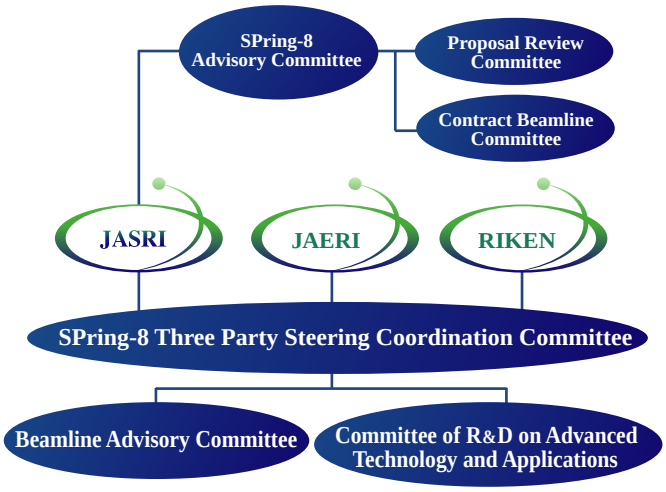


## Synchrotron Radiation Research Laboratory

The Synchrotron Radiation Research Laboratory is divided into five divisions, which are the Accelerator-, Beamline-, Materials Science-, Life and Environmental Science-, and Facilities and Utilities Divisions. The laboratory is responsible for operating, maintaining, and upgrading the accelerator complex and beamlines as well as for carrying out related research activities. It is also responsible for expediting scientific utilization of the facility, supporting the users methodologically and technologically, establishing a database of scientific and technical information, and keeping the SR community informed about the usage of the beamlines.

## Administration Sector

The Administration Sector is made up of five divisions, which are the General Affairs-, Finance-, Planning-, User Administration- and Public Relations Divisions. The sector is responsible for the planning and coordination of research-related projects of JASRI, financial affairs, overall management, documentation, personnel supervision, welfare programs for JASRI staff, provision of information to the public, beamline management, user support and services and library information management.

## Safety Office

The Safety Office is independent from both the Synchrotron Radiation Research Laboratory and the Administration Sector. It regulates overall safety site-wide such as radiation safety, handling of chemical wastes and biohazards, and environmental preservation.

## SPring-8 Advisory Committee

The SPring-8 Advisory Committee was established on the basis of the “Law regarding Promotion of Common Use of the Synchrotron Radiation Facility (SPring-8).” The committee meets at least twice a year at the request of JASRI to deliberate and makes recommendations on important matters such as the acceptance of applications for beam time and subsequent selection of proposals to conduct experiments at the public beamlines. For the purposes, the Proposal Review Committee and the Contract Beamline Committee are sub-structured under this committee.

## Proposal Review Committee

The Proposal Review Committee (PRC) was formed to report to the advisory committee on the review policy, procedures and review results. The PRC has six subcommittees to evaluate proposals in the following disciplines;

(i) Life Science,
(ii) Diffraction & Scattering,
(iii) XAFS,
(iv) Spectroscopy,
(v) Method & Instrumentation, and
(vi) Industrial Use.

In addition to the six subcommittees, a special subcommittees: long-term use was set up and the first special subcommittee was held in April 2000.

The members of the PRC are mostly scientists outside the SPring-8 Facility, but one scientist from JASRI must participate in each subcommittee.

## Contract Beamline Committee

This committee deliberates upon the construction of contract beamlines. It first reviews letters of intent submitted by organizations planning to construct their own beamlines and subsequently evaluates formal proposals that are submitted after the approval of letters of intent. Finally the committee reports the results of their evaluations to the SPring-8 Advisory Committee. To date, it has accepted letters of intent from nine organizations to construct eleven contract beamlines in total, and has approved seven proposals so far.

## JAERI-RIKEN-JASRI Steering Coordination Committee

For effective and efficient management, JAERI-RIKEN-JASRI discuss important matters regarding the operation of SPring-8 in this committee.

## Beamline Advisory Committee

The committee is responsible for evaluating the proposals submitted for public beamline construction. The committee first reviews the letters of intent submitted, and will deliberate the proposals on the basis of scientific feasibility and impact on the corresponding field of science. It reports the result of review to the JAERI-RIKEN-JASRI Steering Coordination Committee.

## Committee of R&D on Advanced Technology and Applications

This committee promotes and enhances the in-house research program known as the R&D Project on Advanced Technology and Applications, which are to be carried out in collaboration among JAERI, RIKEN and JASRI.

**Editor**
Seishi Kikuta
SPring-8 / JASRI

**Editing & Layout**
Marcia M. Obuti-Daté
SPring-8 / JASRI

**Printing**
Ono Printing Co., Ltd.

**J A S R I**
Users Administration Division

Kouto 1-1-1, Mikazuki, Sayo
Hyogo 679-5198, JAPAN
Tel. +81-(0) 791 58-2797 FAX: +81-(0) 791 58-2798

frontiers@spring8.or.jp
http://www.spring8.or.jp/

SPring-8

**Japan Synchrotron Radiation Research Institute**

Kouto 1-1-1, Mikazuki, Sayo
Hyogo 679-5198
JAPAN